DISSERTATION
SUBMITTED TO THE
COMBINED FACULTIES FOR THE NATURAL SCIENCES AND FOR MATHEMATICS
OF THE RUPERTO-CAROLA UNIVERSITY OF HEIDELBERG, GERMANY
FOR THE DEGREE OF
DOCTOR OF NATURAL SCIENCES

PRESENTED BY
DIPLOM-PHYSIKER COSIMO FEDELI
BORN IN SAN MARCELLO (PT), ITALY
ORAL EXAMINATION: FEBRUARY 06, 2008

ON STRONG LENSING

BY

GALAXY CLUSTERS

REFEREES:	PROF. DR. MATTHIAS BARTELMANN
	PROF. DR. LAURO MOSCARDINI

Über den starken Linseneffekt von Galaxienhaufen

Zusammenfassung

Wir stellen eine neue, semi-analytische Methode vor, um die Effizienz des starken Linseneffekts in Galaxienhaufen zu berechnen. Sie reproduziert die Ergebnisse vollständig numerischer Simulationen, ist aber wesentlich schneller. Wir wenden sie auf eine Galaxienhaufenpopulation an und zeigen, dass Verschmelzungsprozesse die Wahrscheinlichkeit für starke Linseneffekte erheblich erhöhen. Eine Analyse des starken Linseneffekts in kosmologischen Modellen mit verschiedenen Arten dynamischer dunkler Energie zeigt, dass die Anzahl stark verzerrter Bilder beträchtlich zunimmt, wenn frühe dunkle Energie zugelassen wird. Wir untersuchen die starken Gravitationslinseneigenschaften und die Röntgenemission von Galaxienhaufen, um Auswahleffekte zu quantifizieren. Wir berechnen optische Tiefen von Galaxienhaufen als Funktion der Beobachtungszeit und untersuchen, wie sich die Konzentrationsverteilung der Dichteprofile darauf auswirkt. Wir stellen fest, dass die Profilkonzentration einen Auswahleffekt auf die Linseneffizienz und die Röntgenleuchtkraft erzeugt. Schließlich zeigen wir, dass das Arc-Statistik-Problem in einem Universum mit realistisch normierten Schwankungen der Materiedichte auch dann fortbesteht, wenn die Rotverschiebungsverteilung der Quellen und Wechselwirkungen zwischen Galaxienhaufen angemessen berücksichtigt werden. Eine abschließende Untersuchung des starken Linseneffekts in der TeVeS-Theorie bestätigt, dass zusätzliche unsichtbare Masse notwendig ist, um die beobachteten Linseneffekte im verschmelzenden Galaxienhaufen $1\mathrm{E}0657-558$ zu sehen.

On Strong Lensing by Galaxy Clusters

Abstract

We present a novel, semi-analytic method for computing the strong-lensing efficiency of galaxy clusters. It nicely reproduces the results of fully numerical simulations while being substantially faster. Applying the method to a cluster population, we find that mergers considerably increase the probability for strong lensing. Analysing strong lensing in cosmological models with various forms of dynamical dark energy, we show that the number of highly distorted images is substantially larger when early-dark energy is allowed for. We jointly study strong-lensing and X-ray characteristics of clusters in order to quantify selection effects. We compute cluster optical depths as a function of exposure time and study how the concentration distribution of density profiles affects their strong-lensing and X-ray properties. We reveal a bias between lensing efficiency and X-ray luminosity and the profile concentration. Finally, we show that the arc-statistics problem persists in a universe with realistically normalised matter-density fluctuations even if the source redshift distribution and cluster interactions are appropriately taken into account. A concluding study of strong lensing in the TeVeS theory confirms that additional unseen mass is needed to explain observed lensing effects in the merging cluster $1\mathrm{E}0657-558$.

To Irene

That is the exploration that awaits you,
not mapping stars and studying nebulas,
but charting the unknown possibilities of existence.

Contents

Introduction **15**

1 Cosmological Background **19**
1.1 Introduction 19
1.2 Robertson-Walker Spacetimes 19
1.3 Friedmann’s Equations 20
1.4 Content of the Universe 21
  1.4.1 Radiation and Matter 21
  1.4.2 Dark Energy 22
1.5 Cosmological Parameters 23
1.6 Big Bang and Horizon 24
1.7 Early-Dark Energy and Cosmological Models 24
  1.7.1 Primordial Quintessence 24
  1.7.2 Cosmological Models 25
1.8 Cosmological Redshift and Distance Measures 26
1.9 Current Observational Status 28

2 Structures in the Universe **33**
2.1 Introduction 33
2.2 Linear Evolution 33
  2.2.1 Jeans Scale 33
  2.2.2 Perturbation Theory 34
  2.2.3 Statistics of Gaussian Random Fields 36
  2.2.4 Evolution of the Power Spectrum 37
2.3 Nonlinear Evolution 38
  2.3.1 Zel’dovich Approximation 38
  2.3.2 Spherical Collapse 39
  2.3.3 Mass Function 41
  2.3.4 Merger Rate 42
  2.3.5 Numerical Simulations 43
2.4 Galaxy Clusters 46
  2.4.1 Structure 46
  2.4.2 Emission and Mass Determination 47
  2.4.3 Non-Linear Scaling Relations 48
2.5 Current Observational Status 49

3 Gravitational Lensing **53**
3.1 Introduction 53
3.2 Fermat’s Principle 53
  3.2.1 Arrival Time 53
  3.2.2 Lens Equation 54
3.3 Lens Mapping 55
3.4 Lens Models 57
  3.4.1 Axially Symmetric Models 57
  3.4.2 Elliptical Models and Substructures 59
3.5 Arc Statistics 60
3.6 Current Observational Status 62

3.6.1 Strong Lensing 62
3.6.2 Weak Lensing 63

4 A Fast Method for Computing Strong Lensing Cross Sections: Application to Merging Clusters 65
4.1 Introduction 65
4.2 Lensing Cross Sections 65
4.2.1 Ray-tracing Simulations 66
4.2.2 Semi-analytic Method 66
4.3 Lensing Optical Depth 69
4.3.1 Halo Model 69
4.3.2 Modelling Halo Mergers 70
4.3.3 Mass Cut-off 70
4.4 Results 71
4.4.1 Cross Sections 71
4.4.2 Optical Depths 72
4.4.3 Sources Properties 73
4.5 Summary and Discussion 73
4.6 Approximate Convolution of a Function with a Step Function on the Source Plane 76

5 Effects of Early-Dark Energy on Strong Cluster Lensing 79
5.1 Introduction 79
5.2 Merger Trees 80
5.2.1 Monte-Carlo Simulations 80
5.2.2 Our Sample 80
5.3 Strong-lensing Statistics 81
5.4 Expectations 83
5.5 Results 85
5.6 Summary and Discussion 86

6 Selection Effects on X-ray and Strong-lensing Clusters in Various Cosmologies 89
6.1 Introduction 89
6.2 Luminosity and Temperature Boost 89
6.3 Fluxes Obtained From Individual Clusters 91
6.3.1 Ideal Flux 91
6.3.2 Instrumental Effects 93
6.3.3 Nominal Flux 93
6.4 Cluster Number Counts 94
6.5 Results 96
6.6 Summary and Conclusions 98

7 Effects of Halo Concentration Distribution on Strong-lensing Optical Depth and X-ray Emission 101
7.1 Introduction 101
7.2 Dark-matter Halo Concentration 101
7.3 Cluster Population 103
7.4 Results 103
7.4.1 Different Concentration Prescriptions 103
7.4.2 Scatter in the Concentration 104
7.4.3 Lensing Concentration Bias 106
7.4.4 X-ray Concentration Bias 107
7.4.5 Additional Effects 111
7.5 Summary and discussion 112

8 Strong Lensing Statistics and the Power Spectrum Normalization 115
8.1 Introduction 115
8.2 Expectations 115
8.3 Results 118
8.3.1 Optical Depth 119
8.3.2 Number of Arcs 121
8.4 Summary and Discussion 123

9 Asymmetric Gravitational Lenses in TeVeS and Application to the Bullet Cluster 125
9.1 Introduction 125
9.2 Fundamentals of TeVeS 125
9.2.1 Fields and Actions 126
9.2.2 The Free Function 126
9.2.3 Quasi-static Systems 127
9.2.4 Cosmology 127
9.3 Gravitational Lensing in TeVeS 128
9.4 Influence of the Free Function 129
9.4.1 Parameterization of the Free Function 130
9.4.2 Comparison to the Analytic Model 130
9.4.3 Varying Parameters 131
9.5 Non-spherical Lens Models 131
9.5.1 Choice of the Free Function 131
9.5.2 Calculating the Scalar Potential 132
9.5.3 Thin Lens Approximation 135
9.5.4 Elliptical Lenses 136
9.5.5 Lenses with Multiple Components 137
9.5.6 Modeling the Bullet Cluster 139
9.6 Conclusions 142

Conclusions 143

Bibliography 156

List of Figures

1.1 The equation of state parameter for DE (solid line), the density parameter for radiation (long dashed line) and that for matter (short dashed line) as a function of the scale factor. A DE model is considerd where the leaping kinetic term of the form Eq. (1.38) has parameters $k_0 = 1.1$ and $\varphi_0 = 276.6$ (Hebecker & Wetterich, 2001). 25

1.2 The density parameter for DE in the four cosmological models introduced in the text and detailed in Table 1.1. EDE1 (black solid line), EDE2 (red short-dashed line), a model with constant $w_\mathrm{x} = -0.8$ (blue long-dashed line) and a ΛCDM model (green dot-dashed line). 27

1.3 The angular diameter distance (lower pair of curves) and luminosity distance (upper pair) as a function of redshift for two of the cosmological models introduced. These are the EDE1 (black solid line) and the ΛCDM model (green dot-dashed line). 28

1.4 Constraints on the constant equation of state parameter for DE and the curvature density parameter form the 3-years WMAP data release jointly with 2dFGRS, SDSS and both main supernovae data sets (see text for details). Shown are 68% and 95% confidence levels (Spergel et al., 2007). 29

1.5 Constraints for the matter and cosmological constant density parameters from WMAP-3 data.The 68% and 95% confidence levels are shown as gray solid lines for the WMAP only constraints, and red-shaded areas for the WMAP data jointly with other cosmological probes, as labeled in the panels. The black solid line identify flat space sections (Spergel et al., 2007). 29

1.6 Constraints on the equation of state parameter for DE and the matter density parameter from the WMAP-3 data. 68% and 95% confidence leveles are shown as black solid lines for the WMAP only constraints, and red-shaded areas for the WMAP data jointly with other probes, as labeled in the four panels. Space flatness and a constant DE equation of state parameter are assumed (Spergel et al., 2007). 30

1.7 *Left panel.* Constraints on the matter and cosmological constant density parameters from the 1-year SNLS data release. 68.3%, 95.5% and 99.7% confidence levels are shown with solid contours for the SNLS data, dotted contours for the BAO data and dashed contours for the joint constraints. *Right panel.* Constraints on the DE equation of state parameter today and the matter density parameter. Linestyle is the same as for the left panel (Astier et al., 2006). 31

2.1 The growth factor times $(1 + z)$ as a function of redshift for the four cosmological models detailed in Table 1.1. These are EDE1 (black solid line), EDE2 (red short-dashed curve), a model with constant DE equation of state parameter $w_\mathrm{x} = -0.8$ (blue long-dashed curve) and the ΛCDM model (green dot-dashed curve). 35

2.2 The typical mass collapsing at redshift z as a function of redshift itself. The black solid line is for EDE1 model, the red short-dashed line for EDE2 model, the blue, long-dashed line is for the model with constant DE equation of state parameter $w_\mathrm{x} = -0.8$ and finally the green dot-dashed line is for the ΛCDM model. 38

2.3 *Left panel.* Linear power spectrum for the EDE1 model (black solid line) and the ΛCDM models (green dot-dashed curve). *Right panel.* Linear (red dot-dashed line) and nonlinear (black solid line) power spectrum for the EDE1 model. 39

2.4 Mass function in a ΛCDM universe as a function of mass at present day computed using the three different prescriptions detailed in the text. The black solid line refers to the original Press & Schechter (1974) formulation. The red dashed curve represents the Sheth & Tormen (2002) generalization and the green dot-dashed curve the Jenkins et al. (2001) fit to numerical simulations. 43

2.5 The red empty points with errorbars represent the mass function (times the square of the mass and divided by the background matter density) extracted from the Millennium Simulation (Springel et al., 2005) at various redshifts, as labelled in the plot. The blue dotted lines represent the relative prediction of the Press & Schechter (1974) mass function, while the black solid lines refer to the Jenkins et al. (2001) mass function. 44

2.6 The relation between the concentration of a virialised DM halo at redshift $z = 0.3$ and the virial mass as prescribed by the original NFW algorithm (black solid line), the Bullock et al. (2001) algorithm (red dashed line) and the Eke et al. (2001) algorithm (green dot-dashed line). 45

2.7 Marginalised likelihood contours (68% and 95% confidence levels) for the index and normalization of the power spectrum of density fluctualtions, assuming a power-law form. The black, solid contours are for the WMAP data only, while the red dashed regions combine WMAP data with supernovae and large scale structure measurements (Spergel et al., 2007). 49

2.8 Cumulative space density of GCs as a function of the DM velocity dispersion within r_{200} computed for two different values of S_8, as labelled. The curves are the predictions based on the Jenkins et al. (2001) mass function using three different values for the present matter density. The magenta shaded region shows the observed local space density of clusters with temperature greater than 6 keV ($\sigma_{\rm DM} \sim 1000$ km s^{-1}, Ikebe et al. 2002; Henry 2004), while black solid squares with errorbars show the space density of CIRS clusters (Rines et al., 2007; Evrard et al., 2007). 50

2.9 Thick solid contours show the 1σ and 3σ confidence levels in the $\Omega_{\rm m,0} - \sigma_8$ plane from CIRS GCs virial mass function. Dashed contours show the constraints from the caustic mass function (see text for details) and dot-dashed contours constraints from the virial mass function with masses computed using only red galaxies. The thin solid contours are the 68% and 95% confidence levels from the three-years data release of WMAP (Rines et al., 2007). 50

3.1 The radius of the tangential critical curve (black solid line), of the radial critical curve (red dashed line) and of the radial caustic (green dot-dashed line) for an NFW lens placed at redshift 0.3 with sources placed at redshift 1. The background cosmology is the ΛCDM model detailed before. . . . 58

3.2 Convergence (left panel) and shear (rigt panel) for a gravitational lens with SIS (black solid line) and NFW (red dot-dashed line) density profile. The background cosmology is the ΛCDM model detailed before, while lens and source redshift are set to 0.3 and 1 respectively. The mass of the halos is set to be $10^{15} M_\odot h^{-1}$ 59

3.3 *Left panel.* The tangential (outer curves) and radial (inner curves) critical lines for an NFW gravitational lens with elliptical isopotential contours. The values of the eccentricity are 0.1 (black curve) 0.2 (red curve) and 0.3 (green curve). As costumary, the origin of the coordinate frame is coincident with the center of the lens. The mass of the lens is $10^{15} M_\odot h^{-1}$, and lens and source redshifts are 0.3 and 1 respectively. *Right panel.* The corresponding caustics. For clarity only tangential caustics are shown. The underlying cosmology is the ΛCDM model detailed in Table 2.1. 60

3.4 *Upper panels.* The radial and tangential critical curves for two axially symmetric NFW density profiles of mass $10^{15} M_\odot h^{-1}$ each in the ΛCDM cosmological model. The lens redshift is 0.3 and the source redshift is at 1. In the left panel the distance between the centers of the profiles is 300 kpc h^{-1}, while in the right panel it is 200 kpc h^{-1}. *Lower panels.* As in the upper panels but shown are the caustics on the source plane. Radial caustics are omitted for clarity. 61

3.5 Marginalised 68% and 95% confidence levels in the $\Omega_{\rm m,0} - \sigma_8$ plane. Blue dashed regions indicate the constraints from the WMAP-3 data release, the pink ones those from the Canada-France-Hawaii Telescope Lensing Survey and the green ones are the combination of the two, as labelled in the plot (Spergel et al., 2007). 64

4.1 Lensing cross sections for long and thin arcs with a length-to-width ratio exceeding d as a function of the distance between the centres of two DM halos, for two (lens and source) redshifts. The halos are modelled as NFW density profiles with elliptically distorted lensing potential with eccentricity $e = 0.3$ (see Section 3.4.2). Green lines show the results of ray-tracing simulations for five different realisations of the random source distribution. Black lines are the results obtained with our semi-analytic method. 68

4.2 Mass of the lowest-mass halo producing large arcs in the sample of 46 halos used here to compute the lensing optical depth. The source redshift is $z_{\rm s} = 2$. The overall trend in the curve reflects the geometrical lensing sensitivity, while the fluctuations and the depth of the minimum reflect how mergers can lift low-mass halos above the strong-lensing threshold that would otherwise not be capable of strong lensing. 71

4.3 Evolution of the lensing cross section for gravitational arcs with a length-to-width ratio equal to or greater than $d = 7.5$ (top panels) and $d = 10$ (bottom panels) for four of the most massive halos in the sample. Sources are at redshift $z_{\rm s} = 2$. Red-dashed lines show cross sections calculated without taking account of merger processes. Black lines show cross sections enhanced by cluster interactions. Filled blue dots are the counterparts of the black lines obtained from fully numerical ray-tracing simulations. 72

4.4 The evolution with redshift of the optical depth per unit redshift for gravitational arcs with a length-to-width ratio equal to or larger than d. Solid lines include the effect of cluster mergers, while dashed lines do not. Upper curves refer to sources with $z_{\rm s} = 2$ and lower curves to sources with $z_{\rm s} = 1$. 73

4.5 Cross section for gravitational arcs with a length-to-width ratio exceeding $d = 10$ for a dark-matter halo of mass $10^{15}M_{\odot}h^{-1}$ as a function of the source size in arcseconds. Black and green lines show the results of the semi-analytic and of ray-tracing simulations, respectively, which are repeated with different random-number seeds for the ellipticities and the position angles of the sources, as in Figure 4.1. The source redshift is $z_{\rm s} = 1$, and the lens redshift is $z_{\rm l} = 0.3$. 74

4.6 Cross section for gravitational arcs with a length-to-width ratio exceeding $d = 10$ for several halos of increasing mass. Black and red lines refer to point-like or extended sources with area equal to that of a circle of radius $0.5''$, respectively. Short dashed lines indicate circular sources, long dashed lines refer to sources with random eccentricity drawn from the interval $[0, 0.5]$ ($q_{\rm s} \in [0.5, 1]$), and solid lines refer to sources with eccentricity 0.5. Sources are at redshift $z_{\rm s} = 1$ and the lens redshift is $z_{\rm l} = 0.3$. 75

4.7 Cross section for arcs with a length-to-width ratio exceeding $d = 10$ for a DM halo of mass $10^{15}\,M_{\odot}h^{-1}$ as a function of the source redshift. Three different lens redshifts are considered, as labeled in the plot. 75

5.1 Exemplary merger histories for five DM halos randomly selected from our sample in the ΛCDM model. The merger histories are extended up to the source redshift for each individual halo. 81

5.2 The differential (black solid line) and cumulative (red dash-dotted line) source-redshift distributions given by Eq. (5.5). 82

5.3 The Press & Schechter (1974) mass function for DM halos in the mass range $[10^{13}, 2.5{\times}10^{15}]M_{\odot}h^{-1}$ at redshift $z = 0.5$ for the four cosmological models studied in this Chapter, as labelled in the plot. 83

5.4 The probability that a DM halo of mass $M_{\rm p} = 10^{14}M_{\odot}h^{-1}$ merges with a sub-halo of mass $M_{\rm p}/2$ as a function of redshift per unit logarithmic mass of the merging sub-halo and per unit logarithmic cosmic time. Results are shown for all four cosmological models considered here, as labelled in the plot. 84

5.5 The logarithm of the optical depth per unit redshift for arcs with length-to-width ratio exceeding $d = 7.5$ for each of the cosmological models studied here (top and bottom-left panels), and for $d = 10$ in the model EDE1 (bottom-right panel). Black curves show the optical depths obtained including halo mergers with sub-halos, while red curves are obtained after ignoring the effect of halo interactions. 84

5.6 The logarithm of the optical depth per unit redshift for arcs with length-to-width ratio exceeding $d = 7.5$ obtained for the four DE cosmological models considered here. The lensing efficiency shown in the left panel takes transient boosts by cluster mergers into account, while that shown in the right panel ignores it. 85

5.7 *Top panels*. Logarithm of the cumulative optical depth per unit redshift, normalised to its value in the ΛCDM universe. Curves representing the four cosmologies studied in this work are shown, as labelled in the plot. *Bottom panels*. Logarithm of the cumulative optical depth per unit redshift, normalised to its value at present in a ΛCDM universe. Left and right panels show results that include and ignore cluster mergers, respectively. 86

6.1 The enhancement of temperature (left panel) and luminosity (right panel) of an interacting system according to Randall et al. (2002), where the main cluster has mass $M_1 = 7.5 \times 10^{14}M_{\odot}$, and the substructure's mass M_2 takes four different values, as labelled in the plot. Time is measured in units of the sound-crossing time of the main structure (Eq. 6.2) and starting from the instant t_0 of maximum boost. 91

6.2 The mass-temperature relation of our synthetic cluster sample. Black, empty circles represent our sample clusters at low redshift. The green dashed line is the original $M-T$ relation given by Eq. (6.7). The red filled squares with errorbars are the observed clusters of the HIFLUGCS sample, and the blue solid line is a relation with the same slope as Eq. (6.7) but with a normalization higher of a factor ~ 2. 92

6.3 The normalized difference between the nominal and the ideal flux as a function of the ideal flux itself is shown for the synthetic cluster population used in this work. The upper solid and lower dash-dotted curves show the mean and the scatter, respectively. The nominal flux is always $\sim 20\%$ larger than the ideal flux, while the scatter in the relation can be neglected only for high fluxes. . . 94

6.4 The total number of GCs observable on the whole sky, given as a function of the limiting nominal flux for the four different cosmological models considered here. Black solid lines are obtained by ignoring the transient boost due to cluster mergers, red lines are obtained taking it into account. The cyan horizontal line gives the number of GCs obtained from the *Reflex* cluster sample extrapolated to the whole sky ($F_{\rm n,lim} = 3 \times 10^{-12}$ erg s^{-1} cm^{-2}). 95

6.5 As Figure 6.4, but combining all curves in the same plot. Black and red curves are for the EDE1 and EDE2 models, respectively. The blue curve is for the model with constant equation-of-state parameter $w_{\rm x} = -0.8$, and the green line is for the ΛCDM model. For each model, the solid and dashed curves are obtained ignoring mergers and taking them into account, respectively. The horizontal line shows the number of clusters observed in the *Reflex* cluster sample. 95

6.6 Histograms for the cluster redshift distributions expected in the cosmological models studied here, as labelled in the boxes. The limiting flux is the same as for the *Reflex* cluster sample, $F_{\rm n,lim} = 3 \times 10^{-12}$ erg s^{-1} cm^{-2}. As before, the black lower curve does not account for cluster mergers, while the red upper curves do. 96

6.7 Contour lines for the nominal flux (upper panels) and for the lensing cross section for gravitational arcs with $d \geq 7.5$ (lower panels) in the ΛCDM model. The thick cyan contours correspond to the limiting nominal flux of the *Reflex* cluster sample. The upper heavy black contour line in the upper panels corresponds to a flux of 10^{-14} erg s^{-1} cm^{-2}, the others are spaced by one order of magnitude. Analogously, the lowest black contour in the lower panels corresponds to a cross section of 10^{-4} Mpc$^2 h^{-2}$, and the others are spaced of one order of magnitude. Merger processes are taken into account in the right panels, while they are ignored in the left ones. 97

6.8 The observed average optical depth for arcs with length to width ratio larger than $d = 7.5$ (left panel) and $d = 10$ (right panel) as a function of the nominal X-ray flux limit. Results are shown for the four different cosmologies considered here. Black solid lines represents results obtained by ignoring mergers processes, while broken red lines are obtained taking them into account. 98

6.9 The fraction of the optical depth for the formation of large gravitational arcs, contributed by X-ray selected clusters in a flux-limited sample, compared to the total optical depth. Different line styles represent different cosmological models, as labelled in the plot. The effects of cluster mergers are taken into account in the right panels and ignored in the left panels. The upper and lower panels show results for arcs with length-to-width ratios exceeding $d = 7.5$ and $d = 10$, respectively. . . . 99

7.1 The cross section for arcs with length-to-width ratio $\geq d$ is shown as a function of d. The mass of the lensing halo is $2 \times 10^{15} M_{\odot} h^{-1}$, the lens redshift is $z_{\rm l} = 0.3$ and the source redshift is $z_{\rm s} = 1$. Results for three different prescriptions for $c - M$ relation are presented as labeled in the plot. The two panels show results for axially-symmetric (top) and elliptical (bottom) lenses with an isopotential eccentricity of $e = 0.3$. 103

7.2 *Left panel.* Optical depth per unit redshift for arcs with length-to-width ratio $d \geq 7.5$ as a function of the lens redshift. The thin black and green lines show the results obtained ignoring and accounting for cluster mergers, respectively, both using the nominal $c - M$ relation. The heavy red and blue curves include the scatter in the $c - M$ relation. *Right panel.* Similar to the left panel, but for arcs length-to-width ratios $d \geq 10$, and using a different random-number seed. 104

7.3 Unnormalised distribution of the concentrations for all the halos in our sample with redshifts between $z_1 = 0.28$ and $z_2 = 0.32$. The black solid histogram shows the result obtained adopting the fiducial $c - M$ relation of Eke et al. (2001). The log-normal concentration scatter is taken into account for the red-dashed histogram. The vertical dashes indicate the median concentration in both cases. 105

7.4 Unnormalised distribution of the cross sections for gravitational arcs with length- to-width ratios $d \geq 10$ for all halos in our subsample with redshifts between $z_1 = 0.28$ and $z_2 = 0.32$. As in Figure 7.3, the black solid and red dashed histograms show results ignoring the concentration scatter and accounting for it, respectively. Dashed vertical lines mark the median cross sections for both cases. 106

7.5 The black and blue solid curves show the median, and the red and green dashed curves the mean cross section for arcs with length-to-width ratio $d \geq 10$. Only halos with concentrations above the threshold on the abscissa are included. The bottom pair of lines shows the result without any mass selection, while only halos more massive than $7.5 \times 10^{14} M_\odot h^{-1}$ are included in the top pair. . . 107

7.6 The black and blue solid curves show the median, the red and green dashed curves the mean concentration. Only halos with strong-lensing cross sections above the threshold on the abscissa are taken into account. The top pair of curves shows the result obtained without mass selection, while only halos more massive than $7.5 \times 10^{14} M_\odot h^{-1}$ contribute to the bottom pair of curves. . . 108

7.7 Black and blue solid curves show the median, red and green dashed curves the mean concentration for the subsample of DM halos between $z_1 = 0.28$ and $z_2 = 0.32$. Only halos with relative temperatures exceeding the threshold on the abscissa are included. The top pair of curves shows the result without mass selection, while only halos with mass larger than $7.5 \times 10^{14} M_\odot h^{-1}$ contribute to the bottom pair. 109

7.8 Black and blue solid curves show the median, red and green dashed curves the mean concentration for the subsample of DM halos between $z_1 = 0.28$ and $z_2 = 0.32$. Only halos with relative X-ray luminosities exceeding the threshold on the abscissa are taken into account. The top pair of curves was obtained without mass selection, while only massive halos with mass larger than $7.5 \times 10^{14} M_\odot h^{-1}$ contribute to the bottom pair. 110

7.9 The *rms* of the concentration distribution accounting for halos in the subsample with strong-lensing cross sections (left panel) or relative X-ray luminosities (right panel) exceeding the thresholds on the abscissa. The solid black lines are obtained without mass selection, while only massive halos with mass larger than $7.5 \times 10^{14} M_\odot h^{-1}$ contribute to the red dashed curves. 111

7.10 Cross section distributions. The vertical blue line shows the cross section for arcs with length-to-width ratio $d \geq 10$ computed for a DM halo of mass $2 \times 10^{15} M_\odot h^{-1}$ at redshift $z_1 = 0.3$ with sources at redshift $z_\mathrm{s} = 1$ and lensing-potential eccentricity $e = 0.3$. The red dot-dashed line is the distribution of the cross sections caused by the variation of halo concentrations with triaxiality. The green dashed line includes the ellipticity distribution of projected triaxial halos, and the black solid line contains both effects. 112

8.1 *Left panel*. Concentration of DM halos according to the prescription of Eke et al. (2001) as a function of virial mass at fized redshift $z = 0.3$. The five different values for the normalization of the power spectrum σ_8 analysed in this Chapter are considered, as labelled in the plot. *Right panel*. Collapse redshift according to Eke et al. (2001) as a function of σ_8 for DM halos at $z = 0$ with three different values of the mass: $M = 10^{14} M_\odot h^{-1}$ (black solid line), $M = 5 \times 10^{14} M_\odot h^{-1}$ (blue dashed line) and $M = 10^{15} M_\odot h^{-1}$ (red dot-dashed line). 116

8.2 *Left panel*. Press & Schechter (1974) mass function as a function of mass at fixed redshift $z = 0.3$. *Right panel*. Merger rate between a cluster of mass $M = 10^{15} M_\odot h^{-1}$ and a substructure of the mass m indicated on the abscissa, at $z = 0.3$. In both panels the different values of σ_8 used in this work are labelled. Note that here and in Figure 8.3 the merger rate is the probability for a DM halo to merge with a substructure per unit logarithm of the merging mass and per unit logarithmic time. 117

8.3 *Left panel*. Press & Schechter (1974) mass function as a function of redshift at fixed mass $M = 7.5 \times 10^{14} M_\odot h^{-1}$. *Right panel*. Merger rate between a cluster of mass $M = 10^{15} M_\odot h^{-1}$ and a substructure of mass $m = 5 \times 10^{13} M_\odot h^{-1}$ as a function of redshift. In both panels the different values of σ_8 used in this work are labelled 117

8.4 The optical depth per unit redshift for arcs with length to width ratio larger than $d = 7.5$ (top panels) and $d = 10$ (bottom panels) for the five different values of the normalization σ_8 used in this Chapter, as labelled in the plots. The left panels shows the results including the boosting effect of cluster mergers and the right ones, on the same scale, the results got ignoring it. 118

8.5 The total, average optical depth for arcs with length to width ratio larger than or equal to $d = 7.5$ (left panel) and $d = 10$ (right panel) as a function of the normalization of the power spectrum σ_8. The red, dot-dashed line shows the results including mergers, while the black, solid line shows the results ignoring them. 119

8.6 The ratio of the total, average optical depth for arcs with length to width ratio larger than or equal to $d = 7.5$ (black solid line) and $d = 10$ (red dot-dashed line) to that obtained ignoring the boosting effect of cluster mergers, as a function of σ_8. 120

8.7 The ratio between the cumulative optical depth for the different values of the normalization used in this work and that for $\sigma_8 = 0.7$. The left panel show the result with cluster mergers taken into account, while the right panel ignores their boosting effect. Only the case with length-to-width threshold $d = 10$ is shown, since the case $d = 7.5$ is extremely similar. 120

8.8 The $\mathrm{R} - \mathrm{I}$ color index as a function of redshift, computed from the spectra of three different morphological types of spirals and for elliptical galaxies, as labelled in the plot. 121

8.9 Conditional probability distribution for the magnification of images given a threshold for the length-to-width ratio of $d = 7.5$ (left panel) and $d = 10$ (right panel). The black solid lines show the result of ray-tracing simulations, while the red dot-dashed curves are the two-Gaussian best fit whose parameters are summarised in Table 8.1. 122

8.10 The number of arcs with length-to-width ratio threshold $d = 7.5$ (left panel) and $d = 10$ (right panel) predicted to be observed in a Λ-dominated cosmological model with normalization of the linear power spectrum as reported on the abscissa. Black solid lines refers to I-band magnitudes, while red dot-dashed lines to R-band ones. Three different limiting magnitudes are reported: 21.5 (bottom pair of curves), 24 (middle pair) and 26 (top pair). In the right panel it is also shown the observed number of giant arcs (see Section 3.6 for a definition) according to Le Fevre et al. (1994); Gioia & Luppino (1994) as a green shaded area, that should be compared with the lower red curve. Moreover, the filled black and red points represent the original result of Bartelmann et al. (1998) (in the I and R bands respectively) rescaled by using the source number counts computed in this Chapter. 123

9.1 The TeVeS Hernquist lens (dashed) with $r_{\mathrm{H}} = 2$ kpc compared to its corresponding point lens (solid) with respect to the reduced deflection angle $\hat{\alpha}$ for $M = 10^{11} M_{\odot}$ and $a_0 = 10^{-10}$ m s^{-2}. For $\xi \gg 1$, both angles approach the constant $\hat{\alpha}_{\infty} \equiv 2\pi\sqrt{GMa_0} \simeq 0.58''$. The transition to the MONDian regime can be characterized by the critical radius $r_0 \equiv \sqrt{GM/a_0} \simeq 10$ kpc. 129

9.2 Absolute (left) and relative (right) difference between the TeVeS reduced deflection angles of the analytic and the numerical Hernquist lens choosing the parameters from Section 9.3: Clearly, the deviations are small, $\Delta\hat{\alpha} \lesssim 10^{-4}$ arcseconds and $\Delta\hat{\alpha}/\hat{\alpha}_{\mathrm{analy}} \lesssim 10^{-4}$. For the numerical calculation, we have assumed $k_{\mathrm{s}} = 0.01$ and $y(\mu) = \mu^2/(1-\mu)$. 130

9.3 Accuracy test of our numerical method: Assuming a Hernquist lens with the parameters from Section 9.3, we compare the numerical result for the reduced deflection angle $\hat{\alpha}$ to the analytic one. The left panel shows the relative difference $\Delta\hat{\alpha}_{\mathrm{rel}} = (\hat{\alpha}_{\mathrm{analy}} - \hat{\alpha}_{\mathrm{num}})/\hat{\alpha}_{\mathrm{analy}}$. Please note that the quantity $\Delta\hat{\alpha}_{\mathrm{rel}}$ is limited by $-0.02 \leq \Delta\hat{\alpha}_{\mathrm{rel}} \leq 0.01$ for reasons of presentation, values outside this range are truncated. The right panel illustrates the relative deviation for the central part where $\Delta\hat{\alpha}_{\mathrm{rel}}$ reaches a maximum of approximately 20%. 133

9.4 *Left panel.* Numerically calculated TeVeS convergence map for the King-like profile Eq. (9.49) expressed in terms of the GR convergence κ_{gr} assuming $\zeta_0 = 50$ kpc. *Right panel.* Since Eq. (2.49) corresponds to an axisymmetric configuration, the effective TeVeS convergence κ and the ratio $\kappa/\kappa_{\mathrm{gr}}$ depend on the radial coordinate ξ only. As the calculated convergence maps relatively deviate from circular symmetry by $\mathcal{O}(10^{-3})$, which is due to our Fourier method, the presented results are averaged over all directions. Choosing $\zeta_0 = 50$ kpc (solid) and $\zeta_0 = 400$ kpc (dashed), we see that κ is significantly amplified in the central region when moving to higher values of ζ_0. . 134

9.5 Radii of the inner (left) and outer (right) critical curve for different choices of ζ_0: Increasing the lens' extent along the line of sight, the radius of the inner (outer) critical curve is driven outwards showing relative changes of up to roughly 6% (16%). The critical lines are calculated by interpolation between the grid points. 135

9.6 Numerically calculated TeVeS convergence κ (left panel) and the corresponding ratio $\kappa/\kappa_{\mathrm{gr}}$ (right) for an elliptical profile of type Eq. (9.52) with $\xi_{1,0} = 350$ kpc and $\xi_{2,0} = \zeta_0 = 200$ kpc: In the central part, the TeVeS convergence κ is unevenly amplified, thus breaking the elliptical symmetry. Compared to the dominant GR contributions, however, this effect is almost negligible. 136

9.7 *Left panel*. Numerically calculated TeVeS convergence ratio $\kappa/\kappa_{\rm gr}$ for the rotated profile Eq. (9.52) with $\xi_{1,0} = 350$ kpc: In the central part, the TeVeS convergence κ is unevenly amplified, similar to the unrotated case shown in the bottom panel of Figure 9.6. Thus, it seems unlikely that the observed effect is a numerical artifact caused by our method. *Right panel*. Critical curves for both TeVeS (solid) and GR (dashed) assuming an elliptical profile of type Eq. (9.52) with $\xi_{1,0} = 150$ kpc and $\xi_{2,0} = \zeta_0 = 200$ kpc. 137

9.8 Lensing properties of our two-bullet system assuming $\xi_1^{(2)} = 100$ kpc and $M_1 = M_2$ (top panel), $\xi_1^{(2)} = 300$ kpc and $M_1 = M_2$ (middle panel), and $\xi_1^{(2)} = 100$ kpc and $3M_1 = M_2$ (bottom panel), respectively: We present the numerical results for both the TeVeS convergence κ (left) and the corresponding ratio $\kappa/\kappa_{\rm gr}$ (middle) setting $\zeta_2 = 400$ kpc. On the right, the TeVeS critical lines are plotted for $\zeta_2 = 0$ (dashed) and $\zeta_2 = 400$ kpc (solid). Note that the radial critical curve for $\xi_1^{(2)} = 300$ kpc and $\zeta_2 = 0$ does not appear due to the grid's finite resolution. 138

9.9 TeVeS convergence maps for our toy model of the bullet cluster 139

9.10 TeVeS convergence ratio $\kappa/\kappa_{\rm gr}$ for our toy model of the bullet cluster 140

9.11 TeVeS maps of the shear component γ_1 for our toy model of the bullet cluster 141

9.12 TeVeS maps of the shear component γ_2 for our toy model of the bullet cluster 142

List of Tables

1.1 Cosmological parameters for four cosmological models described in Section 1.7. 26

2.1 Parameters for the cosmolology and the cold DM power spectrum for the four cosmological models detailed in Section 1.7. 37

4.1 Present-day masses and virial radii for the three most massive and the three least massive halos in our sample. 69

6.1 Best-fit amplitudes and exponents for the temperature (top row) and luminosity (bottom row) boosts during cluster mergers. 90

8.1 Parameters for the two-gaussian fit to the conditional probability for magnification given a threshold for the length-to-width ratio of simulated gravitational arcs. 122

9.1 Component masses and positions for our toy model of the cluster merger $1\mathrm{E}0657-558$: Concerning the masses of our toy model components, we use those derived by Clowe et al. (2006). The plasma mass is reconstructed from a multicomponent 3-dimensional cluster model fit to the Chandra X-ray image. Assuming a mass-to-light ratio of $M/L_{\mathrm{I}} = 2$, stellar masses are calculated from the I-band luminosity of all galaxies equal in brightness or fainter than the component's brightest cluster galaxies. Please note that all masses are averaged within an aperture of 100 kpc radius around the given position. For each component, the position perpendicular to the line of sight is approximately determined from the corresponding Magellan and Chandra images. 139

9.2 Parameter sets used within the toy model of the cluster merger $1\mathrm{E}0657-558$: In our simulations, the above sets are used to specify the component's alignment along the line of sight, i.e. the ζ-direction. 141

Introduction

Over the past two decades the commonly accepted picture of the Universe underwent dramatic changes, due mainly to unprecedent observational efforts. Such efforts were made possible by the great advances in instrumentation and observational and data compression tecniques that characterised recent years.

Just at the beginning of the 90s the COBE satellite (Smoot et al., 1992) succesfully measured to a high precision the mean temperature of the Cosmic microwave background, and detected for the first time deviations therefrom. Among other things, the tiny amplitude of such deviations confirmed the case for the dominance of collisionless dark matter on cosmological scales. About ten years later, the WMAP satellite (Spergel et al., 2003, 2007) much refined the COBE measurements and for the first time an experiment detected the E-mode polarization of the relic radiation (Kovac et al., 2002). The polarization signal is mainly induced by the Thomson scattering between photons and free electrons at the emission surface, and has been used as an additional source of cosmological information. Also, gravitational light deflection acting on the background radiation was only very recently detected using, among others, WMAP data (Smith et al., 2007).

In the near future, the ESA satellite Planck promises to refine the measurements related to the cosmic radiation even more, thanks to a wider frequency coverage, a much improved sensitivity and resolution and a better understanding of the foreground systematics. Likely, it will allow the detection of the polarization B-modes, possible indication for the presence of primordial gravity waves, and will thighten by more the constraints on the values of cosmological parameters. In addition to this, Planck data will provide the most sensitive all-sky survey in the sub-millimeter band, permitting the detection of up to thousands galaxy clusters due to their thermal Sunyaev-Zel'dovich effect (Schäfer & Bartelmann, 2007). This will provide invaluable information on the number counts of distant clusters and the properties and evolution of the intra-cluster plasma.

Much attention was also recently devoted to the identification of distant supernovae of type Ia, that can be used as standard candles for probing the geometry of the Universe. Such data provided one of the first independent proofs of the accelerated expansion of the Universe, and the subsequent need for a dark energy component in the cosmic fluid (Astier et al., 2006). Until today very few supernovae have been observed at redshift above unity (Riess et al., 2004), but many other projects are ongoing in order to enlarge this number by much. The SNAP project for instance (Aldering et al., 2002), forecast the observation of up to $2,000$ new supernovae at redshift smaller than ~ 2.

The knowledge of the large scale distribution of matter in the Universe greatly improved as well thanks to the wide optical surveys (Tegmark et al., 2004; Cole et al., 2005), that allowed to determine the redshift and position of hundreds of thousands of galaxies. This permitted to constrain the dark and luminous matter structure on the largest scales, thanks also to the application of techniques involving gravitational lensing. As will be explained in more detail in the course of this thesis, cosmic shear and cosmic tomography indeed permit to put constraints on the projected and 3-dimensional distribution of matter in the Universe.

Finally, recent years saw the advent of a new generation of X-ray satellites, like ROSAT (Voges, 1993) first and Chandra (Weisskopf et al., 2002) and XMM-Newton (Jansen et al., 2001) then. These allowed both to have all-sky surveys of X-ray emitting galaxy clusters and to resolve the finer details of the X-ray structure of individual objects, revealing a variety of phenomena like shock fronts and cooling flows. The data gathered permit to track the dynamical and thermodynamical history of galaxy clusters, both as individuals and as a population, giving priceless information about the formation process of cosmic structures. Moreover, the Sunyaev-Zel'dovich effect from the hot plasma in galaxy clusters will be an object of much attention in the near future, not only because of the Planck satellite, but also because of forthcoming dedicated observatories like ALMA (Brown et al., 2004).

In addition to the observational tecniques, the ability of formulating theoretical predictions also improved dramatically thanks to the use of numerical simulations. The advances in the computer technology and in the numerical algorithms allow simulations of the large scale structure of the Universe with a space and time resolution unconceivable just two decades ago. Also individual objects like galaxies and galaxy clusters can be simulated to a very high accuracy, providing a large number of key details to be compared with observations. One of the main successes in numerical cosmology consists of the understanding of the distribution and clustering properties of dark matter. Baryonic matter, due to the related complex physical processes, is much more difficult to simulate, and there are several points where numerical works fail to reproduce the observational data in this respect. Advances in computational tecniques, as well as in the theoretical understanding of the main processes affecting gas physics will be key issues in future research.

From the combination of the above observational and theoretical efforts, a quite clear general cosmological picture has emerged. According to that, the Universe is well described by general relativity and spatially flat. Moreover it is filled in for three quarters of some unknown kind of uniform dark energy and the remaining content is basically made up of matter, of which about 80% is not visible. This standard cosmological model has proven to be unprecedentedly succesful in describing the observable Universe, and up to date managed to broadly pass almost all the observational tests it went through.

While from the observational point of view the standard model works very well, from a theoretical perspective it is highly unsatisfactory. Firstly, for several reasons the dark matter component cannot be constituted by known particles, implying that the current standard model for particle physics is either wrong or inaccurate for high energies. Direct search for new dark matter particle candidates is currently ongoing. Secondly, and maybe more fundamentally, the dark energy component lacks any theoretical explanation. One possibility is that it is the vacuum energy of known fields that permeate the Universe. However, naive computation of the vacuum energy density for the electromagnetic field for instance, leads to a value that is more than one hundred orders of magnitude larger than the observed value. Alternatively, vacuum energy could be replaced by some kind of scalar field that mimicks it, but this still poses problems on why such a field should be dominant just recently, as shown by observations. Understanding the properties of dark energy (Albrecht et al., 2006) will be of fundamental importance in the future to put limits on the many theoretical possibilities.

An alternative route to avoid such theoretical inconvenience is, rather than postulate some exotic content of the Universe, to change the way in which the dynamics of the Universe itself and of matter inside it reacts to such a content. In other words, the alternative is to modify the gravity law, either extending general relativity, where possible, or replacing it with some more fundamental theory, possibly with quantum-mechanical motivation. Several attempts have been made in this direction, using as starting point both the dynamics of galaxies and galaxy clusters and the dynamics of the Universe. However, many of these attempts did not pass more elaborated tests, like solar system phenomenology, and for others the development of the necessary formalism is lengthy and still partially lacking. In summary, for the time being there is no alternative theory that shares the great success of general relativity within the standard cosmological model, though several good candidates exist.

The standard cosmological model gives a global picture of the Universe that is relatively clear. Nevertheless, there remain several details of the structure formation process that are still not thoroughly understood. Key ingredients to clarify them, expecially concerning galaxy clusters, are the gravitational deflection of light and X-ray emission.

Despite the fact that X-ray emission is related to the intra-cluster hot plasma, hence to the baryonic matter only, its bulk properties like temperature and luminosity are sensitive to the overall potential well of the structure. Also, the finer details in the distribution of dark matter possibly influence the details of the observed X-ray emission pattern. As a consequence, this kind of observations give a wealth of information also about the dark mass of galaxy clusters. Unlike gravitational lensing however, the attempt to determine global properties of clusters using X-ray emission only often assumes the gas to be in hydrostatic equilibrium in the overall dark matter potential well, which needs not always be the case. Combining X-ray with lensing studies, for instance, can allow to understand to which extent the hydrostatic equilibrium hypothesis is satisfied, which in turn is valuable in order to constrain the dynamical activity of galaxy clusters (Puchwein & Bartelmann, 2007). Also, measuring the fraction of the clusters' mass that resides in gas and comparing that to the cosmic baryon fraction permits to test the correctness of the structure formation and baryonic infall paradigm.

It was already explained that the new X-ray satellites revealed a variety of phenomena concerning the intracluster medium, some of which are not yet succesfully reproduced in numerical hydrodynamical simulations, and therefore much work remains to be done in this direction as well. These kind of details are of fundamental importance in understanding the baryonic physics and its interplay with the dark matter component.

As mentioned above, the gravitational deflection of light is a tool of fundamental importance in probing the dark side of the Universe. First of all, photons' path are bent by matter clumps independently of matter's intrinsic nature and physical state. As a consequence, gravitational lensing is the ideal technique to understand the properties and distribution of invisible matter. In addition, light deflection can be used in combination with other kinds of observations that are sensitive only to luminous matter, in order to disentangle the contribution and separate the effects of the two components. This is of extreme importance for understanding the baryons' effect on the dark matter density profiles.

The internal structure of galaxies and galaxy clusters probed through gravitational lensing yelds already a big deal of information on their formation process, that ultimately depends on the underlying cosmology and on the initial conditions. However, light deflection by galaxy clusters gives also seldomly rise to strongly distorted images like gravitational arcs that can be used statistically to gather cosmological information, or at least as a cross-check for the standard model. In spite of their rarity, the abundance of these strong lensing events is highly sensitive to the source and galaxy-clusters distributions, in addition to the deflectors' internal structure and the distances involved. All of these factors are somehow influenced by the underlying cosmology, and in particular by the properties of dark energy.

The number of gravitational arcs predicted from numerical simulations for a standard cosmological model is highly in contrast with the actually observed number (Bartelmann et al., 1998). This make up one of the few instances in which the standard picture of the Universe is not succesful, and hints at some important piece of cluster physics that has been ignored or not properly treated. Alternatively, this could hint at an extension of the cosmological constant paradigm, with the introduction of some form of dynamical quintessence.

Despite the big theoretical effort in the past decade, many questions about arc statistics still remain without a precise answer. Namely, what are the most relevant contributions to the global strong lensing efficiency of the galaxy cluster population? What is the role played by the internal structure of dark matter halos in this context? What is the effect of a dynamical form of dark energy? What is the amplitude of the strong lensing statistics problem when the source distribution and the dynamical evolution of clusters are properly taken into account? How is the strong lensing framwork modified when using theories of gravity alternative to general relativity?

The aim of this thesis is to shed some new light on some of these questions. Part of this goal is accomplished by developing a novel, semi-analytic approach to strong lensing statistics. The method is illustrated and tested in Chapter 4, together with a discussion of its validity and limitations. In the same Chapter, this method is applied to the computation of the global strong lensing efficiency of a model population of galaxy clusters, extracted from a cosmological simulation. The mergers and interactions between structures, that play a fundamental role in the strong lensing efficiency and in the formation of galaxy clusters, are properly taken into account with a simplified model.

In Chapter 5 the same investigation is extended to models beyond the standard one. To that end, the semi-analytic calculation of lensing effciency is combined with Monte-Carlo generated merger trees for cluster-sized dark matter halos, according to the guidelines of Somerville & Kolatt (1999). The total and differential lensing efficiencies are computed and compared between four different dark energy models, including the usual cosmological-constant one and two models with early-dark energy, whose relevance has recently been pointed out. As an improvement with respect to previous analyses, we use a realistic redshift distribution for the background galaxy population.

Since up to date the search for strong lensing events in general and for gravitational arcs in particular is performed in galaxy clusters that are selected through their X-ray luminosity, it is natural to ask how the previous results hold if a flux threshold is applied to the synthetic cluster population. An answer to this question is given in Chapter 6, where the lensing efficiency of X-ray luminous clusters is studied. The boost in temperature and luminosity that cluster mergers cause is also taken into account with a simple analytic prescription that Randall et al. (2002) calibrated against numerical hydrodynamical simulations. Predictions are made about the strong lensing efficency observed in flux-limited cluster samples.

In Chapter 7 we turn more attention to the inner structure of cluster-sized dark matter halos, and in particular to the effect that a broad concentration distribution can have on the overall statistics of gravitational arcs and on the observed X-ray properties, namely gas temperature and luminosity. The concentration distribution that emerges from cosmological simulations of structure formation is used, togheter with the previously produced synthetic cluster population for the first goal. For the second one, extended scaling relations between general properties of clusters that take into account the inner structure of host dark matter halos are employed.

In Chapter 8 care is taken for evaluating the effect on strong lensing statistics of the normalization of the power spectrum for primordial density fluctuations. The results are analysed in light of the new data release for the WMAP satellite. Moreover, a realistic luminosity function for background sources is used in order to predict the number of gravitational arcs seen in a low-normalization standard cosmological model. The relation to the observational status and to previous work is discussed.

As a final goal, we also study in detail how theories of gravity alternative to general relativity cope with gravitational lensing. In Chapter 9, a numerical algorithm is presented and tested that allows gravitational lensing studies in the context of the recently proposed tensor-vector-scalar theory of gravity, that incorporates in a fully covariant way the modified newtonian dynamics first developed by Milgrom (1983a). The algorithm is also applied to a toy model of the cluster $1\mathrm{E}0657-558$, that was recently pointed out as the direct evidence for the existence of dark matter (Clowe et al., 2006)

The first three Chapters of this thesis are meant for introductory pourposes, in order to give all the important concepts relevant for the subsequent discussion. In particular, in Chapter 1 we review the standard cosmological model derived from general relativity with the postulated presence of dark matter and dark energy. We also explore some important properties of cosmological models with early-dark energy. In Chapter 2 we continue the discussion by describing the structure formation paradigm implanted within the standard cosmological model. In particular we stress how the presence of primordial quintessence and the normalization of the power spectrum for density fluctuations alter this scenario. Finally, in Chapter 3 we describe the formalism and phenomenology of the gravitational deflection of light, with particular emphasis on the strong lensing features that are the center of this work.

In this thesis we shall use notation according to which the speed of light in vacuum c is explicitly written, unless otherwise stated. For tensors and vectors, greek letters will run over the full set of the four spacetime coordinates, while latin letters will be restricted to spatial or angular coordinates only. The adopted signature of the spacetime metric is $(-,+,+,+)$. Boldface will be exclusively used to denote two and three-dimensional vectors, and summation over repeated indices for vectors and tensors will be always considered implicit, according to Einstein's summation convention.

Chapter 1

Cosmological Background

1.1 Introduction

The very foundation of modern cosmology is Einstein's gravitation theory, General Relativity (GR henceforth, Einstein 1915a,b, 1916), that allows a global description of the dynamics and evolution of the Universe on large scales. One of the basic assumptions of the theory is that gravity is not an actual force, but the action of matter and energy distributions on test particles is mediated by the metric tensor g of the 4-dimensional spacetime manifold. While the striking predictive power of GR is shared by other metric theories of gravity (Brans & Dicke, 1961; Starobinskij, 1980; Dvali et al., 2000; Bekenstein, 2004; Moffat, 2006; Zlosnik et al., 2007), up to now Einstein's gravity proved unprecedentedly successful in describing and forecasting a variety of phenomena, especially on cosmological scales. One of these phenomena, the gravitational deflection of light, is the focus of this thesis and will be described in detail in Chapter 3

The basic equations of GR are *Einstein's equations* which link the metric tensor to the matter-energy content of the spacetime. This set of equations is usually written in compact, tensor form as

$$\mathcal{G} = \frac{8\pi G}{c^4}\mathcal{T}. \tag{1.1}$$

Here, $\mathcal{G}$ is *Einstein's tensor*, containing derivatives up to the second order of the metric g, while $\mathcal{T}$ is the *energy-momentum tensor*, specifing the matter-energy content of the system at hand. Both $\mathcal{G}$ and $\mathcal{T}$ are rank-2 symmetric tensors, hence Eq. (1.1) is in general made of 10 independent equations.

In the rest of this Chapter we shall review the standard cosmological model derived from GR, with particular focus on those aspects that will be most relevant for the development of this thesis. Cosmology and light deflection in an alternative gravitation theory will be dealt with in Chapter 9.

1.2 Robertson-Walker Spacetimes

The number of independent Einstein's equations can usually be reduced employing the symmetry of the system at hand, and this is particularly true in cosmology. The symmetry assumption usually undertaken in this case is historically called *cosmological principle*, and it states that there is no preferred position nor direction in space, or in other words that the Universe is homogeneous and isotropic on large scales.

The requirement, implied by the cosmological principle, according to which the Universe looks spatially isotropic to a comoving observer, has the consequence that the spacetime manifold can be written as the warped product of $\mathbb{R}$, representing the time direction, with a 3-dimensional submanifold of constant curvature k, representing the space. Moreover, the metric of such a spacetime must have a unique form, that takes the name of *Robertson-Walker* metric (Robertson, 1933; Walker, 1933; Robertson, 1935), and reads

$$g = -c^2dt^2 + a(t)^2\gamma. \tag{1.2}$$

The time variable t is called *cosmic time*, γ is the metric on the space submanifold and the *scale factor* a describes the global dynamics of space itself. Note that, if ω is a 1-form on the spacetime manifold, here and in the following we use the notation $\omega^2 = \omega \otimes \omega$.

For some applications, it proves convenient to define a *conformal time* as $d\eta \equiv dt/a(t)$, by means of which the Robertson-Walker metric Eq. (1.2) takes the form

$$g = a(\eta)^2\left(-c^2d\eta^2 + \gamma\right). \tag{1.3}$$

In this way, it becomes apparent that the metric Eq. (1.3) is conformally static, in the sense that the related geodesic structure is independent of time.

Since no preferred position is possible on the space submanifold, freedom is given to choose an arbitrary point as the origin of the coordinate system and use spherical polar coordinates around that point. Conventionally, the origin of any reference frame is assumed to coincide with the observer's position, though this is not strictly necessary. The metric of a space with constant curvature k expressed using a spherical polar coordinate system takes the form

$$\gamma = \frac{dr^2}{1-kr^2} + r^2\left(d\theta^2 + \sin^2\theta d\varphi^2\right). \tag{1.4}$$

It is discernible from the last equation that three possible spatial geometries are allowed, depending on the sign of the constant k. In particular, if $k = 0$, then the space is Euclidean, or *flat*. If $k > 0$ then it is positively curved, i.e. it is a hypersphere and it must be $r < \sqrt{1/k}$. Finally, if $k < 0$, the space is negatively curved. In some circumstances, a replacement of the radial coordinate r is recommended, using instead the coordinate χ such that

$$d\chi \equiv \frac{dr}{\sqrt{1-kr^2}}. \tag{1.5}$$

With this substitution the spatial metric Eq. (1.4) assumes the new form

$$\gamma = d\chi^2 + f_k^2(\chi)\left(d\theta^2 + \sin^2\theta d\varphi^2\right), \tag{1.6}$$

where the function f_k is such that

$$f_k(\chi) = \begin{cases} k^{-1/2}\sin(k^{1/2}\chi) & \text{if } k > 0 \\ \chi & \text{if } k = 0 \\ (-k)^{-1/2}\sinh[(-k)^{1/2}\chi] & \text{if } k < 0 \end{cases}. \tag{1.7}$$

It is important to note that neither the two radial coordinates r and χ, nor the angular coordinates (θ, φ) depend on time, and for this reason they are said to be *comoving coordinates*. The time evolution of the Robertson-Walker metric's space part is completely encapsulated in the scale factor $a(t)$, hence, if $\boldsymbol{x}$ is the set of three comoving coordinates, the related *physical coordinates* are defined as $\boldsymbol{r}(t) \equiv a(t)\boldsymbol{x}$.

1.3 Friedmann's Equations

As explained above, GR describes the interplay of matter-energy and the metric of the spacetime manifold through Einstein's equations. In order to be able to solve the set of Eqs. (1.1), it is necessary to specify the matter-energy content of the Universe, that is the energy-momentum tensor $\mathcal{T}$. The uniformly distributed cosmic fluid is made of various components, of which ordinary non-relativistic matter and radiation are two obvious ones. However, independently of what these components exactly are, the energy-momentum tensor of the cosmic fluid is often assumed to take the perfect fluid form

$$\mathcal{T}^{\alpha\beta} = (\rho c^2 + p)u^\alpha u^\beta + p g^{\alpha\beta}, \tag{1.8}$$

where ρ is the matter density, p is the pressure and u is the four-velocity field of the fluid itself, normalised such that $g_{\alpha\beta}u^\alpha u^\beta = -1$. Obviously, to preserve the isotropy of space, u must have no spatial components, and must therefore be parallel to the time direction.

Introducing the Robertson-Walker metric given by Eq. (1.2) and Eq. (1.4), and the energy-momentum tensor of Eq. (1.8) into the field Eqs. (1.1) results in only two independent relations for $a(t)$ and its derivatives up to second order. Indicating with a dot the derivative with respect to cosmic time, they read

$$\frac{\dot{a}^2}{a^2} + \frac{kc^2}{a^2} = \frac{8\pi G}{3}\rho, \tag{1.9}$$

and

$$\frac{\ddot{a}}{a} = -\frac{4\pi G}{3}\left(\rho + 3\frac{p}{c^2}\right). \tag{1.10}$$

The basic structure of the original Einstein equations can still be recognised, since on the left-hand side we have derivatives up to the second order of the metric components, while on the right-hand side the matter-energy content of the Universe is visible, in the form of the density ρ and pressure p of the cosmic fluid. Eqs. (1.9) and (1.10) are called *Friedmann's equations* (Friedmann, 1922), and describe the evolution of the scale factor a as a function of the cosmic time, given the matter-energy content of the Universe.

The local energy-momentum conservation is expressed by $\mathcal{T}^{\alpha\beta}{}_{;\beta} = 0$, where a semicolon denotes covariant derivation with respect to the metric g. These conservation laws do not introduce independent equations, simply giving

$$\dot{\rho} + 3\frac{\dot{a}}{a}\left(\rho + \frac{p}{c^2}\right) = 0, \tag{1.11}$$

that can also be derived as a combination of Eq. (1.9) and Eq. (1.10). Replacing the independent variable t with the scale factor a returns for the last equation

$$\frac{d}{da}(\rho a^3) = -3\frac{p}{c^2}a^2. \tag{1.12}$$

This is nothing but the first law of thermodynamics applied to the entire Universe as an adiabatic system, namely the change in internal energy equals minus the pressure times the change in volume.

1.4 Content of the Universe

1.4.1 Radiation and Matter

For the system formed by the two Friedmann equations (or one of the Friedmann equations and the energy-momentum conservation equation) to be closed, additional constraints are needed in the form of the equation of state for the cosmic fluid, that is a relation between pressure and density. The usual assumption is that $p = w\rho c^2$, where the *equation of state parameter* w is in general a function of cosmic time, and depends on which kind of component is considered. Using the scale factor as the independent variable and inserting this equation of state in the conservation Eq. (1.12) we obtain

$$\rho = \rho_0 \exp\left[-3\int_1^a (1+w)\frac{da}{a}\right], \tag{1.13}$$

where henceforth the suffix 0 indicates quantities evaluated at present cosmic time t_0, and the scale factor is always normalised such that $a(t_0) = 1$.

What remains to be estabilished are the constituents of the fluid filling the Universe, and more important which one is the dominant one at a given epoch, hence determining the global World dynamics. One obvious component of the cosmic fluid is radiation, for which the pressure is comparable to the energy density, and in particular it can be shown that $w_{\mathrm{r}} = 1/3$. Inserting this in the previous Eq. (1.13) we get $\rho_{\mathrm{r}} = \rho_{\mathrm{r},0}a^{-4}$. The same result holds true also for any other kind of relativistic particle like neutrinos. Assuming that the energy spectrum of the radiation fluid is well described by a thermal black body spectrum, its temperature can be related to the matter density using the Stefan-Boltzmann relation

$$\rho_{\mathrm{r}} = \frac{\pi^2 k_{\mathrm{B}}^4}{15\hbar^3 c^5}T_{\mathrm{r}}^4, \tag{1.14}$$

where k_{B} is the Boltzmann constant. The accuracy of this assumption will be demonstrated in Section 1.9. It follows that the time evolution of the radiation temperature can be expressed as $T_{\mathrm{r}} = T_{\mathrm{r},0}a^{-1}$.

It has now long been known that, assuming correctness of GR, the vast majority of matter in the Universe must be dark, in the sense that it does not couple with photons but is sensitive only to gravitational and (maybe) weak interactions. This fact was first mentioned in Zwicky (1933) (see also Zwicky 1937), but became part of the standard model of the Universe only long after, when evidences for the missing mass problem became stricking (Rubin et al., 1978, 1980, 1982). Also, it is well accepted (see Chapter 2 for details) that this Dark Matter (DM henceforth) component is cold, in the sense that its mean thermal energy became negligible when compared to the rest mass energy of the constituent particles before decoupling from the radiation fluid. As a consequence, the pressure in DM is negligible with respect to the energy density, and hence $w_{\mathrm{m}} = 0$ can be set in this case. This property is obviously also shared by ordinary, luminous matter. For a perfect gas of particles of mass m at ordinary temperature T for instance, one has $w = k_{\mathrm{B}}T/mc^2 \simeq 0$.

It is important to stress that the amount of observed ordinary matter agrees well with the estimate for the abundance of baryons produced during primordial nucleosynthesis (Kneller & Steigman, 2004), meaning that virtually all the DM in the Universe must be non-baryonic in nature.

Inserting $w = 0$ in Eq. (1.13) we obtain $\rho_\mathrm{m} = \rho_{\mathrm{m},0} a^{-3}$. In other words, the matter density is inversely proportional to the volume of the Universe, which is a trivial result if the total mass in the Universe is assumed to be fixed. The fact that the energy density of radiation evolves more quickly than that of non-relativistic matter leads to the conclusion that there must be an equivalence scale factor a_eq at which the two are equal. It is immediate to see also that $a_\mathrm{eq} = \rho_{\mathrm{r},0}/\rho_{\mathrm{m},0}$.

1.4.2 Dark Energy

Mounting evidence has accumulated in the past decade, according to which the Universe is not only expanding (meaning $\dot{a}(t_0) > 0$, as it has long been known, Hubble 1929), but that this expansion is accelerated today, i.e. $\ddot{a}(t_0) > 0$. Such evidence will be described in detail in Section 1.9. As it is clear from the second Friedmann Eq. (1.10), present day acceleration is possible only if $p < -\rho/3$, meaning $w < -1/3$ for the dominating component of the cosmic fluid. A negative equation of state parameter cannot be achieved by non-relativistic matter nor radiation, hence the dynamics of the Universe must be at present time dominated by some form of energy with negative pressure. This energy component cannot participate in the formation of cosmic structure, otherwise it would be detected as DM, thus it must be uniformly distrubuted. Such Dark Energy (DE henceforth) component is often modelled as the energy density of a scalar field φ, called quintessence, that is possibly coupled only to gravity. The Lagrangian describing the evolution of a generic scalar field in the GR framework reads

$$\mathcal{L} = \frac{1}{2} g^{\alpha\beta} \varphi_{,\alpha} \varphi_{,\beta} + V(\varphi), \tag{1.15}$$

where a comma denotes standard coordinate derivation, and the function $V(\varphi)$ is the self-interaction potential of the quintessence scalar field.

By definition, the stress-energy tensor related to such a Lagrangian reads

$$\mathcal{T}_{\alpha\beta} = \varphi_{,\alpha}\varphi_{,\beta} - g_{\alpha\beta} \left[\frac{1}{2} g^{\mu\nu} \varphi_{,\mu}\varphi_{,\nu} + V(\varphi) \right]. \tag{1.16}$$

If the cosmological principle is to be satisfied, then the spatial derivatives of the scalar field must vanish, otherwise preferred positions in space would be singled out, and hence only the time derivative is allowed to be non-zero. Bearing this in mind, and moreover recalling that, if the Robertson-Walker metric Eq. (1.2) is used then $g_{00} = 1/g^{00} = -1$, for the time-time component of the stress energy tensor is found

$$\mathcal{T}_{00} = \frac{\dot{\varphi}^2}{2c^2} + V(\varphi). \tag{1.17}$$

Similarly, the space-space components read

$$\mathcal{T}_{ij} = g_{ij} \left[\frac{\dot{\varphi}^2}{2c^2} - V(\varphi) \right]. \tag{1.18}$$

Comparing the last two relations to the stress-energy tensor of a perfect fluid given in Eq. (1.8), the density and pressure formally associated with the scalar field can be determined as

$$\rho_\mathrm{x} = \frac{\dot{\varphi}^2}{2c^4} + \frac{V(\varphi)}{c^2}, \tag{1.19}$$

$$p_\mathrm{x} = \frac{\dot{\varphi}^2}{2c^2} - V(\varphi). \tag{1.20}$$

The related equation of state parameter is therefore

$$w_\mathrm{x} = \frac{\dot{\varphi}^2 - 2c^2 V(\varphi)}{\dot{\varphi}^2 + 2c^2 V(\varphi)}. \tag{1.21}$$

From the last equation it is apparent how the DE equation of state parameter depends on the interplay between the kinetic and the potential energy of the related scalar field. The detailed behaviour of this component thus depends on the exact shape of the self-interaction potential $V(\varphi)$.

Inserting now Eq. (1.19) and Eq. (1.20) into the Friedmann equations (1.9) and (1.10) it is possible to obtain after straightforward calculation the *Klein-Gordon equation*, that describes the time evolution of the quintessence field in an expanding universe.

$$\ddot{\varphi} + 3\frac{\dot{a}}{a}\dot{\varphi} + c^2 V'(\varphi) = 0, \tag{1.22}$$

where a prime denotes the derivative with respect to φ. A negative equation of state parameter for the DE can evidently be achieved with a suitably small kinetic term today, namely $\dot{\varphi}^2 < c^2 V(\varphi)$.

One limiting case of DE is reached when the kinetic term is negligible with respect to the self-interaction potential, so that w_x approaches -1. Eq. (1.13) then shows that the DE density has no evolution in time, therefore it can be replaced by

$$\Lambda = \frac{8\pi G}{c^2}\rho_\mathrm{x}. \tag{1.23}$$

The constant in Eq. (1.23) is referred to as *cosmological constant* for historical reasons.

1.5 Cosmological Parameters

From a closer inspection of the first Friedmann Eq. (1.9), it appears that the spatial curvature of the Universe is to vanish if and only if the matter density of the cosmic fluid takes the critical value

$$\rho_\mathrm{c} = \frac{3H^2}{8\pi G}, \tag{1.24}$$

where $H = \dot{a}/a$ is the *Hubble parameter*, quantifing the expansion rate of the Universe. When evaluated at present time, it takes the name of *Hubble constant* H_0, and it is often rescaled as $h = H_0/(100$ km s^{-1} Mpc$^{-1})$. In this way, the critical density today can be written as $\rho_{\mathrm{c},0} = 1.87 \times 10^{-29} h^2$ g cm^{-3}.

Since the critical density sets a preferred value for the matter-energy content of the Universe, it is natural to refer any other density to it. Therefore, it is possible to define the *density parameter* of the i-th component of the cosmic fluid as

$$\Omega_i \equiv \frac{\rho_i}{\rho_\mathrm{c}} = \frac{8\pi G \rho_i}{3H^2}. \tag{1.25}$$

With the use of the Hubble parameter and the density parameters, the first Friedmann equation takes a more convenient form, namely

$$H^2 = H_0^2 \left[\Omega_{\mathrm{r},0} a^{-4} + \Omega_{\mathrm{m},0} a^{-3} + \Omega_{\mathrm{x},0} \exp\left(-3\int_1^a (1+w_\mathrm{x})\frac{da}{a}\right) - \Omega_{k,0} a^{-2}\right], \tag{1.26}$$

where Ω_k is the density parameter of the spatial curvature, that can be as well formally included in the source terms for the gravitational field. It equals to

$$\Omega_{k,0} \equiv \frac{kc^2}{H_0^2}. \tag{1.27}$$

When evaluated at present, Eq. (1.26) implies that

$$\Omega_{k,0} = (\Omega_{\mathrm{r},0} + \Omega_{\mathrm{m},0} + \Omega_{\mathrm{x},0}) - 1 \equiv \Omega_0 - 1, \tag{1.28}$$

thus revealing a deep connection between the spatial geometry and the matter-energy content of the Universe. In particular, when the total density parameter today Ω_0 is larger than unity, the curvature of the space is positive, while it is negative if $\Omega_0 < 1$. If $\Omega_0 = 1$ then the Universe is flat, meaning $\Omega_k = 0$, and Eq. (1.26) assumes the form

$$H^2 = H_0^2 \left[\Omega_{\mathrm{r},0} a^{-4} + \Omega_{\mathrm{m},0} a^{-3} + (1 - \Omega_{\mathrm{r},0} - \Omega_{\mathrm{m},0}) \exp\left(-3\int_1^a (1+w)\frac{da}{a}\right)\right]. \tag{1.29}$$

Finally, we also introduce the *deceleration parameter*, given by

$$q = \frac{\ddot{a}a}{\dot{a}^2}, \tag{1.30}$$

whose meaning is clear. If the Universe is accelerating (as is the actual case) it takes negative values, while if it is decelerating it takes positive values.

With the cosmological parameters introduced so far, it is possible to write in a more convenient form the scale factor at the equality between matter and radiation, namely $a_\mathrm{eq} = (4.47 \times 10^{-7}\mathrm{K}^{-4}) T_{\mathrm{r},0}^4 \Omega_{\mathrm{m},0}^{-1} h^{-2}$.

1.6 Big Bang and Horizon

From the Friedmann Eq. (1.9) it follows that $\ddot{a} < 0$ as long as $\rho + 3p/c^2 > 0$, meaning $w > -1/3$ for the dominant component. As stressed, this is not the case in the present day Universe, and in general in any universe dominated by some form of DE. However it is interesting to note that, if this was indeed the case, then the fact that $\dot{a}(t_0) > 0$ would imply the existence of a time in the past when $a = 0$, and therefore where the density, pressure and temperature of the cosmic fluid were infinite. This singular instant in time is historically referred to as *Big Bang*, and it is taken to be the origin of the time axis, $a(t = 0) = 0$.

In a universe dominated by DE at present time, the existence of the Big Bang is not necessary, and in general combinations of the cosmological parameters can be found that avoid the existence of such a singularity.

Nevertheless, the very existence of the Cosmic Microwave Background (CMB henceforth, see Section 1.9) is a direct evidence of the fact that the Universe went through a very hot and very dense phase in the past, or equivalently, through a phase of very small physical volume. Therefore, it is commonly assumed that a singularity at which $a = 0$ existed in the past, although this is not necessarily implied by a given choice of cosmological parameters.

If a singularity in the Robertson-Walker metric existed in the past, then there must be a maximum distance that a light signal can have travelled since the singularity itself to the present day, or more generally to some instant $t > 0$. This distance defines the radius of a spherical surface that is called *cosmological horizon*. Written in formulas it reads

$$R(t) = ca(t) \int_0^t \frac{d\tau}{a(\tau)} = ca(t) \int_0^a \frac{da}{a^2 H(a)}. \tag{1.31}$$

Assuming that the Universe is flat and using Eq. (1.29) into Eq. (1.31) under the hypothesis that the Universe contains only matter, i.e. $\Omega_{\rm m} = 1$ (dubbed *Einstein-de Sitter* universe, Einstein & de Sitter 1932), gives

$$R(t) = \frac{2c}{H_0 \Omega_{\rm m,0}^{1/2}} a(t)^{3/2}. \tag{1.32}$$

When evaluated at present this becomes

$$R(t_0) = \frac{2c}{H_0 \Omega_{\rm m,0}^{1/2}} \equiv \frac{2R_{\rm H}}{\Omega_{\rm m,0}^{1/2}}, \tag{1.33}$$

where we have defined the *Hubble radius* $R_{\rm H}$ as the distance travelled by a light signal in the *Hubble time* $t_{\rm H} \equiv 1/H_0$. It is important to remark that, even though the Hubble radius is often used as an order of magnitude estimate for the cosmological horizon, it has not the same physical meaning. For more generic model universes, including a DE component and/or a curvature term, the relation between the cosmological horizon radius and the Hubble radius is modified with factors depending on the matter-energy content. For instance, for a universe without DE but with $\Omega_{\rm m} < 1$, the horizon radius at present time reads

$$R(t_0) = \frac{R_{\rm H}}{(1-\Omega_{\rm m,0})^{1/2}} \cosh^{-1}\left[1 - \frac{2(\Omega_{\rm m,0} - 1)}{\Omega_{\rm m,0}}\right]. \tag{1.34}$$

The concept of cosmological horizon will be important regarding the evolution of density perturbations in the DM component of the cosmic fluid, as will be presented in Chapter 2.

1.7 Early-Dark Energy and Cosmological Models

1.7.1 Primordial Quintessence

Among all the infinite DE models that can be identified by choosing different forms of the self-interaction potential for the quintessence field φ, a class of them is particularly interesting for the present discussion and will be thoroughly investigated in this thesis. It is the class of *Early-DE* models (Wetterich, 1988a,b, 1995), named after the requirement for the density parameter of DE at early times, meaning $a \ll 1$, to be still significant, of the order of few $\%$, as compared to totally negligible for other models. As is possible to observe, a simple way to obtain a significant DE contribution at early times is to require the DE density to be always a constant fraction of the density of the dominant fluid at that time. If the equation of state parameter of this dominant fluid is $w_{\rm d}$, and assuming that $w_{\rm d}$ is constant, as it is for matter or radiation for instance, then this is equivalent to require

$$\dot{\rho}_{\rm x} + 3(1 + w_{\rm b})\frac{\dot{a}}{a}\rho_{\rm x} = 0. \tag{1.35}$$

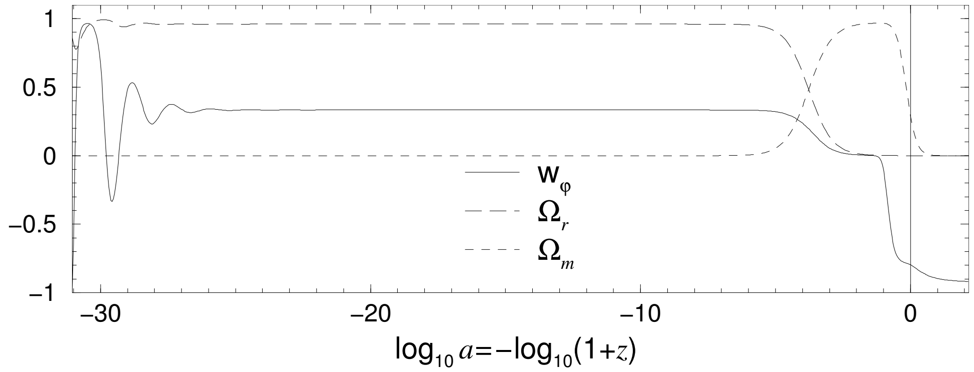

Figure 1.1: The equation of state parameter for DE (solid line), the density parameter for radiation (long dashed line) and that for matter (short dashed line) as a function of the scale factor. A DE model is considerd where the leaping kinetic term of the form Eq. (1.38) has parameters $k_0 = 1.1$ and $\varphi_0 = 276.6$ (Hebecker & Wetterich, 2001).

This can obviouly be satisfied only if the equation of state parameter for DE is itself constant and equal to w_d. In this way, by setting the initial condition $\rho_{\mathrm{x},0}$ to an appropriate value, it is possible to obtain the desired value for the DE density parameter at any early time.

It is also interesting to note in passing that a constant equation of state parameter for the DE fluid implies, if spatial curvature k vanishes and DE is the dominating fluid (as it must be in the present day Universe), an exponential potential for the quintessence field, namely

$$V(\varphi) = A \exp\left[-\frac{\sqrt{24\pi G(1+w_\mathrm{x})}}{c^2}\varphi\right]. \tag{1.36}$$

The tendency of the DE equation of state parameter to approach a constant value (not necessarily the equation of state parameter of the dominant component) for a wide range of initial conditions is named *tracking behaviour*, and an exponential potential is just a particular way to ensure it (Ratra & Peebles, 1988; Ferreira & Joyce, 1998; Baccigalupi et al., 2000, 2002). More general conditions for the presence of a tracking solution can be found depending on the exact shape of the potential $V(\varphi)$, see for instance Steinhardt et al. (1999).

As announced previously however, DE is required to dominate the expansion of the Universe at late time, $z \simeq 0$, to comply with the present observational status. This cannot obviously be obtained with a tracking solution for the quintessence scalar field, hence some *ad hoc* mechanism is needed in order to break down the tracking at low redshift. An often used solution to this problem (Hebecker & Wetterich, 2001; Doran et al., 2001; Doran & Robbers, 2006) is a modification of the kinetic term to the Lagrangian of the scalar field, that reads

$$\mathcal{L} = \frac{1}{2}k(\varphi)g^{\alpha\beta}\varphi_{,\alpha}\varphi_{,\beta} - V(\varphi). \tag{1.37}$$

A particularly simple case in which the DE can be brought to mimick a cosmological constant at low redshift is given by a *leaping kinetic term*, where $k(\varphi)$ changes abruptly from a small value $(k(\varphi) < 0.22$, consistent with primordial nucleosynthesis) to a relatively large one $(k(\varphi) > 1/\sqrt{3(1+w_\mathrm{b})})$. A way to obtain this is to use a function

$$k(\varphi) = k_0 + \tanh\left[\frac{\sqrt{8\pi G}}{c^2}(\varphi - \varphi_0)\right]. \tag{1.38}$$

The equation of state parameter that is obtained with the choice $k_0 = 1.1$ and $\varphi_0 = 276.6$ is shown in Figure 1.1. As can be seen, $w_\mathrm{x} = 1/3$ in the radiation dominated era, and $w_\mathrm{x} = 0$ in the matter dominated era, indicating a tracking behaviour. At low redshift however, w_x approaches the -1 limit of a cosmological constant.

1.7.2 Cosmological Models

Four different cosmological model will be mainly (but not only, see Chapetr 8) investigated in this thesis. Two of them are early-DE models, that will be labelled as EDE1 and EDE2 henceforth. They have slightly different Hubble constants and density parameters today. The equation of state parameter is close to -1 at low redshift and increases with increasing redshift, in order to approach the outlined matter tracking. The third model has a

Table 1.1: Cosmological parameters for four cosmological models described in Section 1.7.

	EDE1	EDE2	$w_{\rm x} = -0.8$	ΛCDM
h	0.67	0.62	0.65	0.65
$\Omega_{\rm m,0}$	0.33	0.36	0.30	0.30
$\Omega_{\rm x,0}$	0.67	0.64	0.70	0.70

constant DE equation of state parameter $w_{\rm x} = -0.8$, and the last one is a model where DE is a cosmological constant, labeled as ΛCDM model.

The detailed parameters relevant for cosmology are summarised in Table 1.1. Further parameters related to the structure formation process will be given in Chapter 2. It is just to be noted in passing that all these cosmological model are constructed to comply with presently available cosmological data sets, as will be more extensively discussed in Section 1.9. In particular, the radiation contribution is set to zero, and the sum of matter and DE density parameters equals 1, corresponding to a flat universe.

To have a better idea of the main difference between early-DE models and models with constant equation of state parameter, the redshift evolution of the DE density parameter is plotted in Figure 1.2 for the four cases. It is clear that while the DE density parameter decreases indefinitely at high redshift for models with constant equation of state, it tends to asymptote to a constant, small but not negligible, value in early-DE models.

For practical pourposes, it is useful to parametrize the DE fluid properties, that is to identify few parameters that globally describe the main properties of the quintessence field and that can be constrained observationally. An often used parametrization for instance makes use of the DE abundance today and the equation of state parameter and its derivative at present. This however contains no information about the early behaviour of the quintessence field. For this reason, in the case of early-DE, the most convenient parametrization choice is the one proposed by Wetterich (2004), that makes use of three quantities. The first two are the DE density parameter at present, $\Omega_{\rm x,0}$ and the equation of state parameter at present, $w_{\rm x,0}$. The last one is an average value for the DE density parameter at $a \ll 1$, where the linear stage of structure formation takes place. This is defined as

$$\bar{\Omega}_{\rm x,sf} \equiv -(\ln a_{\rm eq})^{-1} \int_{\ln a_{\rm eq}}^{0} \Omega_{\rm x}(a) d \ln a, \tag{1.39}$$

where $a_{\rm eq}$ is the scale factor at matter-radiation equivalence as computed previously. In the models EDE1 and EDE2 above this last parameter is chosen such that $\bar{\Omega}_{\rm x,sf} = 0.04$.

1.8 Cosmological Redshift and Distance Measures

The very fact that the Universe is expanding implies a stretch in the wavelength λ of electromagnetic radiation emitted at some time t in the past during its journey to the observer at t_0. Due to this effect, the frequency ν we observe today, is smaller than the emitted frequency, i.e. the radiation is redshifted and energy lost on the way to us. The amount of redshift is defined as

$$z \equiv \frac{\nu(t)}{\nu(t_0)} - 1 = \frac{\lambda(t_0)}{\lambda(t)} - 1, \tag{1.40}$$

and since it is easily understood that the radiation wavelength increases proportionally to the scale factor a, the consequence is that

$$z = \frac{1}{a} - 1. \tag{1.41}$$

The radiation redshift vanishes at present time and grows positive by decreasing the cosmic time or the scale factor.

The redshift of electromagnetic waves provides us also with a physical explanation for the behaviour of the radiation density during cosmic evolution, namely $\rho_{\rm r} = \rho_{\rm r,0} a^{-4}$. In fact, the energy of a photon at frequency ν is $E = h\nu \propto a^{-1}$, hence for the energy (or matter) density it must be $\rho_{\rm r} \propto E a^{-3} \propto a^{-4}$. In other words, a factor a^{-3} in the evolution of $\rho_{\rm r}$ is given by the diluition of photon inside the expanding space, while the additional factor a^{-1} comes from the cosmological redshift.

The expansion of the Universe and the fact that the spatial geometry might not necessarily be Euclidean make the concept of distance in cosmology a delicate issue. To face this, several different operational distance measures are usually defined. Here we describe only the two of them relevant to the present discussion. The first one is

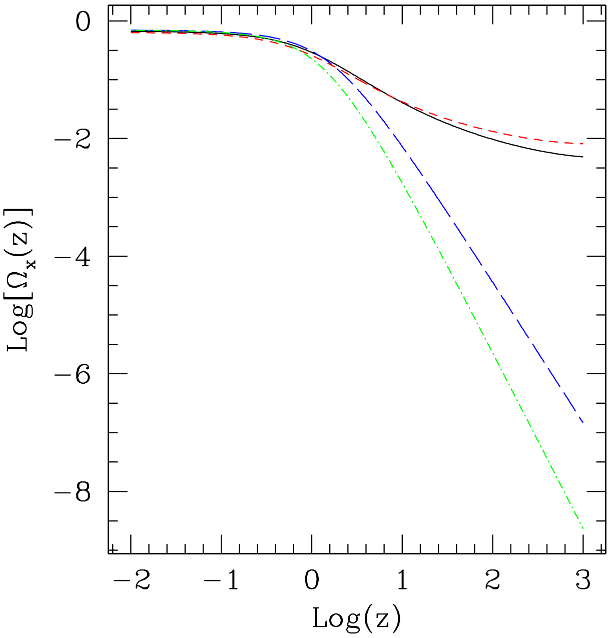

Figure 1.2: The density parameter for DE in the four cosmological models introduced in the text and detailed in Table 1.1. EDE1 (black solid line), EDE2 (red short-dashed line), a model with constant $w_\mathrm{x} = -0.8$ (blue long-dashed line) and a ΛCDM model (green dot-dashed line).

the *angular diameter distance* d_a, that is the ratio of the physical, intrinsic size to the angular, apparent size of a light source. The second one is the *luminosity distance* d_l, defined as the ratio of the intrinsic luminosity of a light source to $4\pi F$, where F is the observed flux. Clearly, both these definitions match the usual Euclidean distance definition in a static, flat space.

If r is the radial comoving coordinate used in Eq. (1.4), then it can be shown that, for a light source placed at scale factor a, $d_\mathrm{a} = ra$, and $d_\mathrm{l} = r/a$ (Coles & Lucchin, 2002). Using the cosmological redshift as time variable this means

$$d_\mathrm{l}(z) = (1+z)^2 d_\mathrm{a}(z). \tag{1.42}$$

The relation (1.42) is called *Etherington relation* (Etherington, 1933). It is easy to realize that close to the present time, when z approaches zero, $d_\mathrm{a} \simeq d_\mathrm{l} \simeq r$.

More generally, the angular diameter and luminosity distance of a source placed at a_2 as measured from an observer placed at a_1 (with $a_2 < a_1$) can be written as $d_\mathrm{a}(a_1, a_2) = r_{1,2}a_2$, and $d_\mathrm{l}(a_1, a_2) = r_{1,2}/a_2$, where $r_{1,2} \equiv f_k(\chi_2 - \chi_1)$. In the rest of this work however we will refer to observers placed at $a_1 = 1$, unless explicitely stated.

Next, consider a first order Taylor expansion of the scale factor close to t_0,

$$a(t) \simeq 1 + H_0(t - t_0), \tag{1.43}$$

from which follows, again to first order, that

$$t_0 - t \simeq \frac{z}{H_0}. \tag{1.44}$$

Now, in GR light rays propagate along null geodesics of the spacetime metric g. Recalling Eq. (1.2) and Eq. (1.4) this means that, for the trajectory of a photon,

$$c\int_{t_0}^{t} \frac{dt}{a(t)} = \int_0^r \frac{dr}{\sqrt{1-kr^2}} \simeq r, \tag{1.45}$$

with the last approximation coming from a first order expansion around $r = 0$. Making use of the approximate relations between scale factor, redshift and cosmic time derived above we obtain

$$r \simeq \frac{cz}{H_0}. \tag{1.46}$$

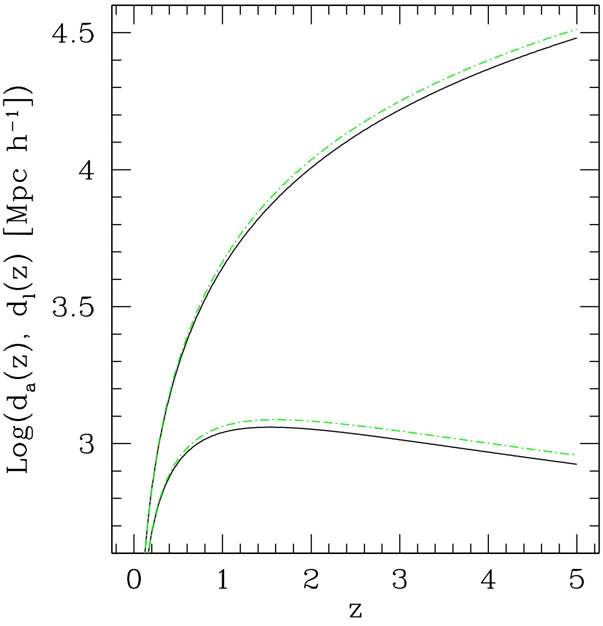

Figure 1.3: The angular diameter distance (lower pair of curves) and luminosity distance (upper pair) as a function of redshift for two of the cosmological models introduced. These are the EDE1 (black solid line) and the ΛCDM model (green dot-dashed line).

This means that locally, i.e. in a sufficiently small neighborhood of the observer, the expansion of the Universe implies a linear relation between the redshift and the radial comoving coordinate. This also means that, locally,

$$d_{\mathrm{a}}(z) \simeq d_{\mathrm{l}}(z) \simeq \frac{cz}{H_0}. \tag{1.47}$$

It is not important which distance measure is used, as long as the object we are referring to is close enough to the observer. The linear relation between distance and redshift implied by Eq. (1.47) is referred to as *Hubble law* (Hubble, 1929).

In Figure 1.3 the angular diameter and luminosity distances are shown for two of the four cosmological models introduced in the previous section. It is obvious that all the distances share the same behaviour in a neighborhood of $z = 0$, irrespective of the cosmology. Also, while the luminosity distance increases steadily with redshift, the angular diameter distance has a maximum at $z \simeq 1.5$, and then decreases very slowly. This means that any object with the same physical size will have roughly the same angular size if placed at any redshift $\gtrsim 1$.

1.9 Current Observational Status

Up to date, there are numerous sources of cosmological information that are accessible to astronomical observations and can be used to test the value of the various model parameters introduced in Section 1.5. The cosmological tests can be divided into two broad categories: the *geometrical tests*, and the tests based on the structure formation process (see Chapter 2). The main idea behind any kind of geometrical cosmological probe is basically one: to find a physical length scale, or a reference luminosity, that can be known somehow, and compare it with the observed related angular scale or flux, in order to find the behaviour of the corresponding (angular diameter or luminosity) distance with redshift.

The main geometrical source of cosmological information certainly is the CMB, i.e. the light emitted when the Universe became transparent, after the recombination of hydrogen and helium, at $z \simeq 10^3$. Before the recombination, ordinary matter and radiation were tightly coupled due to Thomson scattering off free electrons. The tendency of matter to fall inside the potential well of the already forming DM density fluctuations and the opposite tendency of radiation to free stream cause the matter radiation fluid to oscillate in and out of such potential wells, imprinting a characteristic pattern in the CMB angular power spectrum that serves as a standard ruler.

The most recent analysis of the CMB temperature fluctuations is built upon the 3-years data release of the WMAP satellite (Spergel et al. 2007; Page et al. 2007; Hinshaw et al. 2007; Jarosik et al. 2007, WMAP-3

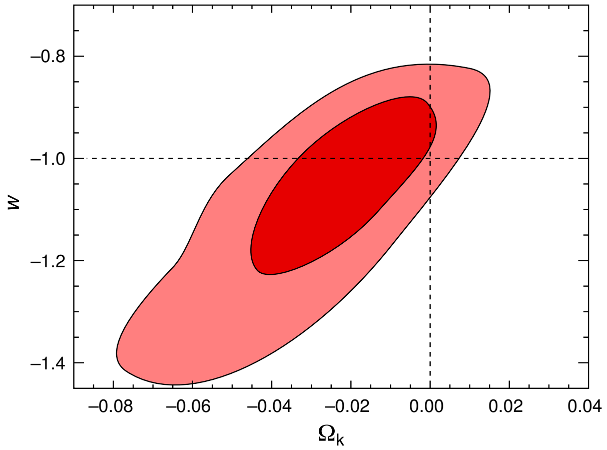

Figure 1.4: Constraints on the constant equation of state parameter for DE and the curvature density parameter form the 3-years WMAP data release jointly with 2dFGRS, SDSS and both main supernovae data sets (see text for details). Shown are 68% and 95% confidence levels (Spergel et al., 2007).

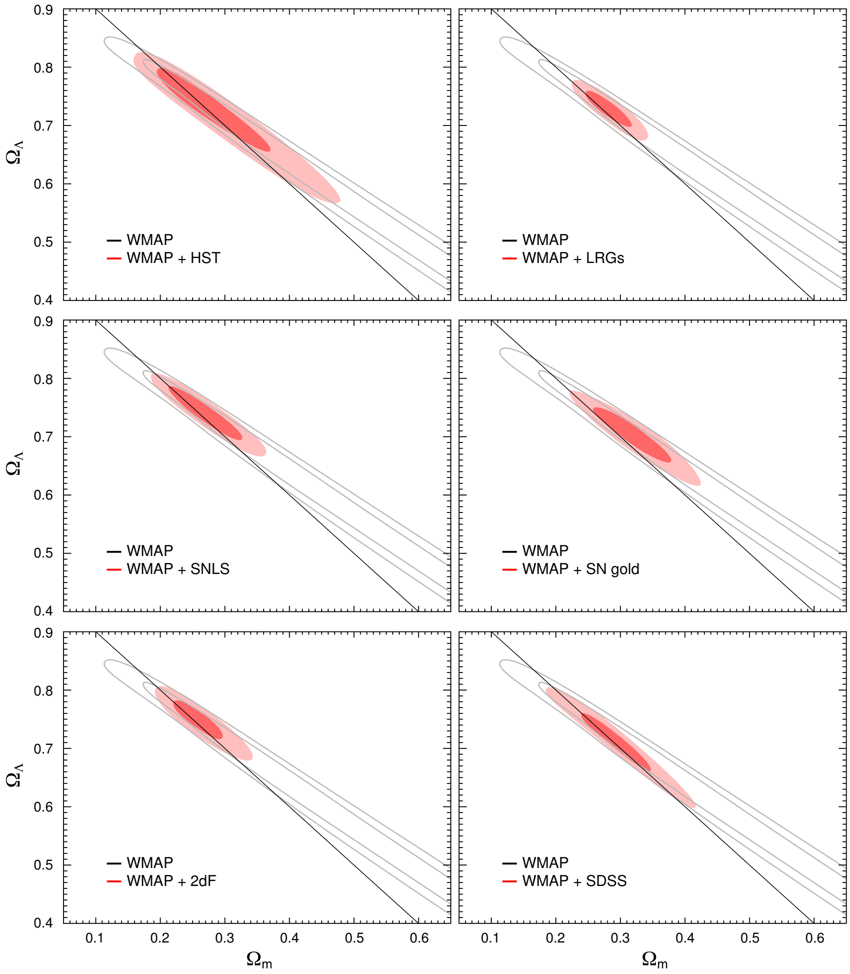

Figure 1.5: Constraints for the matter and cosmological constant density parameters from WMAP-3 data.The 68% and 95% confidence levels are shown as gray solid lines for the WMAP only constraints, and red-shaded areas for the WMAP data jointly with other cosmological probes, as labeled in the panels. The black solid line identify flat space sections (Spergel et al., 2007).

henceforth). Previously, data from the COBE satellite confirmed that the background radiation has an almost perfect blackbody energy spectrum corresponding to a temperature $T_{\mathrm{r},0} \simeq 2.728$ K. This allows one to com-

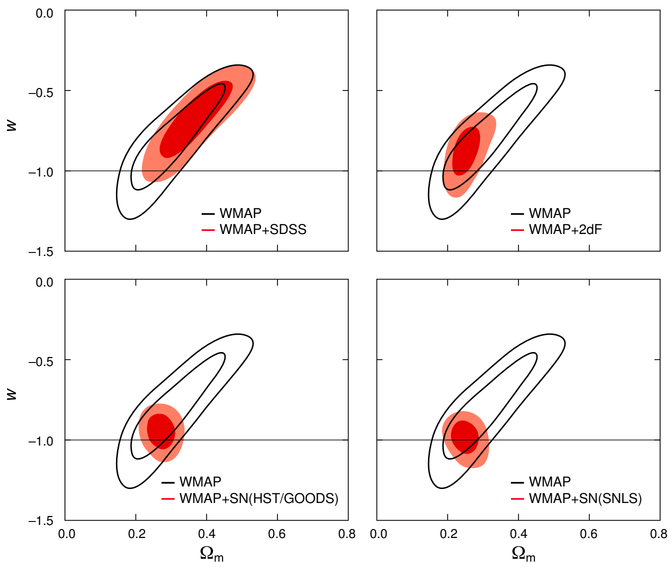

Figure 1.6: Constraints on the equation of state parameter for DE and the matter density parameter from the WMAP-3 data. 68% and 95% confidence leveles are shown as black solid lines for the WMAP only constraints, and red-shaded areas for the WMAP data jointly with other probes, as labeled in the four panels. Space flatness and a constant DE equation of state parameter are assumed (Spergel et al., 2007).

pute the radiation density today, according to Eq. (1.14), and to compare it to the matter density, obtaining $\rho_{\mathrm{r},0}/\rho_{\mathrm{m},0} \simeq 2.47 \times 10^{-5}\Omega_{\mathrm{m},0}^{-1}h^{-2}$. This both tells that the radiation contribution is negligible when compared to matter contribution today, and gives an estimate for the redshift at matter-radiation equality, namely $z_{\mathrm{eq}} \simeq 4.04 \times 10^{4}\Omega_{\mathrm{m},0}h^{2}$. Therefore, it turns out that for all the redshifts of interest in this work, the radiation contribution can be safely neglected, as done for the cosmological models introduced in Section 1.7.

The latest WMAP data release allowed for a significant shrink of the allowed region in the cosmological parameter space. However, degeneracies between different cosmological parameters exist, in the sense that different sets of parameters can give rise to the same (or approximately the same) angular power spectrum for the CMB. This forces one to combine CMB data with different kind of astronomical observations that produce complementary or orthogonal information in order to have tighter constraints. Here we mention the main three of them, keeping in mind that also with the introduction of this additional information, priors on the parameters are usually enforced.

The first one is the measurement of the Hubble constant using secondary distance indicators based on primary ones, mainly cepheids. This was performed in the Hubble Space Telescope (HST) key project (Freedman et al., 2001), finding a best-fit value for the Hubble constant $h \simeq 0.72$. The second one is the measurement of the luminosity distance-redshift relation of supernovae of type Ia. It is known that the peak luminosity of this kind of events is in tight correlation with the width of the light curve, so that all supernovae Ia can be calibrated to have the same peak luminosity, working as a standard candle. The two main data sets available up to date are the Supernova Legacy Survey (SNLS, Astier et al. 2006) and the Supernova Gold Sample (Riess et al., 2004). Both the key project and supernovae experiments are obviously geometrical probes.

The third test is instead based on structure formation, and in particular on the large scale distribution of matter in the Universe. This cannot be observed directly because the vast majority of it is dark. Nevertheless, the gravitational deflection of light can be used to infer the DM distribution (Section 3.6, Semboloni et al. 2006; Hoekstra et al. 2006) and the galaxies can be used as a tracer of the underlying distribution itself. The standard ruler in this case is represented by features in the power spectrum of matter distribution (see Section 2.2.3 for details) and the leading projects are the Sloan Digital Sky Survey (SDSS, Tegmark et al. 2004) and the 2-degree Field Galaxy Redshift Survey (2dFGRS, Cole et al. 2005). A subsample of the galaxies observed in the former, the Luminous Red Galaxies (LRG), have been used for an additional geometrical test, namely the measurement of the Baryon Acoustic Oscillations (BAO) in the two point correlation function (Eisenstein et al., 2005). This is nothing but a signature of the acoustic oscillations in the CMB angular power spectrum that survives in the baryon distribution.

Strikingly enough, the combination of all these various cosmological observations converge to what in the last decade has been called the *standard cosmological model*. In this model, the expansion of the Universe is dominated today by DE in the form of a cosmological constant. In fact, actual data are insufficient to detect a significant redshift evolution of w_{x}, and the case for $w_{\mathrm{x}} = -1$ at present is rather strong. In Figure 1.4 the constraints on a constant w_{x} and the curvature of space k are depicted. Here and in the remainder of this section it is always

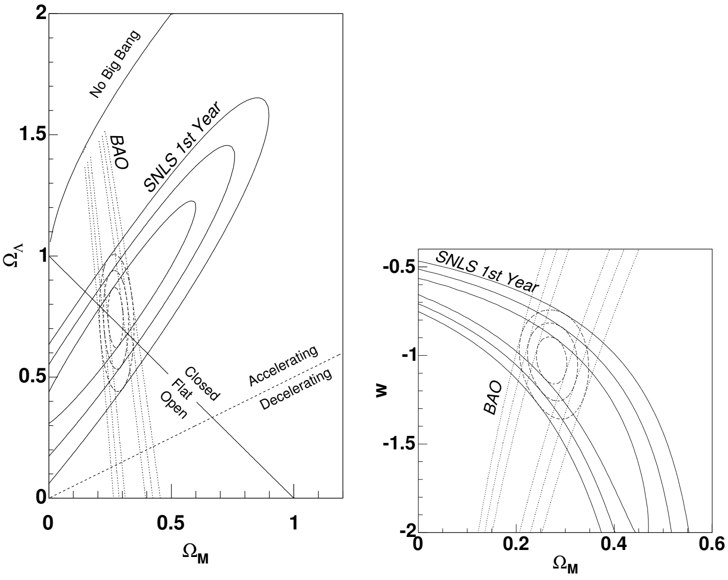

Figure 1.7: *Left panel.* Constraints on the matter and cosmological constant density parameters from the 1-year SNLS data release. 68.3%, 95.5% and 99.7% confidence levels are shown with solid contours for the SNLS data, dotted contours for the BAO data and dashed contours for the joint constraints. *Right panel.* Constraints on the DE equation of state parameter today and the matter density parameter. Linestyle is the same as for the left panel (Astier et al., 2006).

assumed that the DE fluid is perfectly uniform, without any possibility for clustering not even on the largest scales. Besides the support to the cosmological constant scenario, also apparent is the fact that Ω_k is consistent with 0, supporting the case for an Euclidean universe. If this is the case then it must be $\Omega_0 = \Omega_{\mathrm{m},0} + \Omega_{\Lambda,0} = 1$, since the radiation contribution today has to be negligible. In fact, Figures 1.5 and 1.6 bring further support this view, with a matter density parameter $\Omega_{\mathrm{m},0} \simeq 0.3$ and a cosmological constant density parameter $\Omega_{\Lambda,0} \simeq 0.7$. In the bottom left panel of Figure 1.6, the supernovae data from the GOODS survey (Vanzella et al., 2005, 2006) are used.

It is interesting to note the fact that, while $\rho_\Lambda = \rho_{\Lambda,0}$, the matter energy density evolves quite steeply with redshift, $\rho_{\mathrm{m}} = \rho_{\mathrm{m},0}(1+z)^3$, implying that the equivalence between matter and DE is reached at rather small redshift, $z \simeq 0.5$. For higher redshift the expansion of the Universe is matter dominated, until the matter-radiation equality. As a matter of fact, the detection of the transition redshift between DE and matter domination is one of the key challenges for future observational cosmology.

In Figure 1.7, the standard picture gains further strength without the inclusion of CMB measurements, but only supernova data and BAO measurements. Both the matter-energy content of the Universe and the nature of DE are in agreement with the standard model as detailed above.

As a conclusive remark, it must be stressed that the value of the individual parameters for the cosmologies detailed in Table 1.1 is not exactly equal to the best fit values collected in the Figures above. Nevertheless the combination of the various parameters is such that each model is in agreement with CMB observations, large scale structure data and type Ia supernova luminosity distance.

Chapter 2

Structures in the Universe

2.1 Introduction

The standard cosmological model outlined in Chapter 1 faces some obvious problems that require an extension of the picture. The most promising extension up to date is the *inflationary scenario,* that predicts an early evolution of the Universe dominated by a scalar field analogous to quintessence, driving an exponential expansion. The first model of inflation was formulated by Guth (1981), although many ideas were already presented in Starobinsky (1979). Following these preliminar works, many other inflationary models were developed in the subsequent years (Linde, 1982a,b; Albrecht & Steinhardt, 1982; Linde, 1983).

One of the major advantages of this scenario is that it not only solves the classical problems of the standard cosmological model, but also provides a mechanism for the formation of tiny density fluctuations in the cosmic fluid of the primordial Universe. According to such mechanism, shortly after the Big Bang quantum fluctuations in the matter and gravitational fields are amplified due to the exponential inflationary expansion.

After the end of inflation, density fluctuations in DM are predicted to grow due to self-gravity, and eventually to detach from the overall expansion of the Universe and collapse to form bound structures, dubbed DM *halos*. As explained in Section 1.9, baryonic matter is strongly coupled to radiation before recombination of hydrogen and helium, that avoid it from following the gravitational pull of DM overdensities. Only after recombination is the gas free to fall into the potential wells of DM structures, forming galaxies and galaxy clusters that are observed today.

In this Chapter we proceed into developing the post-inflationary picture in more detail, describing the formation and evolution of the more massive structures in the Universe and their properties relevant for the present work. In the following discussion we shall assume that the DM component is a collisionless fluid, due to its particles' very low interaction cross section.

2.2 Linear Evolution

2.2.1 Jeans Scale

An important issue related to the evolution of density fluctuations in a matter fluid is the interplay of the opposite effects given by gravity, that tends to pull particles together, and random motion of particles themselves, that tends instead to dissipate any kind of perturbation. When the first effect is more important than the second, then an overdensity is allowed to grow and eventually collapse into a bound object.

The order of magnitude of the scale length separating the two regimes, called the *Jeans length*, can be derived by comparing the kinetic energy to the potential energy of a density perturbation. For the former we have $K \simeq Mv^2$, and for the latter

$$U \simeq -\frac{GM^2}{R}, \tag{2.1}$$

where M and R are the mass and spatial extent of the perturbation while v is a measure of the typical velocity of particles in the fluid. It corresponds to the speed of sound in a collisional gas, and to the *rms* of the velocity distribution in a collisonless fluid like DM. By setting $K + U \simeq 0$ and using the approximate relation $M \simeq \rho R^3$, we obtain an approximate expression for the Jeans length, namely

$$R_{\rm J} \simeq \frac{v}{\sqrt{G\rho}}. \tag{2.2}$$

The precise definition, complete with all the constant factors, will be given shortly. However, Eq. (2.2) is rather useful as an order of magnitude estimate, telling that only perturbations on scales significantly larger than R_J are allowed to grow and collapse without being dissipated by random motion of particles.

It is also important to note that the mean velocity v and the density ρ appearing in Eq. (2.2) may not refer to the same component of the cosmic fluid. In particular, v is the typical velocity of the component that is perturbed, since the perturbation itself produces pressure support against collapse. On the other hand, ρ has to be the density responsible for the gravitational pull, hence the density of the dominant component of the cosmic fluid.

In the case of cold DM, the typical velocity of particles is negligibly small after decoupling fom radiation, thus leading to an arbitrarily small Jeans length. This means that perturbations in cold DM can grow on any cosmologically relevant scale, and the dissipating effect due to random motions can be safely neglected.

2.2.2 Perturbation Theory

As long as relative perturbations in matter and gravitational fields are small compared to unity, their time evolution can be followed analitically by means of standard perturbation theory. The main idea behind this approach is to consider a background universe with a Robertson-Walker metric and a uniform density, and then slightly perturb the relevant fields to the linear order. The complete, generally relativistic treatment of this kind of problem is outlined in excellent textbooks, like Weinberg (1972), Padmanabhan (1993) and Straumann (2004). However, for perturbations on scales much smaller than the cosmological horizon (see Eq. (1.31)), like those involved in the present thesis, it is sufficient to restrict attention to the semi-Newtonian treatment that is henceforth described.

In the Newtonian approximation, the relevant fields for the evolution of a self-gravitating fluid are the density ρ, the velocity field $\boldsymbol{u}$, the potential Φ and the pressure p, that is usually linked to the density by means of an unspecified equation of state. The two main equations involving these fields, written in physical coordinates, are the continuity equation, ensuring the mass conservation,

$$\frac{\partial \rho}{\partial t} + \frac{\partial \rho u_i}{\partial r_i} = 0, \tag{2.3}$$

and Euler's equation, ensuring the conservation of the three components of the momentum,

$$\frac{\partial u_i}{\partial t} + u_j \frac{\partial u_i}{\partial r_j} = -\frac{\partial \Phi}{\partial r_i} - \frac{1}{\rho}\frac{\partial p}{\partial r_i}. \tag{2.4}$$

It should be noted that the pressure p appearing on the right hand side of Euler's equation is meaningful only for collisional fluids, like gas. Due to the small interaction cross section on the other hand, DM behaves as a collisionless fluid, and the same is true for stars in galaxies and galaxies in galaxy clusters (see Section 2.4 for details). Hence their mean-field evolution is described by the collisionless Boltzmann's equation (Binney & Tremaine, 1987; Ciotti, 2000). However, the first two velocity moments of this equation are identical to Eqs. (2.3) and (2.4), except for the term involving the pressure, which is replaced by

$$-\frac{1}{\rho}\frac{\partial (\rho \sigma_{ij}^2)}{\partial r_j}. \tag{2.5}$$

The quantities σ_{ij}^2 are the components of the velocity dispersion tensor, and the expression in Eq. (2.5) reduces to the last term on the right hand side of Eq. (2.4) with the replacement $\rho\sigma_{ij}^2 = p\delta_{ij}$.

In addition to the Euler and continuity equations, the Poisson equation relates the gravitational potential to the density distribution,

$$\Delta\Phi = 4\pi G\rho. \tag{2.6}$$

The perturbation analysis consists in making the *ansatz* according to which the generic field q equals the sum of a background field and a perturbation, namely $q = q_\mathrm{b} + \delta q$, such that $\delta q \ll q_\mathrm{b}$. The background quantities are assumed to be referred to an unperturbed Robertson-Walker universe, hence $\boldsymbol{u}_\mathrm{b} \equiv \dot{\boldsymbol{r}} = H\boldsymbol{r}$. This ansatz can then be inserted into the continuity, Euler and Poisson equations, removing the unperturbed solutions and limiting the analysis to the lowest non-trivial order. This returns equations for the perturbations that are then solved using the Fourier transformation method. Fourier transformation is denoted by a hat, and we furthermore introduce the definitions $\delta \equiv \delta\rho/\rho_\mathrm{b}$ and $c_\mathrm{s}^2 \equiv \delta p/\delta\rho$ for the *density contrast* and *sound speed* of a collisonal fluid. Like the pressure, the sound speed must be replaced with a quantity related to the velocity dispersion when dealing with collisionless fluids.

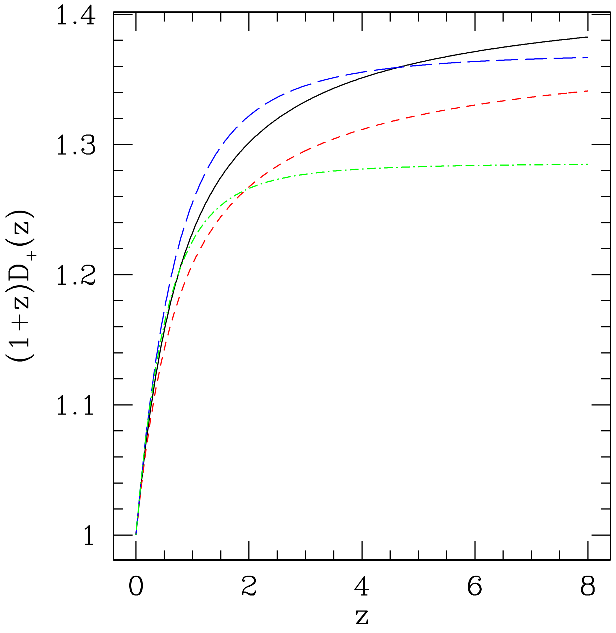

Figure 2.1: The growth factor times $(1+z)$ as a function of redshift for the four cosmological models detailed in Table 1.1. These are EDE1 (black solid line), EDE2 (red short-dashed curve), a model with constant DE equation of state parameter $w_{\rm x} = -0.8$ (blue long-dashed curve) and the ΛCDM model (green dot-dashed curve).

Combining now the three equations, a single second order ordinary differential equation for the time evolution of $\hat{\delta}$ is obtained,

$$\frac{\partial^2 \hat{\delta}}{\partial t^2} + 2H\frac{\partial \hat{\delta}}{\partial t} + \left(k^2 c_{\rm s}^2 - 4\pi G \rho_{\rm b}\right)\hat{\delta} = 0. \tag{2.7}$$

This same equation is also obtained in the non-relativistic limit of the more general treatment. It is basically an oscillator equation, where the damping term is due to the expansion of the Universe as would be naively expected. It is also evident that the last two terms on the left hand side describe the interplay between the pull of gravity and the free streaming due to random motion of particles. Hence, they provide a more accurate definition of the Jeans length according to

$$k^2 c_{\rm s}^2 - 4\pi G\rho_{\rm b} \equiv 4\pi G\rho_{\rm b}\left(k^2 R_{\rm J}^2 - 1\right) \equiv 4\pi G\rho_{\rm b}\left(\frac{k^2}{k_{\rm J}^2} - 1\right), \tag{2.8}$$

where the physical *Jeans wavenumber* $k_{\rm J}$ has been introduced as well. As announced, in the case of DM density fluctuations the Jeans length is always negligible, or the Jeans wavenumber is arbitrarily large. Therefore, the third term on the left hand side of Eq. (2.7) can be safely neglected.

The general solution of Eq. (2.7) is the linear combination of two particular solutions, that can be found analytically only for particularly simple cosmological models, while in general one has to resort to numerical integration. For instance, assuming the Universe to be DM dominated (but not necessarily flat), we find a solution of the type $\hat{\delta}_-(t) = A_- H(t)$, and one of the type

$$\hat{\delta}_+(t) = A_+ H(t)\int_0^t \frac{d\tau}{a^2(\tau)H^2(\tau)}, \tag{2.9}$$

where A_- and A_+ are normalization constants. The minus and plus subscripts indicate that the first solution is decreasing with time, while the second one is increasing. This has the consequence that after a suitably long period of time, the general solution of Eq. (2.7) can be identified solely with its growing part. If, additionally, it is required for the Universe to be spatially flat and without DE, then the growing solution reduces to

$$\hat{\delta}_+(t) = \frac{18^{1/3}}{5}\frac{A_+}{H_0^{4/3}}t^{2/3} = \frac{2}{5}\frac{A_+}{H_0^2}\frac{1}{(1+z)}. \tag{2.10}$$

Also, it is convenient to normalize the Fourier transform of the density fluctuation to the present time, defining the *growth factor* as $D_+ \equiv \hat{\delta}_+/\hat{\delta}_{+,0}$, so that for a simple Einstein-deSitter universe we get $D_+(z) = (1+z)^{-1}$. The growth factor for the four cosmological models detailed in Table 1.1 is presented in Figure 2.1. Models with early-DE have a larger value for the growth factor than models with constant DE equation of state parameter do. This means that the amplitude of linear density fluctuations is always larger in the former for a fixed redshift.

2.2.3 Statistics of Gaussian Random Fields

In the attempt to explain the observed statistical properties of the large scale matter distribution, the density fluctuation field $\delta(\boldsymbol{x})$ that emerges from the inflationary epoch is assumed to be a random field, of which the observed Universe is just one particular realization. This means that the value of the density fluctuation δ at any particular comoving position $\boldsymbol{x}$ is a stochastic variable following some characteristic probability distribution.

In principle, the statistical properties of any random field should be determined using averages over many different realizations of the field itself. This is obviously not possible for the observable Universe, therefore an implicit assumption, named *ergodic hypothesis*, is often used. According to this assumption, regions of the Universe far away enough between each other can be considered as statistically independent, and hence, *de facto*, as independent realizations of the density fluctuation field. The ergodic hypothesis has been rigorously proven for a particular class of random fields by Adler (1981). An immediate consequence of it is that averaging over different realizations of the same random field is equivalent to spatial averaging over a sufficiently large region of the Universe. It must also be noted in passing that when dealing with very large scales, there are just very few far enough regions of the Universe, therefore the averaging process looses its statistical significance. This fact is named *cosmic variance*.

One of the most robust predictions of inflation is that the probability distribution of density fluctuations emerging from the phase of exponential expansion should be close to Gaussian, since for quantum-mechanical reasons each Fourier mode of the field should be independent of the others. This has been verified to some extent by CMB experiments, even though properties of non-Gaussian cosmological models have been explored (Moscardini et al., 1991; Grossi et al., 2007). Since the average value of the density fluctuation field vanishes by definition, the only relevant quantity charcterising the field itself is the *rms* σ. This is often replaced by the *variance* $S \equiv \sigma^2$, defined such that

$$S \equiv \frac{1}{V}\int_{\mathbb{R}^3} \delta^2(\boldsymbol{x}) d^3\boldsymbol{x} = \frac{1}{V}\int_{\mathbb{R}^3} \left|\hat{\delta}(\boldsymbol{k})\right|^2 \frac{d^3\boldsymbol{k}}{(2\pi)^3} = \frac{1}{V}\int_0^{+\infty} \left|\hat{\delta}(k)\right|^2 k^2 \frac{dk}{2\pi^2}, \tag{2.11}$$

where the last step follows from the fact that no preferred directions can be singled out in space, according to the cosmological principle. Moreover, V is the volume of a region of space where the integrals are computed, and is required to be large enough to comply with the ergodic assumption, but at the same time small enough to safely neglect possible space curvature. The *power spectrum* of the density fluctuations field is defined as

$$P(k) \equiv \frac{\left|\hat{\delta}(k)\right|^2}{V}, \tag{2.12}$$

hence giving

$$S = \int_0^{+\infty} P(k) k^2 \frac{dk}{2\pi^2}. \tag{2.13}$$

Inflation is predicted to produce a scale free power spectrum, namely $P(k) = Ak^n$, with some normalization constant A and spectral index n. A particular case of this is the scale invariant *Harrison-Zel'dovich* spectrum (Harrison, 1970), for which $n = 1$.

For future convenience it is insightful to smooth the density fluctuations field on a comoving scale L, thus defining the related *smoothed* or *filtered field* as

$$\delta_\mathrm{f}(\boldsymbol{x}, L) = \int_{\mathbb{R}^3} \delta(\boldsymbol{y}) W(\boldsymbol{y} - \boldsymbol{x}, L) d^3\boldsymbol{y}. \tag{2.14}$$

This is just the convolution of the original field with a suitably chosen function W whose characteristic width is L, like a top-hat function or a Gaussian. It turns out that the variance of the new smoothed field reads

$$S(L) = \int_0^{+\infty} P(k) \hat{W}^2(k, L) k^2 \frac{dk}{2\pi^2}. \tag{2.15}$$

Table 2.1: Parameters for the cosmolology and the cold DM power spectrum for the four cosmological models detailed in Section 1.7.

	EDE1	EDE2	$w_{\rm x} = -0.8$	ΛCDM
h	0.67	0.62	0.65	0.65
$\Omega_{\rm m,0}$	0.33	0.36	0.30	0.30
$\Omega_{\rm x,0}$	0.67	0.64	0.70	0.70
σ_8	0.82	0.78	0.80	0.84
n	1.05	0.99	1	1

It is easily seen that when the smoothing radius approaches 0, the kernel W approaches a Dirac delta distribution, so that the variance of the smoothed field approaches that of the original field. Vice versa, when the smoothing radius diverges the variance tends to vanish, and in general the variance is a decreasing function of the smoothing scale. Since the mass "contained" within the function W scales as $M \propto L^3$, it follows that the variance is also a decreasing function of mass.

For future reference, we adopt here a sharp top-hat filter in Fourier space, meaning that the function $\hat{W}(k, L)$ equals unity if $k < 2\pi/L$ and vanishes otherwise. It follows that, with a scale free power spectrum for the original density fluctuation field, the variance of the smoothed field equals

$$S(L) = \frac{2A}{(n+3)} \frac{(2\pi)^{n+1}}{L^{n+3}}. \tag{2.16}$$

This means that, if the slope of the power spectrum is fixed, the normalization can be expressed in terms of the *rms* computed for a specific scale L_* as

$$A = \sigma^2(L_*) \frac{L_*^{n+3}}{(2\pi)^{n+1}} \frac{n+3}{2}. \tag{2.17}$$

Due to historical reasons, the choice $L_* = 8$ Mpc h^{-1} is made, thus expressing the normalization in terms of $\sigma_8 \equiv \sigma(L_*)$. In order to comply with existing observations, the four cosmological models introduced in Chapter 1 have different spectral index and normalization of the power spectrum. The full details for the models at hand are given in Table 2.1, where the value of the other cosmological parameters is rewritten for completeness.

2.2.4 Evolution of the Power Spectrum

The discussion so far involves the power spectrum of the primordial density fluctuation field, that emerges from the inflationary era. However, several physical processes affect both the amplitude and the slope of the power spetrcum itself in the subsequent cosmological evolution. Regarding the amplitude, by definition it evolves as the square of the growth factor (see Section 2.2.2), therefore the variance scales as $\sigma^2(L,t) \propto D_+^2(t)L^{-(n+3)}$. Recalling that $M \propto R^3$ we also have that $\sigma^2(M,t) \propto D_+^2(t)M^{-(n+3)/3}$. As suggested by the spherical collapse model, (see Section 2.3.2 for further details) when the amplitude of a density fluctuation approaches unity it enters the nonlinear regime and eventually collapses to form a bound structure. Accordingly, the typical non-linear mass scale at a given cosmic time can be estimated as $M_*(t) \propto D_+(t)^{6/(3+n)}$. This is the typical mass of objects collapsing at cosmic time t, and the fact that it grows with time for $n > -3$ reflects the fact that small DM halos tend to form first than large ones (*hierarchical paradigm*). The evolution of the characteristic mass with redshift, decorated with the appropriate normalization, is shown in Figure 2.2.

As can be seen, the typical non-linear mass is up to one order of magnitude larger in early-DE models than in models with a constant DE equation of state parameter for suitably high redshift. Another way to put it is that, given a value of the typical mass, the redshift at which this is reached is significantly higher in early-DE models, and hence structure formation is shifted to higher redshifts.

The slope of the power spectrum is mainly modified by the *Meszaros effect* (Meszaros, 1974). Before the matter-radiation equality the expansion of the Universe is driven by radiation. As a consequence, the expansion time-scale (that is the Hubble time) is larger than the free fall time-scale for DM density perturbations, and thus DM overdensities cannot grow on scales smaller than the cosmological horizon. This brings a change in the slope of the power spectrum on scales smaller than the horizon radius Eq. (1.31) at matter-radiation equality. The action of this physical process is conventionally encapsulated in the *transfer function* $T(k)$, defined such that the power spectrum at present is obtained from the primordial power spectrum at an early time $t_{\rm e}$ as

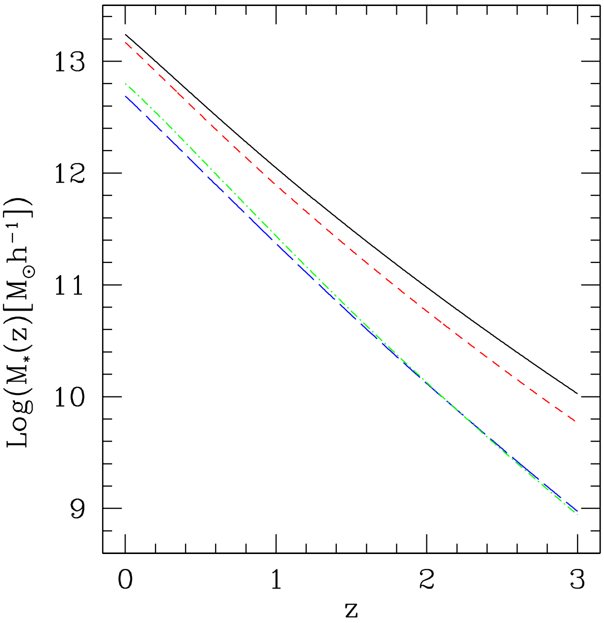

Figure 2.2: The typical mass collapsing at redshift z as a function of redshift itself. The black solid line is for EDE1 model, the red short-dashed line for EDE2 model, the blue, long-dashed line is for the model with constant DE equation of state parameter $w_\mathrm{x} = -0.8$ and finally the green dot-dashed line is for the ΛCDM model.

$$P(k, t_0) = P(k)\frac{T^2(k)}{D_+^2(t_\mathrm{e})}. \tag{2.18}$$

The commonly used transfer function is a fit to numerical simulations (Section 2.3.5) first given in Bardeen et al. (1986), that reads

$$T(k) = \frac{\ln(1+2.34q)}{2.34q}\left[1 + 3.89q + (16.1q)^2 + (5.46q)^3 + (6.71q)^4\right]^{-1/4}, \tag{2.19}$$

(see also Eisenstein & Hu 1998) where $q \equiv k\theta^{1/2}/(\Omega_{\mathrm{m},0}h^2\ \mathrm{Mpc})$, and θ is a measure of the ratio between the energy density in relativistic particles (photons plus neutrinos) to that in photons only. Note that when the scale is very small, $k \gg \Omega_{\mathrm{m},0}h^2\theta^{-1/2}$, the transfer function behaves as $T(k) \propto k^{-2}$, and therefore $P(k, t_0) \propto k^{-4}P(k)$.

Finally, the power spectrum of linear density fluctuations is further modified when nonlinear effects due to collapse of structures are inserted in, which cause perturbations of different size to interact. Such effects can be followed only by means of fully numerical simulations (Peacock & Dodds, 1996; Smith et al., 2003). In Figure 2.3 the linear and nonlinear power spectra for several models are shown. The different normalizations between the EDE1 and the ΛCDM models are evident, reflected in the different value of σ_8, see Table 2.1. Also, the change in slope induced by the Meszaros effect and encapsulated into the transfer function is visible, as the peak at $k \sim 10^{-2}h$ Mpc^{-1}. As expected, non-linear effects become important on small scales, $k > 0.1h$ Mpc^{-1}.

2.3 Nonlinear Evolution

2.3.1 Zel'dovich Approximation

When the amplitude of the density fluctuation field approaches unity, the picture outlined in the previous section no longer holds, and in particular the linear evolution Eq. (2.7) cannot be used any more. The description of the non-linear evolution of density perturbations is a complicated subject, and in general it must be treated numerically. There are however several analytic approximations that, even though they are unable to describe the most realistic astrophysical situations, can give valuable insight into the physics of the problem.

One of these tools is due to Zel'dovich (1970), and is therefore called *Zel'dovich approximation*. Recalling the relation between physical and comoving coordinates $\boldsymbol{r}(t) = a(t)\boldsymbol{x}$, this approximation consists in an *ansatz* for the peculiar motion of particles, that is the velocity with respect to the background expansion. This ansatz reads

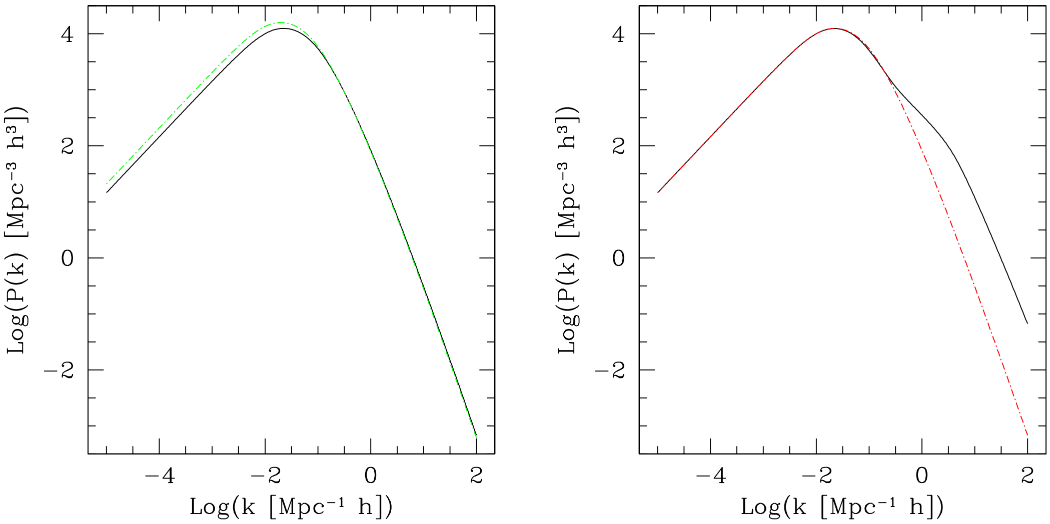

Figure 2.3: *Left panel*. Linear power spectrum for the EDE1 model (black solid line) and the ΛCDM models (green dot-dashed curve). *Right panel*. Linear (red dot-dashed line) and nonlinear (black solid line) power spectrum for the EDE1 model.

$\boldsymbol{x} = \boldsymbol{x}_0 + b(t)\boldsymbol{p}(\boldsymbol{x}_0)$. It corresponds to introducing a time dependent displacement into the comoving position of particles due to the presence of density fluctuations, the quantity $\boldsymbol{x}_0$ representing some starting position. The physical coordinates then take the form

$$\boldsymbol{r}(t) = a(t)\left[\boldsymbol{x}_0 + b(t)\boldsymbol{p}(\boldsymbol{x}_0)\right], \tag{2.20}$$

and the related peculiar velocity can easily be computed as

$$\frac{d\boldsymbol{r}}{dt} - H\boldsymbol{r} = a\dot{b}\boldsymbol{p}(\boldsymbol{x}_0). \tag{2.21}$$

Eq. (2.20) is a time dependent mapping from the original, comoving coordinates $\boldsymbol{x}_0$ to the final, physical position $\boldsymbol{r}(t)$. Locally, all the relevant properties of such a mapping are encapsulated in the Jacobian matrix $\mathcal{J}$ defined as $\mathcal{J}_{ij} = \partial r_i/\partial x_{0,j}$. As long as the Jacobian matrix is non-singular, particle trajectories do not cross, hence mass conservation holds and implies

$$\rho(\boldsymbol{x}_0, t) = \frac{a(t)^3\rho_\mathrm{b}}{\det\mathcal{J}(\boldsymbol{x}_0, t)} = \frac{\rho_\mathrm{b}}{[1 + b(t)\lambda_1][1 + b(t)\lambda_2][1 + b(t)\lambda_3]}. \tag{2.22}$$

In the previous equation the three functions $\lambda_i = \lambda_i(\boldsymbol{x}_0)$ are the eigenvalues of the matrx $\partial p_i/\partial x_{0,j}$. For times close enough to the initial time the peculiar displacement is small, hence $b(t)\lambda_i(\boldsymbol{x}_0) \ll 1$. It follows that the density fluctuation can be written to the first order as $\delta(\boldsymbol{x}_0, t) \simeq -b(t)(\lambda_1 + \lambda_2 + \lambda_3)$. Vice versa, when the crossing of trajectories is approached at t_c, the Jacobian matrix must become singular, hence one (or more) of the three eigenvalues tend to vanish, namely $b(t_\mathrm{c}) = -1/\lambda_i(\boldsymbol{x}_0)$, impling a collapse of the density fluctuation along the respective principal axis. If only one eigenvalue vanishes at t_c, then a planar structure or *pancake* is formed. If two eigenvalues vanish simultaneously, then a 1-dimensional structure or *filament* is formed. In the zero-probability case in which all the three eigenvalues vanish simultaneously, then a spherical structure is formed.

The Zel'dovich approximation is a purely kinematical description of the effect that density fluctuations have on the trajectories of particles. As such, after the crossing of trajectories it loses its validity, and cannot be used to follow the subsequent relaxation process.

2.3.2 Spherical Collapse

One obvious circumstance in which an analytic solution for the non-linear evolution of density fluctuations can be found is the spherically symmetric case. In this case we limit the study to DM fluctuations for which the pressure contribution is negligible, and we assume in addition that DM is the only constituent of the cosmic fluid, thus driving the gravitational pull. The dynamics of the spherically symmetric overdense region is in this case completely determined by the potential $\Phi = \Phi_\mathrm{b} + \delta\Phi$, where $\delta\Phi$ is the potential perturbation related to the density fluctuation $\delta\rho$, while the potential due to the uniform background can be written, to the lowest non-trivial order, as $\Phi_{\rm b} = -\ddot{a}r^2/2a$ (Padmanabhan, 1993). From the second Friedmann Eq. (1.10) then follows

$$\Phi = \frac{2\pi G}{3}\rho_{\rm b} r^2 + \delta\Phi. \tag{2.23}$$

The equation of motion for a thin shell of particles located at a physical distance r from the centre of the perturbation then reads $\ddot{r} = -GM/r^2$, where

$$M \equiv \frac{4}{3}\pi r^3 \rho_{\rm b}(1+\overline{\delta}) \equiv \frac{4}{3}\pi r^3 \rho_{\rm b}\left[1 + \frac{3}{r^3}\int_0^r \delta(\tau)\tau^2 d\tau\right], \tag{2.24}$$

and $\overline{\delta}(r)$ is the average value of the overdensity inside radius r.

The total energy of the shell

$$E = \frac{1}{2}\dot{r}^2 - \frac{GM}{r} \tag{2.25}$$

is a first integral of the equation of motion for the shell itself, as can be easily verified. If $E > 0$, then $\dot{r}$ cannot vanish, hence the shell will expand forever together with the background universe. If $E = 0$, then the expansion will eventually stop, but only at $r \to +\infty$. Finally, if $E < 0$, $\dot{r}$ will vanish at a given finite time $t_{\rm m}$, indicating a turn-around of the overdensity and subsequent collapse. Now, it is easily shown that the kinetic part of the shell energy reads $\dot{r}^2/2 = H^2r^2/2$, while the potential part becomes

$$-\frac{GM}{r} = -\frac{1}{2}H^2r^2(1+\overline{\delta})\Omega_{\rm m}, \tag{2.26}$$

where $\Omega_{\rm m}$ is the background DM density parameter. The collapse condition $E < 0$ can be rewritten as $\overline{\delta} > \Omega_{\rm m}^{-1} - 1$. In a flat or overcritical universe this condition is obviously always satisfied for a positive density fluctuation, while in an underdense universe the perturbation will be wiped out by the overall expansion if the overdensity is not large enough.

Assuming that the condition $E < 0$ is satisfied and setting $\dot{r} = 0$ it is possible to find the turn-around radius, that is also the maximum radius occupied by the considered shell, as

$$r(t_{\rm m}) \equiv r_{\rm m} = r_{\rm i}\frac{1+\overline{\delta}_i}{1+\overline{\delta}_i - \Omega_{{\rm m},i}^{-1}}. \tag{2.27}$$

Initial quantities enter because of the conservation of energy and mass within each single shell.

After collapse, and after a few relaxation times have passed, the system will reach virial equilibrium, meaning that $U = -2K$, or $E = -K = U/2$, implying a final radius for the virialised DM halo of $r_{\rm v} = r_{\rm m}/2$. The relation between the radius of a shell and time can be parametrically found by solving Eq (2.25), thus finding the time $t_{\rm v}$ corresponding to complete virialization. The *virial overdensity* $\Delta_{\rm v}$ is then defined as the ratio between the average density of the perturbation at virialization to the critical density of the Universe. It can be shown that, for an Einstein-de Sitter model universe, $\Delta_{\rm v} \simeq 178$. For comparison, the linear overdensity given by the solution to Eq. (2.7), extrapolated to the same instant $t_{\rm v}$ equals only $\delta_{\rm c} \simeq 1.686$.

We stress again that these results hold only if the perturbed DM component of the cosmic fluid is the only present. In particular, the presence of DE introduces an additional energy contribution to the virial relations, thus changing the conclusions outlined above (see for instance Wang & Steinhardt 1998; Mota & van de Bruck 2004; Zeng & Gao 2005a,b; Maor & Lahav 2005; Wang 2006; Bartelmann et al. 2006). Approximate solutions for the virial overdensity and for the linear overdensity extrapolated at virialization time for a model with a cosmological constant and $\Omega_{\rm m} + \Omega_\Lambda = 1$ are as follows.

$$\Delta_{\rm v} = 9\pi^2\left[1 + 0.7076(\Omega_{\rm m} - 1) + \Omega_{\rm m}^{0.4403}\right], \tag{2.28}$$

$$\delta_{\rm c} = \frac{3}{5}\left(\frac{3\pi}{2}\right)^{2/3}\left[1 + 0.0123\log(\Omega_{\rm m})\right]. \tag{2.29}$$

Note that, while in the Einstein-de Sitter case both $\Delta_{\rm v}$ and $\delta_{\rm c}$ do not depend on time, such a dependence is present in more generic models, and is encapsulated in the density parameter $\Omega_{\rm m}(z)$ in Eqs. (2.28) and (2.29). More details about fitting formulae and approximate solutions for general cosmologies are given in Lacey & Cole (1993); Eke et al. (1996) and Bryan & Norman (1998).

The virial overdensity defined above allow one to additionally define the *virial radius* $r_{\rm v}$ and the *virial mass* $M_{\rm v}$ of a spherical collapsed DM halo. The first one is the radius of the sphere inside which the average density is

$\Delta_{\rm v}$ times the critical density of the Universe at the relevant redshift. The second one is just the mass inside this sphere. Hence, virial mass and radius belong to the relation

$$M_{\rm v} = \frac{4}{3}\pi r_{\rm v}^3 \Delta_{\rm v} \rho_{\rm c}. \tag{2.30}$$

Even though, in principle, the virial overdensity should be computed in each case according to the background cosmology, often the position $\Delta_{\rm v} = 200$ is used. This has a practical advantage since it does not depend on the cosmological model, and is justified by the fact that in numerical simulations of structure formation (Section 2.3.5) r_{200} does indeed approximately separate the inner, equilibrium part of a galaxy cluster from the outer, infall part (Eke et al., 1998). The virial mass and radius when $\Delta_{\rm v} = 200$ are conventionally denoted by M_{200} and r_{200} respectively.

2.3.3 Mass Function

The statistics of Gaussian random fields together with nonlinear evolution models like the spherical collapse described in Section 2.3.2 can be used to derive analytically the abundance of DM halos as a function of mass and redshift, dubbed *mass function*. More in detail, the mass function $n(M, z)$ returns the comoving number density of objects in the unit mass around M and in the unit redshift around z. In the following we outline the derivation, following the steps of Press & Schechter (1974); Bond et al. (1991); Lacey & Cole (1993).

Let $Q(M, z)$ be the fraction of volume of the Universe that in the unit redshift around z is occupied by structures of mass larger than M. Then it is easily seen that the mass function can be written as

$$n = -\frac{\rho_{\rm b}}{M}\frac{\partial Q}{\partial M} = \frac{\rho_{\rm b}}{M}\left|\frac{dS}{dM}\right|\frac{\partial Q}{\partial S}, \tag{2.31}$$

where the minus sign on the right hand side has been deleted using the fact that the variance is a decreasing function of the mass scale (Section 2.2.3), and $\rho_{\rm b}$ represents the mean DM density of the Universe. What remains to be done is now to quantify the partial derivative on the rightmost side, and this can be done elegantly in the following way.

Fix a comoving position $\boldsymbol{x}$ in space, and consider the evolution of the filtered field $\delta_{\rm f}(\boldsymbol{x}, S)$ as a function of the variance $S = S(M)$. As explained in Section 2.2.3, when the filtering scale is arbitrarily large, the fluctuation field is completely smoothed out, so that $\delta_{\rm f}(\boldsymbol{x}, 0) = 0$. Moreover, if the chosen filter function is a top-hat in Fourier space, then it is easy to understand that variations in the smoothing length, hence in the variance, will provide random variations into the smoothed field, uncorrelated with the previous values. This means that $\delta_{\rm f}(\boldsymbol{x}, S)$ is a random walk as a function of S, starting at the point $(\delta_{\rm f}, S) = (0, 0)$.

The key assumption in the derivation is now that a collapsed structure forms at position $\boldsymbol{x}$ when the filtered density fluctuations field at that position equals some critical value that has to be of order unity. A simple choice is to use the linear overdensity extrapolated at virialization for a spherical collapse model (see Section 2.3.2), suitably normalised to the growth factor, in order to account for the time evolution of the amplitude of linear density fluctuations. In summary, we shall assume that a virialised object of mass M formes at comoving position $\boldsymbol{x}$ and at redshift z if $\delta_{\rm f}(\boldsymbol{x}, S) = \omega(z) \equiv \delta_{\rm c}(z)/D_+(z)$. Recall that $\delta_{\rm c}$ does not depend on redshift only for the simple case of an Einstein-de Sitter model universe.

The problem is hence reduced to finding the probability distribution for a random trajectory in the $(\delta_{\rm f}, S)$ plane to be absorbed by a constant barrier. This problem has been solved by Chandrasekhar (1943), where it is shown that if $W(\delta_{\rm f}, S, \omega)$ is the fraction of trajectories that, for variance S, have smoothed density fluctuation in the unit interval around $\delta_{\rm f}$, then

$$W(\delta_{\rm f}, S, \omega) = \frac{1}{\sqrt{2\pi S}}\left[\exp\left(-\frac{\delta_{\rm f}^2}{2S}\right) - \exp\left(-\frac{(2\omega - \delta_{\rm f})^2}{2S}\right)\right]. \tag{2.32}$$

This distribution follows the diffusion equation

$$\frac{\partial W}{\partial S} = \frac{1}{2}\frac{\partial^2 W}{\partial \delta_{\rm f}^2}, \tag{2.33}$$

with the obvious boundary condition $W(\omega, S, \omega) = 0$. It follows straightforwardly that the fraction of trajectories that at variance S have already been absorbed by the barrier ω reads

$$Q(S, \omega) = 1 - \int_{-\infty}^{\omega} W(\delta_{\rm f}, S, \omega) d\delta_{\rm f}, \tag{2.34}$$

which is equivalent to the fraction of volume in the Universe that in the unit redshift around z is occupied by structures of mass larger than M. Therefore,

$$\frac{\partial Q}{\partial S} = -\int_{-\infty}^{\omega} \frac{\partial W}{\partial S} d\delta_{\rm f} = -\frac{1}{2}\left[\frac{\partial W}{\partial \delta_{\rm f}}\right]_{-\infty}^{\omega} = \frac{\omega}{\sqrt{2\pi}S^{3/2}} \exp\left(-\frac{\omega^2}{2S}\right). \tag{2.35}$$

Using Eq. (2.35) into Eq. (2.31) we gain immediately the final expression for the mass function, first derived with a different approach by Press & Schechter (1974)

$$n(M,z) = \frac{\rho_{\rm b}(z)}{M}\frac{\omega(z)}{\sqrt{2\pi}S^{3/2}} \exp\left[-\frac{\omega^2(z)}{2S}\right]\left|\frac{dS}{dM}\right|. \tag{2.36}$$

This expression for the mass function becomes very simple when a scale free spectrum is considered. As it has been shown in Section 2.2.4, in this case

$$S(M) = \left(\frac{M}{M_0}\right)^{-\alpha}, \tag{2.37}$$

with some suitable normalization M_0 and $\alpha \equiv (n+3)/3$. The mass function then reads

$$n = \alpha\rho_{\rm b}\frac{\omega}{\sqrt{2\pi}}\frac{M^{\alpha/2-2}}{M_0^{\alpha/2}} \exp\left[-\frac{\omega^2}{2}\left(\frac{M}{M_0}\right)^{\alpha}\right]. \tag{2.38}$$

Here, it is possible to recognise two different regimes: a power-law trend, $n \propto M^{\alpha/2-2}$, dominating when $(M/M_0) \ll \omega^{-2/\alpha}$ (low masses) and an exponential cut-off in the opposite tail (high masses).

As will be discussed in Section 2.3.5, the mass function in Eq. (2.36) is in remarkable agreement with more sophisticated numerical results, indicating that despite the roughness of the model and of the assumptions, the basic physical process is fairly captured. The agreement can however be further improved with the introduction of the set of parameters (A, B, p) and the related *generalised mass function*

$$n^{(\rm g)}(M,z) = A\sqrt{B}\frac{\rho_{\rm b}(z)}{M}\frac{\omega(z)}{\sqrt{2\pi}S^{3/2}}\left[1+\left(\frac{S}{B\omega(z)}\right)^{2p}\right] \exp\left[-B\frac{\omega^2(z)}{2S}\right]\left|\frac{dS}{dM}\right|. \tag{2.39}$$

Obviously, if $A = 1/2$, $B = 1$ and $p = 0$ the original mass function by Press & Schechter (1974) is recovered. Sheth & Tormen (2002) improved this model by using the linear overdensity extrapolated at the virialization time for a more realistic ellipsoidal perturbation (see also Sheth et al. 2001) as barrier. Difficulties in this case arise because the barrier is not constant anymore but depends on the variance, $\omega = \omega(z, S)$. However, approximate expressions for the probability distribution of random trajectories can be found, leading to a generalised mass function with coefficients $A = 0.3222$, $B = 0.707$ and $p = 0.3$. Finally, Jenkins et al. (2001) found yet different values for the same set of coefficients through a fit to cosmological numerical simulations (see also Warren et al. 2006). Their result can be summarised as $A = 0.353$, $B = 0.73$ and $p = 0.175$.

A comparison between the three different prescriptions for the mass function is reported in Figure 2.4. As is shown, the Press & Schechter (1974) mass function slightly overpredicts the number of structures in the low mass regime when compared to the Sheth & Tormen (2002) and Jenkins et al. (2001), while it generally underpredicts it in the high mass tail. Also, the power-law regime and exponential cut-off described above are clearly visible in all three mass functions. A comparison of the structure abundance in different cosmological frameworks will be presented in Chapters 5 and 8.

2.3.4 Merger Rate

The random walk approach outlined above can be used also to infer the rate at which low mass cosmic structures aggregate with one another to form higher mass objects, according to the hierarchical paradigm for structure formation. This rate is dubbed *merger rate*, and is naturally related to the appropriate limit of the conditional probability distribution of random trajectories. With that we mean the probability for a trajectory to cross a barrier ω_2 at a variance S_2 given that the same trajectory already crossed a lower barrier $\omega_1 < \omega_2$ (later time) for a lower value of the variance $S_1 < S_2$ (higher mass). This can be easily obtained if the spherical collapse model is used, because in this case the barrier is independent on the variance, and hence the same argument as before can be applied if the origin of the random walks is shifted from $(0,0)$ to (ω_1, S_1). The conditional probability distribution per unit change in variance reads

$$K(\Delta S, \Delta\omega) = \frac{1}{\sqrt{2\pi}}\frac{\Delta\omega}{\Delta S^{3/2}} \exp\left(-\frac{\Delta\omega^2}{2\Delta S}\right), \tag{2.40}$$

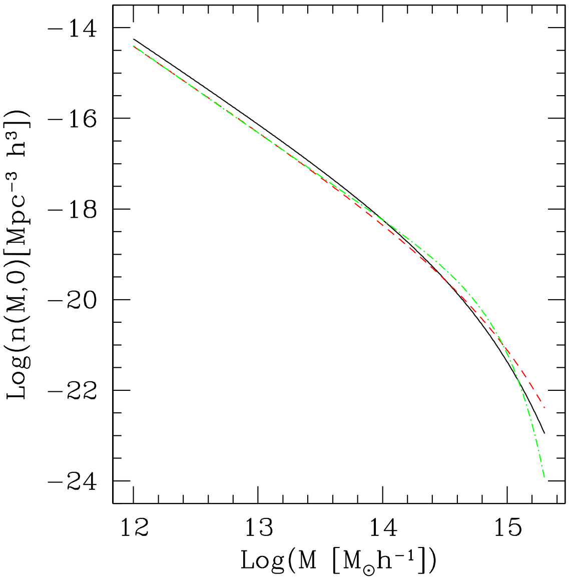

Figure 2.4: Mass function in a ΛCDM universe as a function of mass at present day computed using the three different prescriptions detailed in the text. The black solid line refers to the original Press & Schechter (1974) formulation. The red dashed curve represents the Sheth & Tormen (2002) generalization and the green dot-dashed curve the Jenkins et al. (2001) fit to numerical simulations.

where $\Delta\omega = \omega_2 - \omega_1$ and $\Delta S = S_2 - S_1$. Eq. (2.40) gives the probability of a DM halo undergoing a change in variance ΔS due to hierarchical accretion in the redshift interval Δz, per unit change in variance. With the positions $S_1 = S(M_0)$, $S_2 = S(M_\mathrm{p})$, $\omega_2 = \delta_\mathrm{c}(z + \Delta z)/D_+(z + \Delta z)$ and $\omega_1 = \delta_\mathrm{c}(z)/D_+(z)$ Eq. (2.40) returns the probability of a DM halo with a given mass M_0 at a given redshift z to have a progenitor of a lower mass $M_\mathrm{p} < M_0$ at a higher redshift $z + \Delta z$, per unit change in variance.

Finally, in the limit $\Delta z \to 0$, or $\omega_2 \to \omega_1$, and with the suitable translation between mass and variance (see Lacey & Cole 1993 for details) Eq. (2.40) can be arranged so as to return the probability that in the unit redshift interval around z a structure of mass M_p undergoes a merger with a structure in the unit mass interval around $\Delta M = M_0 - M_\mathrm{p}$, namely

$$W(M_\mathrm{p}, \Delta M, z) = \frac{1}{\sqrt{2\pi}} \left|\frac{dS_1}{dM_0}\right| \left|\frac{d\omega}{dz}\right| \left[\frac{S_2}{S_1(S_2 - S_1)}\right]^{3/2} \exp\left[-\omega^2 \frac{(S_2 - S_1)}{2S_1S_2}\right]. \tag{2.41}$$

The kind of approach outlined above cannot be applied if, for instance, the ellipsoidal collapse model is used, because in that case the barrier is not constant, and therefore a simple shift of the origin in the (δ_f, S) plane is not sufficient. Merger rates for different cosmological models will be showed again in Chapters 5 and 8.

2.3.5 Numerical Simulations

Even though analytic or semi-analytic prescriptions like those outlined above can give much physical insight on the nature of structure formation, the fully non-linear evolution of cosmic structure can be followed only with the use of numerical simulations. In the present discussion we are mainly interested in n-body simulations, that follow the evolution of a discrete set of particles self-interacting through gravity only. Numerical methods to describe also different pieces of physics, like hydrodynamics of gas, star formation, chemical evolution, feedback from supernovae and so forth exist. However, these kinds of processes are relatively difficult to parametrize, and have little effect on the dynamics of the large scale structure or of galaxy clusters we will be interested in. This is so because structure formation is mainly driven by DM, which is collisonless and hence interacting only through gravity. Therefore, the focus here will be on pure n-body simulations and their results on DM halos.

It is a well known fact that the equations of motion of n-body systems cannot be integrated exactly if $n > 2$. Several approximated and asymptotic results hold if $n = 3$, however for $n \gg 1$, as typical for astrophysical situations, the problem is not directly tractable. The mean-field approach detailed in Section 2.2.2 must instead be used, but even in this case the amount of information that can be extracted about non-linear evolution is limited. The alternative approach followed by n-body codes is in essence to compute for each particle at each discrete time

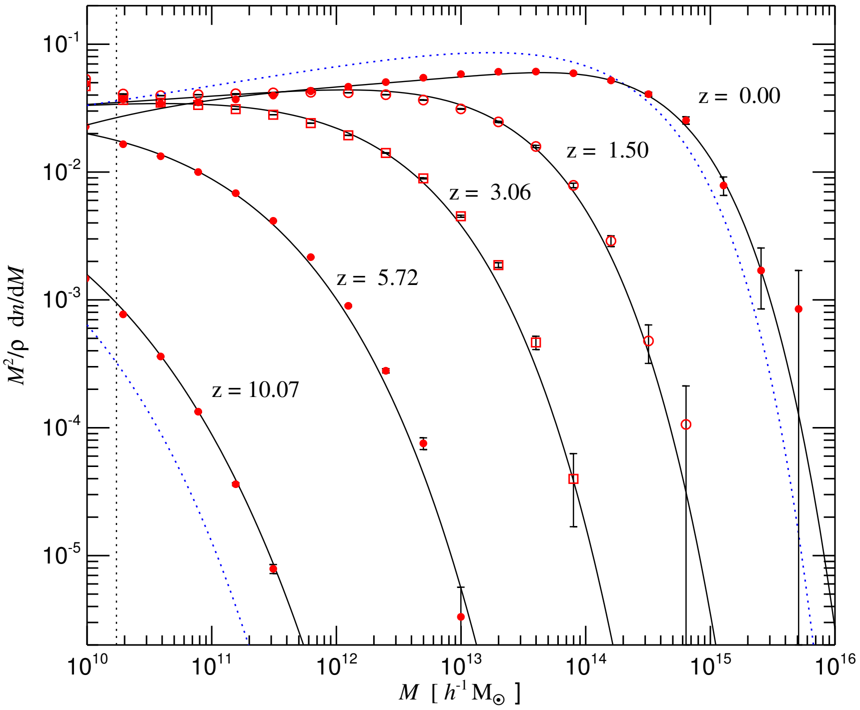

Figure 2.5: The red empty points with errorbars represent the mass function (times the square of the mass and divided by the background matter density) extracted from the Millennium Simulation (Springel et al., 2005) at various redshifts, as labelled in the plot. The blue dotted lines represent the relative prediction of the Press & Schechter (1974) mass function, while the black solid lines refer to the Jenkins et al. (2001) mass function.

step the force felt due to the presence of all other particles, and then integrate numerically the equations of motion. As is easy to realise, the computational time of such an algorithm scales as $\propto n^2$, hence cannot be realistically used for high numbers of particles.

More refined versions of the basic algorithm exist, like *mesh* codes or *tree* codes, that compute the force on each particle in a more clever way, and allow the reduction of the computational time scaling to $\propto n \log(n)$ (see references in Springel et al. 2001; Springel 2005). This, together with the continuos improvement in the performances of machines allows nowaday to follow the evolution on cosmological scales of self-gravitating systems of up to $n \sim 10^{10}$ particles, with good mass, time and force resolution.

Once a numerical n-body simulation is realised, DM halos can be identified by grouping neighbouring particles together, and the relative statistical and structural properties can be studied. Regarding the statistical properties, in Figure 2.5 we show a comparison between the mass function of DM halos identified in the *Millennium Simulation* (Springel et al., 2005) and the Press & Schechter (1974) semi-analytic predicition, Eq. (2.36). The agreement is remarkably good, but as announced above, the latter tends to overpredict the number of objects at low mass and to underpredict the number of high mass halos. Vice versa, the Sheth & Tormen (2002) (not shown) and Jenkins et al. (2001) mass functions perform pretty well in this respect.

Turning to the internal structure of simulated DM halos, perhaps the most characteristic feature that virtually all of them share, at least up to the present available resolution, is the presence of a central cusp in the density profile. This makes sense in light of the fact that DM is collisionless, hence, without the stabilising action of hydrodynamical pressure, the particles are free to sink down to the very center of the structure. The presence of a cusp in numerical simulation of cosmic structures was recognised first in Dubinski & Carlberg (1991), but has been commonly accepted after the series of works of Navarro et al. (1995, 1996, 1997) (NFW henceforth, see also Power et al. 2003). There, it was highlighted how the spherically-averaged density profile of DM halos follows a particular double power-law shape for a wide range of masses, from dwarf galaxies to massive galaxy clusters. The NFW density profile reads

$$\rho(r) = \frac{\rho_{\rm s}}{r/r_{\rm s}(1 + r/r_{\rm s})^2}. \tag{2.42}$$

Its two free parameters are the scale radius $r_{\rm s}$, where the logarithmic profile slope reaches -2, changing from -3

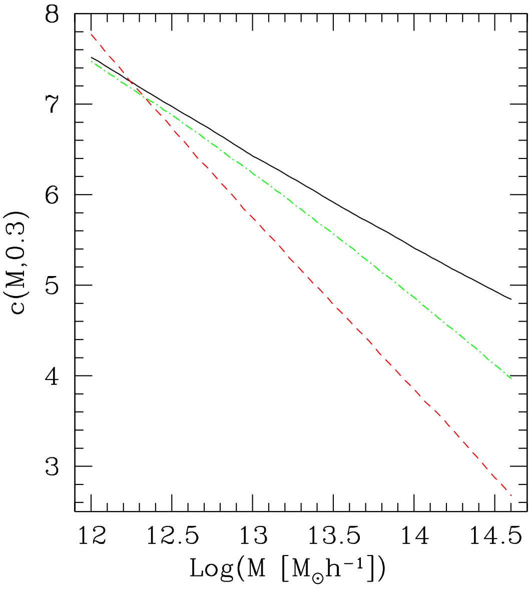

Figure 2.6: The relation between the concentration of a virialised DM halo at redshift $z = 0.3$ and the virial mass as prescribed by the original NFW algorithm (black solid line), the Bullock et al. (2001) algorithm (red dashed line) and the Eke et al. (2001) algorithm (green dot-dashed line).

outside towards -1 inside, and the scale density $\rho_\mathrm{s} = 4\rho(r_\mathrm{s})$.

The *concentration* of the halo is defined as $c \equiv r_{200}/r_\mathrm{s}$. In terms of c, the scale radius and the scale density can be expressed as

$$r_\mathrm{s} = \left(\frac{3M_{200}}{800\pi c^3 \rho_\mathrm{c}}\right)^{1/3} \quad \text{and} \quad \rho_\mathrm{s} = \frac{200}{3}\rho_\mathrm{c}\frac{c^3}{F(c)} \tag{2.43}$$

respectively, where

$$F(c) \equiv \ln(1+c) - \frac{c}{1+c}\,. \tag{2.44}$$

Halo mass and concentration can thus replace the scale radius and the scale density as the two parameters fully describing the halo density profile.

It has been firmly established in numerical simulations and observations (Navarro et al., 1997; Bullock et al., 2001; Eke et al., 2001; Wu & Xue, 2000; Buote et al., 2007; Comerford & Natarajan, 2007) that the halo concentration decreases with the halo mass. This is usually explained by the fact that low-mass halos form earlier than massive halos in the hierarchical structure formation scenario in a cold DM universe, and the assumption that the central halo density reflects the mean cosmic density at the formation redshift. This explains why massive haloes are typically found to be less concentrated than low-mass halos. The average relation between mass and concentration allows us to characterise halos by a single parameter, usually taken to be the virial mass M_{200}. There exist basically three prescription for relating the concentration of a DM halo to the virial mass, all based on different assumptions. The first one dates back to the original NFW works, while the other two are given in Bullock et al. (2001) and Eke et al. (2001) respectively. In Chapter 7 they will be described in more detail (see also Fedeli et al. 2007) while here we just plot them in Figure 2.6.

The three prescriptions agree to a good extent on galactic scales but they strongly differ on galaxy cluster scales. In particular it has been shown that the original NFW algorithm fails to drop significantly with redshift, and therefore always overestimate the concentration of DM halos at $z > 0$.

It must be recalled that the value of the inner slope of the density profile Eq. (2.42) is not universally accepted: some authors seem to find a steeper trend (Fukushige & Makino, 1997; Moore et al., 1998, 1999), while in other works, cored profiles seem to provide as good fit as the NFW profile to the structure of DM halos (Navarro et al., 2004). Despite this however, the universal profile Eq. (2.42) in general, and the presence of the inner cusp in particular, are key theoretical predictions to be compared with observations. We also stress that despite several attempts (Syer & White, 1998; Henriksen, 2006, 2007; Salvador-Solé et al., 2007a,b), a formal derivation of a density profile equal or similar to Eq. (2.42) for the equilibrium state of DM halos from first principles is still missing.

To conclude, we note that while baryonic luminous matter like gas and stars might have an effect on the density profile of galaxy-sized DM halos, such an effect is certainly less important, at least to a first approximation, on cluster scale and large scale structure of the Universe.

2.4 Galaxy Clusters

2.4.1 Structure

Galaxy Clusters (GCs henceforth) are the most massive bound objects in the Universe, and they constitute the extreme tail of the mass function. They are mainly constituited by DM, about 80% in mass, with a smaller amount of baryonic matter subdivided between gas and galaxies. Because of this their formation and evolution is relatively well understood through numerical simulations. Assuming dynamical equilibrium, the velocity dispersion of galaxies inside a cluster can be estimated as $\sigma^2 \sim GM/R$, and selecting $M \sim 10^{15} M_\odot h^{-1}$ and $R \sim 1$ Mpc for the more massive GCs, we obtain $\sigma \sim 10^3$ km s^{-1}. In a similar way, assuming the Intra-Cluster Medium (ICM henceforth) gas to be in hydrostatic equilibrium in the overall GC potential well, the temperature can be estimated as $k_\mathrm{B} T \sim \sigma^2$, thus ielding $T \sim 10^8$ K. Such extremely high temperatures imply that the hydrogen and helium in the ICM are completely ionised, and this has important consequences for the emission processes of GCs (see Section 2.4.2).

As shown in Eq. (2.36), the mass function of cosmic structures at the high mass tail depends exponentially on the variance of the density fluctuation field, and hence on the normalization σ_8 of the power spectrum. Therefore, even small variations of σ_8 can cause large effects on the abundance of clusters, and this makes GCs one of the ideal tools to probe the underlying cosmology. This will be better explored in Chapter 8.

As described in Section 2.3.5, the density profile of DM halos on virtually all mass scales is well described by the NFW fit of Eq. (2.42), and this is in particular observed to hold in GCs. In fact, several observational probes of the matter distribution in clusters agree on the presence of a central cusp (among these the presence of strong lensing features, see Section 3.6), and in many cases the NFW profile is a good fit to the shape of relaxed GCs (Schmidt & Allen, 2007).

A little more detail deserves the distribution of the gas in a GC. Pressure due to the collisional nature of gas makes sure that a cuspy density profile is not an accurate description for the ICM mass distribution. Useful insight on the equilibrium distribution of the intergalactic hot plasma can be gained by studying the behaviour of a self-gravitating gas sphere. In this case the formal equilibrium configuration can be obtained by maximising the Shannon-Boltzmann entropy (Shannon, 1948; Jaynes, 1957a,b)

$$H(f) = -k_\mathrm{B} \int_{\mathbb{R}^6} f \ln(f), \tag{2.45}$$

with the additional constraints of the conservation of mass and total energy. In Eq. (2.45), $f(x)$ represents the distribution function of the gas, and the integral is extended to the entire phase space of the system. Associating the Lagrange multiplier related to the energy conservation with the 1-dimensional (constant) velocity dispersion σ of gas particles implies the following relation between density and potential,

$$\rho(r) = \rho_0 \exp\left[\frac{\Phi(r)}{\sigma^2}\right], \tag{2.46}$$

where the normalization ρ_0 is fixed by the boundary conditions. It is interesting to recall that Eq. (2.46) is also obtained as the equilibrium structure of a self-gravitating, collisionless system that underwent violent relaxation (Lynden-Bell, 1967; Binney & Tremaine, 1987; Padmanabhan, 1990). Therefore it reveals a profound origin in the statistical mechanics treatment of systems dominated by long-range forces.

The picture above can be refined further, introducing for instance the additional constraints of the conservation of angular momentum and the three components thereof. This brings to modifications of Eq. (2.46), most likely a flattening of the density profile in the inner part due to rotational support.

Inserting Eq. (2.46) into the Poisson equation gives the *Lane-Emden equation* for the density,

$$\frac{d^2\rho}{dr^2} + \frac{2}{r}\frac{d\rho}{dr} - \frac{1}{\rho}\left(\frac{d\rho}{dr}\right)^2 + \frac{4\pi G}{\sigma^2}\rho^2 = 0. \tag{2.47}$$

The same equation can be also derived by assuming a constant temperature for the gas cloud, working on the hydrostatic equilibrium equation (Euler's equation with vanishing streaming velocity) and setting $\sigma^2 = k_\mathrm{B} T/\mu m_\mathrm{p}$. It is intended that μ is the mean molecular weight of the ICM (assumed to be $\mu = 0.59$ throughout this work) and

$m_{\rm p}$ is the proton mass. The (unique) power-law solution to the Lane-Emden equation is the *Singular Isothermal Sphere* (SIS henceforth), and is expressed as

$$\rho(r) = \frac{\sigma^2}{2\pi G}\frac{1}{r^2}. \tag{2.48}$$

This model Eq. (2.48) is widely used due to its simplicity and to the good fit that it provides to the surface brightness profile and velocity dispersion measurements of elliptical galaxies (Treu & Koopmans, 2002). Nevertheless, it is a poor fit for the ICM distribution observed in GCs, besides, the central cusp is not physically acceptable for a collisional fluid. Generalizations of the Lane-Emden equation can be found using different forms for the entropy, for instance accounting for the non-extensive nature of self-gravitating systems (Tsallis, 1999; Zavala et al., 2006).

Looking for a description of more realistic situations, the solution to the Lane-Emden equation must be found numerically, imposing the desired boundary conditions, i.e. a finite central density $\rho_0 < +\infty$. An analytic approximation to this numerical solution is given by the *modified Hubble profile* (Reynolds, 1913; Hubble, 1930; Rood et al., 1972)

$$\rho(r) = \frac{\rho_0}{[1+(r/r_0)^2]^{3/2}}. \tag{2.49}$$

Here we have set $r_0^2 \equiv 9\sigma^2/4\pi G\rho_0$, and the error given by the use of Eq. (2.49) instead of the exact numerical solution to Eq. (2.47) is less than 5% in the range $0 < r < 2r_0$. The modified Hubble profile can be generalised to the *β-profile* (Cavaliere & Fusco-Femiano, 1976, 1978)

$$\rho(r) = \frac{\rho_0}{[1+(r/r_0)^2]^{3\beta/2}}. \tag{2.50}$$

Even though the previous discussion concerns isothermal, self-gravitating gas spheres, Eq. (2.50) is often used to fit the ICM distribution inside clusters, and for relaxed systems the value $\beta = 2/3$ is found to give good agreement with observations (see Section 6.3.2).

To conclude this section, we note in passing that the modified Hubble profile of Eq. (2.49) is often referred to as *King profile*. The reason for this is that the surface density profile related to Eq. (2.49) is a good approximation to the surface density profile derived from the King distribution function (Michie, 1963; Michie & Bodenheimer, 1963; King, 1966, 1972, 1981).

2.4.2 Emission and Mass Determination

Except for the light emitted by the member galaxies, the main source of radiation from GCs is the ICM. Since the gas is almost completely ionised, the relevant emission process is the bremsstrahlung due to the scattering of free electrons off atomic nuclei. At the typical temperature of the ICM the emitted radiation lies in the X-ray band. As is well known, the bremsstrahlung emission is proportional to the square root of the gas temperature and to the square of the free electron density. Therefore, an ICM distributed according to the β-model of Eq. (2.50) produces a surface brightness profile of the type

$$B(\theta) = \frac{B_0}{[1+(\theta/\theta_0)^2]^{3\beta-1/2}}, \tag{2.51}$$

where, if z is the redshift of the cluster and F the total flux received by the observer (that is the integral of the surface brightness profile over the solid angle), $\theta_0 \equiv r_0/d_{\rm a}(z)$ and $B_0 \equiv F/2\pi\theta_0^2$.

It must be noted that the implicit assumption made so far is that the ICM gas is isothermal, i.e. it can be described by a single value of the temperature. This is not strictly true, and as a matter of fact the latest generation of X-ray satellites revealed a variety of phenomena affecting the thermodynamical state of the ICM, like shocks, cold fronts and cooling flows. However, for the study of global properties of GCs, when the details of the gas distribution are not relevant, the isothermality assumption is often used as a good approximation.

In addition to the bremsstrahlung emission, free electrons of the ICM interact via inverse Compton scattering with the low-energy CMB photons. In this kind of process, the photons gain energy from the collision with very hot electrons, and this leads to a distortion in the energy spectrum of the microwave background. In particular, photons are moved from low to high frequency. This effect is called *thermal Sunyaev-Zel'dovich* effect (Sunyaev & Zeldovich, 1972), and it is now becoming measurable, promising to be one of the most important probes of the ICM in the next years. A similar effect, the *kinetic Sunyaev-Zel'dovich* effect (Sunyaev & Zeldovich, 1980) is also based on the interaction between free electrons of the ICM medium with CMB photons, but in this case the distortion of the spectrum is caused by the peculiar motion of the cluster as a whole and the related Doppler effect.

The light emitted by the member galaxies and the X-ray radiation related to the hot intergalactic plasma allow independent determinations of the mass of a GC. Let us start with the first: using the Doppler effect, the velocity dispersion of galaxies can be determined, at least along the line of sight. The second velocity moment of the collisionless Boltzmann's equation under the assumption of no streaming motions reads

$$\frac{\partial\Phi}{\partial r_i} = -\frac{1}{\rho}\frac{\partial\rho\sigma_{ij}^2}{\partial r_j}, \tag{2.52}$$

where Φ is the overall potential of the cluster, while ρ is the density of galaxies only, that can be observed in projection. Assuming now spherical symmetry and an isotropic velocity dispersion tensor, meaning $\sigma_{ij}^2 = \sigma^2\delta_{ij}$, it is easily obtained that the total mass inside a radius r is

$$M(r) = -\frac{r\sigma^2}{G}\left(\frac{d\log\rho}{d\log r} + \frac{d\log\sigma^2}{d\log r}\right). \tag{2.53}$$

A similar approach can be followed for the ICM. Making the usual assumption $\rho\sigma_{ij}^2 = p\delta_{ij}$ and replacing the galaxy density with the gas density in Eq. (2.52) returns the hydrostatic equilibrium equation. From there, using again the assumption of spherical symmetry, we get

$$M(r) = -\frac{rk_\mathrm{B}T}{G\mu m_\mathrm{p}}\left(\frac{d\log\rho}{d\log r} + \frac{d\log T}{d\log r}\right). \tag{2.54}$$

Both these methods rely on assumptions about the dynamical and thermodynamical state of the cluster that can be sometimes too strong. For instance is not guaranteed at all that the ICM is in hydrostatic equilibrium during a cluster merger (Puchwein & Bartelmann, 2007), and the same holds true for the isotropy of the galaxy velocity dispersion. This is particularly worrysome since GCs are at the high mass tail of the mass function, and hence are the youngest objects in the Universe, mostly still in the formation process. There exists however a third method for the determination of the mass of a GC, namely the gravitational deflection of light, that will be explored in detail in Chapter 3. For the time being however it is important to know that this tecnique does not rest on any assumption about the state or the nature of the matter in clusters. A possible consequence of this fact is that the lensing mass estimates agree quite well with optical and X-ray estimates for relaxed clusters (Hoekstra, 2007) but can be factors between 2 and 3 larger for substructured ones.

2.4.3 Non-Linear Scaling Relations

Starting from the linear evolution of the power spectrum of density fluctuations and using simple dimensional arguments it is possible to derive relations between the global quantities that non-linear structures in general and GCs in particular should satsfy. The assumption behind this derivation is that only gravity and other scale free processes dominate in the formation of GCs. While this is true to a good extent as long as only adiabatic gas physics is considered, particular processes like radiative cooling of gas can invalidate this assumption and the resulting scaling relations.

Let us start with the radius. It is known from Eq. (2.30) that

$$r_{200} \propto \frac{M_{200}^{1/3}}{h(z)^{2/3}}. \tag{2.55}$$

Then, the gas temperature of the ICM and the velocity disperion of galaxies are measures of the depth of the potential well of the GC. Therefore it can be written that

$$T \propto \frac{M_{200}}{r_{200}} \propto M_{200}^{2/3}h(z)^{2/3}. \tag{2.56}$$

Finally, if the emission mechanism for the ICM is thermal bremsstrahlung, then the bolometric luminosity is proportional to the integral over the cluster volume of the square root of the temperature times the square of the density, giving

$$L \propto \sqrt{T}\frac{M^2}{R^3} \propto M_{200}^{4/3}h(z)^{7/3}. \tag{2.57}$$

Note that the mass and redshift dependence of the luminosity is significantly stronger than for the temperature. Generalizations of these scaling relations taking into account also the internal structure of the host DM halo will be described in Chapter 7.

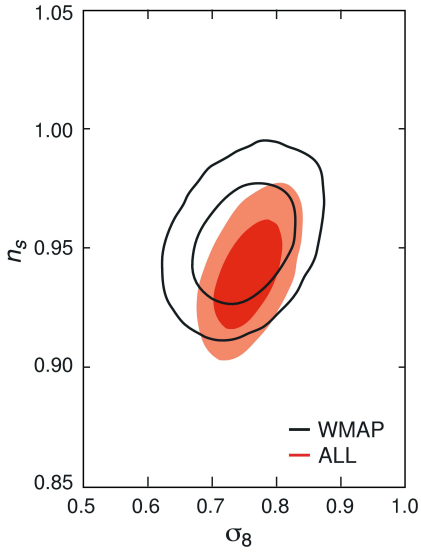

Figure 2.7: Marginalised likelihood contours (68% and 95% confidence levels) for the index and normalization of the power spectrum of density fluctualtions, assuming a power-law form. The black, solid contours are for the WMAP data only, while the red dashed regions combine WMAP data with supernovae and large scale structure measurements (Spergel et al., 2007).

2.5 Current Observational Status

As explained in Section 2.2.3, the complete statistical description of the primordial density fluctuation field is provided by the power spectrum. Under the assumption of a power-law form, the primordial power spectrum is in turn determined by the amplitude, or σ_8, and the spectral index n. Once again, the main source of information in this respect is provided by the angular power spectrum of the CMB. In Figure 2.7 the likelihood regions in the $n - \sigma_8$ plane are shown, for WMAP-3 data alone and for a combination of CMB experiments with large scale structure and supernova datasets.

It is evident that, the best fit value for the normalization is around $\sigma_8 \sim 0.75$, altough degeneracies with other parameters exist. This value is significantly smaller than the one derived from the first-year WMAP data release (Spergel et al., 2003) and of the value derived from independent cosmological tests, like GC abundance and evolution and weak lensing surveys (see Section 3.6), that tend to prefer $\sigma_8 \sim 0.9$. We stress again that the normalization σ_8 enters in the exponential of the mass function Eq. (2.36), therefore small variations produce large effects in the abundance of cosmic structures.

Regarding the spectral index n, a value slightly smaller than unity is preferred. This is in agreement with the inflationary scenario, that predicts $n = 1$ in the case of eternal inflation, but favors a value different from unity if the inflationary epoch has a finite duration, as it must be the case.

The preference of GC-based cosmological tests for a higher normalization of the power spectrum (Yepes et al., 2007) can be also understood from an analysis of Figure 2.8 (Evrard et al., 2007). There, it is shown the DM cumulative velocity dispersion function, that is basically related to the mass function. Evidently, current observations of the cluster space density agree well with $S_8 \sim 0.9$, where

$$S_8 = \sigma_8 \left(\frac{\Omega_{\rm m,0}}{0.3} \right)^{0.35} , \tag{2.58}$$

while using the best fit values from the three-years WMAP data release, a value of $S_8 \sim 0.7$ is preferred. Little changes to this conclusion are obtained by varying $\Omega_{\rm m,0}$.

A similar consequence can be drawn from the analysis of Figure 2.9. There the constraints on the $\Omega_{\rm m,0} - \sigma_8$ plane obtained from the cluster mass function are shown, where cluster masses are computed using different criteria. The cluster sample is the Cluster Infall Regions (CIRS) from Rines & Diaferio (2006), and the masses are computed using the virial theorem and the caustic tecnique (Diaferio, 1999; Geller et al., 1999) respectively. The comparison with the WMAP likelihood contours confirms that a certain tension exist between the two sources of cosmological information.

The internal structure of GCs deserves separate analysis. There are basically two points where the theoretical predictions, mainly based on numerical work, are at odds with the observational evidence. The first one is the

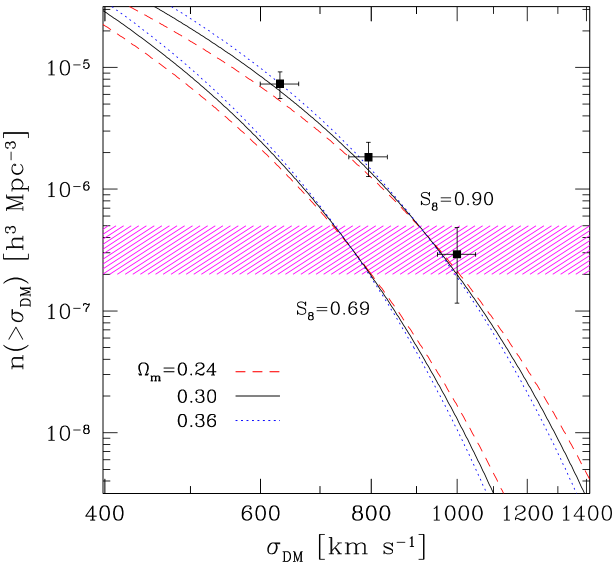

Figure 2.8: Cumulative space density of GCs as a function of the DM velocity dispersion within r_{200} computed for two different values of S_8, as labelled. The curves are the predictions based on the Jenkins et al. (2001) mass function using three different values for the present matter density. The magenta shaded region shows the observed local space density of clusters with temperature greater than 6 keV ($\sigma_{\rm DM} \sim 1000$ km s^{-1}, Ikebe et al. 2002; Henry 2004), while black solid squares with errorbars show the space density of CIRS clusters (Rines et al., 2007; Evrard et al., 2007).

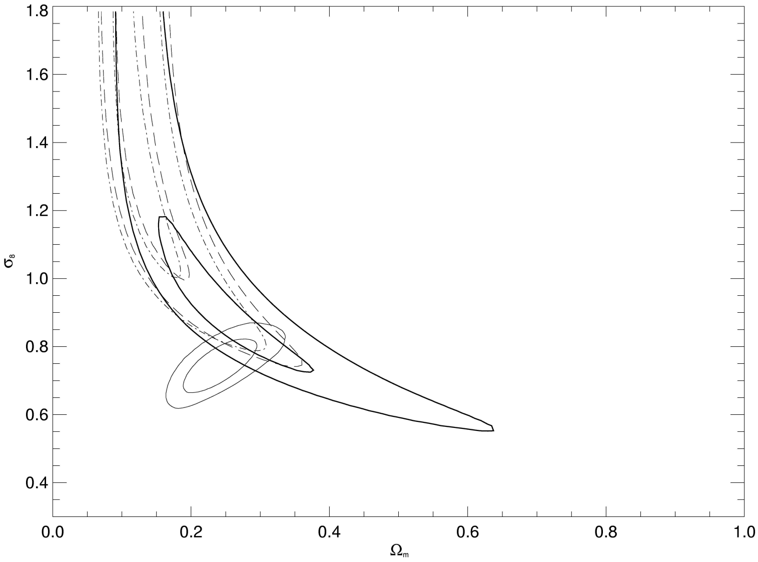

Figure 2.9: Thick solid contours show the 1σ and 3σ confidence levels in the $\Omega_{\rm m,0} - \sigma_8$ plane from CIRS GCs virial mass function. Dashed contours show the constraints from the caustic mass function (see text for details) and dot-dashed contours constraints from the virial mass function with masses computed using only red galaxies. The thin solid contours are the 68% and 95% confidence levels from the three-years data release of WMAP (Rines et al., 2007).

number of subhalos associated with galaxy or cluster-scale DM halos. According to n-body simulations, the number of such substructures should be much larger than the currently observed abundance of e.g. satellites of the Milky Way. This kind of tension could be explained with the fact that the smallest subhalos are not able to retain gas due to the shallow potential well, or with the introduction of a minor contribution from warm DM.

Also a matter of dispute at the moment is the second point, namely the presence of the inner cusp at the centre of DM density profile (Section 2.3.5). While strong lensing seems to require steep density profiles in the very inner regions of GCs (see Section 3.6 for details), rotation curves of low surface brightness spiral galaxies seems to be better fit by an internally flat density profile. The explanation that is usually put forward for this is that unlike in GCs, in the inner regions of galaxies the luminous matter contributes significantly to the density profile of the structure, and the presence of a core could be a consequence of the collisional nature of the gas. However, this line of argument seems difficult to apply to low surface brightness objects, and general agreement in both cases has not been reached yet.

Chapter 3

Gravitational Lensing

3.1 Introduction

Gravitational deflection of light is one of the most astonishing predictions of GR. Even though the modification of photon' paths due to distributions of matter was predicted in Newtonian dynamics as well, as a consequence of the equivalence principle (Soldner, 1804), the magnitude of the effect (Eddington 1919, see also Einstein 1919) is correctly forecasted only in the GR setting (or, more generally, in the context of metric theories of gravitation, see Chapter 9 and Feix et al. 2007). Deflection of light implies distortion and amplification of the images of distant sources, a phenomenon that is currently referred to as *gravitational lensing*. In addition to the fact that lensing can magnify faint sources bringing them above the threshold for detection, distortion of images can be also used to probe the distribution of matter in the Universe, without any assumption on its nature or dynamical state.

Moreover, the analysis of distorted images can return information on the internal structure of deflectors, their statistical abundance and the geometry of the Universe. Hence, gravitational lensing is a fundamental tool to gain insights on the structure formation scenario, background cosmology and the contribution of DE to the cosmic fluid.

Gravitational lensing manifests itself mainly in two forms. When the strength of the deflector (to be appropriately quantified later) is low, then only minor shearing of the images is possible, hence a significant distortion signal can be gained only with the statistical analysis of a high number of images. This regime is named *weak lensing*, and allows for instance the non-parametric reconstruction of the mass distribution of GCs and the tomography of the large scale structure in the Universe. More details on this and the related insights about the background cosmology are deferred to Section 3.6.

More seldomly the deflector is strong enough to cause spatial light trajectories to cross each other, giving rise to multiple and highly distort images (rings and arcs) of the same background source. This regime is called *strong lensing*. As for the weak regime, strong lensing can be used both to gain information about single deflectors (for instance a GC) or in a statistical manner. The latter will be the focus of this and the following Chapters of this thesis.

In this Chapter the main theoretical aspects of gravitational lensing are worked out, with particular emphasis on the strong lensing properties of GCs relevant to this work.

3.2 Fermat's Principle

3.2.1 Arrival Time

As in standard optics, the starting point for the developement of gravitational lensing theory is the Fermat's principle for the propagation of light. As is well known, this principle states that light rays, or photons, always follow actual paths that minimize the travel time from a given source to the observer. This is a standard result of Hamiltonian theory of light propagation, following just from the least action principle in the reduced Maupertuis form (Landau & Lifshitz, 1975; Arnold, 1978). However, it is *a priori* not guaranteed to hold in the GR framework, where the concept of travel time depends on the reference frame, and in particular no eigentime can be defined for a particle moving at the speed of light. It has been shown however, that a suitably modified version of Fermat's principle holds in GR as well, for arbitrary spacetimes (Perlick, 1990a,b). Further details and applications of this proof can be found in Perlick (2000a,b, 2004), and are here summarised as follows. For a given lightlike curve λ connecting an emission event to the worldline of an observer, it is possible to define a functional $\tau(\lambda)$, called *arrival time functional*, that is extremal on the actual (geodesic) path followed by photons. It can be shown that, in the particular case of a conformally stationary spacetime, the arrival time functional takes the form

$$\tau(\lambda) = \int_{\nu_1}^{\nu_2} \sqrt{\hat{g}_{ij} \frac{dx^i}{d\nu} \frac{dx^j}{d\nu}} d\nu, \tag{3.1}$$

where $\hat{g}$ is the metric in the three-dimensional spatial submanifold orthogonal to the time direction, and ν is the parameter of the curve λ, such that $\lambda(\nu_1)$ is the emission event, while $\lambda(\nu_2)$ is some point on the observer's worldline.

Assume now a Robertson-Walker spacetime that is locally weakly perturbed by some potential Φ related to a positive density fluctuation, that in our view represents the deflector. The related metric takes the form

$$g = a^2 \left(1 + \frac{2\Phi}{c^2}\right) \left[-c^2 d\eta^2 + \left(1 - \frac{2\Phi}{c^2}\right)^2 \gamma\right], \tag{3.2}$$

where we made use of the fact that $\Phi \ll c^2$. This weak field assumption is satisfied in the vast majority of astrophysical situations not involving exotic objects like black holes or collapsed stars. For instance, for a typical GC, the potential is of the order $\Phi \sim GM/R \sim 10^{-4}c^2$.

Using the metric Eq. (3.2) in the definition of the arrival time functional Eq. (3.1), together with the assumption that the deflection experienced by light paths is small (at the same order of Φ/c^2, dubbed Born's approximation) the arrival time functional takes the form

$$\tau(\lambda) = -\frac{1}{c} \int_0^{\chi_\mathrm{s}} \left(1 - \frac{2\Phi}{c^2} + \frac{1}{2} f_k^2 \left\| \frac{d\boldsymbol{\theta}}{d\chi} \right\|\right) d\chi. \tag{3.3}$$

Here χ_s is the comoving coordinate of the source and $\boldsymbol{\theta}$ is the light ray's position on the observer's sky. The integral is performed along the unperturbed ligth path, in accord with the Born approximation.

The actual light path is then found by extremising the right hand side of Eq. (3.3) between fixed endpoints. Therefore, Eq. (3.3) actually plays the role of the action when finding trajectories of free point particles in standard mechanics.

3.2.2 Lens Equation

Given the variational nature of the problem outlined in the previous section, a relevant Lagrangian function for light trajectories can be identified, namely

$$\mathcal{L} = \frac{1}{2} f_k^2 \left\| \frac{d\boldsymbol{\theta}}{d\chi} \right\| - \frac{2\Phi}{c^2}. \tag{3.4}$$

Using the momenta associated with the generalised angular coordinates $\boldsymbol{p} = f_k^2 d\boldsymbol{\theta}/d\chi$, and performing a Legendre transformation of the Lagrangian, the Hamiltonian function of the problem is readily obtained,

$$\mathcal{H} = \frac{1}{2} f_k^2 \left\| \boldsymbol{p} \right\| - \frac{2\Phi}{c^2}. \tag{3.5}$$

From here, combining the solutions of the two canonical Hamilton equations, we finally obtain the solution of the problem, that is the angular motion of photons on the sky sphere of the observer,

$$\boldsymbol{\beta} = \boldsymbol{\theta} - \frac{2}{c^2} \int_0^{\chi_\mathrm{s}} \frac{f_k(\chi_\mathrm{s} - \chi)}{f_k(\chi_\mathrm{s}) f_k(\chi)} \boldsymbol{\nabla}\Phi d\chi, \tag{3.6}$$

where the assumptions $\boldsymbol{\beta} = \boldsymbol{\theta}(\chi_\mathrm{s})$ and $\boldsymbol{\theta} = \boldsymbol{\theta}(0)$ have been used, and the gradient is taken here with respect to the two-dimensional coordinate set $\boldsymbol{\theta}$.

A further assumption that is often justified for astrophysical gravitational lensing is the thin lens approximation. This means that the spatial extent of the lens is very small when compared to the distances between the lens itself and the sources and the observer. Hence, we can always think of the matter of the lens as projected on a plane orthogonal to the line of sight, and placed at a comoving radial coordinate χ_l from the observer. This plane is dubbed *lens plane*, and likewise we shall name the plane where the relevant sources lie the *source plane*. A consequence of this approximation is that astrophysical gravitational lensing theory deals almost exclusively with projected quantities, hence giving almost no information on the matter distribution of the lens along the line of sight.

The deflection of light is assumed to happen impulsively at the location of the lens plane, while the photon's path is unperturbed in the remaining journey. This approximation allows us to rewrite the lens equation in the simplified form

$$\boldsymbol{\beta} = \boldsymbol{\theta} - \frac{2}{c^2}\frac{D_{\rm ls}}{D_{\rm s}D_{\rm l}}\int_0^{r_{\rm s}} \boldsymbol{\nabla}\Phi d\zeta, \tag{3.7}$$

where, in the integral on the right hand side, the comoving radial distance of the source $\chi_{\rm s}$ has been replaced by the physical distance $r_{\rm s}$. In Eq. (3.7), the quantities $D_{\rm l} \equiv d_{\rm a}(z_{\rm l})$, $D_{\rm s} \equiv d_{\rm a}(z_{\rm s})$ and $D_{\rm ls} \equiv d_{\rm a}(z_{\rm l}, z_{\rm s})$ represent shortly the angular diameter distances from the observer to the lens, to the source, and from the lens to the source, respectively.

We define the *scaled lensing potential* as

$$\overline{\Psi}(\boldsymbol{\theta}) \equiv \frac{2}{c^2}\frac{D_{\rm ls}}{D_{\rm s}D_{\rm l}}\int_0^{r_{\rm s}} \Phi(\boldsymbol{\theta},\zeta) d\zeta, \tag{3.8}$$

so that we can recast the lens equation in its final, compact form,

$$\boldsymbol{\beta} = \boldsymbol{\theta} - \boldsymbol{\nabla}\overline{\Psi}(\boldsymbol{\theta}) \equiv \boldsymbol{\theta} - \overline{\boldsymbol{\alpha}}(\boldsymbol{\theta}), \tag{3.9}$$

with $\overline{\boldsymbol{\alpha}}$ being the *scaled deflection angle*.

Given the source position $\boldsymbol{\beta}$, the solution to the lens equation returns the position of the related images on the lens plane. It is obvious that in general this solution is not unique, meaning that multiple images are possible under specified circumstances that will be described shortly. Also, the details of the solution, hence the exact number and position of images and their distortion pattern depends on the exact shape of the (projected) potential of the lens object.

3.3 Lens Mapping

It is often convenient to rewrite the lens equation using physical coordinates on the lens and source planes instead of angular ones. By defining $\boldsymbol{\eta} \equiv \boldsymbol{\beta} D_{\rm s}$ and $\boldsymbol{\xi} \equiv \boldsymbol{\theta} D_{\rm l}$, we obtain

$$\boldsymbol{\eta} = \frac{D_{\rm s}}{D_{\rm l}}\boldsymbol{\xi} - D_{\rm l}D_{\rm s}\overline{\boldsymbol{\alpha}}(\boldsymbol{\xi}). \tag{3.10}$$

Also, it is possible to recast the lens equation using dimensionless coordinates, replacing $\boldsymbol{\xi} \equiv \xi_0 \boldsymbol{x}$, and $\boldsymbol{\eta} \equiv \eta_0 \boldsymbol{y}$, where ξ_0 and $\eta_0 = \xi_0 D_{\rm s}/D_{\rm l}$ are arbitrary scale lengths on the lens and source plane respectively. The final result is

$$\boldsymbol{y} = \boldsymbol{x} - \frac{D_{\rm l}^2}{\xi_0^2}\overline{\boldsymbol{\alpha}}(\boldsymbol{x}) \equiv \boldsymbol{x} - \boldsymbol{\alpha}(\boldsymbol{x}). \tag{3.11}$$

The *deflection angle* $\boldsymbol{\alpha}$ is proportional to the scaled deflection angle, and is related to the *lensing potential* Ψ, in turn proportional to the scaled lensing potential, via $\boldsymbol{\alpha}(\boldsymbol{x}) \equiv \boldsymbol{\nabla}\Psi(\boldsymbol{x})$. The gradient is now taken with respect to the dimensionless coordinates $\boldsymbol{x}$, and

$$\Psi(\boldsymbol{x}) \equiv \frac{2}{c^2}\frac{D_{\rm l}D_{\rm ls}}{D_{\rm s}\xi_0^2}\int_0^{r_{\rm s}} \Phi(\boldsymbol{x},\zeta) d\zeta. \tag{3.12}$$

The lens equation (3.11) can be seen as a coordinate mapping from the sorce to the lens plane. Under the condition that the source dimension is small compared to the typical scale on which the lensing properties of the deflector change significantly, such a mapping can be locally linearised. In particular, in a neighborhood of the (arbitrary) origin of the coordinate system on the lens plane it can be written that $\boldsymbol{y} = \mathcal{A}\boldsymbol{x}$, where $\mathcal{A}$ is the Jacobian matrix of the lens mapping. It is defined as

$$\mathcal{A}_{ij} = \frac{\partial y_i}{\partial x_j} = \delta_{ij} - \frac{\partial \alpha_i}{\partial x_j} = \delta_{ij} - \frac{\partial^2\Psi}{\partial x_i \partial x_j}. \tag{3.13}$$

Locally, the properties of the images of a small source are determined by the Jacobian matrix of the lens mapping, and in particular by its eigenvalues. A more convenient form of the matrix $\mathcal{A}$ can be found as

$$\mathcal{A} = (1-\kappa)\mathcal{I} - \Gamma, \tag{3.14}$$

where $\mathcal{I}$ is the unit matrix, κ is the *convergence*, defined as $\kappa \equiv \Delta\Psi/2$ (the Laplacian operator is again taken with respect to the 2-dimensional coordinate set $\boldsymbol{x}$), and Γ is the trace free *shear* tensor, defined as

$$\Gamma = \begin{pmatrix} \gamma_1 & \gamma_2 \\ \gamma_2 & -\gamma_1 \end{pmatrix}, \text{ with } \gamma_1 \equiv \frac{1}{2}\left(\frac{\partial^2\Psi}{\partial x_1^2} - \frac{\partial^2\Psi}{\partial x_2^2}\right) \text{ and } \gamma_2 \equiv \frac{\partial^2\Psi}{\partial x_1 \partial x_2}. \tag{3.15}$$

Hence, the local distorsion pattern due to gravitational lensing is given by a diagonal part and a trace-free part. The first one is boosted by the convergence, and affects only the size of the image, enlarging or reducing it with respect to the source size. The second one is instead given by the shear, and changes the shape of the image.

As a simple consequence of the Poisson equation, indicating with ρ the density distribution source of the potential Φ, it can be written that

$$\kappa = \frac{1}{c^2}\frac{D_\mathrm{l}D_\mathrm{ls}}{D_\mathrm{s}\xi_0^2}\int_0^{r_\mathrm{s}} \Delta\Phi d\zeta = \frac{1}{c^2}\frac{D_\mathrm{l}D_\mathrm{ls}}{D_\mathrm{s}}\int_0^{r_\mathrm{s}} \left(4\pi G\rho - \frac{\partial^2\Phi}{\partial\zeta^2}\right) d\zeta. \tag{3.16}$$

The last term on the right-hand side disappears under appropriate boundary conditions, namely that the derivatives of the potential of the lens approach zero very far away fom the lens plane. This is justified in the thin lens approximation. Therefore a 2-dimensional version of the Poisson equation is recovered,

$$\Delta\Psi = 2\kappa = \frac{8\pi G}{c^2}\frac{D_\mathrm{l}D_\mathrm{ls}}{D_\mathrm{s}}\int_0^{r_\mathrm{s}} \rho d\zeta \equiv \frac{8\pi G}{c^2}\frac{D_\mathrm{l}D_\mathrm{ls}}{D_\mathrm{s}}\Sigma \equiv \frac{2\Sigma}{\Sigma_\mathrm{c}}. \tag{3.17}$$

The surface density Σ is just the projection of the 3-dimensional matter distribution of the deflector onto the lens plane, while the *critical surface density* Σ_c is an order of magnitude estimate for the strength of the gravitational lens, as will become clear in a moment. It can also be written as $\Sigma_\mathrm{c} \simeq 0.35$ g cm$^{-2}D_\mathrm{s}/D_\mathrm{l}D_\mathrm{ls}$ if the distances are expressed in Gpc. Note that when the deflector is very close to the sources or to the observer, the critical surface density diverges.

By definition now, the Jacobian matrix of the lens mapping is always symmetric, hence a reference frame with respect to which it is diagonal can always be found. The eigenvalues of the Jacobian matrix can be written as $\lambda_1 = 1 - \kappa - \gamma$ and $\lambda_2 = 1 - \kappa + \gamma$, with $\gamma^2 = \gamma_1^2 + \gamma_2^2$. They express the magnitude of the lensing distortion along the respective principal axes, and they are called *tangential* and *radial* eigenvalue because, for a spherically symmetric lens, the principal axes are in the tangential and radial direction with respect to the center of the lens itself.

It must be noted that, if no photons are emitted or absorbed along the path from the source (transparent deflector), then the surface brightness profile is always conserved, and the flux transmitted by each image changes proportionally to the change in the solid angle covered in the sky by the image itself. Hence, it makes sense to introduce the *magnification* as

$$\mu \equiv \frac{1}{\det\mathcal{A}} = \frac{1}{\lambda_1\lambda_2}. \tag{3.18}$$

If the sum or the difference between convergence and shear equals unity, then one of the two eigenvalues of the lens mapping vanishes, therefore the lens mapping becomes singular, meaning that the trajectories of photons emitted by the same source cross each other. In this case the distortion of images along the principal axis of the vanishing eigenvalue becomes formally infinite, as does the magnification μ. Obviously, an infinite magnification cannot be realised in practice, because sources are not exactly point-like, and they do not emit an infinite amount of photons. However, the distortion can be severe, producing highly elongated images like rings and arcs. It is to be noted that the magnification Eq. (3.18) can possibly be negative. An image with negative magnification is interpreted to have inverted parity.

A point of the lens plane where the lens mapping become singular is called *critical point*. Such points form closed curves on the lens plane, called *critical curves*. The images of the critical curves onto the source plane are named *caustics*. As can be seen from the definition of the tangential eigenvalue, a sufficient condition for the production of a critical curve is that at least one point of the lens plane $\kappa > 1$, i.e. $\Sigma > \Sigma_\mathrm{c}$. Therefore, a lens has critical curves, that is it is capable of producing highly distorted images, if its surface density is higher than the critical density in at least one point. If the lens is very close to the sources or to the observer, then the critical surface density becomes arbitrarily large, and consequently it is not possible for realistic deflectors to produce critical curves. Such geometrical suppression of the lensing efficiency will be better illustrated in Chapter 4.

3.4 Lens Models

3.4.1 Axially Symmetric Models

Models of deflectors with axial symmetry are widely used for lensing analysis due to their simplicity and because they can provide physical understanding of problems and set the stage for more realistic and complicated analysis. In this section two of the most popular models together with the exemplary point lens will be presented.

In the axially symmetric case, Gauss' theorem applied to the 2-dimensional Poisson Eq. (3.17) implies that the magnitude of the deflection angle at a dimensionless distance $x = \|\boldsymbol{x}\|$ from the center of the lens reads

$$\alpha(x) = \frac{2}{x}\int_0^x \kappa(x')x'dx' \equiv \frac{m(x)}{x}, \tag{3.19}$$

where the *dimensionless mass* inside the circle of radius x, $m(x)$, was defined. This result holds true also for particular classes of lenses with elliptical surface contours, like homeoids (Schramm, 1990).

Also, in the case of axial symmetry, the eigenvalues of the lens mapping can be written in a simplified manner as

$$\lambda_1(x) = 1 - \frac{m(x)}{x^2}, \text{ and } \quad \lambda_2(x) = 1 - \frac{d}{dx}\left[\frac{m(x)}{x}\right]. \tag{3.20}$$

This means that the position of tangential critical curves is sensistive to the total mass of the lens, while that of radial critical curves is sensitive to the slope thereof.

Point Lens

For a point lens with mass M, the surface density and the convergence are almost everywhere zero. It follows that the deflection angle takes the simple form $\alpha(x) = x^{-1}$, when the (arbitrary) scale length on the lens plane is set to

$$\xi_0 = \sqrt{\frac{M}{\pi\Sigma_\mathrm{c}}}. \tag{3.21}$$

Therefore, the strength of the deflection decreases linearly with distance from the central point lens. As announced, the convergence vanishes, while the shear reads $\gamma(x) = x^{-2}$

The absence of convergence implies that the radial eigenvalue is always positive, therefore there is no radial critical line. Conversely, the tangential critical line always exists and is parametrised by the circle $x^2 = 1$. Note that the existence of a critical line is consistent with the sufficient condition given in the previous section. As a matter of fact, a point mass has infinite density at the origin, hence it has one point on the lens plane at which the convergence is larger than unity.

The magnification for the Schwarzschild lens finally reads

$$\mu(x) = \frac{x^4}{x^4 - 1}. \tag{3.22}$$

Singular Isothermal Sphere

For the SIS density profile of Eq. (2.48), the convergence reads, in terms of physical coordinates, as

$$\kappa(\xi) = \frac{\sigma^2}{2G\Sigma_\mathrm{c}\xi}. \tag{3.23}$$

By choosing the length scale on the lens plane as

$$\xi_0 = \frac{\sigma^2}{2G\Sigma_\mathrm{c}}, \tag{3.24}$$

we reduce to the simple function $\kappa(x) = x^{-1}$. It follows that the deflection angle is constant, $\alpha(x) = 2$ and the shear can be calculated as $\gamma(x) = x^{-1} = \kappa(x)$. As a consequence, the radial eigenvalue is always unity, therefore no radial critical line exists. On the other hand, the tangential critical line always exists, and it is parametrised by the circle $x^2 = 4$.

The magnification can be written in this case as

$$\mu(x) = \frac{x}{x - 2}. \tag{3.25}$$

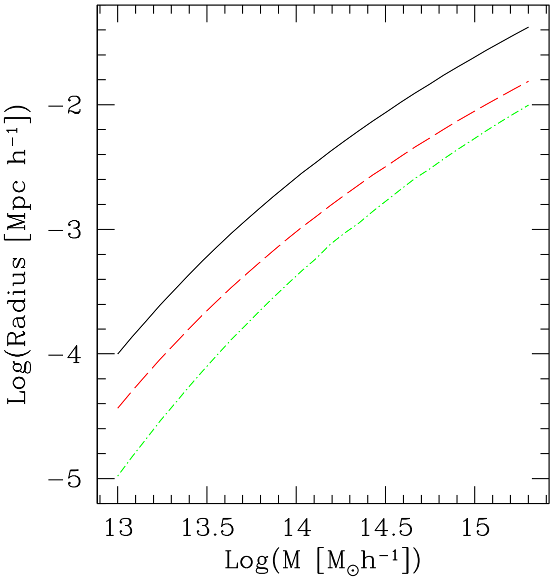

Figure 3.1: The radius of the tangential critical curve (black solid line), of the radial critical curve (red dashed line) and of the radial caustic (green dot-dashed line) for an NFW lens placed at redshift 0.3 with sources placed at redshift 1. The background cosmology is the ΛCDM model detailed before.

Universal Dark-matter Halo Profile

Things get more complicated for a NFW density profile lens Eq. (2.42), whose lensing properties have been illustrated for the first time in Bartelmann (1996) (see also Keeton 2001a). It turns out that, using dimensionless coordinates on the lens and source planes with $\xi_0 = r_\mathrm{s}$, the convergence can be written as

$$\kappa(x) = \frac{2\rho_\mathrm{s} r_\mathrm{s}}{\Sigma_\mathrm{c}} \frac{f(x)}{x^2 - 1}, \tag{3.26}$$

where the function f is defined by

$$f(x) = \begin{cases} 1 - \frac{2}{\sqrt{x^2-1}} \arctan \sqrt{\frac{x-1}{x+1}} & \text{if } x > 1 \\ 0 & \text{if } x = 1 \\ 1 - \frac{2}{\sqrt{1-x^2}} \operatorname{arctanh} \sqrt{\frac{1-x}{1+x}} & \text{if } x < 1 \end{cases} . \tag{3.27}$$

Likewise, the magnitude of the deflection angle can be computed as

$$\alpha(x) = \frac{4\rho_\mathrm{s} r_\mathrm{s}}{\Sigma_\mathrm{c}} \frac{g(x)}{x}, \tag{3.28}$$

with

$$g(x) = \ln \frac{x}{2} + \begin{cases} \frac{2}{\sqrt{x^2-1}} \arctan \sqrt{\frac{x-1}{x+1}} & \text{if } x > 1 \\ 1 & \text{if } x = 1 \\ \frac{2}{\sqrt{1-x^2}} \operatorname{arctanh} \sqrt{\frac{1-x}{1+x}} & \text{if } x < 1 \end{cases} . \tag{3.29}$$

In this case both radial and tangential critical lines exist, and both are stable under small external shear perturbation from e.g. surrounding structure (Bartelmann, 1996). The radii of the NFW critical curves as a function of the halo mass are presented in Figure 3.1. The radius of the tangential caustic is not shown because it degenerates to a single point.

In Figure 3.2 a comparison between the convergence and the shear of a SIS and an NFW lens is shown. While the convergence of the SIS lens diverges as $\propto x^{-1}$ for small radii, the divergence of the NFW lens convergence is milder, $\propto -\ln x$ as a consequence of the flatter core in the 3-dimensional density profile. A similar trend is also recognised in the shear profile.

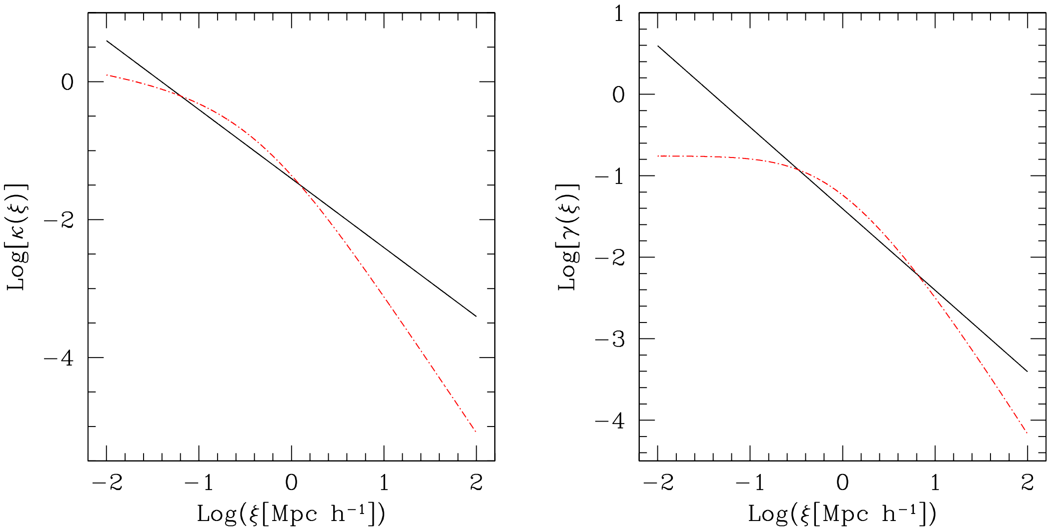

Figure 3.2: Convergence (left panel) and shear (rigt panel) for a gravitational lens with SIS (black solid line) and NFW (red dot-dashed line) density profile. The background cosmology is the ΛCDM model detailed before, while lens and source redshift are set to 0.3 and 1 respectively. The mass of the halos is set to be $10^{15} M_\odot h^{-1}$

3.4.2 Elliptical Models and Substructures

Axially symmetric models are useful for their simplicity, but they do not represent realistic astrophysical objects, that are usually rather irregular. Much better in this sense perform models with elliptical symmetry. Particular lens models with elliptical isodensity contours can be constructed (Schramm, 1990; Schneider et al., 1992; Schramm, 1994), however their implementation, and in particular the computation of the related deflection angle and lensing properties is somewhat cumbersome.

In this work an alternative approach has therefore been used, namely to introduce the ellipticity directly in the lensing potential (Blandford & Kochanek, 1987; Kochanek & Blandford, 1987). This has the drawback that the density distribution related to elliptical potential is not elliptical itself (tipically dumbbell shaped) for eccentricities significantly larger than zero (Kassiola & Kovner, 1993; Golse & Kneib, 2002; Meneghetti et al., 2003b). While this feature might be unwanted for galaxies, where the isophotes are rather regular ellipses, it is not a big matter of concern for GCs we are interested here. As a matter of fact, clusters are in general relatively young objects, mainly still in the process of formation. Therefore it is expected that their density distribution to be somewhat irregular.

The introduction of ellipticity into the lensing potential consists of the modification of the deflection angle components according to

$$\begin{aligned} \alpha_1^{(\mathrm{e})}(\boldsymbol{x}) &= \frac{x_1}{(1-e)X}\alpha(X), \\ \alpha_2^{(\mathrm{e})}(\boldsymbol{x}) &= \frac{x_2(1-e)}{X}\alpha(X), \end{aligned} \tag{3.30}$$

where e is the eccentricity of the isopotential contours, and the new variable X is defined as

$$X \equiv x\sqrt{\frac{1-e}{1+e}}. \tag{3.31}$$

It is quite obvious that for an axially symmetric model $e \to 0$, and the previous relations reduce to the circularly symmetric ones between the magnitude and the components of the deflection angle.

With the deflection angles at hand, the other lensing properties are readily computed. The critical curves and caustics for an NFW lens profile with elliptical lensing potential are shown for a few values of the ellipticity in Figure 3.3.

As can be seen, the radial critical curve tends to shrink when the eccentricity is increased, while the tangential critical curve is widely extended, making the production of higly distorted images more likely, as explained in Section 3.5. Also, the shape of the critical curves is highly non-elliptical, as a consequence of the fact that isodensity contours are dumbbell shaped. As for the tangential caustic, it goes from a point in the axially symmetric case to the typical diamond shape in the elliptical case, expanding more and more as the ellipticity of the isopotential contours is increased.

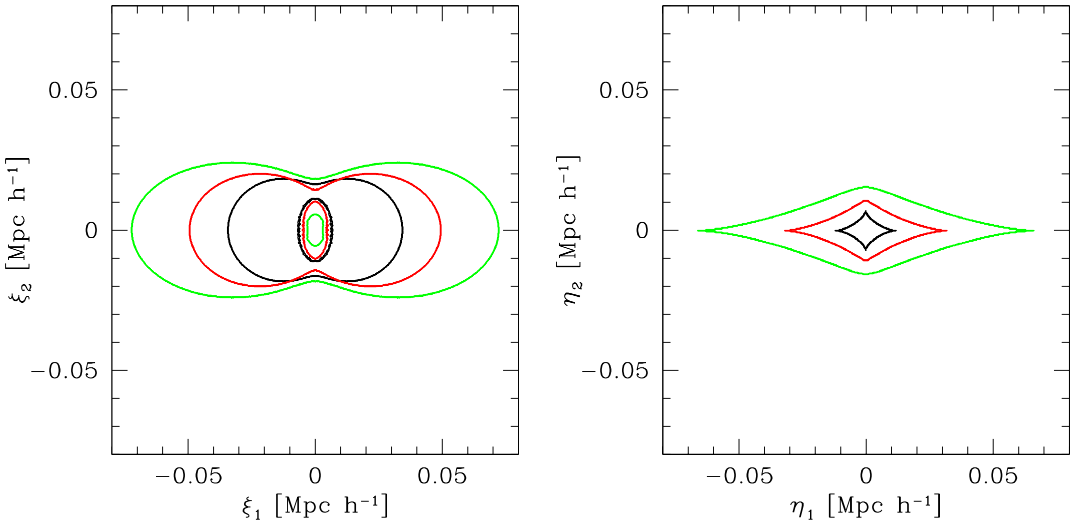

Figure 3.3: *Left panel*. The tangential (outer curves) and radial (inner curves) critical lines for an NFW gravitational lens with elliptical isopotential contours. The values of the eccentricity are 0.1 (black curve) 0.2 (red curve) and 0.3 (green curve). As costumary, the origin of the coordinate frame is coincident with the center of the lens. The mass of the lens is $10^{15} M_\odot h^{-1}$, and lens and source redshifts are 0.3 and 1 respectively. *Right panel*. The corresponding caustics. For clarity only tangential caustics are shown. The underlying cosmology is the ΛCDM model detailed in Table 2.1.

The reason for the increase in the length and extension of critical curves after increasing the eccentricity of the isopotential contours lies in the augmented shear field of the lens. Actually, it can be shown that the effect of ellipticity can be mimicked by an external shear (Narayan & Bartelmann 1996, see also Keeton et al. 1997). A similar effect happens when the lens is perturbed e.g. by a merging substructure (Torri et al., 2004). In this case however the increase in the shear field is accompanied by an increase in the surface density, and hence of the convergence, of the lens. The consequence is an even more acute distortion of the critical curves, as shown in Figure 3.4.

In more detail, when a substructure is approaching head-on a DM halo during a merger event, three characteristic regimes can be identified in the caustic structure of the lens. At first the caustics (and as a consequence the critical curves) are stretched towards each other, increasing in length. When the shear and convergence fields between the two objects are large enough the tangential caustics merge together to form a single very extended curve. Finally, the single caustic shrinks along the approaching direction and then expands isotropically due to the enhanced projected density.

A trace of these three characteristic moments will be found in the lensing efficiency of merging clusters in Section 4.2.2.

3.5 Arc Statistics

Gravitational arcs are among the most spectacular realizations of gravitational lensing. They are images highly distorted along one particular direction, and therefore they form in proximity of critical curves of the lens mapping. Even though arcs can be produced by lens galaxies, we will be exclusively interested here in arcs produced by GCs, and in particular on the total amount of arcs produced by the whole cluster population (*arc statistics*).

The sources that are lensed into arcs usually belong to a population of high-redshift galaxies that are bluer than the local ones, dubbed *faint blue galaxies* (Tyson, 1988; Ellis, 1997) Their surface density detectable with present ground-based telescopes is approximately of $30 - 50$ per square arcminute and the relevant redshift distribution for such a population of background galaxies will be presented in Section 5.3. Likewise critical lines and caustics, gravitational arcs are also divided in tangential and radial. Tangential critical curves are usually more extended than radial ones (see Figures 3.3 and 3.4 for instance), and therefore radial arcs appear much more rarely than tangential ones. Moreover, radial critical curves appear only in the very center of GCs, hence it is often likely that radial arcs are embedded in the light received from the Brightest Cluster Galaxy.

Gravitational arcs are usually classified using some kind of morphological property, like the curvature radius, the length or the width. In this thesis we shall conform to the common use and classify arcs according to their

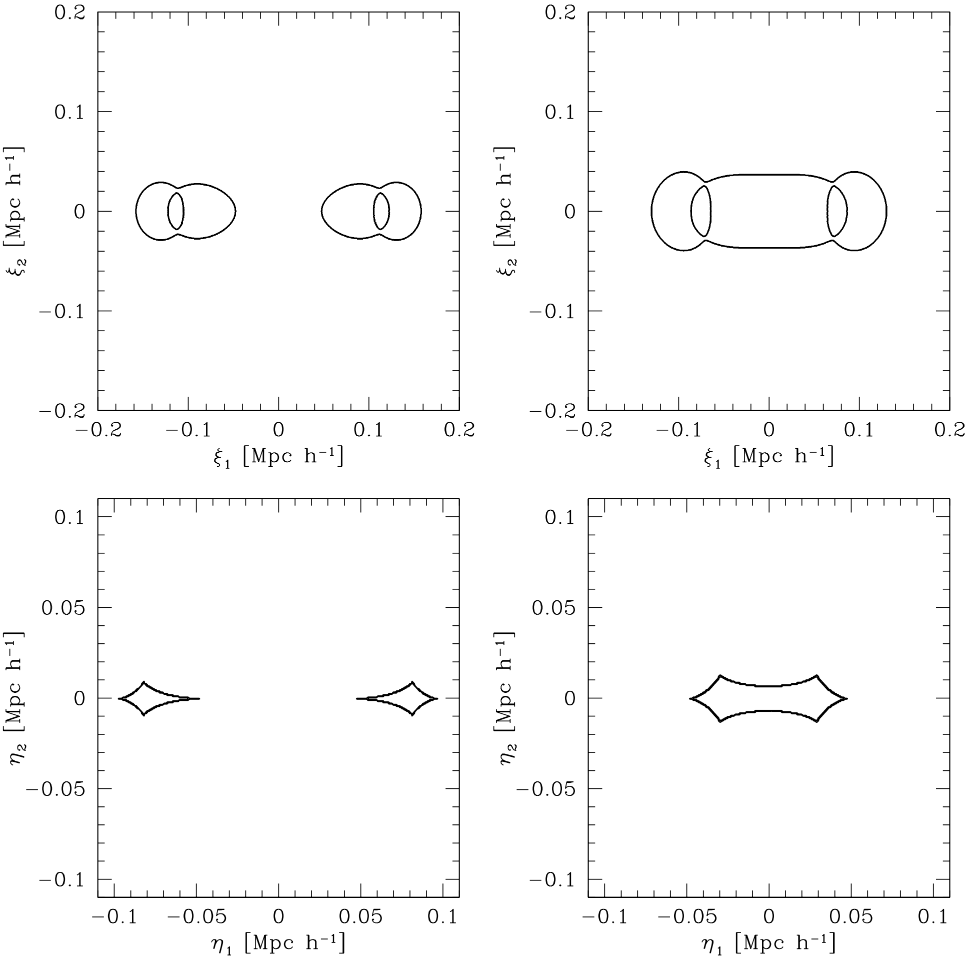

Figure 3.4: *Upper panels.* The radial and tangential critical curves for two axially symmetric NFW density profiles of mass $10^{15} M_{\odot} h^{-1}$ each in the ΛCDM cosmological model. The lens redshift is 0.3 and the source redshift is at 1. In the left panel the distance between the centers of the profiles is 300 kpc h^{-1}, while in the right panel it is 200 kpc h^{-1}. *Lower panels.* As in the upper panels but shown are the caustics on the source plane. Radial caustics are omitted for clarity.

length-to-width ratio. The measurements of this quantity on astronomical images is usually not an easy task, since it depends on the depth of the image and often tangential arcs are not even resolved in the radial direction (Section 3.6).

Given the discussion above, it is quite intuitive that the size of the critical curves is directly related to the probability of a GC for the production of long and thin arcs. In turn, the size of the critical curves depends mainly on two factors that shall be mentioned in the following.

First of all, the extension of critical lines depends on the internal structure of the lens. If the density profile of the deflector is more concentrated then the critical curves will be pushed outwards, and hence their length will increase. Also, the asymmetry in the density distribution and the presence of clumpiness and substructure tend to increase both the shear and the convergence fields of the lens (Section 3.4.2), and hence to render easier the production of long caustics. Needless to say, the internal structure of GCs depends ultimately on underlying cosmology and on the content of the Universe. Dynamical DE (Chapter 5) and increased normalization σ_8 (Chapter 8) shift the structure formation at higher redshift (see Figure 2.2 and related discussion), causing GCs to have more time to relax and reach higher concentrations. Also, the amount and rate of interactions with substructures can be significantly changed.

Secondly, the length of lensing caustics depends on the relative position of sources, lens and observer. As explained in Section 3.3, when the deflector is placed too close to the sources or to the observer, the critical surface density tends to increase indefinitely. Therefore the light cannot be deflected efficiently, and the critical curves shrink or disappear. Given the source position with respect to the observer, only in a reduced redshift range, approximately half the way from the observer to the source, will the deflector be highly efficient and have the possibility to produce strong lensing events.

Besides the properties of individual deflectors, the total number of arcs produced in the sky depends also on the statistical properties of the source and cluster population. The first is characterised by the redshift distribution of the faint blue galaxy population. The latter is instead defined by the mass function and the merger rate, that depend deeply on the underlying cosmology as the length of the critical curves does. By putting the various pieces together, it turns out that arc statistics is correlated in a highly non-linear way to the structure formation paradigm and to the value of the cosmological parameters.

Given this, a number of definitions are given in order to better quantify arc statistics and to understand the various different contributions to it. The first one is the *cross section* of a GC for images with a property q, for instance to have a length-to-width ratio larger than some threshold d. It is defined as the area σ_q of the region in the source plane (at a given fixed redshift z_s) where a source has to be in order to produce at least one image with property q. For gravitational arcs, this region will be realistically some sort of stripe surrounding the caustic curves. The ratio between the cross section and the total area of the source sphere $4\pi D_\mathrm{s}^2$ obviously gives the probability that the GC at hand host at least one image with the property q. The cross section encapsulates the effect on arc statistics of the internal properties of the deflector like density profile, asymmetry, substructures and so forth, and of the sources, like their intrinsic shape.

The probability of producing images with the property q in the whole cluster population is given by the sum of the cross section of the individual GCs normalised to the area of the entire source sphere and weighted by their relative abundance. This is summarised by the *optical depth*

$$\tau_q(z_\mathrm{s}) \equiv \frac{1}{4\pi D_\mathrm{s}^2}\int_0^{z_\mathrm{s}}\int_0^{+\infty} N(M,z)\sigma_q(M,z)dMdz. \tag{3.32}$$

The redshift integral obviously extends only up to the source redshift, and the function $N(M,z)$ represents the total number of structures present in the unit redshift around z and in the unit mass around M. It can be written in terms of the mass function Eq. (2.36) as

$$N(M,z) = \left|\frac{dV(z)}{dz}\right| n(M,z), \tag{3.33}$$

where $V(z)$ is the cosmic volume included in the sphere that extends up to redshift z around the observer. The function $N(M,z)$ expresses the contribution to arc statistics given by cluster abundance and formation history.

Next let us assume a redshift distribution for the background source population, indicated by $p(z_\mathrm{s})$. Then, the total number of images with property q that are produced by the cluster population reads

$$N_q = n_\mathrm{s}\bar{\tau} \equiv n_\mathrm{s}\int_0^{+\infty} p(z_\mathrm{s})\tau_q(z_\mathrm{s})dz_\mathrm{s}, \tag{3.34}$$

where n_s is the total number of sources present in the entire sky at all redshifts, and $\bar{\tau}$ is the *average optical depth*. In the particular case where all the sources are at one and the same redshift $z_{\mathrm{s},*}$, then the previous equation reduces to

$$N_q = n_\mathrm{s}\tau_q(z_{\mathrm{s},*}). \tag{3.35}$$

The source redshift distribution $p(z_\mathrm{s})$ contains statistical information about the sources, which is the last piece of information needed.

Given the large number of different effects that play a role on the statistics of strong lensing events, it is difficult to disentangle the various contributions and to understand which one is dominant. Part of the work present in the literature and directed toward this goal is described in the next Section. Additional resuts in this direction are part of this thesis, and will be detailed in the susequent Chapters.

3.6 Current Observational Status

3.6.1 Strong Lensing

The discovery of the first strong lensing event dates back to Walsh et al. (1979), a quasar multiply imaged by a lens galaxy. As for gravitational arcs in GCs, the main subject of this work, the first ones were discovered in Cl2244-02 by Lynds & Petrosian (1986) and A 370 by Soucail et al. (1987). As expalined in Section 3.5, single gravitational arcs are tracers for the position of the critical curves in GCs, therefore they bring a wealth of information about their internal structure. One of the most significant, especially in relation with the discussion in Section 2.5 is that the density profile of GCs displaying tangential and radial arcs must be steep (Hammer & Rigaut, 1989). This is an immediate consequence of the fact that usually tangential arcs are very thin, and often not even resolved, in the radial direction. Therefore, the radial magnification at the position of the tangential critical line, that can be written as $1/2(1-\kappa)$ must be very small. As a consequence we must have $\kappa \ll 1$ at the approximate position of the tangential critical curve. But if also radial arcs are present, at their position $\kappa = 1+\gamma \geq 1$ must hold, implying that the surface density profile must be steep enough.

Coming now to the statistics of long and thin arcs, at the moment only few, rather old searches for such events in statistically complete GC samples exist in the literature (Le Fevre et al., 1994; Gioia & Luppino, 1994; Gioia et al., 1996; Luppino et al., 1999). This is mainly due to the lack of automatic detection algorithms for gravitational arcs. Such algorithms are becoming available in recent years, (see Section 6.6 for some references) and their application to large area optical and infrared surveys will be of fundamental importance.

According to the results of Gioia & Luppino (1994), who used GCs selected in the X-ray band, the number of arcs with ratio between length and width larger than $d = 10$ and B-band magnitude less than 22.5 (corresponding to R-band magnitude less than 21.5, so called *giant arcs*, Wu & Hammer 1993) is about $0.2 - 0.3$ per cluster. Extrapolating this number to the entire cluster population would mean a total number of giant arcs $\sim 10^3$. On the other hand, theoretical investigations performed using numerically simulated DM halos as lenses in a flat universe dominated by the cosmological constant predict a number of arcs that is about one order of magnitude smaller (Bartelmann et al., 1998; Li et al., 2005). In addition to that, recent analysis of high-redshift clusters (Gladders et al., 2003; Zaritsky & Gonzalez, 2003) revealed an unexpectedly high incidence of long and thin arcs, though the samples used are not complete and made of a relatively low number of clusters. This fact remains however difficult to explain in the framework of the standard cosmological model.

The discrepancy between the observed and the predicted abundance of long and thin arcs, dubbed arc statistics problem, hints to some important piece of cluster physics that has not been taken into account. The results from Bartelmann et al. (1998) therefore boosted a variety of works to explain the lack of arcs in theoretical models and to understand which of the various contribution to arc statistics explored in Section 3.5 is the most relevant and not properly modeled. Among the various effects studied, it was found that the finer details of GCs, like individual galaxies and in particular the presence of a Brightest Cluster Galaxy have little influence on the strong lensing efficiency (Flores et al., 2000; Meneghetti et al., 2000, 2003a). Vice versa, the impact of mergers with substructures is potentially highly important for the global arc counts, as was shown in Torri et al. (2004) on single GCs and as naively expected from the discussion in Section 3.4.2. A major part of this thesis consists in quantifying this effect on the entire cluster population, and therefore we refer to the following Chapters for further detail. Also, the ICM can have some effect on the cross section of single deflectors, even though probably this is limited to a factor of a few (Puchwein et al., 2005). As a matter of fact, despite the evidence that the formation and evolution of GCs is mainly driven by DM, the presence of gas can subsequently modify the structural properties of clusters in the very inner regions, the most relevant for strong lensing.

In summary it is not yet certain if the arc statistics problem is solved by the introduction of all the aforementioned effects. One certain thing is that the low value of the normalization for the linear power spectrum measured by WMAP-3 data (Section 2.5) tends to make the situation worse, since it reduces the abundance of GCs and hence of potential strong lenses. Chapter 8 is dedicated to quantify the arc statistics problem in dependence of the value of σ_8. To conclude we also note that the inclusion of dynamical forms of DE in the cosmic fluid can have a potentially significant effect on cluster abundance and merger rate, i.e. on the strong lensing statistics (Meneghetti et al., 2005b). This issue will be further explored in Chapter 5.

3.6.2 Weak Lensing

The weak gravitational lensing regime is characterised by $\kappa \ll 1$ and $\gamma \ll 1$. In this regime it is not possible to use the information on the distortion of one single image, rather the average distortion of many different images must be computed, giving a proxy for the shear field and hence for the convergence of the deflector. The number density of images with measured ellipticity required to have a decent distortion signal is rather high, of the order on few tenths per arcminute squared. Consequently, only in very recent years weak lensing tecniques could be fully developed.

Weak lensing can be used for the non-parametric reconstruction of the mass distribution of e.g. GCs and early algorithms suited to this purpose date back to Kaiser et al. (1995). Algorithms of this kind suffer from an intrinsic degeneracy, called the *mass-sheet degeneracy*, due to the fact that a given distortion pattern determines the lens' convergence map only up to a linear transformation. As a consequence, while the general shape of the projected density profile can be reconstructed, the normalization cannot. Fortunately, solutions to this problem exist, both combining the distortion with the magnification information, or complementing the weak lensing analysis with strong lensing data (Bradač et al., 2005, 2006; Cacciato et al., 2006).

The combination of weak and strong lensing measurements is particularly useful for the reconstruction of the

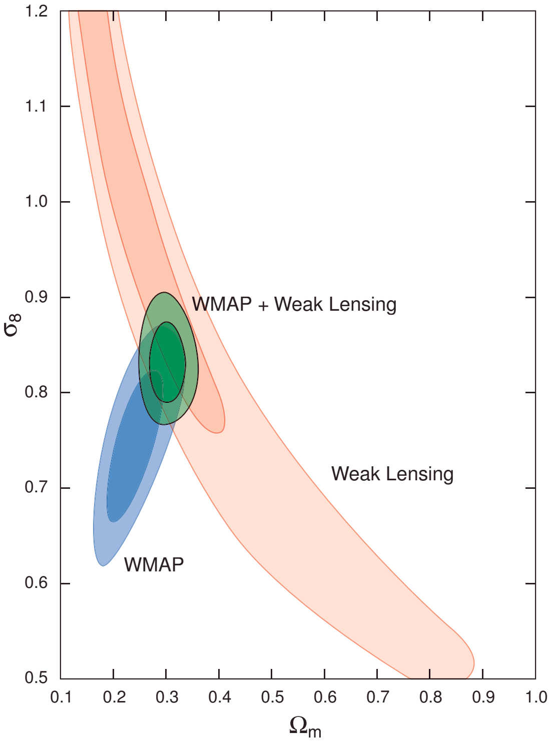

Figure 3.5: Marginalised 68% and 95% confidence levels in the $\Omega_{\mathrm{m},0} - \sigma_8$ plane. Blue dashed regions indicate the constraints from the WMAP-3 data release, the pink ones those from the Canada-France-Hawaii Telescope Lensing Survey and the green ones are the combination of the two, as labelled in the plot (Spergel et al., 2007).

mass distribution in GCs. As a matter of fact, all weak lensing inversion algorithms mainly work in the outskirts of GCs, while they break down in the very center of clusters that display strong lensing features like long and thin arcs. Therefore, the combination of results from both techniques allows to probe efficiently both small and large radii, hence being an ideal tool for recovering the overall mass distribution of GCs.

Finally, weak lensing from the large scale structure can be used to put constraints on the matter distribution, complementary to big optical surveys that use galaxies as tracers. By studying the 2-point correletion function of the ellipticity of faint blue galaxies it is possible to gain information about the 2-dimensional distribution of matter in the large scale structure (*cosmic shear*, Mellier 1999). Also, information on the 3-dimensional distribution of DM can be obtained by using images of sources at different redshifts. Since the lensing signal is strong enough only in a relatively narrow range about half the way between the observer and the sources themselves, this allow one to probe the large scale structure at different redshifts (*weak lensing tomography*, Hu 1999). It is also important to stress that the weak lensing reconstruction of the large scale structure does not require to make assumptions about e.g. the bias between galaxies and DM distribution.

In Figure 3.5 the cosmic shear constraints on the matter density parameter today $\Omega_{\mathrm{m},0}$ and the normalization of the primordial power spectrum of density fluctuations σ_8 are shown, together with the constraints coming from the third year data release of WMAP. It is evident that the results from weak lensing surveys are in slight tension with CMB data, in the sense that the first tend to prefer a higher value of normalization than the second. In this sense, weak lensing data are in better agreement with the cluster abundance estimates (Section 2.5).

Chapter 4

A Fast Method for Computing Strong Lensing Cross Sections: Application to Merging Clusters

4.1 Introduction

Strong gravitational lensing by GCs is a highly non-linear effect that is very sensitive to the details of lensing mass distribution. As explained in Section 3.5, the cluster core densities, the asymmetries of their mass distribution, their substructures, and their close neighbourhoods all contribute to their lensing properties. The ongoing debate about whether the observed statistics of arcs is or is not compatible with the expectations in the standard cosmological model shows that we do not sufficiently understand yet what aspects of the source and cluster populations as a whole determine the statistics of its strong-lensing effects (see Section 3.6 and Wambsganss et al. 2004; Dalal et al. 2004; Hennawi et al. 2007)

It is an obstacle for theoretical, as well as observational, studies that the cross sections of GCs for strong lensing are costly to compute. So far, they require highly-resolved simulations tracing large numbers of light rays through realistically simulated cluster mass distributions, used for finding the images of sources that need to be classified automatically (Miralda-Escude, 1993; Bartelmann & Weiss, 1994). This needs to be done often, i.e. for different cosmological models and for many clusters in large cosmological volumes seen with many different angles, for the results to reach a reliable level. The fact that the enhanced tidal and density fields around merging clusters substantially enhance strong-lensing cross sections (Torri et al. 2004 and Section 3.4.2) adds the necessity to study clusters with a time resolution that is sufficiently fine to resolve cluster merger events.

The increasing demands to be met by reliable strong-lensing calculations and the desire to carry them out for varying cosmological models call for a substantially faster and equally reliable method than ray-tracing. We develop such a method in this Chapter. It is based on the fact that highly elongated arcs occur near the critical curves in the lens plane and that imaging properties near critical curves can be summarised by the eigenvalues of the Jacobian matrix of the lens mapping (see Schneider et al. 1992 and Chapter 3 for detail). This allows the cross section calculation to be reduced to an area integral to be carried out on the lens plane itself. In that sense, the method is analytic, but the irregular shapes of the integration domains require it be carried out numerically. Since the eigenvalues of the Jacobian matrix ideally describe imaging properties for infinitesimally small, circular sources, the method needs to be supplemented by techniques for taking extended, elliptical sources into account without losing computational speed.

4.2 Lensing Cross Sections

So far, the most reliable method for calculating cross sections for long and thin arcs has been using fully numerical ray-tracing simulations. If performed adequately, such simulations return realistic cross sections, but with the disadvantage of being very expensive in computational time. In view of cosmological applications, the mass and redshift ranges to be covered are large, in particular because the temporal sampling needs to be dense to properly resolve cluster merger events. The number of cross sections to be calculated can thus be very large. A reliable alternative to the costly ray-tracing simulations is therefore needed. We develop here a semi-analytic method that reproduces well fully numerical lensing cross sections, while lowering the computational cost by factors of ~ 30.

We believe this method provides an elegant alternative to ray-tracing simulations for many applications of lensing statistics.

In the following subsections, we shall first describe the fully numerical method for reference, and then the semi-analytic method.

4.2.1 Ray-tracing Simulations

Given the lensing mass distribution, which can be given as either an analytic density profile or a simulated density map, and the statistical properties of the source sample, strong lensing cross sections are commonly estimated by using fully numerical ray-tracing simulations. The method we use here was first described by Miralda-Escude (1993) and further developed and adapted to asymmetric, numerical lens models by Bartelmann & Weiss (1994). It has been widely used by Meneghetti et al. (2000, 2003b) and, with several modifications, by Puchwein et al. (2005). We only address its main features here, referring the interested reader to their papers and the references.

Briefly, a bundle of $n \times n$ light rays ($n = 2048$ here) with an opening angle β is sent from the observer through the lens. The opening angle depends on the lens' properties and the distances involved, and it must be large enough to encompass the entire region on the lens plane where strong lensing events may occur. The deflection angle is calculated from the surface-mass distribution at all points where light rays intersect the lens plane, thus allowing each ray to be propagated back to the source plane by means of the lens Eq. (3.11).

A set of sources is then placed on a regular and adaptive grid on the source plane. The sources are modelled as ellipses whose orientation angles and axis ratios (minor to major) are randomly drawn from the intervals $[0, \pi]$ and $[0.5, 1]$, respectively, with the prescription that each source has the area of a circle with a 1 arcsecond diameter. The source-grid resolution is iteratively increased near the caustics, i.e. where the magnification of the related images is highest and undergoes rapid variations. This artificial increase in the probability of strong lensing events must be corrected when calculating cross sections. We do so by assigning a statistical weight to each source that is proportional to the area of the grid cell it represents.

The images of each source are found by identifying all rays of the bundle falling into the source. Simple geometrical shapes (ellipses, rectangles, and rings) are then fit to all images, and their characteristics (length, width, curvature radius, etc.) are determined. When an image has the property we are interested in (i.e. a length-to-width ratio equal to or greater than some value d), we increment the cross section by the pixel area of the source grid, times its statistical weight.

4.2.2 Semi-analytic Method

Point Sources

We aim at determining cross sections for the formation of gravitational arcs with a length-to-width ratio that exceeds some fixed threshold d. Initially assuming infinitesimal (or point-like) sources, the discussion in Section 3.3 implies that such arcs will form where the ratio

$$\Pi(\boldsymbol{x}) \equiv \max\left[\left|\frac{\lambda_2(\boldsymbol{x})}{\lambda_1(\boldsymbol{x})}\right|, \left|\frac{\lambda_1(\boldsymbol{x})}{\lambda_2(\boldsymbol{x})}\right|\right] \tag{4.1}$$

between the eigenvalues of the lens mapping satisfies

$$\Pi(\boldsymbol{x}) \geq d \; . \tag{4.2}$$

We denote this region by $B_\mathrm{l} = B_\mathrm{l}(d)$. By means of the lens equation, B_l can be mapped onto an equivalent region $B_\mathrm{s} = B_\mathrm{s}(d)$ on the source plane, whose area is by definition (see Section 3.5) the cross section σ_d we are searching for. Thus,

$$\sigma_d = \int_{B_\mathrm{s}} d^2\eta = \eta_0^2 \int_{B_\mathrm{s}} d^2y \; . \tag{4.3}$$

The lens equation then maps the infinitesimal area element on the lens plane to the one on the source plane by means of the Jacobian determinant $\det \mathcal{A}(\boldsymbol{x})$, thus

$$\sigma_d = \eta_0^2 \int_{B_\mathrm{l}} |\det \mathcal{A}(\boldsymbol{x})| d^2\boldsymbol{x} = \eta_0^2 \int_{B_\mathrm{l}} \frac{d^2\boldsymbol{x}}{|\mu(\boldsymbol{x})|} \; , \tag{4.4}$$

where Eq. (3.18) was used.

Extended Circular Sources

Although this line of reasoning is exact, it fails to reproduce simulated cross sections, for it does not account for real sources (and also the sources used in ray-tracing simulations) not being point-like. Extended sources are much more likely to produce strongly distorted images than point-like sources, and their imaging properties will only be approximated by the eigenvalue ratio $\Pi(\boldsymbol{x})$. This implies that the integral in Eq. (4.4) has to be extended beyond the region $B_{\rm l}$, because an extended source can produce a long and thin arc even if it is centred where the eigenvalue ratio is less than d.

By introducing extended sources into the framework just outlined, we wish to convolve the eigenvalue ratio $\Pi(\boldsymbol{x})$ on the lens plane with a suitable function to be determined that significantly differs from zero only on the image of an extended source. For consistency with ray-tracing simulations, we assume circular sources with radius $\beta_{\rm s} = 0.5''$ for now. Effects of source ellipticities will be included later.

The obvious problem with this approach is that the properties of the image vary wildly across the lens plane, thus the convolution should use a function which rapidly changes shape and extent across the lens plane. We can avoid this problem by transferring the calculations to the source plane. We first introduce the eigenvalue ratio on the source plane. Since multiple points $\boldsymbol{x}_i$ on the lens plane may be mapped onto a single point $\boldsymbol{y}$ on the source plane, we define it as $\bar{\Pi}(\boldsymbol{y}) \equiv \max\{\Pi[\boldsymbol{y}(\boldsymbol{x}_i)]\}$. This ratio $\bar{\Pi}(\boldsymbol{y})$ is then convolved with a function $g(\boldsymbol{y})$ that differs significantly from zero only on the circular area covered by a source, that is the same everywhere on the source plane. Let the convolution in the source plane be $\bar{h}(\boldsymbol{y}) \equiv \bar{\Pi}(\boldsymbol{y}) * g(\boldsymbol{y})$; then we put $h(\boldsymbol{x}) = \bar{h}[\boldsymbol{y}(\boldsymbol{x})]$ to obtain the convolved function on the lens plane, as desired. Again, we need to take into account that single points on the source plane may be mapped on multiple points in the lens plane. Assigning $\Pi(\boldsymbol{x})$ to $\bar{\Pi}[\boldsymbol{y}(\boldsymbol{x})]$ now sets the convolved length-to-width ratio equal on all image points, which may not be exact, but is a tolerable error. The problem is now reduced to carrying out the convolution $\bar{h}(\boldsymbol{y})$, as discussed in Section 4.6. As described there, we speed up the convolution by approximating it with a simple multiplication after essentially assuming that the eigenvalues of the lens mapping and their ratio do not change significantly across a single source.

Finally, what form should be chosen for the function $g(\boldsymbol{y})$? A two-dimensional Gaussian of width $\beta_{\rm s}$ may appear intuitive, but the ray-tracing simulations we use for reference do not adopt a surface-brightness profile for sources because they simply bundle all rays falling into the ellipse representing a source. Thus, a choice for g consistent with the ray-tracing simulations is a step function with width $\beta_{\rm s}$,

$$g(\boldsymbol{y}) = \begin{cases} (\pi\beta_{\rm s}^2)^{-1} & \text{where} \quad \boldsymbol{y}^T\mathcal{B}\boldsymbol{y} \le 1 \\ 0 \quad \text{else} & \end{cases} \quad , \tag{4.5}$$

where $\mathcal{B}$ is a matrix describing the shape of the source. Since we are only considering circular sources of radius $\beta_{\rm s}$, $\mathcal{B}$ has the form $\mathcal{B} = \mathcal{I}/\beta_{\rm s}^2$, where $\mathcal{I}$ is the unit matrix. The factor $(\pi\beta_{\rm s}^2)^{-1}$ in (4.5) normalises $g(\boldsymbol{y})$ to unity. Substituting $h(\boldsymbol{x})$ for $\Pi(\boldsymbol{x})$, we can again apply the condition in Eq. (4.2) to obtain a new region $B_{\rm l}$ that will now of course be larger than before.

Extended Elliptical Sources

We finally have to account for elliptical rather than circular sources. It is quite obvious, and was shown by many authors (e.g. Bartelmann et al. 1995; Keeton 2001b), that elliptical sources are more likely to produce strongly distorted images.

Here we adopt the simple and elegant formalism by Keeton (2001b). He shows that an elliptical source at position $\boldsymbol{y}(\boldsymbol{x})$ with axis ratio $q_{\rm s} = a/b = q_{\rm s}[\boldsymbol{y}(\boldsymbol{x})]$ and orientation angle $\theta = \theta[\boldsymbol{y}(\boldsymbol{x})]$ is imaged as an allipse with an axis ratio of

$$q_{\rm obs} = \sqrt{\frac{T + \sqrt{T^2 - 4D}}{T - \sqrt{T^2 - 4D}}} \tag{4.6}$$

where T and D are the trace and the determinant of the matrix that describes the image ellipse. They can be expressed as functions of the intrinsic source properties and of the (convolved) lensing distortion:

$$T = h^2 + q_{\rm s}^2 + (h^2 - 1)(q_{\rm s}^2 - 1)\cos^2\theta \; , \quad D = h^2 q_{\rm s}^2 \; . \tag{4.7}$$

Again, $h(\boldsymbol{x})$ can be replaced by $q_{\rm obs}(\boldsymbol{x})$ to obtain a modification of the region $B_{\rm l}$, once again larger than before, whose area is now a close approximation of the cross section we seek to determine, accounting for extended and elliptical sources.

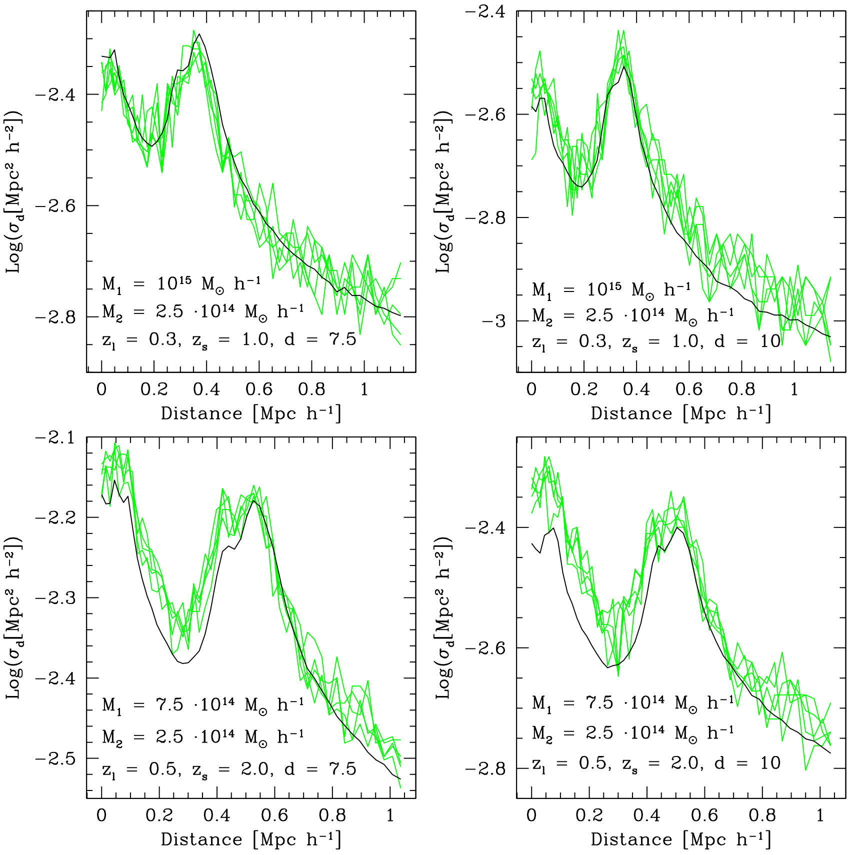

Figure 4.1: Lensing cross sections for long and thin arcs with a length-to-width ratio exceeding d as a function of the distance between the centres of two DM halos, for two (lens and source) redshifts. The halos are modelled as NFW density profiles with elliptically distorted lensing potential with eccentricity $e = 0.3$ (see Section 3.4.2). Green lines show the results of ray-tracing simulations for five different realisations of the random source distribution. Black lines are the results obtained with our semi-analytic method.

Comparison to Ray-tracing

As a final step, we test the accuracy of our calculations and approximations, especially those concerning the replacement of the convolution by a multiplication (cf. Section 4.6), by comparing lensing cross sections obtained with the semi-analytic method to their fully numerical counterparts obtained by ray-tracing. Since the main purpose of this Chapter is to estimate the effects of cluster mergers, we compare the cross sections as they evolve while two DM halos merge. The halos are modelled as NFW profiles, Eq. (2.42), whose lensing potential is elliptically distorted to have eccentricity $e = 0.3$ (see Section 3.4.2 for detail). The results of the comparison are shown in Figure 4.1 for various masses, redshifts, and thresholds d.

The ray-tracing simulation was repeated five times for each modelled merger event, each time changing the seed for the random generation of source ellipticities and orientations. As the Figure shows, this has quite a significant effect on the numerical cross sections, by causing a substantial scatter. The reason is fairly easy to understand. When a given source produces an arc, variations in the source's intrinsic ellipticity and in the orientation with respect to the caustic structure can easily push the length-to-width ratio of the image arc below or above the chosen threshold d. This causes the irregular trend seen in Figure 4.1. It is worth noting that the same problem showed also affect the semi-analytic results. In this case, however, ellipticity and orientation are assigned to each ray traced back through the lens plane simply to identify the extended region over which we integrate. Since the number of rays is much larger than the number of individual sources used in the fully numerical algorithm, the random scatter in the semi-analytic results is very small. In fact, the fluctuations are close enough to the width of the black curve to be omitted.

Moreover, it must be noted that the results given by the ray-tracing code we use might differ slightly from other codes using different resolution, different image finding algorithms, and different ways to fit the image shapes.

We can draw two interesting conclusions from Figure 4.1. The first is that, reassuringly, the numerical and the semi-analytic cross section agree excellently. This means that the approximations we made are substantially

Table 4.1: Present-day masses and virial radii for the three most massive and the three least massive halos in our sample.

Halo Id.	Virial Mass $[h^{-1}\, M_\odot]$	Virial Radius $[h^{-1}\,\mathrm{Mpc}]$
g8-a	2.289×10^{15}	2.146
g1-a	1.530×10^{15}	1.876
g72-a	1.374×10^{15}	1.810
g696-y	5.219×10^{13}	0.608
g696-z	5.171×10^{13}	0.607
g696-#	5.060×10^{13}	0.602

correct. There is, however, a small discrepancy for higher-redshift sources, as shown in the lower panels. We believe that this discrepancy is due to the fact that the scale over which the lensing properties on the source plane change significantly is in this case comparable to the source dimension; hence one of the approximations we made in Section 4.6 fails, namely that the function $\Pi[\boldsymbol{y}(\boldsymbol{x})]$ does not vary much across a source. Nonetheless, the discrepancy is no where larger than 20%, which is more than acceptable for our purposes, especially in view of the considerable scatter in the ray-tracing results.

The second observation is that the behaviour of the cross sections (both numerical and semi-analytic) as a function of the distance between the halos closely reflects that found by Torri et al. (2004) and described in Section 3.4.2. Namely, while the substructure is swallowed by the main halo, (i) there is a first peak in the lensing cross section when the increasing shear field between the lumps causes the critical lines to merge (see Figure 3.4), (ii) a local minimum while cusps disappear in the caustic branches, and (iii) another peak caused by the increased convergence when the two density profiles overlap. All these features are recovered in the panels of Figure 4.1.

This level of agreement between ray-tracing and semi-analytic cross sections shows that the semi-analytic method developed above for cross section calculations is essentially correct and constitutes a valid and useful, ~ 30 times faster, alternative to the costly ray-tracing simulations.

4.3 Lensing Optical Depth

Given reliable lensing cross sections, lensing optical depths need to be determined. In the present Chapter it shall be assumed that all sources are at one and the same redshift, therefore the use of Eq. (3.32) is sufficient. For that purpose, we use the merger trees for a set of 46 numerically simulated DM halos, whose main properties are described in the next subsection. The merger tree of a DM halo provides two types of information. First, we know how the mass of each halo evolves with time or redshift. Second, we know at which redshift merger events happen with substructures of known mass. Regarding this, it is worth recalling that the evolution of a dark-matter halo is characterised by the continuous accretion of infalling external material. We account for all mergers in which the main halo accretes sub-halos with at least 5% of the main halo's mass. Nonetheless, it should be kept in mind that halos continuously accrete matter apart from merger events.

4.3.1 Halo Model

We base our study of the merger trees on a sample of 46 numerically simulated DM halos. These halos were re-simulations at higher resolution of a large-scale cosmological simulation. The cosmological model used was a standard model with a cosmological constant density parameter of $\Omega_{\Lambda,0} = 0.7$, a (dark) matter density parameter of $\Omega_{\mathrm{m},0} = 0.3$, and a Hubble constant of $h = 0.7$. The power spectrum of the primordial density fluctuations field is scale invariant (i.e. with a spectral index of $n = 1$), and the *rms* linear density fluctuations on a comoving scale of 8 Mpc h^{-1} is $\sigma_8 = 0.9$, which is the typical value required to match the local abundance of massive GCs (White et al. 1993; Eke et al. 1996 and Section 2.5). As explained, while this value agrees with the first-year WMAP data release it is in tension with WMAP-3 results. The mass of DM particles in the simulations is $m = 1.3 \times 10^9 M_\odot h^{-1}$. In Table 4.1 we list the present masses and virial radii for the three most massive and the three least massive halos in the sample.

The present masses of the halo models vary between about $5 \times 10^{13} M_\odot h^{-1}$ (barely exceeding the mass of a massive Brightest Cluster Galaxy) and more than $2 \times 10^{15} M_\odot h^{-1}$, which is characteristic of a rich GC.

We note in passing that, owing to the dependence of the cluster evolution history on cosmology, the typical redshift of the structure formation in the cosmological model used here is higher than in an Einstein-de Sitter universe, and lower than in an open low-density universe. Models of the DE component alternative to the cosmological constant typically shift this redshift towards higher redshifts, thus changing the contribution of cluster mergers to arc statistics. We refer to Chapter 5 for a study on this issue.

For specifically describing each individual merger process and its effects on gravitational arc statistics, we proceed in a similar way as in Figure 4.1, modeling each DM halo as NFW spheres, Eq. (2.42). We follow the prescription of Eke et al. (2001) for linking the virial mass of the halo to its concentration and in addition we adopt elliptically distorted lensing potentials as described in Section 3.4.2. In their work, Meneghetti et al. (2003b) also estimate the value of the eccentricity e for the lensing potential that produces the best fit to the deflection angle maps of simulated halos. Following their result, we adopt $e = 0.3$ throughout.

4.3.2 Modelling Halo Mergers

Once the redshift is fixed, the halo we consider may be isolated or may interact with a substructure. In the first case the deflection angle can be obtained directly by means of Eq. (3.28). In the second, we can sum the deflection angles of the two structures at each point on the lens plane, owing to the linearity of the problem (Schneider et al., 1992; Torri et al., 2004). In both cases, the eigenvalues of the local mapping follow from the deflection angle maps by differentiation, and can be applied in the semi-analytic method for calculating cross sections as described in Section 4.2.2.

Individual merger events are modelled as follows. The main halo and the substructure start at a mutual distance equal to the sum of their virial radii. Then the centres approach at a constant speed calculated by the ratio of the initial distance to the typical time scale of a merger event, i.e. 0.9 Gyr (Torri et al., 2004; Tormen et al., 2004). The process is assumed to be concluded when the two density profiles overlap perfectly. The direction of approach, always assumed to be perpendicular to the observer's line of sight, is parallel to the directions of the major axes of the lensing potential, which are also assumed to be parallel. This last assumption is justified by recent work (Lee et al., 2005; Hopkins et al., 2005) that points out, with both analytic models and numerical analyses, that there is an intrinsic alignment between a DM halo and the surrounding halos and sub-lumps due to the tidal field of the major halo itself. We note that assuming all mergers to proceed along directions perpendicular to the line-of-sight slightly *underestimates* the cumulative contribution of cluster mergers to the lensing optical depth, because if the merger direction is partially aligned with the line-of-sight, the time spent by the system in configurations leading to high cross sections is longer (see again Figure 4.1). Several tests we made show, however, that this underestimation is typically about 20%, thus we neglect it here and in the subsequent Chapters.

Once we know the cross section with and without the effect of mergers for each halo at every redshift, we can compute the optical depths for lensing. Since we sample the mass range discretely, we cannot apply Eq. (3.32) directly, but need to approximate it as

$$\tau_d(z_\mathrm{s}) = \frac{1}{4\pi D_\mathrm{s}^2} \int_0^{z_\mathrm{s}} \left[\sum_{i=1}^{n-1} \bar{\sigma}_{d,i}(z) \int_{M_i}^{M_{i+1}} N(M,z) dM \right] dz \ , \tag{4.8}$$

where the masses M_i ($1 \le i \neq n$) have to be sorted from the smallest to the largest at each redshift step, and the quantity $\bar{\sigma}_{d,i}(z)$ is defined as

$$\bar{\sigma}_{d,i}(z) = \frac{1}{2} \left[\sigma_d(M_i, z) + \sigma_d(M_{i+1}, z) \right] \ . \tag{4.9}$$

This is essentially equivalent to assigning the average cross section of the halos with masses M_i and M_{i+1} to all structures with mass within $[M_i, M_{i+1}]$, weighted with the number density of massive structures within that interval.

4.3.3 Mass Cut-off

Since a sufficient condition for strong lensing is satisfied once the surface density of a lens exceeds the critical density somewhere, any lens model with a cuspy density profile, such as the NFW profile, will formally be a strong lens and thus produce critical curves and caustics. However, the caustics of low-mass halos will be smaller than the typical source galaxies. Averaging the local distortion due to a low-mass lens across an extended source will then lead to a small or negligible total distortion. This implies that the mass necessary for halos to cause large arcs is bounded from below by the requirement that the halo's caustic must be sufficiently larger than the available sources.

This mass limit obviously depends on the lens and source redshifts due to the geometrical sensitivity of lensing. Higher masses are required at low and high redshifts for lensing effects comparable to lenses at intermediate

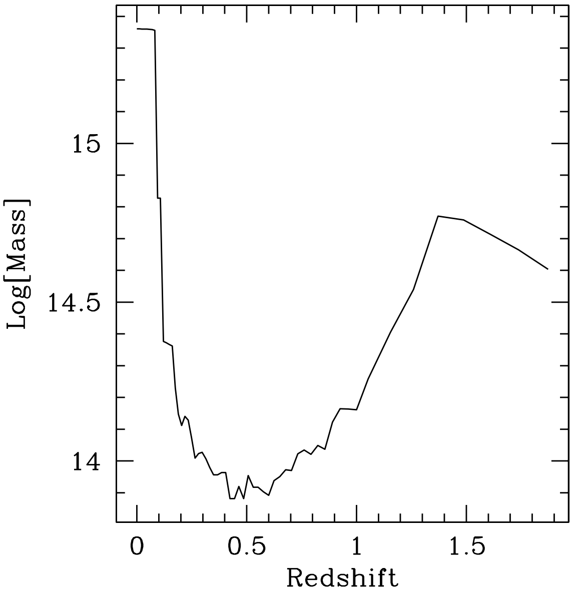

Figure 4.2: Mass of the lowest-mass halo producing large arcs in the sample of 46 halos used here to compute the lensing optical depth. The source redshift is $z_\mathrm{s} = 2$. The overall trend in the curve reflects the geometrical lensing sensitivity, while the fluctuations and the depth of the minimum reflect how mergers can lift low-mass halos above the strong-lensing threshold that would otherwise not be capable of strong lensing.

redshifts. In addition, the caustic structures can change substantially during major halo mergers. As a sub-halo approaches the main halo, the initially separated caustics of the two merging components will increase and merge to form a larger caustic. Thus, even though the total mass is unchanged, the mass limit for strong lensing may decrease while a merger proceeds. Even halos that are individually not massive enough for arc formation may be pushed above the mass limit while they merge. In view of the exponentially dropping cluster mass function, this is potentially a huge effect.

Thus, we have to monitor the extent of the caustics as we compute the lensing optical depth of a halo sample, taking into account that the mass limit may change rapidly as halos merge with sub-halos. The lowest mass of a halo (from our sample of 46) that still contributes to strong lensing is shown in Figure 4.2 as a function of lens redshift with fixed source redshift $z_\mathrm{s} = 2$.

Following these prescriptions, we are able to calculate the strong-lensing cross section of each model halo at every redshift step of the simulation, by first ignoring the effects of merger processes and then accounting for them. Thus, we sort the masses from the smallest to the largest at every redshift step and calculate the quantities $\sigma_{d,i}(z)$. Finally, we calculate the lensing optical depth with and without the effect of merger processes.

4.4 Results

4.4.1 Cross Sections

We calculated the optical depth for the formation of gravitational arcs with a length-to-width ratio greater than an arbitrary threshold d. We used two popular choices, $d = 7.5$ and $d = 10$.

Before discussing the calculation of the optical depth, it is interesting and useful to study the behaviour of lensing cross sections for individual halos with redshift. In Figure 4.3 we show the cross sections for four of the most massive halos, both with $d = 7.5$ (top panels) and $d = 10$ (bottom panels). The sources are put at a fixed redshift $z_\mathrm{s} = 2$. Apart from the obvious fact that cross sections for arcs with higher length-to-width ratio are smaller than those including shorter arcs, we see that all cross sections tend to zero when the redshift approaches either zero or the source redshift. This suppression due to the lensing efficiency is caused by the geometry of the problem, and in particular by the fact that lenses very close to the sources or the observer have arbitrarily large critical density (Section 3.3). Moreover we note that the increase in the cross section due to merger events can exceed half an order of magnitude in some cases. Torri et al. (2004) find an increase in the lensing cross section up to an order of magnitude, but here, even if mergers happen at redshifts with higher lensing efficiency

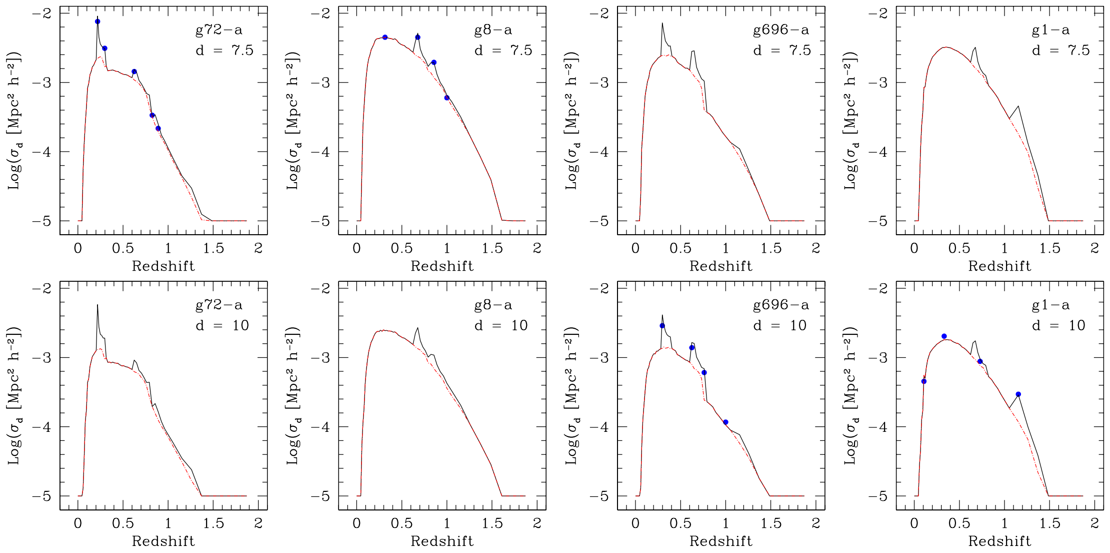

Figure 4.3: Evolution of the lensing cross section for gravitational arcs with a length-to-width ratio equal to or greater than $d = 7.5$ (top panels) and $d = 10$ (bottom panels) for four of the most massive halos in the sample. Sources are at redshift $z_s = 2$. Red-dashed lines show cross sections calculated without taking account of merger processes. Black lines show cross sections enhanced by cluster interactions. Filled blue dots are the counterparts of the black lines obtained from fully numerical ray-tracing simulations.

($z_l \simeq 0.2 - 0.5$), the masses involved are lower, so we cannot reach these higher increases. In particular, high-redshift ($z_l \gtrsim 1$) mergers are quite inefficient in boosting total lensing cross sections, both because of low involved masses and the proximity to the source plane. To further test the reliability of our semi-analytic calculations, we show the cross sections obtained from ray-tracing simulations in Figure 4.3. The agreement is again reassuringly good.

4.4.2 Optical Depths

In Figure 4.4 we show the optical depth per unit redshift, i.e. the contribution to the lensing optical depth by structures in different redshift bins per unit lens redshift. In other words, the integrand of the redshift integral in Eq. (4.8) is shown. The integration over mass is carried out above the mass limit illustrated in Figure 4.2, i.e. included are all the halos that have caustic structures sufficiently larger than individual source galaxies. The two panels show $d = 7.5$ and $d = 10$. Four curves are shown in each panel, one obtained by ignoring mergers and the other taking mergers into account. In both panels, the upper and lower curves refer to source redshifts $z_s = 2$ and $z_s = 1$, respectively.

The overall trend of the differential optical depths in Figure 4.4 resembles individual cross sections, i.e. it drops to zero as the lenses approach the observer or the sources. The dashed (upper) curve for $z_s = 2$ broadly peaks at redshift $z_p \simeq 0.4$, slightly larger than the typical redshift for the peak of the individual cross sections shown in Figure 4.3. This is due simply to the fact that in the differential optical depth the lensing cross sections are weighted with the number density of structures within mass bins. It is interesting to note that the same peak occurs even in the corresponding solid curve; thus it is not due to dynamical processes in the cluster lenses, but rather to the combination of the mass evolution of the lenses with the particularly high lensing efficiency for clusters at that redshift.

Apart from that, the most remarkable result shown by the solid curves is that the impact of cluster mergers is important particularly at moderate and high redshifts, $0.5 \lesssim z \lesssim 0.8$. The pronounced peaks in the differential optical depth seen there, even after averaging over the halo sample, indicate that cluster mergers can substantially increase the lensing optical depth of high-redshift clusters. Above redshift ~ 0.5, mergers almost double the optical depth.

Shifting the source plane from $z_s = 2$ to $z_s = 1$ significantly lowers the total optical depth, as well as the impact of cluster mergers on the optical depth per unit redshift. The first effect obviously occurs because for lower source redshift, the redshift interval of high lensing efficiency narrows. The second effect reflects that sources at lower redshift miss a significant part of the lensing halos' formation history and the merger processes related to it.

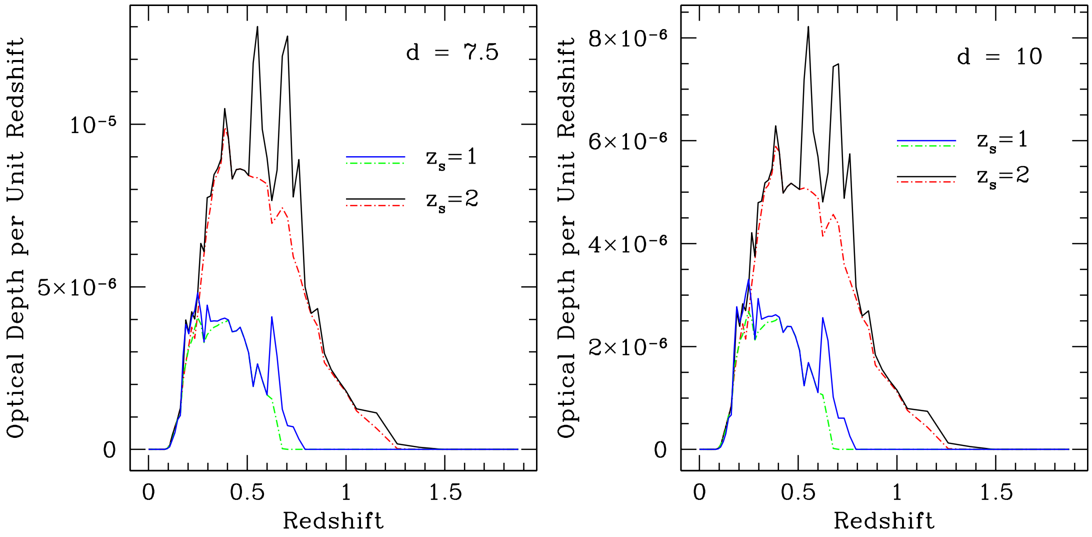

Figure 4.4: The evolution with redshift of the optical depth per unit redshift for gravitational arcs with a length-to-width ratio equal to or larger than d. Solid lines include the effect of cluster mergers, while dashed lines do not. Upper curves refer to sources with $z_{\rm s} = 2$ and lower curves to sources with $z_{\rm s} = 1$.

4.4.3 Sources Properties

A full analysis of the effect of various source properties on the cross sections of individual halos is well beyond the scope of this work. Moreover, the method we have outlined in the previous Sections is probably not the ideal tool for that purpose. For example, it would be interesting to check the variation of cross sections with the source size. Figure 4.5 shows that numerical and semi-analytic cross sections agree (as already shown) and initially increase with increasing source size. However, when the sources become too large compared to the size of the caustic structure, the assumption that the lensing properties are approximatively constant across the area of a source fails (see the Section 4.6 for details). Thus, while numerical cross sections start to decrease because the sources are too large to be efficiently distorted, the semi-analytic cross section increases dramatically. We note that, as in the rest of this work, DM halos are modelled with NFW density profiles and elliptically distorted lensing potential.

Nonetheless, some testable effects can be briefly addressed here. The first is the influence of the shape (circular or elliptical) of the sources on the lensing efficiency. On these grounds we can compare our results with Keeton & Madau (2001).

Figure 4.6 shows the cross section of several DM halos of increasing mass as a function of the source axis ratio, as explained in the caption. We see in the Figure that the cross sections for small elliptical sources exceed those of small circular sources by a factor of ~ 2, which agrees with the findings of Keeton & Madau (2001). It is quite interesting to note that the corresponding increase is somewhat lower for larger sources, due to the fact that the cross section is higher on average. Thus the contribution from the source ellipticity is relatively less important.

Another quite important effect is the change of the cross section with the source redshift. To investigate this, we keep the source size fixed at a radius of $0.5''$, since the angular diameter distance changes only a little over redshift unity. In Figure 4.7 we plot the cross section for a single DM halo of mass $10^{15} M_{\odot} h^{-1}$ as a function of the source redshift. We adopt three different lens redshifts, 0.3, 0.5, and 0.7. The low-redshift end of that plot shows that the closer the lens is to the source, the lower the cross section, due to the geometrical suppression of the halo's lensing efficiency (see discussion in Section 3.3). The general trend is a rapid increase of the lensing cross section with increasing lens redshift, followed by an almost constant phase and a slightly decreasing phase. This trend agrees with the general evolution of the lensing efficiency with the source redshift.

These few examples show the significant influence of the source redshift and intrinsic properties on a cluster's lensing efficiency, in agreement with earlier work; a deeper analysis of the consequences is certainly needed.

4.5 Summary and Discussion

We have described a novel method for semi-analytically calculating the strong-lensing cross sections of GCs. The method first approximates the length-to-width ratio of images by the ratio of the eigenvalues to the Jacobian matrix of the lens mapping. The requirement that this ratio exceed a fixed threshold defines a stripe on both sides of the

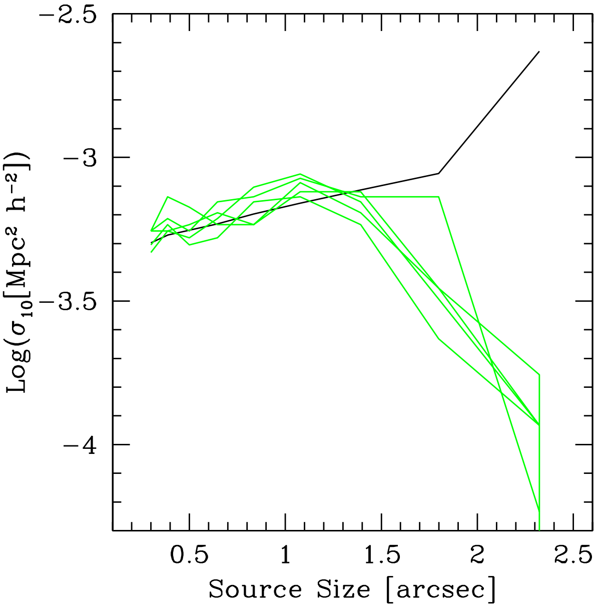

Figure 4.5: Cross section for gravitational arcs with a length-to-width ratio exceeding $d = 10$ for a dark-matter halo of mass $10^{15} M_\odot h^{-1}$ as a function of the source size in arcseconds. Black and green lines show the results of the semi-analytic and of ray-tracing simulations, respectively, which are repeated with different random-number seeds for the ellipticities and the position angles of the sources, as in Figure 4.1. The source redshift is $z_\mathrm{s} = 1$, and the lens redshift is $z_\mathrm{l} = 0.3$.

caustic curves whose area approximates the cluster's strong-lensing cross section.

This approach would be valid for infinitesimally small, circular sources. Extending it to elliptical sources is straightforward using the elegant technique developed by Keeton (2001b). Extended sources can be taken into account after convolving the eigenvalue ratio with a suitable window function quantifying the source size. In order to speed up this convolution, we approximate it by a simple multiplication.

We tested this method by a detailed comparison with cross sections obtained from full ray-tracing simulations. We found excellent agreement within the (considerable) error bars of the ray-tracing results for a variety of lens masses and of lens and source redshifts. Deviations occurred for very weak lenses whose caustics are so small that the crucial assumption that the eigenvalue ratio does not change much across sources is no longer satisfied. In particular, our tests revealed that cross sections rapidly changing during merger events are reproduced well by our new method.

We then proceeded to apply the technique to a sample of halos whose history is described by simulated merger trees. The halos themselves are modelled as pseudo-elliptical NFW density profile whose mass is given as a function of redshift by the merger tree. The merger trees are obtained from a sample of 46 cluster-sized halos numerically simulated in a cosmological volume. We followed the evolution of the halos by simulating merger events at times when the merger trees signal the accretion of a sub-halo with comparable mass to that of the main halo.

This technique allowed us to study the total optical depth for arc formation by the simulated cluster sample at a time resolution that is high enough to properly follow merger events. Comparing the results to those obtained ignoring mergers, we found that the arc optical depth produced by clusters with moderated and high redshifts, $z \gtrsim 0.5$, is almost doubled by mergers.

The resuts just outlined may be potentially relevant in view of the high frequency of arcs recently detected in clusters at moderate and high redshifts (see Section 3.6). For example, Gladders et al. (2003) argue that some physical process must boost the lensing efficiency of high-redshift clusters, which is probably connected with the dynamics and formation histories of the lensing clusters, as merger processes tend to be. This conclusion was supported by Horesh et al. (2005), which compare the lensing efficiency of matched observed and simulated (low-redshift) GCs with a realistic source population taken from the Hubble Deep Field. They find that real clusters are a little bit more efficient lenses than simulated ones, and though the difference is marginally significant, they argue it could be due to a selection effect connected with cluster mergers. In fact, cluster mergers increase not only the lensing efficiency, but also the X-ray luminosity (Randall et al., 2002), and the real clusters used by Horesh et al. (2005) are X-ray selected. In other words, the observed lensing clusters could be a biased sub-set of the entire

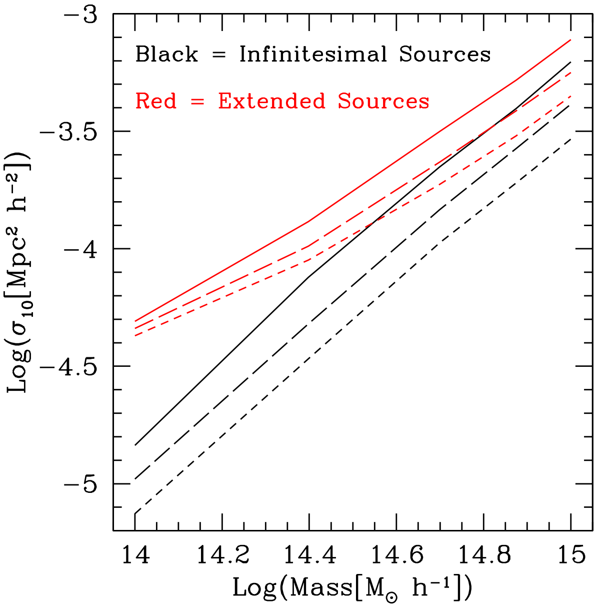

Figure 4.6: Cross section for gravitational arcs with a length-to-width ratio exceeding $d = 10$ for several halos of increasing mass. Black and red lines refer to point-like or extended sources with area equal to that of a circle of radius $0.5''$, respectively. Short dashed lines indicate circular sources, long dashed lines refer to sources with random eccentricity drawn from the interval $[0, 0.5]$ ($q_s \in [0.5, 1]$), and solid lines refer to sources with eccentricity 0.5. Sources are at redshift $z_s = 1$ and the lens redshift is $z_l = 0.3$.

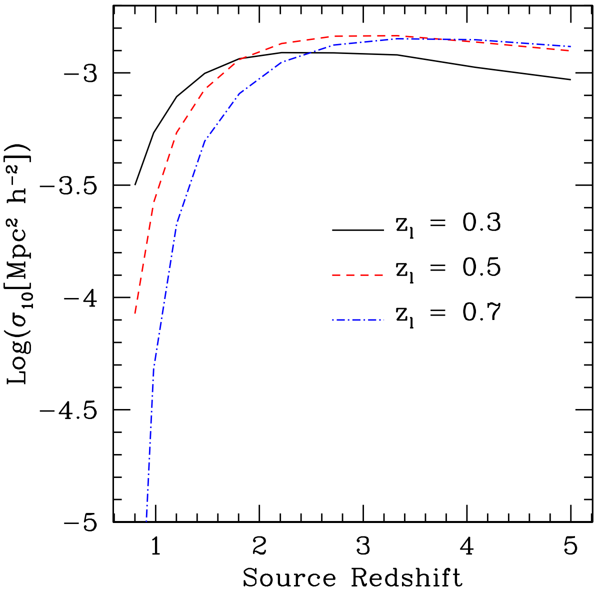

Figure 4.7: Cross section for arcs with a length-to-width ratio exceeding $d = 10$ for a DM halo of mass $10^{15}\,M_\odot h^{-1}$ as a function of the source redshift. Three different lens redshifts are considered, as labeled in the plot.

cluster population. We elaborate more on this issue in Chapter 6.

The method described and developed here reduces computation times for strong-lensing cross sections by factors of ~ 30 compared to ray-tracing simulations. It thus becomes feasible to reliably compute strong-lensing probabilities describing an evolving cluster population by halos accreting mass as encoded by simulated merger trees, whose merging events can be studied at high time resolution.

4.6 Approximate Convolution of a Function with a Step Function on the Source Plane

Consider an arbitrary function $\bar{\Pi}(\boldsymbol{y})$ defined on the source plane. Suppose we wish to convolve $\bar{\Pi}(\boldsymbol{y})$ with another function $g(\boldsymbol{y})$, defined as in Eq. (4.5). The convolution is

$$h(\boldsymbol{y}) = (\bar{\Pi} * g)(\boldsymbol{y}) = \int_{\mathbb{R}^2} \bar{\Pi}(\boldsymbol{z})\, g(\boldsymbol{y}-\boldsymbol{z}) d^2\boldsymbol{z}\ . \tag{4.10}$$

Without loss of generality, any given point $\boldsymbol{y}$ on the source plane can be chosen as the coordinate origin. This means that $\boldsymbol{y} \equiv 0$, hence

$$h(0) = (\bar{\Pi} * g)(0) = \int_{\mathbb{R}^2} \bar{\Pi}(\boldsymbol{z})\, g(\boldsymbol{z}) d^2\boldsymbol{z}\ . \tag{4.11}$$

Now, we choose a position $\boldsymbol{u}$ on the *lens plane* such that $\boldsymbol{z} = \boldsymbol{z}(\boldsymbol{u})$. Applying the lens mapping to the convolution above, we obtain

$$h(0) = \int_{\mathbb{R}^2} \Pi(\boldsymbol{u})\, g(\boldsymbol{u}) \frac{d^2\boldsymbol{u}}{|\mu(\boldsymbol{u})|}\ . \tag{4.12}$$

We assume that $\bar{\Pi}(\boldsymbol{y})$ does not vary much across a source. This assumption is satisfied in almost all interesting cases, except when the sources are at high redshift and the lens is close to them. In that case, the critical curves are very small, so the typical scale on which the lensing properties vary may be comparable to the angular extent of a source. However, even in that case the results of our method remain good, in particular in view of the substantial scatter in the ray-tracing results.

Within this assumption, we can expand the function $\Pi(\boldsymbol{x})$ into a Taylor series around zero, obtaining (we recall that summation over repeated indices is implicit)

$$h(0) \simeq \Pi(0) \int_{\mathbb{R}^2} g(\boldsymbol{u}) \frac{d^2\boldsymbol{u}}{|\mu(\boldsymbol{u})|} + \frac{\partial \Pi(0)}{\partial u_i} \int_{\mathbb{R}^2} u_i g(\boldsymbol{u}) \frac{d^2\boldsymbol{u}}{|\mu(\boldsymbol{u})|} + \frac{1}{2}\frac{\partial^2 \Pi(0)}{\partial u_i \partial u_j} \int_{\mathbb{R}^2} u_i u_j g(\boldsymbol{u}) \frac{d^2\boldsymbol{u}}{|\mu(\boldsymbol{u})|}\ . \tag{4.13}$$

The first integral is unity by normalisation, and the second vanishes because of the symmetry of $g(\boldsymbol{x})$. Thus, Eq. (4.13) reduces to

$$h(\boldsymbol{y}) \simeq \Pi(0) + \frac{1}{2}\frac{\partial^2 \Pi(0)}{\partial u_i \partial u_j} \int_{\mathbb{R}^2} u_i u_j g(\boldsymbol{u}) \frac{d^2\boldsymbol{u}}{|\mu(\boldsymbol{u})|} \equiv \Pi(0) + \frac{1}{2}\frac{\partial^2 \Pi(0)}{\partial u_i \partial u_j} \Omega_{ij}\ . \tag{4.14}$$

Then, we have to carry out the three integrals Ω_{11}, Ω_{22} and $\Omega_{12} = \Omega_{21}$. We show the explicit calculation only for the first, as the others are quite similar:

$$\Omega_{11} \equiv \int_{\mathbb{R}^2} u_1^2 g(\boldsymbol{u}) \frac{d^2\boldsymbol{u}}{|\mu(\boldsymbol{u})|} = \frac{1}{\pi\beta_{\rm s}^2} \int_D u_1^2 \frac{d^2\boldsymbol{u}}{|\mu(\boldsymbol{u})|}\ , \tag{4.15}$$

where D is the set of all positions $\boldsymbol{x}$ on the lens plane where $\boldsymbol{x}^T \Gamma \boldsymbol{x} \le 1$. The matrix Γ defines the shape of the image formed from the source and can be written as $\Gamma = \mathcal{A}^T \mathcal{B} \mathcal{A} = \mathcal{A}^T \mathcal{A}/\beta_{\rm s}^2$. Obviously, the eigenvalues of Γ are $\lambda_1^2/\beta_{\rm s}^2$ and $\lambda_2^2/\beta_{\rm s}^2$. We can now rotate into a reference frame in which $\mathcal{A}$ and, thus, also Γ are diagonal. This is achieved by a rotating about an angle

$$\varphi = \frac{1}{2}\arctan\left(\frac{\gamma_2}{\gamma_1}\right)\ , \tag{4.16}$$

where γ_1 and γ_2 are the two shear components at the origin. This rotation is described by the orthogonal matrix

$$\mathcal{R} = \begin{pmatrix} \cos\varphi & -\sin\varphi \\ \sin\varphi & \cos\varphi \end{pmatrix}\ . \tag{4.17}$$

With $\boldsymbol{v} = \mathcal{R}\boldsymbol{u}$, this rotation transforms Eq. (4.15) into

$$\begin{aligned} \Omega_{11} &= \frac{1}{\pi\beta_{\rm s}^2} \int_D (v_1^2 \cos^2\varphi + v_2^2 \sin^2\varphi) \frac{d^2\boldsymbol{v}}{|\mu(\boldsymbol{v})|} + \frac{1}{\pi\beta_{\rm s}^2} \int_D (2 v_1 v_2 \cos\varphi \sin\varphi) \frac{d^2\boldsymbol{v}}{|\mu(\boldsymbol{v})|} \\ &= \frac{\cos^2\varphi}{\pi\beta_{\rm s}^2} \int_D v_1^2 \frac{d^2\boldsymbol{v}}{|\mu(\boldsymbol{v})|} + \frac{\sin^2\varphi}{\pi\beta_{\rm s}^2} \int_D v_2^2 \frac{d^2\boldsymbol{v}}{|\mu(\boldsymbol{v})|}\ . \end{aligned} \tag{4.18}$$

In the new coordinate system, D is the set of all positions $\boldsymbol{v}$ of the lens plane where

$$\frac{\lambda_1^2}{\beta_\mathrm{s}^2}v_1^2 + \frac{\lambda_2^2}{\beta_\mathrm{s}^2}v_2^2 \leq 1 \; . \tag{4.19}$$

Now we can introduce polar elliptical coordinates (ρ, θ) by

$$v_1 = \frac{\beta_\mathrm{s}}{|\lambda_1|}\rho\cos\theta \; , \quad v_2 = \frac{\beta_\mathrm{s}}{|\lambda_2|}\rho\sin\theta \; , \tag{4.20}$$

in terms of which Eq. (4.18) becomes

$$\Omega_{11} = \frac{\beta_\mathrm{s}^2\cos^2\varphi}{\pi}\int_0^{2\pi}\int_0^1 \rho^3\cos^2\theta\frac{d\rho d\theta}{\lambda_1^2(\rho,\theta)} + \frac{\beta_\mathrm{s}^2\sin^2\varphi}{\pi}\int_0^{2\pi}\int_0^1 \rho^3\sin^2\theta\frac{d\rho d\theta}{\lambda_2^2(\rho,\theta)} \; . \tag{4.21}$$

As a second approximation, we shall assume that the tangential and radial eigenvalues do not vary much across a single image, so we can replace the eigenvalues by their mean values across the image. Then,

$$\begin{aligned}\Omega_{11} &= \frac{\beta_\mathrm{s}^2\cos^2\varphi}{\pi\langle\lambda_1^2\rangle}\int_0^{2\pi}\int_0^1 \rho^3\cos^2\theta d\rho d\theta + \frac{\beta_\mathrm{s}^2\sin^2\varphi}{\pi\langle\lambda_2^2\rangle}\int_0^{2\pi}\int_0^1 \rho^3\sin^2\theta d\rho d\theta \\ &= \frac{\beta_\mathrm{s}^2}{4}\left(\frac{\cos^2\varphi}{\langle\lambda_1^2\rangle} + \frac{\sin^2\varphi}{\langle\lambda_2^2\rangle}\right) \; .\end{aligned} \tag{4.22}$$

Similarly, we find that

$$\Omega_{22} = \frac{\beta_\mathrm{s}^2}{4}\left(\frac{\cos^2\varphi}{\langle\lambda_2^2\rangle} + \frac{\sin^2\varphi}{\langle\lambda_1^2\rangle}\right) \tag{4.23}$$

and

$$\Omega_{12} = \frac{\beta_\mathrm{s}^2\sin\varphi\cos\varphi}{4}\left(\frac{1}{\langle\lambda_2^2\rangle} - \frac{1}{\langle\lambda_1^2\rangle}\right) . \tag{4.24}$$

Substituting into Eq. (4.14), we obtain

$$\begin{aligned} h(0) &\simeq \Pi(0) + \frac{1}{2}\frac{\partial^2\Pi(0)}{\partial x_1^2}\left(\frac{\beta_\mathrm{s}^2\cos^2\varphi}{4\langle\lambda_1^2\rangle} + \frac{\beta_\mathrm{s}^2\sin^2\varphi}{4\langle\lambda_2^2\rangle}\right) \\ &+ \frac{1}{2}\frac{\partial^2\Pi(0)}{\partial x_2^2}\left(\frac{\beta_\mathrm{s}^2\cos^2\varphi}{4\langle\lambda_2^2\rangle} + \frac{\beta_\mathrm{s}^2\sin^2\varphi}{4\langle\lambda_1^2\rangle}\right) \\ &+ \frac{\partial^2\Pi(0)}{\partial x_1\partial x_2}\left(\frac{\beta_\mathrm{s}^2\cos\varphi\sin\varphi}{4\langle\lambda_2^2\rangle} - \frac{\beta_\mathrm{s}^2\cos\varphi\sin\varphi}{4\langle\lambda_1^2\rangle}\right) \; .\end{aligned} \tag{4.25}$$

Within the framework of our approximations, we can thus replace the value of the function Π at a point of the lens plane with its convolution on the source plane at the corresponding point, represented by Eq. (4.25). In this way, we account for finite source sizes.

Chapter 5

Effects of Early-Dark Energy on Strong Cluster Lensing

5.1 Introduction

While the present dominance of DE is well-established (Goldstein et al. 2003; Hawkins et al. 2003; Spergel et al. 2003, 2007; Rebolo et al. 2004; Readhead et al. 2004; Riess et al. 2004; Tegmark et al. 2004 and the discussion in Chapter 1), its evolution is largely unconstrained, in particular in the early Universe. An interesting class of models for dynamical quintessence are the early-DE models introduced in Section 1.7. As was shown in Chapter 2, non-linear structures are expected to form substantially earlier in such early-DE models, if they are normalised so as to be compatible with the large-scale temperature-fluctuation amplitude of the CMB. For the two specific models with early-DE used in this work, Bartelmann et al. (2006) showed thet the population of galaxy clusters is expected to evolve by approximately one order of magnitude less strongly than in the standard ΛCDM scenario.

Should this come close to reality, a rich population of massive GCs would be present at high redshift, which is completely unexpected in ΛCDM. Similarly, the dynamical activity within the cluster population due to substantial mergers with sub-halos would be shifted or extended towards higher redshift.

The problem of the non-linear evolution of cosmic structures in the presence of DE has recently been addressed by several authors and also from a more general point of view. For example, Mota & van de Bruck (2004), Zeng & Gao (2005a,b), Maor & Lahav (2005), and Wang (2006) analyse different aspects of this issue for both constant and time-dependent equation of state parameters for the DE, allowing for DE clustering and coupling to DM. They outline very different properties of the final virialised objects, depending on the behaviour of the DE fluid. Additionally, Zeng & Gao (2005a) and Manera & Mota (2006) explore the effect of the different non-linear evolution on the predicted number counts for GC-sized DM halos, finding several significant effects. They discover, in particular, that the number counts of massive structures increase if small-scale clustering of DE is allowed, while they decrease if the amount of DM coupled to DE grows.

One highly sensitive way, which is interesting due to its non-linearity, to probe the massive end of the cluster population is the strong lensing effect. Although the issue is still controversial it seems to be at least difficult within the ΛCDM model to reproduce the observed abundance of strong-lensing events in cluster cores (Section 3.6). Arcs in clusters at high redshift are similarly puzzling because they indicate that even clusters at $z \gtrsim 1$ can already be concentrated and massive enough to be strong gravitational lenses for a source population that is not too distant from them.

It was also explained in Section 3.4.2 that dynamical activity in GCs is highly important for their strong-lensing abilities (Bartelmann et al., 1995; Meneghetti et al., 2003b; Torri et al., 2004; Fedeli et al., 2006). Major cluster mergers thus open the huge, exponentially rising reservoir of moderately massive clusters for strong lensing.

Cosmological models reconciling an appreciable cluster abundance at high redshift, and thus also a high level of dynamical cluster activity, with independent cosmological constraints - e.g. from the CMB - are thus particularly interesting in view of strong cluster lensing. Sufficiently detailed numerical simulations are costly and beyond the scope of a parameter study, but the semi-analytic method for computing strong-lensing cross sections developed in Chapter 4 opens the way to systematically test a variety of cosmological models for their consequences for strong cluster lensing

We use it in this Chapter to study the statistics of strong cluster lensing in the four DE cosmologies summarised in Table 2.1. We do not consider any other aspects related to the DE fluid behaviour, such as small-scale clustering or coupling to dark matter.

5.2 Merger Trees

In Eq. (2.40) we gave the probability of a halo of a given mass M_0 at a given redshift z having a progenitor of a lower mass M_p at a higher redshift $z+\Delta z$, computed with the extended Press & Schechter (1974) formalism. Since the variance of the density field filtered on a scale corresponding to a given mass M decreases monotonically with M, this is equivalent to the probability that a halo of variance $S(M_0)$ at a given redshift had a higher variance $S(M_\mathrm{p})$ at a higher redshift.

If we now want the probability that the halo of mass M_0 has a progenitor corresponding to a change in variance lower than $\Delta S \equiv S(M_\mathrm{p}) - S(M_0)$ within the same redshift interval, we simply have to integrate Eq. (2.40) over the change in variance, obtaining the cumulative probability distribution

$$J(\Delta S, \Delta\omega) \equiv \int_0^{\Delta S} K(\Delta S', \Delta\omega) d\Delta S' = \mathrm{erfc}\left(\frac{\Delta\omega}{\sqrt{2\Delta S}}\right) , \tag{5.1}$$

where

$$\mathrm{erfc}(x) \equiv \frac{2}{\sqrt{\pi}} \int_x^\infty \mathrm{e}^{-t^2} dt \tag{5.2}$$

is the complementary error function. Equation (5.1) is just the probability of the mass of the progenitor M_p being larger than the mass corresponding to the variance $\Delta S - S(M_0)$.

We now proceed to use the extended Press & Schechter (1974) formalism summarised in Section 2.3.4 for a Monte-Carlo realisation of merger trees. The procedure is quite straightforward, and we refer to Somerville & Kolatt (1999) for a detailed discussion and to Randall et al. (2002) and Cassano & Brunetti (2005) for some applications.

5.2.1 Monte-Carlo Simulations

Consider a halo of mass M_0 at the present time ($z = 0$). If we draw a random number r in the interval $[0, 1]$ and solve the equation $J(\Delta S, \Delta\omega) - r = 0$, we draw a value for the change in the variance corresponding to the halo compliant with the merger rate (5.1).

Given the variance $S(M_0)$ of the halo's original mass, we obtain a new value of the variance and convert it to a new mass that is the mass of the progenitor M_p. If we choose a sufficiently small time interval, we can assume that the entire change in the halo's mass is due to a unique, binary merging process with another halo of mass $\Delta M = M_0 - M_\mathrm{p}$. If we repeat this process for earlier progenitors at subsequent redshift steps, we obtain the merger history of the original halo up to a given redshift. At the end of this procedure, we have obtained the value of the halo's mass and that of its progenitors for each redshift step, i.e. a merger tree.

The choice of the time interval needs some care. It has to be small to justify the assumption of binary mergers, but not too small to avoid the results being dominated by numerical noise. Following the rule-of-thumb given by Lacey & Cole (1993), we use a time step such that

$$\Delta\omega = \sqrt{\frac{dS(M_0)}{dM} \Delta M_\mathrm{c}} , \tag{5.3}$$

(see also Somerville & Kolatt 1999) where ΔM_c is the mass of the smallest sub-halo required to be resolved individually. If M_p or ΔM fall below ΔM_c, the process does not represent an individual merger, but smooth accretion. It follows from the above expression that the lower initial masses M_0 require larger time steps.

A set of Monte-Carlo realisations of merger trees is successful if the population of structures that it produces agrees with the theoretical mass function at any given redshift. As Somerville & Kolatt (1999) pointed out, this is not strictly so if we consider only binary mergers and smooth accretion as we are doing here. Several authors (Benson et al., 2005) argued that this may be due to an intrinsic inconsistency in the extended Press & Schechter (1974) formalism, and Somerville & Kolatt (1999) suggest that the problem can be mitigated considering multiple mergers and smooth accretion. Nonetheless, the difference between the halo-mass distributions following from the merger-tree simulations and expected from the mass function is significant only at redshifts beyond our interest, and several tests confirmed the good agreement between the two halo-mass distributions.

5.2.2 Our Sample

We consider a sample of $\mathcal{N} = 500$ DM halos whose present-day masses are *uniformly* distributed within $M_\mathrm{inf} = 10^{14} M_\odot h^{-1}$ and $M_\mathrm{sup} = 2.5 \times 10^{15} M_\odot h^{-1}$. It is plausible that structures with mass below M_inf at $z = 0$ do not contribute appreciably to the total lensing efficiency (see the discussion in Section 4.3.3). For each halo, we

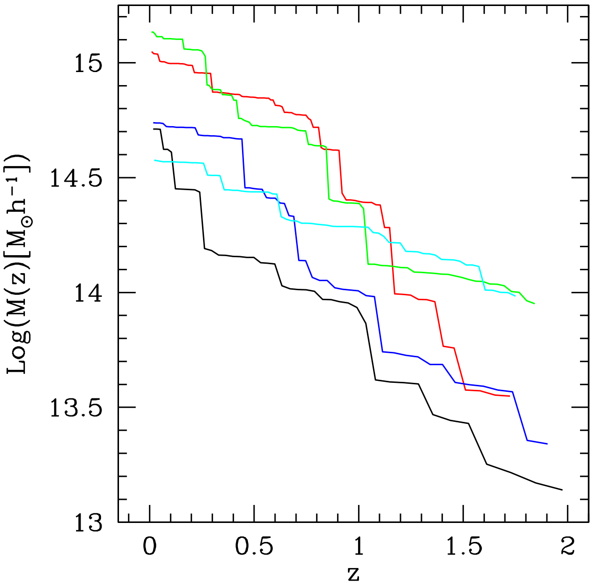

Figure 5.1: Exemplary merger histories for five DM halos randomly selected from our sample in the ΛCDM model. The merger histories are extended up to the source redshift for each individual halo.

compute the appropriate time step from Eq. (5.3) and split it into two progenitor halos. Then, we proceed with the more massive progenitor as the starting point for the next step. We repeat this procedure until the redshift exceeds the source redshift z_s (which is chosen individually for each halo in the sample, see Section 5.3 for details) or the mass of the halo falls below ΔM_c.

We show in Figure 5.1 the merger histories (that is, the evolution of mass with redshift) of five halos selected from our sample of 500 halos for the ΛCDM model. Sudden discontinuities in the mass are evident, each of which corresponds to a merger between the main halo and a massive sub-halo.

5.3 Strong-lensing Statistics

As we did in Chapter 4, in order to compute the efficiency of DM halos as strong cluster lenses, specifically for producing long and thin arcs, we model each halo as an NFW density profile with an elliptically distorted lensing potential. Again, we adopt an eccentricity for the iso-potential contours equal to $e = 0.3$ for all halos. After deflection angle map calculation, we use the fast semi-analytic method developed in the previous Chapter. As the length-to-width threshold for cross sections we choose $d = 7.5$ here and show one plot with $d = 10$ for comparison later

These semi-analytic cross sections are in excellent agreement with the results from fully numerical ray-tracing simulations (see Figure 4.1). Moreover, their computation is substantially faster since the method does not require costly operations such as finding all images for every source and refining the source distribution near caustics on an adaptive grid.

We calculate cross sections both ignoring and accounting for merger processes that transiently increase the lensing efficiency. When a merger with a sub-halo of mass larger than 5% of the main halo's mass occurs, we model the interaction in exactly the same way as we did in Chapter 4, with the only difference that now the duration of the process is not fixed for every event but set to the dynamical timescale

$$t_\mathrm{dyn} \equiv \sqrt{\frac{(r_{200,1} + r_{200,2})^3}{G(M_1 + M_2)}} \; . \tag{5.4}$$

In order to account for the source redshift distribution, we randomly assigned to each DM halo an individual source redshift $z_{\mathrm{s},i}$, $i = 1, \ldots, \mathcal{N}$, drawn from the redshift distribution of the faint blue galaxies population

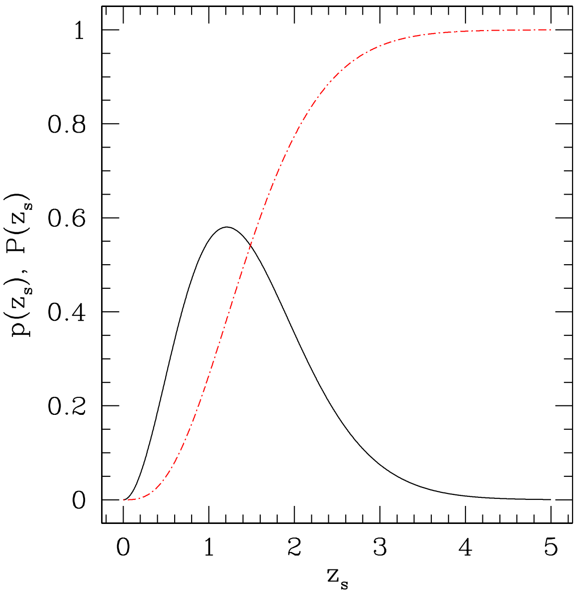

Figure 5.2: The differential (black solid line) and cumulative (red dash-dotted line) source-redshift distributions given by Eq. (5.5).

(Section 3.5) given in Smail et al. (1995) (see also Bartelmann & Schneider 2001)

$$p(z_\mathrm{s}) = \frac{\beta}{z_0^3\Gamma(3/\beta)}\, z_\mathrm{s}^2 \exp\left[-\left(\frac{z_\mathrm{s}}{z_0}\right)^\beta\right] . \tag{5.5}$$

The parameters z_0 and β define the average redshift and the steepness of the high-redshift tail of the distribution, respectively. In this work, we used the conventional values $z_0 = 1$ and $\beta = 3/2$. Given this choice, the distribution peaks at $z_\mathrm{m} \simeq 1.21$. Figure 5.2 shows this distribution together with its cumulative function defined by

$$P(z_\mathrm{s}) \equiv \int_0^{z_\mathrm{s}} p(z)dz . \tag{5.6}$$

Using the distribution Eq. (5.5), we can compute the average optical depth as defined in Eq. (3.34). However, since each halo in our study is characterised by its own source redshift randomly drawn from the distribution Eq. (5.5), we can omit the weighting with $p(z_\mathrm{s})$ when we discretise the integral over source redshift in Eq. (3.34). This is not possible for the mass integration, since the masses of the halos are randomly drawn from a uniform distribution, which requires the weighting with the halo mass function.

The source-redshift distribution $p(z_s)$ formally extends to an infinite source redshift, but obviously this is not true in reality. We set the maximum source redshift to $z_\mathrm{max} = 7.5$. As Figure 5.2 shows, the probability of finding a source at this redshift can safely be neglected. Since we operate on a discrete sample of $\mathcal{N}$ halos, each of which is characterised by a mass M_i and a source redshift $z_{\mathrm{s},i}$, we can rewrite the average optical depth as

$$\bar{\tau}_\mathrm{d} = \int_0^{z_\mathrm{max}} \left[\sum_{i=1}^{\mathcal{N}-1} \frac{\sigma_\mathrm{d}(M_i, z, z_{\mathrm{s},i})}{4\pi D_{\mathrm{s},i}^2} \int_{M_i}^{M_{i+1}} N(M,z)dM\right] dz . \tag{5.7}$$

The integrand of this equation is the optical depth per unit redshift, i.e. the contribution to the optical depth from halos at different redshifts, as defined in Section 4.4.2 but this time accounting for the source-redshift distribution,

$$t_\mathrm{d}(z) \equiv \frac{d\bar{\tau}_\mathrm{d}(z)}{dz} = \sum_{i=1}^{\mathcal{N}-1} \frac{\sigma_\mathrm{d}(M_i, z, z_{\mathrm{s},i})}{4\pi D_{\mathrm{s},i}^2} \int_{M_i}^{M_{i+1}} N(M,z)dM . \tag{5.8}$$

This will be the central quantity in our strong-lensing analysis.

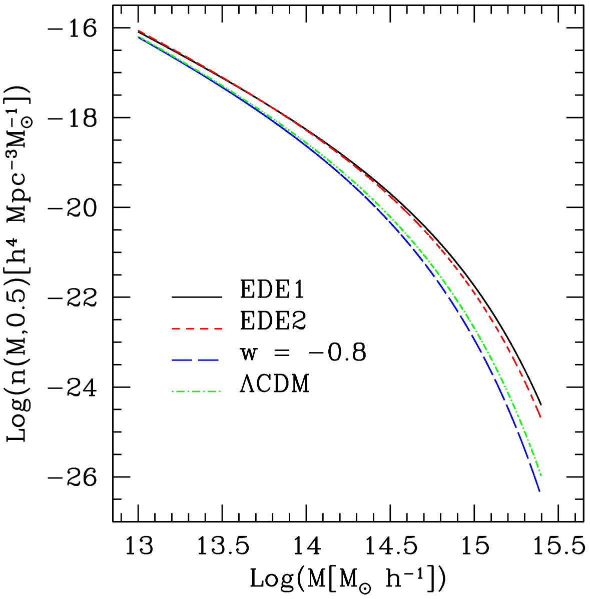

Figure 5.3: The Press & Schechter (1974) mass function for DM halos in the mass range $[10^{13}, 2.5 \times 10^{15}]M_{\odot}h^{-1}$ at redshift $z = 0.5$ for the four cosmological models studied in this Chapter, as labelled in the plot.

5.4 Expectations

Before turning to the results, it is useful to evaluate the expectations in order to gain a better understanding of the problem. As shown by Bartelmann et al. (2006) and outlined earlier, the formation of nonlinear cosmic structures occupies a larger redshift range in early-DE cosmological models. Structures form earlier and the formation process lasts longer. This increases the merger probability for a given halo at high redshift, as well as the total number of structures of a given mass that are found at a given redshift. Figure 5.3 shows the Press & Schechter (1974) mass function of Eq. (2.36) at a fixed redshift $z = 0.5$ for the four cosmological models described in Table 2.1.

Evidently, the mass function is lowest for the ΛCDM model and only slightly higher for the model with constant equation-of-state parameter $w_{\rm x} = -0.8$. It is highest (by up to an order of magnitude at the high-mass tail) for the two early-DE models, reflecting the different halo-formation histories in different cosmologies. In the EDE1 and EDE2 models, structure formation begins earlier, hence at a given (suitably low) redshift, the abundance of halos is higher. This is in qualitative agreement with the discussion performed in Chapter 2.

In Figure 5.4, we show the merger probability between a halo of mass halo of mass $M_{\rm p} = 10^{14}M_{\odot}h^{-1}$ and a sub-halo of mass $M_{\rm p}/2$ as a function of redshift. Instead of using the function $W(M_{\rm p}, \Delta M, z)$ defined in Eq. (2.41), that represents the merger rate per unit mass of the substructure and per unit redshift, we prefer to use here the function $R(M_{\rm p}, \Delta M, z)$ defined as

$$R(M_{\rm p}, \Delta M, z) \equiv W(M_{\rm p}, \Delta M, z) \left| \frac{dz}{d\ln t} \right| \Delta M. \tag{5.9}$$

Eq. (5.9) represents the merger rate per unit logarithmic merging mass and per unit logarithmic cosmic time and it corresponds to the original definition of Lacey & Cole (1993). We also note the difference between the behaviour of early-DE models and of models with a constant equation-of-state parameter. At high redshift, the early-DE merger rate is significantly higher than for the other two models, but becomes essentially the same below redshift ~ 1.2.

This can again be understood in terms of the different dynamics of structure formation. Keeping the mass of the sub-halo fixed, we expect more halos of such mass to be available at high redshift with which the main halo can merge, because structure formation begins earlier in early-DE models. On the other hand, structure growth begins later in models with a constant equation-of-state parameter and proceeds more rapidly. Thus, at a sufficiently low redshift, the abundance of such halos equals that in early-DE models, giving rise to an almost identical merger rate. It is worth emphasising here that the differences shown between the different cosmological models are also due, in part or mainly, to the different normalisation σ_8 of the power spectrum.

Recalling that the source-redshift distribution peaks at redshift ~ 1.2, we expect the different merger rates to

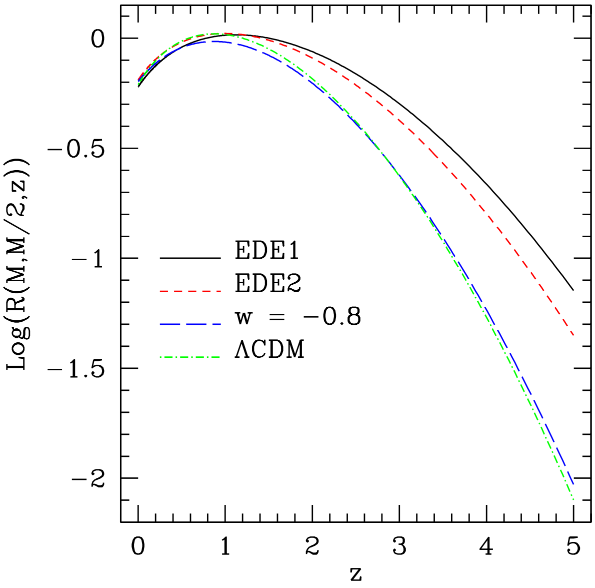

Figure 5.4: The probability that a DM halo of mass $M_\mathrm{p} = 10^{14} M_\odot h^{-1}$ merges with a sub-halo of mass $M_\mathrm{p}/2$ as a function of redshift per unit logarithmic mass of the merging sub-halo and per unit logarithmic cosmic time. Results are shown for all four cosmological models considered here, as labelled in the plot.

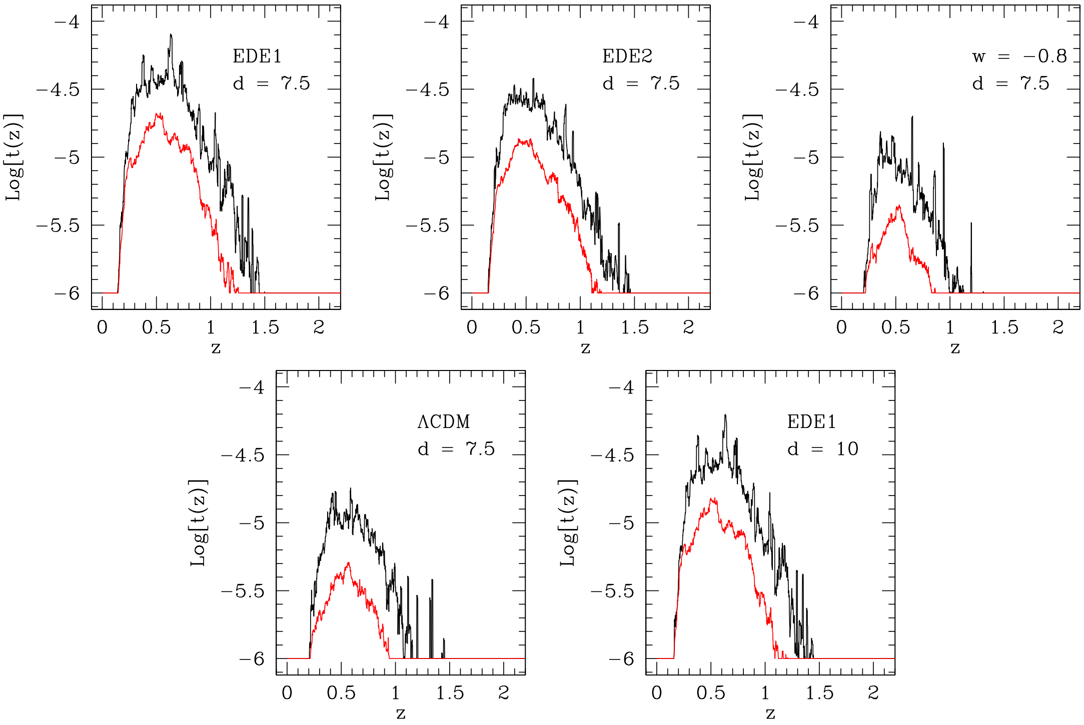

Figure 5.5: The logarithm of the optical depth per unit redshift for arcs with length-to-width ratio exceeding $d = 7.5$ for each of the cosmological models studied here (top and bottom-left panels), and for $d = 10$ in the model EDE1 (bottom-right panel). Black curves show the optical depths obtained including halo mergers with sub-halos, while red curves are obtained after ignoring the effect of halo interactions.

have little influence on the optical depth. On the other hand, since the optical depth is essentially an average of the cross section of different halos weighted by their relative abundances, we expect the difference in the mass function to severely affect the strong-lensing statistics. In early-DE models, the optical depth per unit redshift should exceed that in the ΛCDM model and the model with a constant equation-of-state parameter of $w_\mathrm{x} = -0.8$.

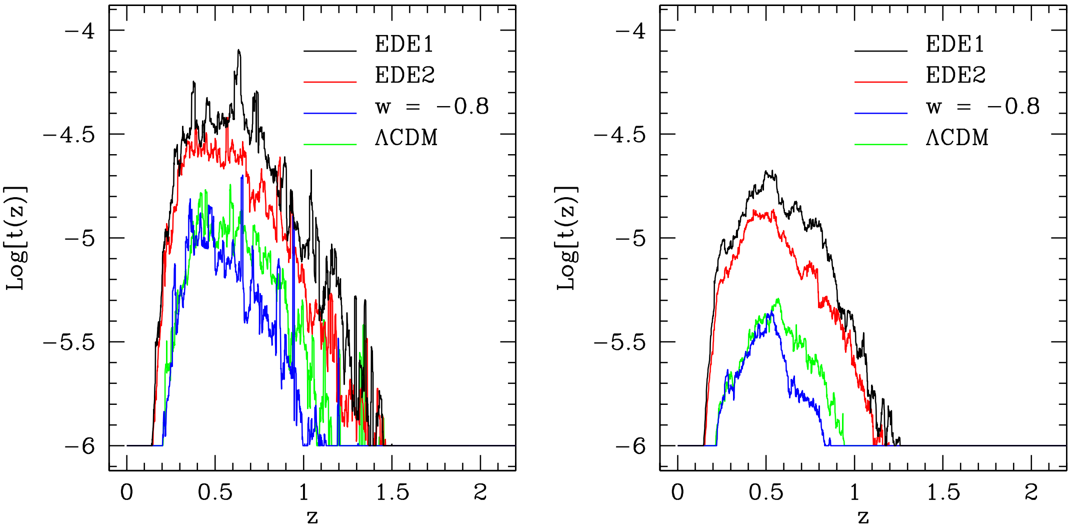

Figure 5.6: The logarithm of the optical depth per unit redshift for arcs with length-to-width ratio exceeding $d = 7.5$ obtained for the four DE cosmological models considered here. The lensing efficiency shown in the left panel takes transient boosts by cluster mergers into account, while that shown in the right panel ignores it.

We show in the next section how well this expectation is satisfied.

5.5 Results

We discuss now the expected behaviour of the optical depth per unit redshift in the different DE cosmologies considered in this work. The occurrence of gravitational arcs is highly sensitive to the abundance and internal structure of GCs, which in turn depends on the linear and non-linear evolution of density fluctuations. We thus expect that the presence and behaviour of DE can affect it.

We show the optical depth per unit redshift in Figure 5.5 for arcs with a length-to-width ratio exceeding $d = 7.5$, obtained for each of our four cosmological models. For model EDE1, we also show the result for $d = 10$. The optical depths accounting for and ignoring halo mergers are compared. As expected, the lensing efficiency vanishes near the observer and approaching the source redshift because of the geometrical drop in lensing efficiency.

Cluster mergers increase the optical depth per unit redshift, and thus also the total, average optical depth, factors up to 2 or 3 in all DE models. The enhancement due to mergers appears more uniform than obtained in Chapter 4. This is due to the sample used here that is more than one order of magnitude larger and to the much higher time resolution adopted (up to 10^{-2} in redshift). Quite obviously, increasing the length-to-width threshold decreases the lensing efficiency, but the features caused by merger processes remain qualitatively the same.

The main result is that mergers enhance the lensing efficiency by about the same amount for each model because the merger rate is almost the same in the redshift range relevant to strong cluster lensing. However, note that the absolute value of the optical depth per unit redshift is higher in early-DE models, which is seen better in Figure 5.6. There, we compare the optical depth per unit redshift for arcs with length-to-width ratios exceeding $d = 7.5$ in the four cosmologies, accounting for (left panel) and ignoring cluster mergers (right panel).

This effect was also expected because of the difference in the abundance of halos of a given mass in various cosmological models. These Figures show that, both with and without the effect of halo mergers, the lensing optical depth per unit redshift is higher by factors up to ~ 3 in early-DE models compared to the other models. At redshifts above ~ 0.5, the lensing efficiency for the model with a constant $w_x = -0.8$ is slightly smaller than in the ΛCDM model because the abundance of halos is also slightly lower (see Figure 5.3). A similar difference appears between the EDE1 and EDE2 models. This is due to the fact that the normalisation of the power spectrum is higher in the first than in the second, causing a higher abundance of clusters.

An effect that we also recognise in these plots is that, in cosmologies with early-DE, the optical depth per unit redshift rises and already reaches a significant level at relatively high redshift, while it is still negligible in a ΛCDM model. As discussed before, the models alternative to ΛCDM that we have studied here have a larger fraction of structures at high redshift, causing this earlier and larger contribution to the strong-lensing efficiency.

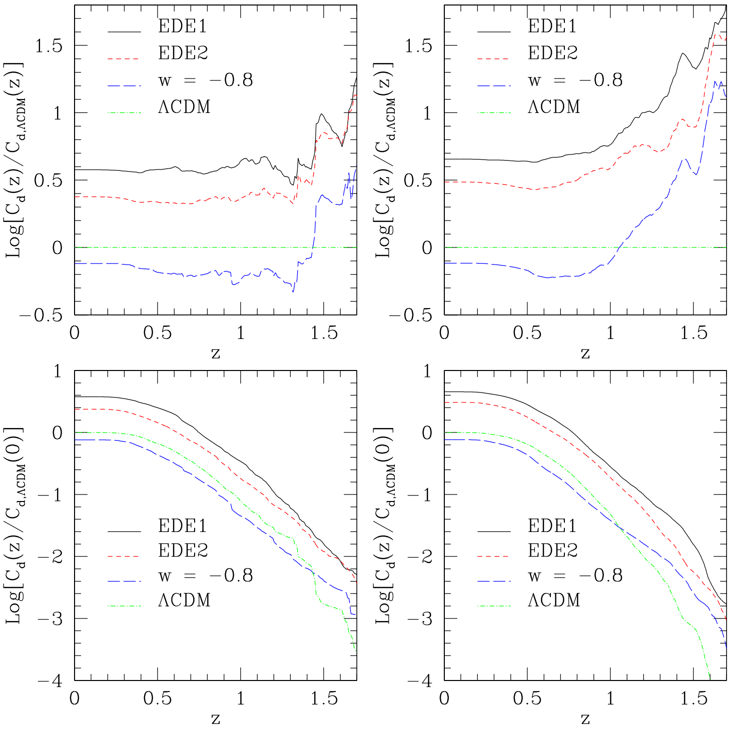

Figure 5.7: *Top panels*. Logarithm of the cumulative optical depth per unit redshift, normalised to its value in the ΛCDM universe. Curves representing the four cosmologies studied in this work are shown, as labelled in the plot. *Bottom panels*. Logarithm of the cumulative optical depth per unit redshift, normalised to its value at present in a ΛCDM universe. Left and right panels show results that include and ignore cluster mergers, respectively.

Further detail on this aspect is provided by Figure 5.7. In its top panels, it shows the cumulative optical depth per unit redshift, which we can write as

$$C_{\rm d}(z) \equiv \int_z^{z_{\rm max}} t_{\rm d}(z')dz' \;, \tag{5.10}$$

normalised to the ΛCDM case. Its increase towards high redshift emphasises directly how the lensing efficiency already drops at lower redshift in a ΛCDM universe with respect to the (early) DE cosmologies. The bottom panels show the cumulative optical depth per unit redshift normalised to the *present* value in the ΛCDM model, $C_{\rm d,\Lambda CDM}(0) = \bar{\tau}_{\rm d,\Lambda CDM}$. This illustrates the same effect in a different way. For instance, we see that the cumulative optical depth per unit redshift in the EDE1 model already reaches the same value $C_{\rm d,\Lambda CDM}(0)$ at $z \sim 0.8$, which ΛCDM reaches today. Conversely, the cumulative optical depth per unit redshift in the ΛCDM case has already dropped by an order of magnitude by $z \sim 0.8$. Similarly, the EDE2 model reaches the total optical depth of the ΛCDM model at $z \sim 0.7$. In agreement with our earlier discussion, we note that this specific evolution does not depend on whether we take dynamical processes into account or not. The enhanced lensing efficiency in the high redshift tail may have stimulating consequences, as we shall discuss later.

The large spikes shown in the left panel of Figure 5.6 are obviously due to the variation in the lensing efficiency of GCs during mergers. Very small spikes also appear in the right panel of the same Figure, where dynamical processes are not taken into account. There, they stem from numerical effects, in particular, now our time resolution is very high and the number of halos is limited. Indeed, the spikes become larger well above redshift unity, where the number of contributing halos is reduced (remember that each halo is characterised by a different source redshift, drawn from a distribution that peaks around $z \simeq 1.2$).

5.6 Summary and Discussion

We have analysed the incidence of pronounced (long and thin) arcs in GCs in the four DE models introduced in Chapters 1 and 2. In particular, we considered two early-DE cosmologies in which the density parameter in DE at high redshift remains small and positive. We compared them to a model with constant equation-of-state parameter $w_{\rm x} = -0.8$ and a ΛCDM model for which $w_{\rm x} = -1$.

For each cosmological model, we used Monte-Carlo techniques to build up merger trees for a set of $\mathcal{N} = 500$ cluster-sized DM halos. By modelling each halo by an NFW density profile with elliptically distorted lensing potential and suitably accounting for cluster interactions during mergers, we calculated the optical depth per unit redshift both accounting for and ignoring cluster mergers. To this end, we also considered a realistic distribution for the source redshift.

We find that, in agreement with the results of Fedeli et al. (2006) (see Chapter 4), cluster mergers enhance the occurrence of arcs by a factor between 2 and 3. This occurs in all the cosmological models we analysed, and the relative increase is approximately the same, because the cluster merger rates in the redshift ranges relevant for strong lensing (below $z \sim 1$) are almost identical (see the discussion in Section 5.4).

However, a potentially more important result is that the optical depth per unit redshift is larger by a factor of ~ 3 in early-DE models compared to the models with a cosmological constant or with a constant equation of state parameter $w_{\rm x} = -0.8$, while the differences between the last two are close to negligible. There is also a significant difference between the two early-DE models due to the fact that model EDE1 has a higher normalisation parameter σ_8 than EDE2 in order to agree with the CMB observations (cf Table 2.1). Thus, halos form earlier in model EDE1. This is also demonstrated by Figures 5.3 and 5.4. Moreover, the lensing efficiency already drops at a lower redshift in a ΛCDM universe than in the different DE models. The optical depth per unit redshift has a significant high-redshift tail in early DE cosmologies, while it is negligible otherwise.

A main consequence of these results is that they indicate an appreciable difference in the incidence of long and thin gravitational arcs between the ΛCDM model and models with early DE. Therefore, arc statistics may provide an interesting way to investigate the reliability of these models, although the precise contribution of $\bar{\Omega}_{\rm x,sf}$ will probably be better constrained using cluster counts in the X-ray or Sunyaev-Zel'dovich regimes, which suffer from lower systematics.

The presence of early-DE, combined with the transient boosts due to cluster mergers, could help resolve the discrepancy between the predicted and observed abundances of gravitational arcs that has been outlined in Section 3.6 and that up to date is not clearly solved neither considering the internal structure of the lensing halos nor the redshift distribution of the sources. It has been shown here that the effects of early DE on structure growth interestingly point in the right direction. Similar conclusions were also drawn by Meneghetti et al. (2005a), where the lensing efficiency of numerically simulated DM halos in different DE cosmologies were analysed. Here the haloes are modelled in an analytical way, allowing a much higher mass and time resolution. Moreover, the DE models studied there were derived from SUGRA (Brax & Martin, 2000) and Ratra-Peebles potentials (Peebles & Ratra, 2003), without an early component. In many aspects, our work is thus complementary to that of Meneghetti et al. (2005a).

Finally, that the lensing efficiency in early-DE models is much higher at high redshift than in the ΛCDM case can be related to the recent unexpected discovery of the high incidence of giant arcs in high-redshift clusters. Future searches for strong lensing in distant GCs may be promising for distinguishing between cosmological models other than the standard ΛCDM, or at least for gaining a deeper understanding of the role of early-DE.

Chapter 6

Selection Effects on X-ray and Strong-lensing Clusters in Various Cosmologies

6.1 Introduction

Cluster selection by X-ray emission is generally believed to produce well-defined samples of massive clusters. This is certainly true for relaxed objects near virial equilibrium, but clusters undergo substantial evolution during the cosmic epoch which we can overlook. Numerical simulations demonstrate that temperatures and X-ray luminosities of the intracluster gas increase by factors of a few for periods which are comparable to the sound-crossing time while clusters undergo major mergers. This may lead to a substantial contamination of X-ray flux-selected cluster samples by less massive, but dynamically active clusters. This bias needs to be quantified before cosmological conclusions based on the cluster population can be considered reliable.

Massive and compact GCs are also efficient strong lenses. This gives rise to the expectation that strong lensing should be particularly frequent in X-ray selected cluster samples, and in fact many X-ray luminous clusters have been found to be strong gravitational lenses.

However, strong cluster lensing can also be transiently increased by factors $\lesssim 10$ during major cluster mergers (see Chapter 4), on time-scales comparable to the dynamical cluster time-scale. This may lift relatively low-mass clusters above the critical limit for strong lensing which would otherwise be undercritical. Based on a relatively small sample of numerically simulated galaxy clusters, Bartelmann & Steinmetz (1996) pointed out that X-ray selection is not guaranteed to select for the most efficient, strongly-lensing GCs. Early work on the interplay between strong lensing statistics and observational selection effects can also be found in Wu & Mao (1996) and Cooray (1999).

Both effects of major mergers, the enhancement of their X-ray visibility and their strong-lensing efficiency, potentially open a huge reservoir of clusters which would remain unobservable in quiescence. The amplitude of this effect must depend on the frequency of major mergers, and thus on the cosmological model and its parameters. Specifically, merger rates at fixed redshift depend on the amount of DM and DE and its cosmic evolution.

In this Chapter, we address the question how X-ray cluster selection may affect the strong-lensing efficiency of the selected clusters, and what fraction of the optical depth for strong lensing we can expect to be produced by GCs visible above a certain X-ray flux limit. We analyse the four cosmological models introduced in section 1.7 and detailed in Table 2.1.

We combine two semi-analytic methods, one derived by Randall et al. (2002) describing the enhancement of X-ray temperatures and luminosities during mergers, and the other developed in Chapter 4 for calculating strong-lensing cluster cross sections. Cluster merger histories are modelled by merger trees planted in the extended Press-Schechter formalism (cf. Chapter 5 for details).

6.2 Luminosity and Temperature Boost

When GCs undergo violent dynamical events, such as interactions with substantial substructures or mergers with galaxy groups and clusters of comparable mass, the ICM is compressed and heated by ram pressure and shock waves. This results in an overall enhancement of the mean gas temperature and the X-ray emissivity due to

Table 6.1: Best-fit amplitudes and exponents for the temperature (top row) and luminosity (bottom row) boosts during cluster mergers.

quantity	A	B	C	D	E	F
temperature	3.98	0.448	0.96	0.539	3.71	2.81
luminosity	8.28	0.659	0.91	0.316	-0.74	3.29

bremsstrahlung (Section 2.4.2). The dynamics of gas and DM in clusters during major mergers is typically very complicated and usually studied based on numerical simulations (see e.g. Faltenbacher et al. 2006; Poole et al. 2006, 2007; Valluri et al. 2007 for a recent review and applications).

It will be sufficient for our purposes to model the short-term increases in temperature and X-ray luminosity in a simplified manner which captures their important characteristics in a statistically correct way. Such a simplified model is given by Randall et al. (2002). There, the authors derive fitting formulae for the time-dependent increase in average temperature relative to its unperturbed value of the combined system of main cluster and merging body during its interaction.

They employ n-body cluster simulations combined with adiabatic hydrodynamics developed and described in earlier work (Ricker & Sarazin, 2001; Ricker et al., 2000). Shocks in the ICM are extremely well resolved in these simulations, allowing temperature and luminosity increases to be studied in detail.

Randall et al. (2002) find that the total time interval Δt during which the average temperature or bolometric luminosity of the ICM of the system are raised above fixed levels T or L is given by

$$\xi = \sqrt{[(\Gamma - \Gamma_\mathrm{c})^2 - 1](\varepsilon^2 - 1)} + \xi_\mathrm{c}, \tag{6.1}$$

where Γ is the ratio between the quantity in question, T or L, and its unperturbed value T_0 or L_0. The parameter Γ_c is related to the maximum value of the boost, as will be explained below. The time interval is measured in units of the sound-crossing time t_sc of the main cluster body by $\xi \equiv \log(\Delta t/t_\mathrm{sc})$. Assuming isothermal gas, the sound-crossing time is

$$t_\mathrm{sc} \equiv \frac{r_{200}}{c_\mathrm{s}} = r_{200}\sqrt{\frac{\mu m_\mathrm{p}}{k_\mathrm{B}T}}, \tag{6.2}$$

where the virial radius of the DM halo of the main cluster, r_{200}, is taken as a characteristic dimension.

The merger is characterised by the mass fraction of the secondary cluster,

$$f = \frac{M_2}{M_1 + M_2} \ , \tag{6.3}$$

which obviously reaches a maximum value of $1/2$ for equal-mass mergers. The fit parameters Γ_c and ε are then expressed as power laws of f,

$$\Gamma_\mathrm{c} = 1 + A\, f^B \ , \quad \varepsilon = C\, f^{-D} \ , \tag{6.4}$$

and

$$\xi_\mathrm{c} = E\left[\ln\left(M_1 + M_2\right) - F\ln\left(M_1^{1/3} + M_2^{1/3}\right)\right] \ . \tag{6.5}$$

The amplitudes and exponents appearing in the last three equations were calibrated by Randall et al. (2002) against their simulations. They are summarised in Table 6.1 for the boosts in both the temperature and the bolometric X-ray luminosity.

Solving Eq. (6.1) for Γ,

$$\Gamma = \Gamma_\mathrm{c} - \sqrt{1 + \frac{(\xi - \xi_\mathrm{c})^2}{\varepsilon^2 - 1}} \ , \tag{6.6}$$

we see that it allows a maximum value for the boost of $\Gamma_\mathrm{m} = \Gamma_\mathrm{c} - 1$.

We plot the function $\Gamma(\xi)$ for the temperature and the luminosity in Figure 6.1. It shows the temperature and bolometric luminosity of the merging system in units of the pre-merger values as a function of time in the interval between the beginning of the boost ($\Gamma = 1$) to the moment of perfect overlap of the two clusters (and thus of the maximum boost, $\Gamma = \Gamma_\mathrm{m}$). The mass of the main cluster is set to $M_1 = 7.5 \times 10^{14} M_\odot$, and results are shown for four different values for the mass M_2 of the merging substructure.

As intuitively expected, these plots show that the maximum temperature and luminosity reached by the system is larger when the masses involved in the merger process are similar. In that case, duration of the boost is also minimal. Moreover, the curves illustrate that the relative increase in bolometric luminosity exceeds the one in

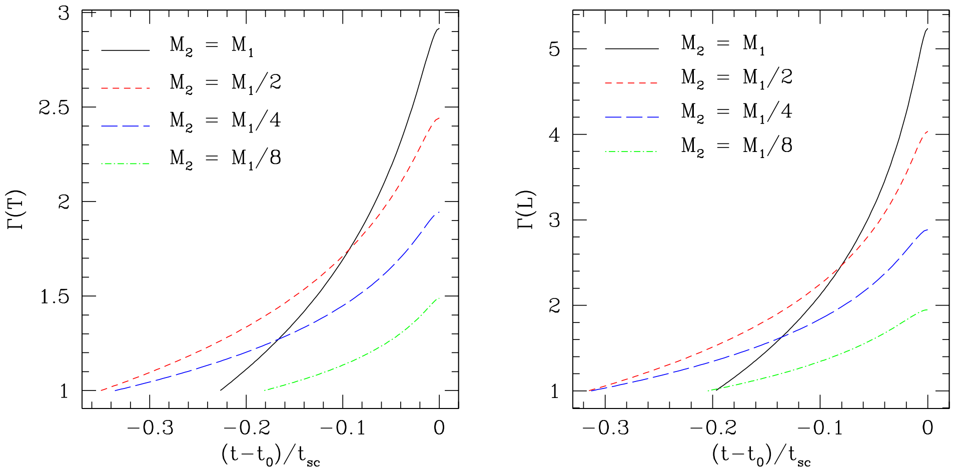

Figure 6.1: The enhancement of temperature (left panel) and luminosity (right panel) of an interacting system according to Randall et al. (2002), where the main cluster has mass $M_1 = 7.5 \times 10^{14} M_\odot$, and the substructure's mass M_2 takes four different values, as labelled in the plot. Time is measured in units of the sound-crossing time of the main structure (Eq. 6.2) and starting from the instant t_0 of maximum boost.

average temperature, reflecting the higher sensitivity of bremsstrahlung emission to the density compared to the temperature.

Finally we emphasise that the fitting formulae for the average temperature and bolometric X-ray luminosity enhancements given above are valid only for head-on mergers. Generalisations to non-zero impact parameters are given in Randall et al. (2002), but we assume head-on mergers throughout for simplicity. Note that, for a non-head on merger, the duration of the boosts in temperature and luminosity is larger, but their maximum values are smaller. These are two somewhat counter-acting effects, and we expect the total influence to be not significant for our pourposes.

6.3 Fluxes Obtained From Individual Clusters

We shall refer mainly to one particular set of observed GCs when comparing to observations, i.e. the ROSAT-ESO Flux Limited X-ray cluster sample (*Reflex*, Collins et al. 2000; Schuecker et al. 2001; Böhringer et al. 2001), which was drawn from the ROSAT All-Sky Survey (RASS, Snowden & Schmitt 1990). In this section, we describe the construction of a synthetic cluster sample imitating the procedure used for the construction of the *Reflex* sample.

6.3.1 Ideal Flux

We describe the merger history of individual clusters by means of the merger trees constructed based on the extended Press & Schechter (1974) theory in Section 5.2. Thus, the only information we have on each individual GC is its mass and its redshift. We first related these properties to the *idealised* X-ray flux, that is the flux that would be measured in the absence of any instrumental issue. Next, we shall add background noise, convolution with the point-spread function (PSF), and the detector response.

We start from the virial relation between mass, redshift and temperature of the ICM (see also Eq. 2.56),

$$k_{\rm B}T = 4.88\,{\rm keV}\left[\frac{M}{10^{15}M_\odot}h(z)\right]^{2/3}, \tag{6.7}$$

where $h(z)$ is the (reduced) Hubble parameter at the redshift z of the cluster (see Section 1.5), and the normalisation constant is calibrated with the cluster simulations of Mathiesen & Evrard (2001).

Introducing the temperature-mass relation Eq. (6.7) into a merger tree, we assign temperatures to individual clusters. When a cluster is merging with a substructure according to its merger tree, we can either ignore the temperature and luminosity boost caused by the merger. In this case, only the increasing cluster mass will cause the temperature to rise. Or, we can boost the temperature according to the description outlined in the previous section, depending on the state of the merger process. In both cases, we obtain a unique temperature for each cluster at each redshift step in its merger tree.

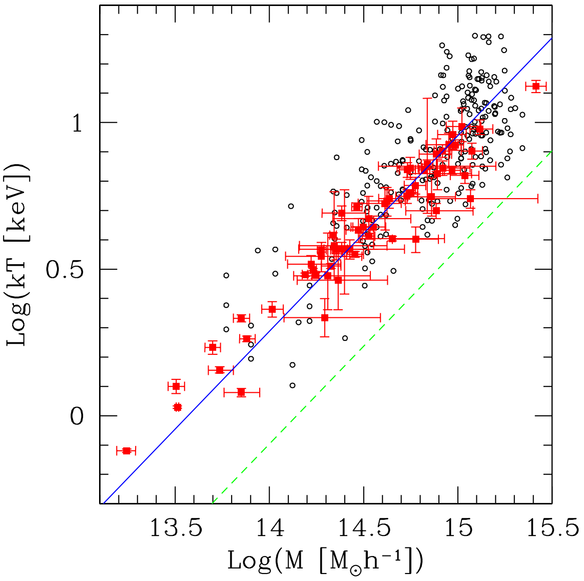

Figure 6.2: The mass-temperature relation of our synthetic cluster sample. Black, empty circles represent our sample clusters at low redshift. The green dashed line is the original $M - T$ relation given by Eq. (6.7). The red filled squares with errorbars are the observed clusters of the HIFLUGCS sample, and the blue solid line is a relation with the same slope as Eq. (6.7) but with a normalization higher of a factor $\sim$ 2.

We note here that no statistical fluctuations are taken into account in our assignment of X-ray temperatures and luminosities to clusters of a given mass. Thus, once the mass of the main cluster body and a merging subclump are fixed, the same merger phase will always lead to the same temperature increase. However, mergers do introduce statistical fluctuations into the temperature-luminosity relations of our simulated clusters. We shall return to this point further below.

We also clarify that we consider only binary mergers here. Whenever a cluster undergoes a multiple merger, we model only the one with the most massive substructure, neglecting the others in comparison. Since the simultaneous interaction of a GC with more than one massive substructure is an extremely rare event, we believe that this approximation is sufficiently accurate for our pourposes.

Figure 6.2 shows the relation between the mass and the temperature for low-redshift model clusters in our synthetic sample, after the temperature boost due to mergers has been applied. The normalization is obviously higher (a factor $\sim$ 2) than that of the original relation Eq. (6.7) because cluster mergers always increase the cluster temperatures. However, the slope of the relation is well preserved, and the resulting sample fairly reproduces the observed HIFLUGCS cluster sample (Reiprich & Böhringer, 2002), which mostly contains low-redshift clusters. This supports the validity of our model.

Next, we need to derive the ideal flux from the mass, the redshift and the temperature. We do so using the publically available software package `xspec` (Arnaud, 1996), assuming that the ICM can be described by a Raymond-Smith (Raymond & Smith, 1977) plasma model. We set the metal abundance to $Z = 0.3Z_\odot$ (Fukazawa et al. 1998; Schindler 1999, see also Bartelmann & White 2003). We normalise the spectrum by means of the observationally calibrated relation

$$L = 2.5 \times 10^{43} \mathrm{erg\,s^{-1}} h^{-2} \left(\frac{k_{\mathrm{B}} T}{1.66\,\mathrm{keV}} \right)^{2.331} , \tag{6.8}$$

derived by Allen & Fabian (1998), where L is the bolometric X-ray luminosity (see also Mushotzky & Scharf (1997); Reichart et al. (1999); Hashimoto et al. (2002) for some discussion on the redshift evolution of this $L_{\mathrm{bol}} - T$ relation).

Several authors (Stanek et al., 2006; O'Hara et al., 2006; Pratt et al., 2006) have discussed that the observed scatter in the temperature-mass and luminosity-temperature relations might not be entirely caused by recent mergers, but rather be sensitive to the complete merger history of the cluster. However, we verified that the scatter in the natural logarithm of mass around the best fit mass-luminosity relation that we obtain for nearby clusters in our synthetic sample is $\sigma_{\ln M} \simeq 0.4$ and thus agrees well with the observed value for the HIFLUGCS data (Reiprich & Böhringer, 2002; Stanek et al., 2006). Hence, we conclude that our modeling of mergers introduces scatter into the luminosity-mass relation compatible with the observed scatter, and thus fairly captures the observed statistical fluctuations.

Finally, we take account of the interstellar absorption by neutral hydrogen in the Milky Way. We do so by combining our Raymond-Smith plasma model with the `phabs` multiplicative model component of the `xspec` software, adopting a constant hydrogen column density of $n_H = 4 \times 10^{20}$ cm^{-2}, appropriate for relatively high Galactic latitudes (Dickey & Lockman, 1990).

6.3.2 Instrumental Effects

In constructing the *Reflex* cluster sample, Böhringer et al. (2001) used the count rate received for each individual cluster by the ROSAT PSPC detector in the energy channels covering the $[0.5, 2.0]$ keV energy band. To compute synthetic count rates for each object in our simulated cluster population, we first need to introduce a model for the distribution of the ICM within the clusters. We adopt the isothermal β-model, Eq. (2.50) assuming $\beta = 2/3$ throughout, following Mohr et al. (1999).

The resulting gas-density profile is

$$\rho(r) = \frac{\rho_0}{1 + r^2/r_0^2}. \tag{6.9}$$

Its core radius r_0 is related to the X-ray luminosity $L_{\rm band}$ in the [0.5,2.4] keV energy band through

$$r_0 = 0.125\,{\rm Mpc}\,h^{-1} \left(\frac{L_{\rm band}}{5 \times 10^{44} {\rm erg\ s}^{-1}} \right)^{0.2} \tag{6.10}$$

(Jones et al. 1998; see Vikhlinin et al. 2002 for a discussion on the redshift evolution of this relation).

We next convolve the corresponding surface-brightness profile of Eq. (2.51) with the instrumental PSF. The shape of the ROSAT-PSPC PSF is summarised in Bartelmann & White (2003) based on Hasinger et al. (1995). Its shape depends slightly both on the energy channel considered and on the off-axis angle of the source. For simplicity, we shall assume on-axis sources and an energy channel at 1 keV, approximately at the centre of the energy bands considered in the present work.

Background count rates are provided in form of a map on the RASS web page[1]. We use a constant median value of $b = 2.6 \times 10^{-4}$ s^{-1} arcmin^{-2}, but note that our results are quite independent of the background correction.

Finally, we obtain the count rate produced by the PSF-convolved, background-corrected surface-brightness profile. We integrate over the complete profile using the `fakeit` command of the `xspec` software, adopting the PSPC response matrix in the $[0.5, 2.0]$ keV energy band.

6.3.3 Nominal Flux

The *nominal flux* $F_{\rm n}$ for the *Reflex* cluster sample is defined as the flux produced in the $[0.1, 2.4]$ keV energy band by a Raymond-Smith model plasma set to redshift zero, with a temperature of 5 keV, metal abundance of $Z = 0.3 Z_\odot$, absorption as given by Dickey & Lockman (1990) and a spectrum normalised so as to reproduce the observed number counts in the energy channels corresponding to the $[0.5, 2.0]$ keV band (Collins et al., 2000; Böhringer et al., 2001).

To each cluster and at each redshift step of its merger tree, we assign a nominal flux exactly in the same way. The only difference between the definitions of our synthetic sample and of the *Reflex* sample is that we normalise the spectrum of the plasma model so as to reproduce the count rates computed at the end of Section 6.3.2.

The *Reflex* cluster sample is flux-limited, in the sense that it contains only GCs with nominal flux $\leq F_{\rm n,lim} = 3 \times 10^{-12}$ erg s^{-1} cm^{-2}. We here adopt the same nominal flux as a threshold for synthetic cluster samples. We shall use the nominal *Reflex* flux limit and four additional lower flux limits in order to create synthetic samples containing a larger number of objects.

The relation between this nominal flux and the ideal flux introduced in Section 6.3.1 (without hydrogen absorption) is shown in Figure 6.3, where the mean difference between the two fluxes, normalised to the ideal flux, and its standard deviation are plotted as functions of the ideal flux itself.

According to the definition given at the beginning of this section, the ideal flux of a cluster is computed in the energy band $[0.5, 2.0]$ keV, while the nominal flux is the flux in the $[0.1, 2.4]$ keV band of a fiducial cluster with fixed physical properties ($Z = 0.3 Z_\odot$, $T = 5$ keV, $z = 0$) that produces the same count rates as the cluster at hand in the $[0.5, 2.0]$ keV band. Since the nominal flux is computed in a wider and softer band than the ideal flux, there is a bias because the nominal flux exceeds the ideal flux typically by $\sim 20\%$. The scatter about the mean is relatively large for small fluxes, but drops to zero as the flux increases because then the effects of PSF convolution

---

[1] `http://www.xray.mpe.mpg.de/cgi-bin/rosat/ rosat-survey`

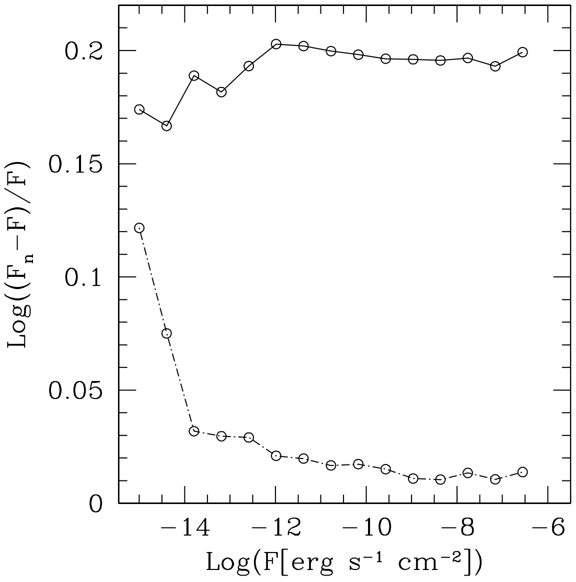

Figure 6.3: The normalized difference between the nominal and the ideal flux as a function of the ideal flux itself is shown for the synthetic cluster population used in this work. The upper solid and lower dash-dotted curves show the mean and the scatter, respectively. The nominal flux is always $\sim 20\%$ larger than the ideal flux, while the scatter in the relation can be neglected only for high fluxes.

and background subtraction are smaller. We conclude from this plot that the ideal may be used instead of the nominal flux, thus saving the time for the computation of hydrogen absorption and instrumental effect, but only when the flux is sufficiently large ($\gtrsim 10^{-12}$ erg s^{-1} cm^{-2}) and accounting for the 20% bias.

6.4 Cluster Number Counts

As already stated, we use here the merger trees produced in Chapter 5 for a set of $\mathcal{N} = 500$ DM haloes with masses uniformly distributed between $10^{14} M_\odot h^{-1}$ and $2.5 \times 10^{15} M_\odot h^{-1}$. Therefore also in this Chapter attention is focused on the two early-DE cosmological models and the two cosmologies with constant w_x detailed in Table 2.1. To the calculation of the strong lensing efficiency we add here calculation of the nominal X-ray flux for each sample cluster at each redshift step. We do that both ignoring and accounting for the effect of mergers which transiently enhance the intrinsic luminosity and temperature (and thus also the nominal flux) of the clusters. Finally, we can combine both pieces of information evaluating the effect of flux selection on the statistics of gravitational arcs in GCs.

It is interesting note in passing how the previous calculations predict the total number of clusters in a flux-limited sample to change as a function of the limiting flux in the different cosmological models, and what the quantitative effect of mergers is in this respect.

We emphasise here that our algorithm for producing synthetic cluster samples is not ideally adapted to cluster-abundance studies because our cluster sample includes only relatively high-mass haloes, and thus the low-mass end of the distribution is not well sampled. Moreover, we did not take into account the likely steepening of the temperature-luminosity relation for low-mass clusters or galaxy groups. While this has no effect on samples of X-ray luminous, hot or strongly lensing clusters, it is likely that the overall number of structures in the different flux-limited samples is overestimated. This is because we tend to assign to objects with very low mass a temperature higher than expected in presence of steepening.

In Figures 6.4 and 6.5, we show the total number of GCs predicted to be observed in the four cosmological models used here as a function of the limiting nominal flux. We plot results obtained by accounting for and ignoring the effects of cluster mergers, and indicate the total number of GCs observed in the *Reflex* cluster sample, extrapolated to the whole sky.

Several interesting pieces of information can be read off these figures. First of all, cluster mergers increase the total number of visible objects by factors between 2 and 3. This factor tends to decrease towards lower flux limits because of two effects. First, at low flux limits, the total number of clusters observable without mergers is larger,

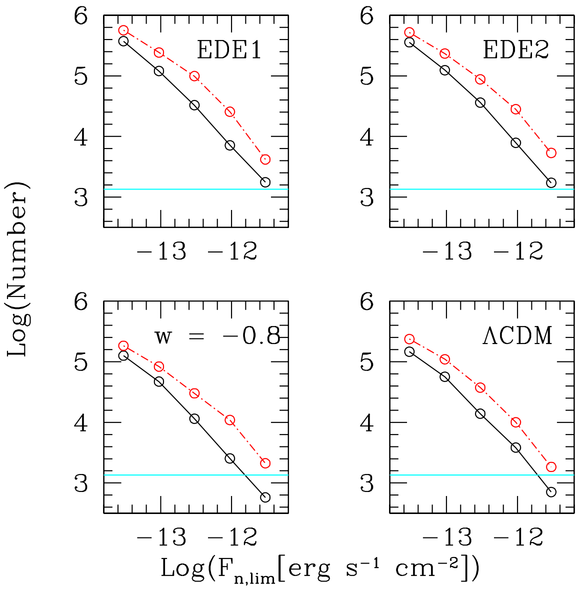

Figure 6.4: The total number of GCs observable on the whole sky, given as a function of the limiting nominal flux for the four different cosmological models considered here. Black solid lines are obtained by ignoring the transient boost due to cluster mergers, red lines are obtained taking it into account. The cyan horizontal line gives the number of GCs obtained from the *Reflex* cluster sample extrapolated to the whole sky ($F_{\rm n,lim} = 3 \times 10^{-12}$ erg $\rm s^{-1}$ $\rm cm^{-2}$).

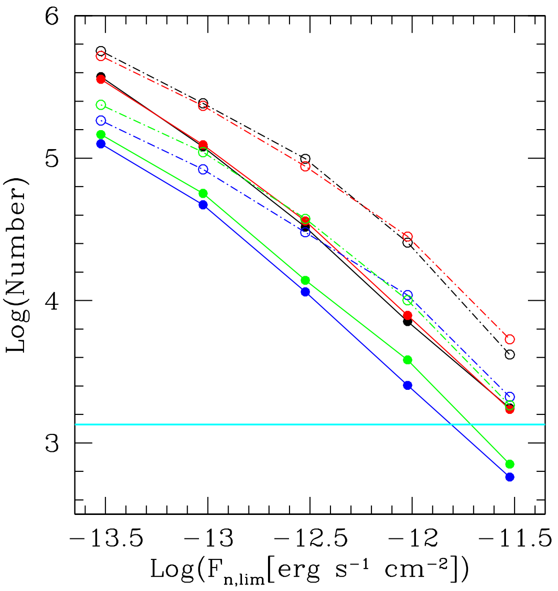

Figure 6.5: As Figure 6.4, but combining all curves in the same plot. Black and red curves are for the EDE1 and EDE2 models, respectively. The blue curve is for the model with constant equation-of-state parameter $w_{\rm x} = -0.8$, and the green line is for the ΛCDM model. For each model, the solid and dashed curves are obtained ignoring mergers and taking them into account, respectively. The horizontal line shows the number of clusters observed in the *Reflex* cluster sample.

thus the fractional increase due to cluster interactions tends to be smaller. Second, at low flux limits, we include low-mass objects into the sample whose merger frequency is lower. We also see that, according to this analysis, only the models with constant equation-of-state parameter are in agreement with the *Reflex* observations, while early-DE models overpredict the cluster abundance by a factor of ~ 2.

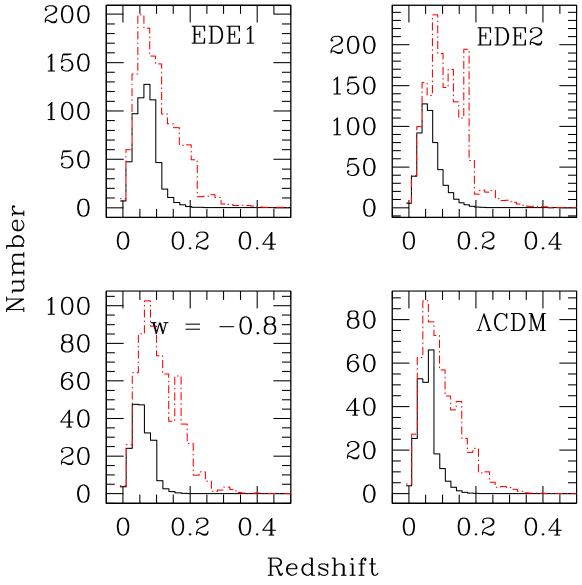

Figure 6.6: Histograms for the cluster redshift distributions expected in the cosmological models studied here, as labelled in the boxes. The limiting flux is the same as for the *Reflex* cluster sample, $F_{\rm n,lim} = 3 \times 10^{-12}$ erg s^{-1} cm^{-2}. As before, the black lower curve does not account for cluster mergers, while the red upper curves do.

In Figure 6.6, we fix the nominal flux limit to that of the *Reflex* sample, $F_{\rm n,lim} = 3 \times 10^{-12}$ erg s^{-1} cm^{-2} and show a histogram of the redshift distribution of observed clusters. Again, we show results with and without the enhancements by cluster mergers. For all models, the number of clusters drops to zero above $z \simeq 0.3$ with mergers, and already above $z \simeq 0.15$ without mergers. The absence of substantial differences between different cosmologies is due to the fact that at low redshift the difference between the structure formation in presence or absence of early-DE tends to disappear (see also the discussion in Chapter 5). It is interesting to note that the observational results from the *Reflex* sample (Collins et al., 2000) are qualitatively very well reproduced only accounting for cluster mergers. Ignoring the effect of interactions in our models leads to an underestimate of objects in the high-redshift tail.

In the context of Figure 6.6, we also note that while the qualitative trend and the peak position of the observed *Reflex* distribution are reproduced, the normalisation is generally too high, for the reasons discussed.

6.5 Results

We finally return to the main purpose of this Chapter, that is probe how cluster selection by their X-ray flux may influence the optical depth of the sample for the production of pronounced gravitational arcs when the effect of cluster mergers are taken into account. In other words, we analyse how the total number of arcs that we can expect to observe in an X-ray selected GC sample depends on the X-ray flux limit of the sample itself. While we have considered only arcs with $d \geq 7.5$ in Chapter 5, we extend the analysis here to arcs with $d \geq 10$.

Figure 6.7 shows contour lines in the mass-redshift plane for the nominal X-ray flux of clusters from our synthetic sample, and for the cross section for arcs with length-to-width ratio larger than $d = 7.5$ for the ΛCDM cosmological model. Contours in the left and right panels were obtained ignoring mergers and taking them into account, respectively. We overplot the flux limit for the *Reflex* cluster sample. The edge in both the X-ray flux and lensing-efficiency contour lines going from the upper left to the lower right corner illustrates the lack of high-mass clusters at high redshift. These figures clearly show the effect of mergers on the lensing efficiency and the average X-ray flux from clusters. Including mergers, the contour lines are much more irregular and extend towards lower masses and higher redshifts, both for the nominal X-ray flux and for the cross section. The geometric suppression of the lensing efficiency at very low redshift is also evident since the black contours in the lower panels never reach $z = 0$, and turn further away from $z = 0$ for lower cluster masses. The lensing efficiency expected to be observed in a ΛCDM model in a *Reflex*-like cluster sample is thus contributed only by those clusters falling between the cyan curve and the lower contour lines in the lower panels.

We emphasise that Figure 6.7 only shows the properties of individual objects in our synthetic sample. In

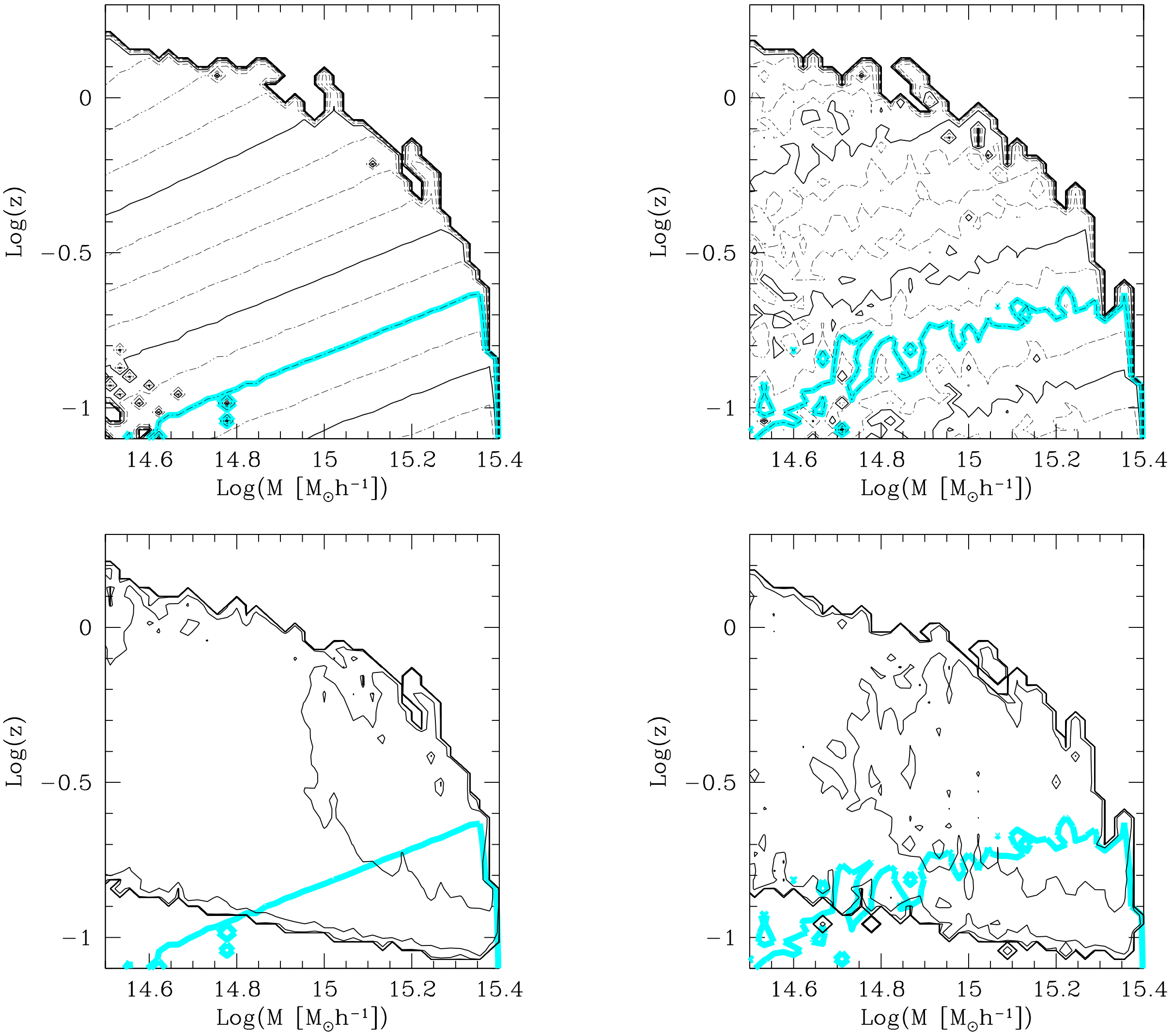

Figure 6.7: Contour lines for the nominal flux (upper panels) and for the lensing cross section for gravitational arcs with $d \geq 7.5$ (lower panels) in the ΛCDM model. The thick cyan contours correspond to the limiting nominal flux of the *Reflex* cluster sample. The upper heavy black contour line in the upper panels corresponds to a flux of 10^{-14} erg s^{-1} cm^{-2}, the others are spaced by one order of magnitude. Analogously, the lowest black contour in the lower panels corresponds to a cross section of 10^{-4} Mpc$^2h^{-2}$, and the others are spaced of one order of magnitude. Merger processes are taken into account in the right panels, while they are ignored in the left ones.

order to find sample properties, this information must be convolved with the cluster mass function. This means that even the small wiggles appearing in the heavy contour in Figure 6.7 when mergers are included will have a substantial effect on lensing statistics and number counts. We prefer not to weight with the mass function in Figure 6.7 to illustrate exclusively the effect of the flux cut. To have an idea of the consequence that small shifts in the $M - z$ plane can have on the quantitative results, the number of structures in the narrow mass interval $14.5 \leq \log M \leq 14.6$ doubles when computed for $z \leq 0.10$ compared to $z \leq 0.13$.

Figure 6.8 shows the average optical depth for gravitational arcs with length to width ratio $d \geq 7.5$ and $d \geq 10$ predicted to be observed in a flux-limited X-ray cluster sample as a function of the limiting flux. Results obtained both ignoring and taking account of cluster mergers are shown. As noted in Fedeli & Bartelmann (2007a) (see Chapter 5) before, mergers increase the optical depth by a factor between 2 and 3. The present figure shows that this remains true for all flux limits considered here even when X-ray selection effects are taken into account. Moreover, we note that the slope of the $\bar{\tau} - F_{\rm n,lim}$ relation tends to increase (decrease in absolute value) towards low limiting fluxes. This is due to the fact that the lensing efficiency drops above $z \simeq 0.3$, and approaches zero towards sufficiently high redshifts. Thus, if the flux limit is low enough, the sample contains all the arcs that are produced and that would be observed without selection effects.

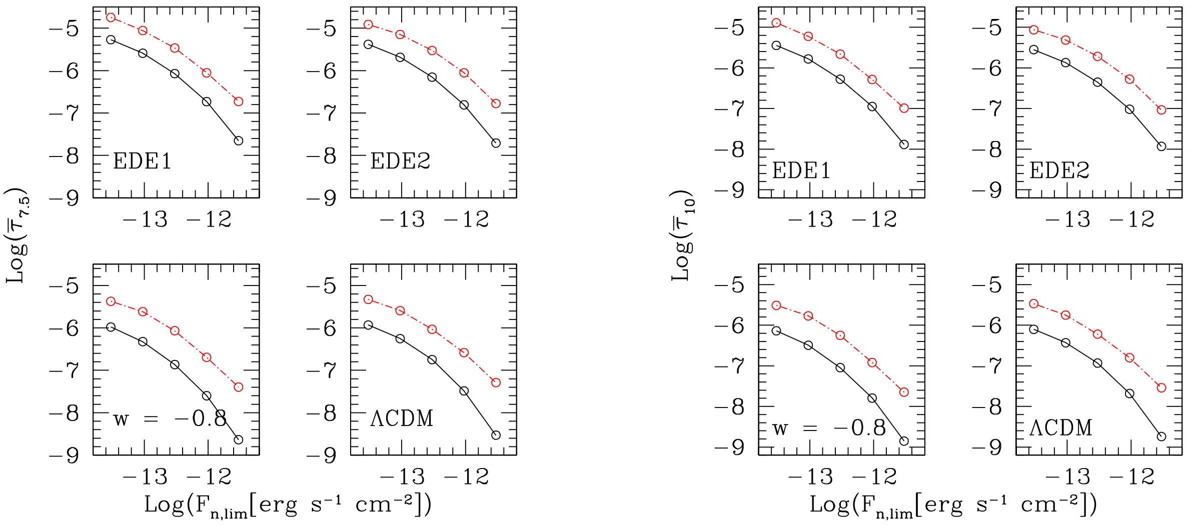

Figure 6.8: The observed average optical depth for arcs with length to width ratio larger than $d = 7.5$ (left panel) and $d = 10$ (right panel) as a function of the nominal X-ray flux limit. Results are shown for the four different cosmologies considered here. Black solid lines represents results obtained by ignoring mergers processes, while broken red lines are obtained taking them into account.

Increasing the length-to-width threshold from $d = 7.5$ to $d = 10$ changes the absolute value of the average optical depth, but not its qualitative behaviour as a function of the limiting flux.

A central result of our study is the ratio between the optical depth for large gravitational arcs in an X-ray selected, flux-limited cluster sample compared to the total, idealised optical depth. Since the average optical depth is related to the number of arcs by a constant factor (determined by the total number density of background sources, see Eq. 3.34), this corresponds to the ratio between the number of arcs expected to be seen in a flux-limited sample of X-ray clusters, and the total number of arcs that would be observable in absence of any X-ray selection effect. This ratio is shown in the right and left panels of Figure 6.9, accounting for and ignoring the transient merger boosts in temperature, X-ray flux and lensing cross section, respectively.

We note that, when we include mergers, the fraction of the average optical depth in an X-ray selected cluster sample increases with respect to the case where mergers are ignored. We attribute this to the facts that (i) cluster mergers tend to enhance the lensing efficiency, which affects both the X-ray selected and the total average optical depth, and (ii) cluster mergers also enhance the clusters' temperature and the X-ray flux, which only affect the X-ray selected optical depth. We also note that there is a slight tendency for models with lower power-spectrum normalisation σ_8 to have a larger fractional importance for the observed average optical depth. For instance, the ratio between the optical depth of X-ray selected clusters to the total optical depth is systematically slightly larger for the model EDE2 ($\sigma_8 = 0.78$) than for the model EDE1 ($\sigma_8 = 0.82$). However, this effect is very small.

6.6 Summary and Conclusions

We have studied here the influence of selection effects on the total observed number of gravitational arcs in X-ray selected GC samples, taking cluster mergers into account.

To perform our study, we considered the assembly history of a synthetic sample of GC. We linked the virial mass of the DM cluster halo to the temperature of the ICM using the virial relation Eq. (6.7). We then used the analytic fitting formulae provided by Randall et al. (2002) for the boost in temperature caused by merger processes between clusters and substructures during the formation. Afterwards, we used the publicly available software package `xspec` (Arnaud, 1996) to convert the (boosted and unboosted) temperature of the ICM into the ideal flux (in front of the instrument) produced by each individual object accounting for redshift, metal emission lines and interstellar absorption. Then, using the response matrix of the PSPC detector on-board the Rosat satellite, we transformed the ideal flux in a photon count rate, also including observational effects such as realistic background count rates and PSF convolution. We finally turned the count rates for each object into a nominal flux, as defined in the construction of the ROSAT-ESO Flux Limited X-ray cluster sample *Reflex*.

We repeated this procedure to the four different cosmological models summarised in Table 2.1 and previously used in Chapter 5 for studying the lensing properties. As an intermediate, qualitative result, we analysed the total

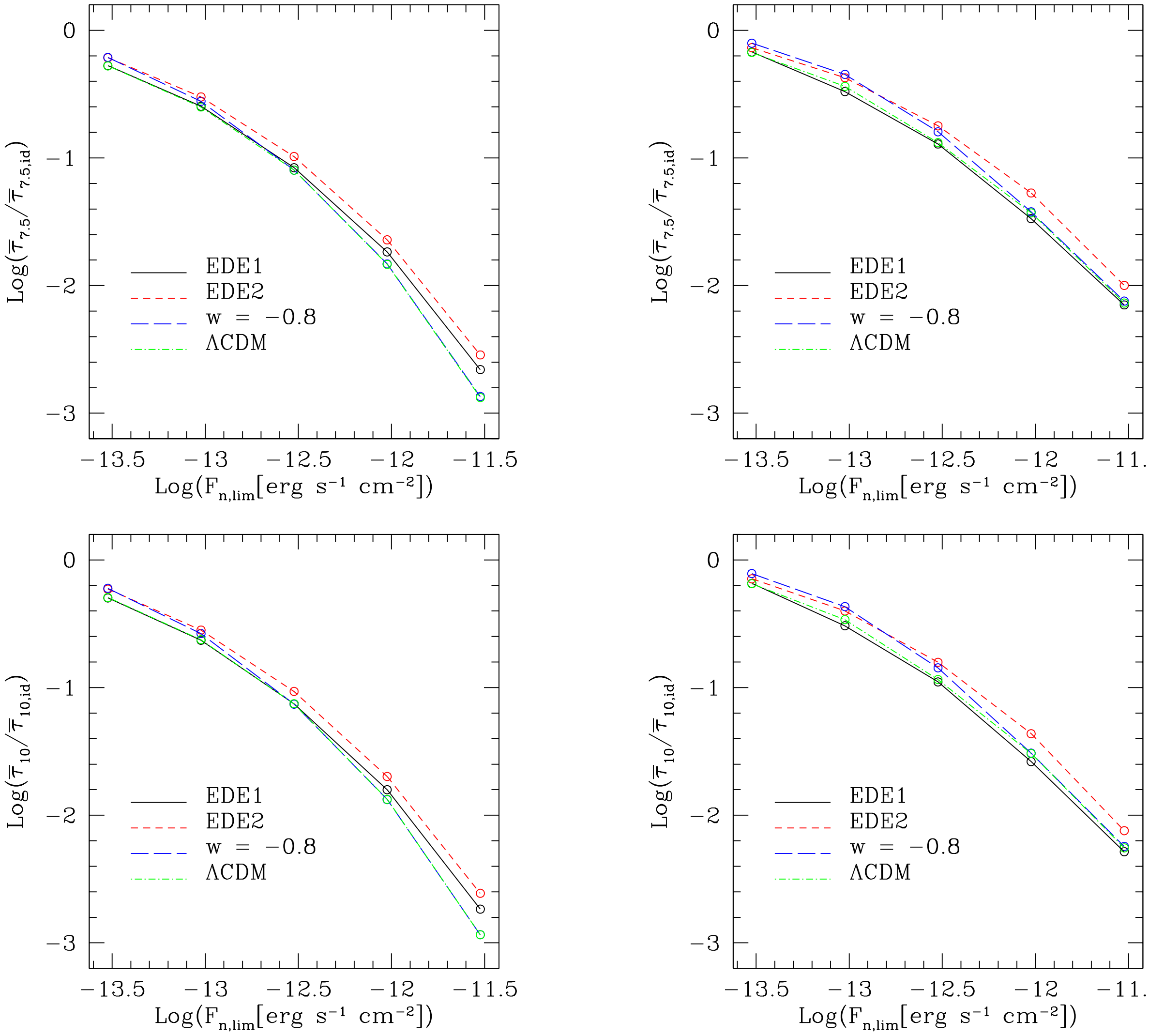

Figure 6.9: The fraction of the optical depth for the formation of large gravitational arcs, contributed by X-ray selected clusters in a flux-limited sample, compared to the total optical depth. Different line styles represent different cosmological models, as labelled in the plot. The effects of cluster mergers are taken into account in the right panels and ignored in the left panels. The upper and lower panels show results for arcs with length-to-width ratios exceeding $d = 7.5$ and $d = 10$, respectively.

number of clusters expected to be visible in X-ray selected cluster samples as a function of the nominal flux limit. We obtain a significant difference between cosmologies with early-DE and the models with constant DE equation-of-state parameter, and also a significant difference due to the introduction of the effect of cluster mergers. In particular, we find that the qualitative redshift distribution of clusters observed in the *Reflex* sample can only be reproduced accounting for merger boosts in temperature and luminosity. Moreover, early-DE models seem to overpredict the total number of observed objects, although our results are not precise at the low-mass end of the distribution, which is irrelevant for strong lensing. Thus, our absolute numbers are likely to be an overestimate. This may hint at a potentially very interesting test for early-DE in particular, and for the dynamics of quintessence models in general, and certainly warrants further investigation in the future.

Finally, our main results are determined by the combination of the nominal X-ray flux selection with the observed strong-lensing statistics. We find that cluster mergers enhance the average observed optical depth by factors between 2 and 3 for all limiting fluxes considered here. We also confirm the result obtained in Chapter 5 ignoring any X-ray selection effects, that the different structure-formation history in early-DE models causes the lensing efficiency to increase by a factor of ~ 3 compared to models with constant equation-of-state parameter for the DE component. This remains true for all limiting fluxes, and we see that, for instance, the same lensing efficiency reached in a ΛCDM model with the help of cluster mergers is reached ignoring mergers in models with early-DE, because of the higher cluster density at moderate and high redshifts. Moreover, the slope of the $\bar{\tau}_{\rm d} - F_{\rm n,lim}$ relation tends to flatten towards lower limiting fluxes, indicating that we are approaching the total average optical depth.

We also find that the ratio of the flux-limited to the total average optical depth is larger when we consider the effect of cluster mergers than when we ignore it. This is due to the fact that the increment in the lensing efficiency affects both the flux limited and the ideal optical depth, while the boost in temperature and luminosity affects only the former.

We carried out these calculations for gravitational arcs with length-to-width ratios $d \geq 7.5$ and $d \geq 10$. We find an (expected) difference in the absolute value of the average optical depth, while the trend with the limiting X-ray flux is qualitatively unchanged.

Predicting the number of long and thin gravitational arcs to be observed in X-ray selected cluster samples and in different cosmological models will be very useful in the near future. Forthcoming strong lensing surveys (Cabanac et al., 2007) and the development of automatic detection algorithms for strong lensing features (Lenzen et al., 2004; Horesh et al., 2005; Seidel & Bartelmann, 2007) will allow to place further constraints on the dynamics of structure formation in a universe dominated by DE (see also the discussion in Section 3.6).

Chapter 7

Effects of Halo Concentration Distribution on Strong-lensing Optical Depth and X-ray Emission

7.1 Introduction

It is widely accepted now that DM halos in both simulations and reality are less concentrated, i.e. have larger relative core sizes, the more massive they are (see Chapter 2.3.5 and Wu & Xue 2000; Buote et al. 2007; Comerford & Natarajan 2007). This is interpreted as a consequence of hierarchical, bottom-up structure formation. More massive halos form later, in a less dense environment, and thus reach lower central densities. The variety of their individual formation histories gives rise to a concentration distribution that simulations show to be approximately log-normal with a standard deviation of ~ 0.2.

What effects does this fairly broad concentration distribution have on observable properties of GCs, most notably their strong gravitational lensing cross sections and their X-ray temperatures and luminosities? The log-normal distribution is substantially skewed and allows larger positive than negative deviations from the mean. At fixed halo mass, this should lead to outliers with higher temperature, higher X-ray luminosity, and larger strong-lensing cross sections than expected for the nominal concentration value.

How are such expectations to be extrapolated to cluster samples? Above a given mass limit, halos with lower mass and generally higher concentration are much more abundant than more massive and typically less concentrated halos. Mass and concentration have counter-acting effects on most observables. For example, at fixed concentration, more massive halos are more efficient lenses as well as hotter and more luminous X-ray emitters. However, since the concentration is decreasing with increasing mass, these effects are at least partially reduced.

Here, we study the effect of the concentration distribution on several cluster properties. We use the simulated merger trees of cluster-sized DM halos constructed for the ΛCDM model in Chapter 5. For the synthetic cluster population, concentrations are randomly drawn from a log-normal distribution. We focus on three observable quantities, namely the strong-lensing efficiency and the X-ray temperature and luminosity of these clusters, and model all of them with semi-analytic algorithms taking the importance of major mergers into account.

Earlier studies on the sensitivity of strong lensing to the concentration of DM halos and its scatter exist. In particular, Wyithe et al. (2001), Keeton & Madau (2001) and Kuhlen et al. (2004) focused on the statistics of multiple images as a probe of the inner structure of halos, in order to put constraints on the DM self-interaction cross section, on the inner slope of the density profile and on the equation of state parameter for DE, respectively. In these studies isolated and spherical cluster models were always considered. In Oguri et al. (2001) the effects of the concentration and inner slope of DM halos on arc statistics were considered, again assuming axial symmetry for both sources and lenses. Finally, in Hennawi et al. (2007), n-body simulations were used to analyse the dependence of strong lensing cross section on several cluster properties.

7.2 Dark-matter Halo Concentration

As announced in Section 2.3.5, three different algorithms were proposed in the past to relate the concentration to the virial mass of a DM halo. The mass-concentration relation produced by these prescriptions is showed in Figure 2.6, and some details about them are given in the following.

The first prescription, by Navarro et al. (1997), defines the formation redshift z_c of a DM halo of virial mass M_{200} collapsed at redshift z as the redshift when half of the final mass was first contained in progenitors more massive than some fraction f of M_{200}.

Based on the extended Press & Schechter (1974) formalism (Section 2.3.3), z_c can then be evaluated as a function of f, z and the final mass M_{200}. In line with hierarchical structure formation, NFW assumed the scale density, which depends only on the concentration once the cosmology is fixed, to be directly proportional to the mean matter density of the Universe at z_c, with a proportionality constant C. They showed that the $c-M$ relation found in a set of numerically simulated, relaxed DM halos at $z=0$ is well reproduced if $f \simeq 0.01$ and $C \simeq 3\times10^3$. This holds for several different cosmological models and initial density-fluctuation power spectra.

Bullock et al. (2001) confirmed that this algorithm works well for $z=0$, but predicts too high halo concentrations at higher redshifts. They require that the typical halo mass $M_*(z_\mathrm{c})$ (see Section 2.2.4) at the halo-formation redshift z_c be a fixed fraction f of the final halo mass M_{200}. They also relate the scale density of the halo to the critical density at the formation redshift, but use a different definition for the scale density. The concentration found in this way scales with redshift as $c \propto (1+z)^{-1}$, in contrast to the much shallower redshift dependence in the NFW algorithm.

Finally, Eke et al. (2001) proposed an alternative explanation for the $c-M$ relation, using a single parameter instead of the two parameters C and f and avoiding problems of the algorithm by Bullock et al. (2001) with the truncated power spectra of warm DM cosmogonies. They define the halo-formation redshift z_c implicitly by

$$D_+(z_\mathrm{c})\sigma(M_\mathrm{s})\left[-\frac{d\ln\sigma(M_\mathrm{s})}{d\ln M}\right] = \frac{1}{C}\,, \tag{7.1}$$

where M_s is the mass contained within $2.17r_\mathrm{s}$, the radius of maximum circular velocity for the NFW density profile, and $\sigma(M)$ is the standard deviation of density fluctuations on the mass scale M. They then equate the scale density as defined by Bullock et al. (2001) to the spherical collapse top-hat density at the formation redshift.

The $c-M$ relation by Eke et al. (2001) is probably the most general and physically best motivated. It makes use of a single fit parameter and turned out to reproduce halo concentrations in a variety of cosmologies, including those with dynamical DE (Dolag et al., 2004). It reproduces the results of the algorithm by Bullock et al. (2001) for galaxy-sized objects, but reveals significant differences on cluster scales, as shown in Figure 2.6 and will be discussed later on.

At fixed halo mass and formation redshift, the concentration parameters of numerically simulated DM halos are log-normally distributed around the median value c_0 reproduced by the algorithms described above,

$$p(c)dc = \frac{1}{\sigma_c\sqrt{2\pi}}\exp\left[-\frac{(\ln c-\ln c_0)^2}{2\sigma_c^2}\right]d\ln c\,, \tag{7.2}$$

with a standard deviation of $\sigma_c \simeq 0.2$ (Jing, 2000; Bullock et al., 2001; Dolag et al., 2004).

The log-normal distribution of Eq. (7.2) is skewed towards high concentrations. Its maximum occurs at $c_\mathrm{m} = c_0\exp\left(-\sigma_c^2\right) < c_0$, and the probabilities for $c<c_0$ and $c \geq c_0$ are equal. The mean concentration is (Coles & Jones, 1991)

$$\mu_1 = c_0\exp\left(\sigma_c^2/2\right)\,, \tag{7.3}$$

its variance is

$$\mu_2 = \mu_1\left[\exp\left(\sigma_c^2\right)-1\right]\,, \tag{7.4}$$

and the skewness is

$$\mu_3 = \frac{1}{\mu_1^3}\frac{\exp\left(3\sigma_c^2\right)-3\exp\left(\sigma_c^2\right)+2}{\left[\exp\left(\sigma_c^2\right)-1\right]^3}\,. \tag{7.5}$$

Setting $\sigma_c = 0.2$, we find $\mu_3 \simeq 70/c_0^3 > 0$, showing that the distribution Eq. (7.2) is substantially skewed towards high c. Thus the probability of finding concentrations $c \gg c_0$ is considerably larger than for $c \ll c_0$. This is also seen when computing the ratio of the absolute deviations $|c-c_0|$ for $c>c_0$ and $c<c_0$, which is

$$\frac{\langle|c-c_0|\rangle_+}{\langle|c-c_0|\rangle_-} = \frac{\mathrm{erf}\left(\sigma_c/\sqrt{2}\right)+\left[1-\exp\left(-\sigma_c^2/2\right)\right]}{\mathrm{erf}\left(\sigma_c/\sqrt{2}\right)-\left[1-\exp\left(-\sigma_c^2/2\right)\right]}\,, \tag{7.6}$$

with the error function $\mathrm{erf}(x)$. For $\sigma_c = 0.2$, this ratio becomes ~ 1.28, indicating that the absolute deviation for $c>c_0$ is on average $\sim 30\%$ larger than for $c<c_0$. We shall return later to this issue to explain some of our lensing statistics results.

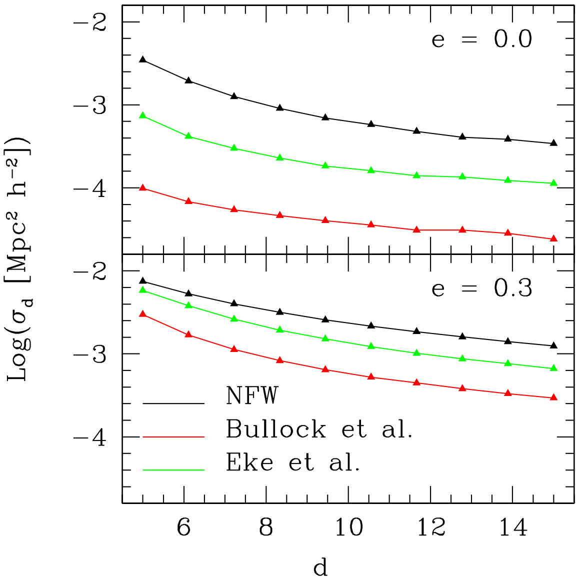

Figure 7.1: The cross section for arcs with length-to-width ratio $\geq d$ is shown as a function of d. The mass of the lensing halo is $2 \times 10^{15} M_{\odot} h^{-1}$, the lens redshift is $z_{\rm l} = 0.3$ and the source redshift is $z_{\rm s} = 1$. Results for three different prescriptions for $c - M$ relation are presented as labeled in the plot. The two panels show results for axially-symmetric (top) and elliptical (bottom) lenses with an isopotential eccentricity of $e = 0.3$.

7.3 Cluster Population

We model the GC population using one of the merger-tree sets used in Chapters 5 and 6, namely the one constructed for the ΛCDM cosmological model.

As in Chapter 5, we twice compute the strong-lensing efficiency of each DM halo at each redshift step, first assuming that the halo can be characterised by an unperturbed NFW density profile with elliptical isopotential contours and a second time including the merger process experienced by the halo, modeled as shown in Section 5.3.

Given the mass and the redshift of a halo in the sample, we use the algorithm by Eke et al. (2001) to compute the nominal concentration $c_0(M, z)$. Again, we distinguish two cases in the strong-lensing analysis, assigning either the nominal concentration c_0 to the halo or a value drawn randomly from the log-normal distribution Eq. (7.2) with a standard deviation $\sigma_c = 0.2$ about c_0.

We thus carry out four strong-lensing analyses for all halos in our $\mathcal{N} = 500$ merger trees, ignoring or including the effects of merger events and the scatter of the concentration about its nominal value set by the $c - M$ relation. Note that this Monte-Carlo generation of merger trees should be considered as a random experiment, representative of the evolution history of the entire cluster population. In line with this view, we draw a new value of the concentration at each new redshift step for each DM halo.

The optical depth per unit redshift that is obtained in the end is computed according to Eq. (5.8), therefore it is simply a sum of the cross sections of each individual halo, weighted by the abundance of such halos at the corresponding redshift. Weighting by the mass function causes this sum to be dominated by the halos with the lowest masses that are still capable of producing a non-vanishing arc cross section. Introducing the scatter into the mass-concentration relation can lift low-mass halos above or push them below the strong-lensing threshold. However, the skewness of the concentration distribution makes it more likely that low-mass halos are lifted above the threshold than the reverse. Thus, it is plausible that the log-normal concentration distribution may have a potentially significant effect on the strong-lensing optical depth.

7.4 Results

7.4.1 Different Concentration Prescriptions

Before we continue, it is interesting to assess how the strong-lensing cross sections differ for the different $c - M$ relation algorithms outlined in Section 7.2. At the same mass and redshift, higher concentrations should push the

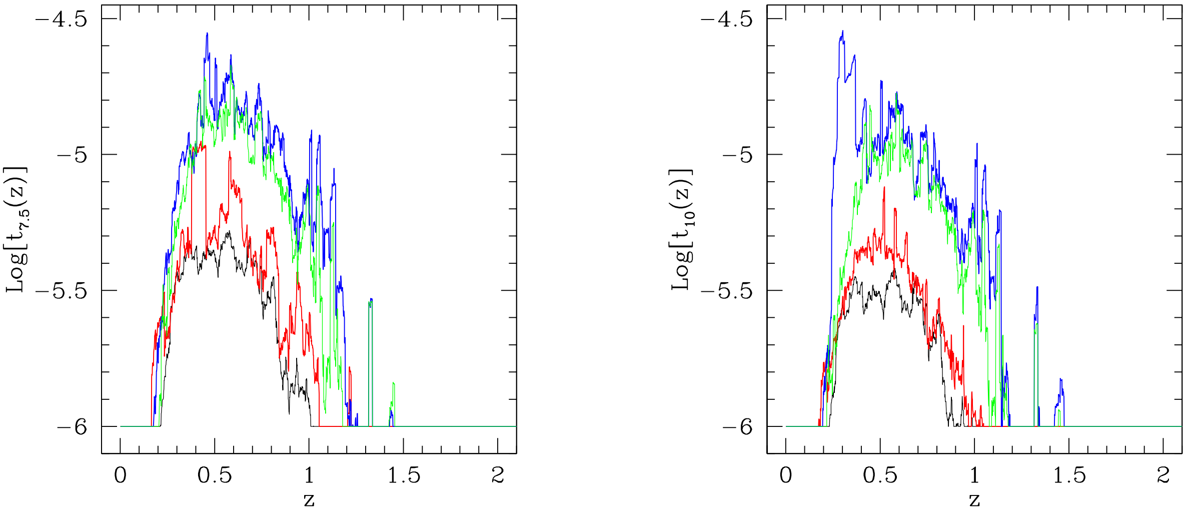

Figure 7.2: *Left panel.* Optical depth per unit redshift for arcs with length-to-width ratio $d \geq 7.5$ as a function of the lens redshift. The thin black and green lines show the results obtained ignoring and accounting for cluster mergers, respectively, both using the nominal $c - M$ relation. The heavy red and blue curves include the scatter in the $c - M$ relation. *Right panel.* Similar to the left panel, but for arcs length-to-width ratios $d \geq 10$, and using a different random-number seed.

critical curves of a lensing halo outwards, thus increasing its strong-lensing cross section.

Results are shown in Figure 7.1, where we plot the cross section for gravitational arcs with length-to-width ratios $\geq d$ as a function of d, using the three algorithms for the $c - M$ relation. We also show the difference between axially-symmetric and elliptical lenses.

Evidently, the impact of different concentrations is much reduced for elliptical compared to circular lenses. For example, if we focus on $d = 10$, we note that the cross sections differ by a factor of ~ 4 for elliptical lenses, while for axially-symmetric lenses, this factor grows up to ~ 20. This is owed to the fact that halo ellipticity largely increases the strong-lensing cross section (Meneghetti et al., 2003b; Oguri et al., 2003; Meneghetti et al., 2007), causing the lensing efficiency to be less sensitive to the internal structure of the lens.

Next, we see that the original NFW prescription for the $c - M$ relation yields the largest cross sections for all values of d. As explained in Section 7.2, this is because the NFW prescription performs well at redshift zero,but overpredicts concentrations at higher redshift. At $z = 0.3$, where we placed the lens, the concentration is thus substantially overestimated, resulting in a very large cross section.

Concentrations computed using Bullock et al. (2001) and Eke et al. (2001) algorithms agree on galactic scales, but differ on cluster scales. Although results obtained with them both fall below the NFW result, they produce quite different cross sections for all d. In particular, the Eke et al. (2001) algorithm yields results falling in between those obtained with the NFW and Bullock et al. (2001) prescriptions, respectively. Such conclusions are in qualitative agreeement with Figure 2.6.

This illustrates that the choice of the $c - M$ relation is very important in analytic and semi-analytic models of GC lensing since different concentrations can have a large effect on the strong-lensing properties. The factors exceeding one order of magnitude between different prescriptions shown in Figure 7.1 for axially symmetric lenses are particularly striking in this regard.

We compared strong-lensing cross sections for several DM halos extracted from a high-resolution numerical simulation with those of analytic lens models with NFW density profile with the same mass and redshift, an isopotential eccentricity of 0.3 and with each of the three different algorithms for the $c - M$ relation. We generally find the best agreement of the strong-lensing efficiencies for concentrations computed with the algorithm by Eke et al. (2001). This further supports the plausibility of this algorithm for the $c - M$ relation. From now on, we assign fiducial concentrations by means of the Eke et al. (2001) algorithm for the $c - M$-relation.

7.4.2 Scatter in the Concentration

We now proceed as anticipated in Section 7.3, performing four different strong-lensing analyses for our DM halo population.

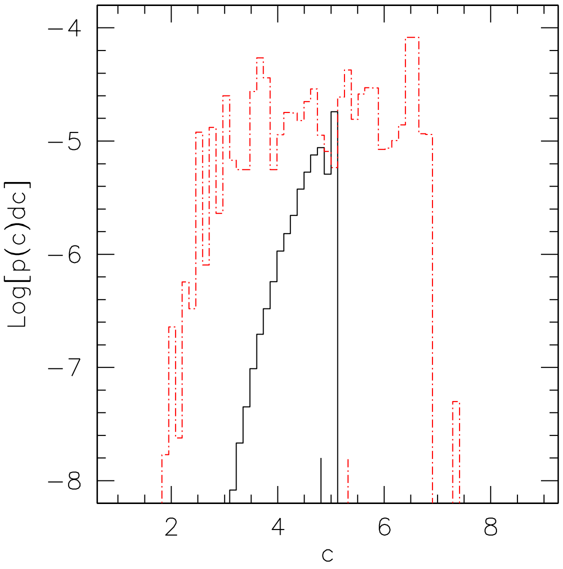

Figure 7.3: Unnormalised distribution of the concentrations for all the halos in our sample with redshifts between $z_1 = 0.28$ and $z_2 = 0.32$. The black solid histogram shows the result obtained adopting the fiducial $c-M$ relation of Eke et al. (2001). The log-normal concentration scatter is taken into account for the red-dashed histogram. The vertical dashes indicate the median concentration in both cases.

We show in Figure 7.2 the optical depth per unit redshift as a function of lens redshift as defined in Eq. (5.8), for arcs with length-to-width ratios $d \geq 7.5$ and $d \geq 10$ respectively. Results are shown both including and ignoring the effect of cluster mergers, and both assuming the ideal $c-M$ relation and introducing a concentration scatter consistent with the log-normal distribution of Eq. (7.2).

For the two cases $d \geq 7.5$ and $d \geq 10$, we used two different seeds for drawing random concentrations from the distribution in order to gain insight into the effect of limited statistics.

We first note the general trend that the introduction of the scatter in the $c-M$ relation systematically increases the optical depth, and this is true irrespective of whether halo mergers are taken into account or ignored. This is a consequence of the skewness of the concentration distribution, cf. Section 7.2. Since concentrations much larger than the fiducial value are more probable than much lower concentrations, it is more likely for the concentration scatter to increase the strong-lensing cross section rather than the reverse. In other words, halo concentrations become larger on average after introducing the scatter, thus producing a larger optical depth per unit redshift.

In closer detail, we note several local maxima of the differential optical depths obtained after introducing a scatter in the $c-M$ relation. These are caused by individual DM halos with relatively low mass that, due to the random assignment of concentrations, reach a particularly high concentration and thus a large cross section. Because of their low mass, they have a large relative abundance, thus they dominate the sum in the optical depth per unit redshift, Eq. (5.8), and cause the peaks.

The position, width and amplitude of these peaks change of course if the seed for the random-number generation is changed. However, even though the *local* increase in the differential optical depth can be quite significant, the increase in the *total* optical depth, i.e. the integral under the curves in Figure 7.2, is limited to $\sim 40-50\%$, both including or ignoring halo mergers.

To study this in more detail, we concentrate on $d \geq 10$ and the more realistic case when mergers are taken into account. We further select a halo subsample with redshifts between $z_1 = 0.28$ and $z_2 = 0.32$, centred on $z = 0.3$. Since our original cluster sample was randomly drawn from a uniform mass distribution at $z = 0$ and then evolved backwards in time to construct merger trees, each DM halo of mass M_{200} at redshift z needs to be statistically weighted by the abundance of such halos according to the mass function for the cosmological model at hand. We note that appropriate weights are included in the optical-depth calculations, see Eq. (5.8).

Figures 7.3 and 7.4 show the distributions of concentrations and strong-lensing cross sections in the halo subsample. In both figures, we contrast results obtained ignoring the concentration scatter (solid black curves) and taking it into account (red dashed curves). Note that all distributions shown are unnormalised.

Without scatter, the concentration distribution is very peaked, but it flattens and widens when the scatter is taken into account, as one would expect. Note also that both concentration distributions drop very sharply at high

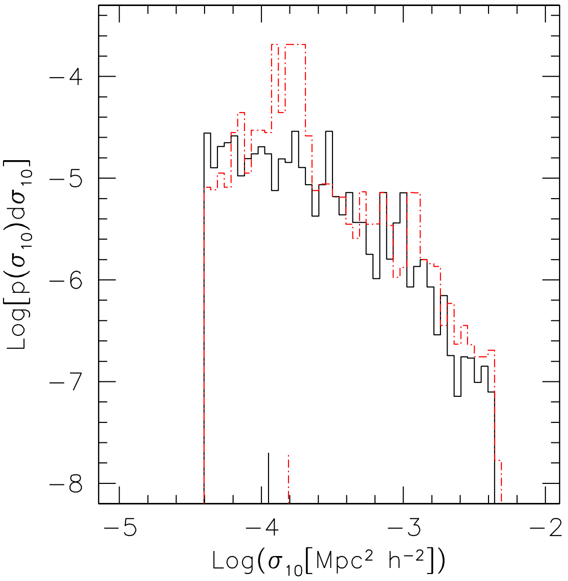

Figure 7.4: Unnormalised distribution of the cross sections for gravitational arcs with length- to-width ratios $d \geq 10$ for all halos in our subsample with redshifts between $z_1 = 0.28$ and $z_2 = 0.32$. As in Figure 7.3, the black solid and red dashed histograms show results ignoring the concentration scatter and accounting for it, respectively. Dashed vertical lines mark the median cross sections for both cases.

concentrations. This reflects the mass cutoff in our halo sample, since high concentrations correspond to low masses.

The cross-section distributions behave similarly. However, in this case the sudden cut-off at low cross sections is due to the strong-lensing threshold. For producing large arcs, a halo's caustics need to be sufficiently larger than the available sources. Below this threshold, the strong-lensing cross sections sharply drop to zero. See also Fedeli et al. (2006) or Section 4.3.3 for more discussion of this issue and its implementation.

Finally, the systematic increase of the differential optical depth shown if Figure 7.2 can be further understood as the contribution of two factors. First, we note that the median concentration (and hence also the median strong-lensing cross section) is larger when the concentrations scatter about the mean $c - M$ relation. Second, the significant peaks in Figure 7.4 (note the logarithmic scale!) appearing in the cross-section distribution at relatively low cross sections are produced by rather low-mass halos that dominate the sum in the optical depth per unit redshift because of their large statistical weight.

7.4.3 Lensing Concentration Bias

Another interesting issue that we are able to explore with our halo sample regards the strong-lensing cross sections expected for concentrated halos, and conversely the concentrations expected in efficient strong-lensing halos.

This will allow us to better understand the relative effect of mass and concentration on the amplitude of the strong lensing cross section, and to quantify the bias expected to be found in dark-halo concentration measurements of strongly-lensing clusters. We can then compare such results to those obtained by Hennawi et al. (2007), who carried out among other things a similar analysis on a large set of numerically simulated DM halos.

Figure 7.5 shows the median $\overline{\sigma}_{10}$ and the mean $\langle\sigma_{10}\rangle$ cross sections of the halo subsample, restricted to those halos with a concentration exceeding the threshold on the abscissa. Results are shown both for all halos irrespective of their mass, and only for halos with masses $\geq 7.5 \times 10^{14} M_{\odot} h^{-1}$.

Without mass selection, the curves are flat within the range of concentrations shown. Remarkably, this indicates that low-mass halos with their typically high concentrations have similar mean or median cross sections as high-mass halos and therefore contribute most of the strong-lensing optical depth in the halo subsample because of their high abundance.

This result may seem at odds with the expectation that the lensing efficiency should increase with increasing halo concentration, as illustrated in Figure 7.1 when we discussed the effect of different algorithms implementing the $c - M$ relation. However, note that Figure 7.1 shows results for a single halo mass. If we select only the most massive halos, we find an increase of the mean and median cross sections with the concentration threshold. Thus,

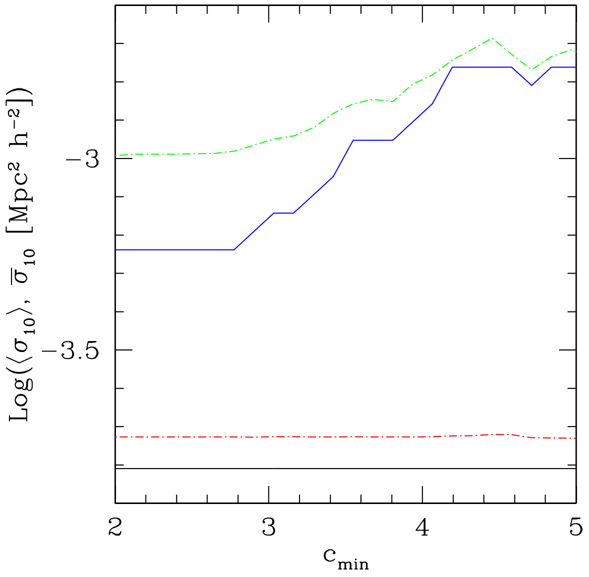

Figure 7.5: The black and blue solid curves show the median, and the red and green dashed curves the mean cross section for arcs with length-to-width ratio $d \geq 10$. Only halos with concentrations above the threshold on the abscissa are included. The bottom pair of lines shows the result without any mass selection, while only halos more massive than $7.5 \times 10^{14} M_{\odot} h^{-1}$ are included in the top pair.

once the mass dependence is effectively suppressed in this way, the concentration dependence of the strong-lensing efficiency can emerge. In other words, although the average strong-lensing cross sections do indeed increase with the halo concentration, this effect is almost precisely cancelled if halos of all masses in a broad mass range are considered.

According to Figure 7.5, the median and mean cross sections of massive halos can increase by a factor of ~ 2.5 as the concentration increases from 2 to 5.

Figure 7.6 shows the mean $\langle c \rangle$ and median $\bar{c}$ concentration of halos with strong-lensing cross sections above the threshold on the abscissa. Again, we compare the complete halo subsample with massive halos above a mass limit of $7.5 \times 10^{14} M_{\odot} h^{-1}$. We note that (i) if we impose no mass threshold, the concentration for strongly lensing halos is always smaller on average compared to the entire population, and (ii) if we allow only massive halos, the mean and median concentrations increase with the lensing cross section.

Specifically, the mean and median concentrations of massive halos shown in Figure 7.6 increase by $\sim 12\%$ across the range of cross-section thresholds shown. If we further raise the mass threshold, the increase rises to $\sim 25\%$.

Without any mass selection, the highest cross sections are produced by the most massive objects, that are on average less concentrated than the low-mass halos. If we restrict the analysis to massive halos, we remove part of the mass dependence of the strong-lensing efficiency and find that the concentrations found in strongly lensing clusters are slightly biased high. Narrowing the mass interval, the effect of the concentration is less diluted by the mass dependence, thus increasing the bias. This result agrees with the corresponding result of Hennawi et al. (2007) and will be discussed later on.

7.4.4 X-ray Concentration Bias

It is now interesting to ask whether comparable concentration biases are expected in X-ray selected cluster samples. At fixed mass, a more concentrated halo creates a deeper potential well and thus causes the intracluster gas to become hotter in thermal and hydrostatic equilibrium. The gas density will also increase, thus raising the X-ray luminosity.

To address this question, we first require a relation between the X-ray observables and mass, the redshift and the concentration of the host DM halo. We achieve this following Eke et al. (1998) who derived an extension to the usual cluster scaling relations described in Section 2.4.3 (see White & Rees 1978; White 1982; Kaiser 1986).

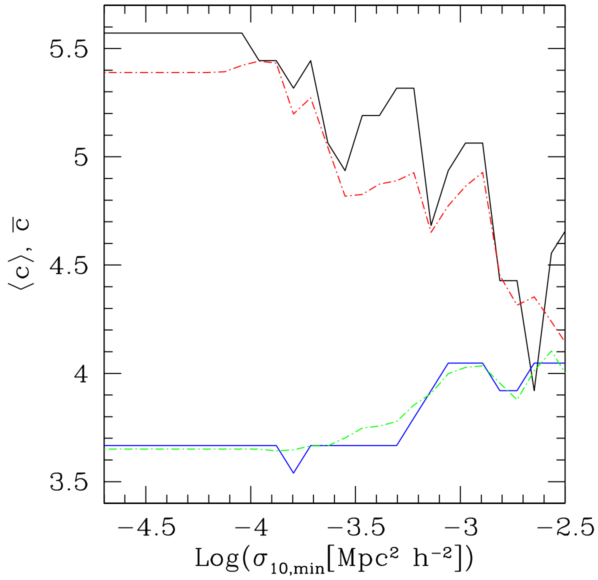

Figure 7.6: The black and blue solid curves show the median, the red and green dashed curves the mean concentration. Only halos with strong-lensing cross sections above the threshold on the abscissa are taken into account. The top pair of curves shows the result obtained without mass selection, while only halos more massive than $7.5 \times 10^{14} M_{\odot} h^{-1}$ contribute to the bottom pair of curves.

First of all, the circular velocity profile for a DM halo with an NFW density profile is (Navarro et al., 1997)

$$\left[\frac{v(r)}{v_{200}}\right]^2 = \frac{r_{200}}{r}\frac{F(cr/r_{200})}{F(c)}\,, \tag{7.7}$$

where v_{200} is the circular velocity at r_{200}, that is $v_{200}^2 \equiv GM_{200}/r_{200}$. This distribution peaks at $r \simeq 2r_{200}/c$, corresponding to

$$v_{\rm m}^2 \simeq 0.22 v_{200}^2 \frac{c}{F(c)}\,. \tag{7.8}$$

This characteristic velocity of the system measures the depth of its potential well. If only gravity or other scale-free processes like pressure gradients or hydrodynamical shocks dominate within the cluster, any other measure of the potential depth, such as the temperature of the intra-cluster gas, must be proportional to $v_{\rm m}^2$, that is

$$T(M_{200}, z, c) \propto \frac{M_{200}}{r_{200}}\frac{c}{F(c)}\,. \tag{7.9}$$

Now, from the first Eq. (2.43) and the definition of concentration it follows that

$$r_{200} = \left[\frac{3M_{200}}{800\pi\rho_c(z)}\right]^{1/3}\,. \tag{7.10}$$

Inserting this into Eq. (7.9), we can write

$$T(M_{200}, z, c) = C_1 M_{200}^{2/3} h(z)^{2/3} \frac{c}{F(c)}\,, \tag{7.11}$$

where C_1 collects now all the constant factors. Note that this relation retains the mass and redshift dependence of the temperature of the common scaling relation Eq. (2.56), but acquires the concentration dependence from the DM density profile. In particular, the function $c/F(c)$ is a monotonically increasing function of the concentration if $c \gtrsim 2$, which is almost always the case in our halo sample (cf. the concentration distribution in Figure 7.3). It is shown that adiabatic simulations of gas in GCs follow relatively well this type of scaling relation (Eke et al., 1998; Bryan & Norman, 1998). With the introduction of more complex physical processes, like non gravitational heating and radiative cooling, the scaling relation is instead not closely reproduced (Babul et al., 2002; Kay et al., 2002). However, in spite of simplicity, we prefer to stick to it, leaving more complicated models for further study.

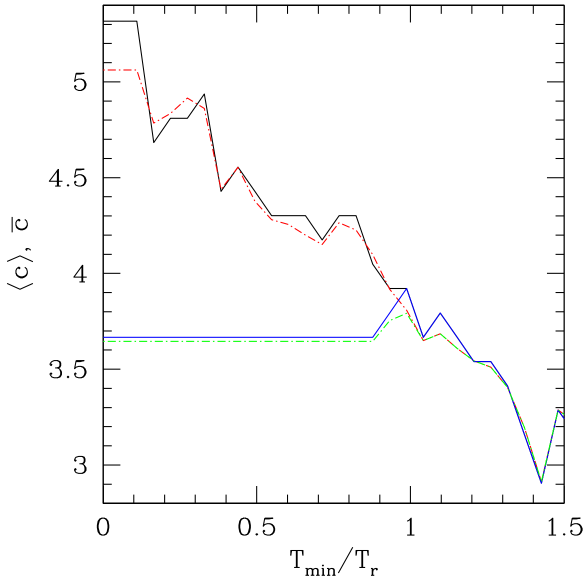

Figure 7.7: Black and blue solid curves show the median, red and green dashed curves the mean concentration for the subsample of DM halos between $z_1 = 0.28$ and $z_2 = 0.32$. Only halos with relative temperatures exceeding the threshold on the abscissa are included. The top pair of curves shows the result without mass selection, while only halos with mass larger than $7.5 \times 10^{14} M_\odot h^{-1}$ contribute to the bottom pair.

Quantifying the bolometric X-ray luminosity of the intra-cluster gas, we start from

$$L_X(M_{200}, z, c) = 4\pi \int_0^{+\infty} r^2 \rho_{\rm g}(r)^2 \frac{\Lambda(T)}{(\mu m_{\rm p})^2} dr \,, \tag{7.12}$$

where $\Lambda(T)$ is the cooling function, depending on the relevant radiative processes, and $\rho_{\rm g}(r)$ is the gas-density profile. We assume that the gas density follows the DM density, $\rho_{\rm g} = f_{\rm g}\rho$, with a constant factor $f_{\rm g}$. This is of course not strictly true, especially in the inner region where the DM density profile is cuspy while the gas distribution forms a finite core due to the gas pressure. However, the final result is insensitive to this simplifying assumption. Further assuming that the intracluster gas is isothermal, the luminosity can be written as

$$L_X(M_{200}, z, c) = 200\Lambda(T) \left(\frac{f_{\rm g}}{3\mu m_{\rm p}}\right)^2 M_{200}\rho_{\rm c}(z) \frac{c^3}{F(c)^2} \,. \tag{7.13}$$

If the main emission mechanism of the intra-cluster gas is thermal bremsstrahlung, then $\Lambda(T) \propto T^{1/2}$. Hence, recalling Eq. (7.11) and collecting all constant factors into C_2, we get

$$L_X(M_{200}, z, c) = C_2 M_{200}^{4/3} h(z)^{7/3} \frac{c^{7/2}}{F(c)^{5/2}} \,. \tag{7.14}$$

The common dependence of the luminosity on the mass and the redshift of the host DM halo Eq. (2.57) is retained again, and an additional dependence on the concentration appears. Note also that the concentration dependence is steeper here than for the temperature. Moreover, the dependence of the bolometric X-ray luminosity on the concentration shown in Eq. (7.14) differs by a factor of $1-(1+c)^{-3}$ from the formula given in Eke et al. (1998). This is because the integral in Eq. (7.12) extends to infinity, while it was limited to the virial radius in Eke et al. (1998). This is unimportant because the missing factor is very close to unity for all reasonable values of the concentration.

In the following, we refer the temperature and the X-ray luminosity of the gas inside each DM halo of our subsample to the temperature $T_{\rm r}$ according to Eq. (7.11) and the luminosity $L_{X,{\rm r}}$ according to Eq. (7.14) of a reference halo with mass $M_{200,{\rm r}} = 10^{15} M_\odot h^{-1}$ placed at redshift $z_{\rm r} = 0$. It has a nominal concentration $c_{\rm r} = 3.74$ according to the Eke et al. (2001) algorithm. Thus, for each halo, we only consider the relative temperature

$$\frac{T(M_{200}, z, c)}{T_{\rm r}} = \left(\frac{M_{200}}{M_{200,{\rm r}}}\right)^{2/3} \left[\frac{h(z)}{h}\right]^{2/3} \frac{c}{F(c)} \frac{F(c_{\rm r})}{c_{\rm r}} \,, \tag{7.15}$$

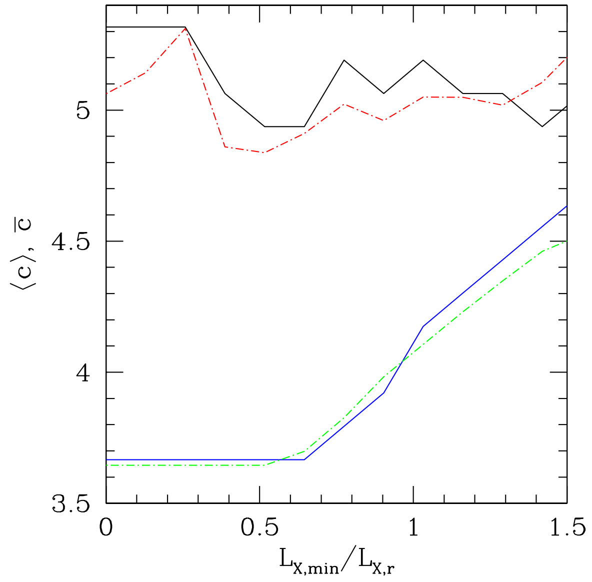

Figure 7.8: Black and blue solid curves show the median, red and green dashed curves the mean concentration for the subsample of DM halos between $z_1 = 0.28$ and $z_2 = 0.32$. Only halos with relative X-ray luminosities exceeding the threshold on the abscissa are taken into account. The top pair of curves was obtained without mass selection, while only massive halos with mass larger than $7.5 \times 10^{14} M_\odot h^{-1}$ contribute to the bottom pair.

and the relative luminosity

$$\frac{L_X(M_{200}, z, c)}{L_{X,\mathrm{r}}} = \left(\frac{M_{200}}{M_{200,\mathrm{r}}}\right)^{4/3} \left[\frac{h(z)}{h}\right]^{7/3} \frac{c^{7/2}}{F(c)^{5/2}} \frac{F(c_\mathrm{r})^{5/2}}{c_\mathrm{r}^{7/2}} \,. \tag{7.16}$$

Figure 7.7 shows the median and mean concentrations for DM halos with a relative gas temperature exceeding the threshold on the abscissa. We show the results both without any mass selection and selecting halos more massive than $7.5 \times 10^{14} M_\odot h^{-1}$. Evidently, the mean and median halo concentrations decrease in both cases as the relative temperature threshold increases. This illustrates that particularly hot gas resides in the most massive halos, quite irrespective of the concentration. Also, if we consider only the most massive objects, a plateau appears at low temperatures because low-temperature clusters are then removed from the sample. Thus, the gas temperature depends so weakly on the halo concentration compared to its dependence on mass that even a narrow mass selection does not reveal the increasing concentration-temperature relation.

Figure 7.8 shows the mean and median concentrations in halos selected for their X-ray luminosity. If all halos in the subsample are included, the curves are almost flat, showing that the concentrations are typically independent of the X-ray luminosity. If only massive halos are included, the mean and median concentrations increase such that the most luminous X-ray clusters can be up to $\sim 25\%$ more concentrated than the entire cluster population.

Hence, unlike for the temperature, we here find increasing mean and median concentrations as a function of the luminosity threshold. In summary, a concentration bias in temperature-selected clusters is not expected, but the most massive and X-ray luminous clusters are typically more concentrated than the population of X-ray clusters indicating a concentration bias similar to that found in strongly-lensing clusters.

The different results for clusters selected by temperature or X-ray luminosity can be understood considering the following numbers. As remarked before, the nominal concentration of the reference cluster is $c_\mathrm{r} = 3.74$. Had we adopted a reference mass of $2.5 \times 10^{14} M_\odot h^{-1}$, the nominal concentration was $c_\mathrm{r} = 4.73$. These two concentrations are 1-σ compatible with the same underlying mass, given the variance of $\sigma_c = 0.2$ in the log-normal concentration distribution. The increase in the gas temperature due to the higher concentration is only $\sim 5\%$, while the X-ray luminosity increases by $\sim 45\%$. On the other hand, the gas temperature drops by a factor of ~ 2.5 because of the lower halo mass, while the bolometric X-ray luminosity drops by a factor of ~ 6.3. On the whole, the ratio between the changes in temperature due to the halo mass and due to the concentration is ~ 12, while the ratio between the changes in X-ray luminosity due to the mass and due to the concentration is ~ 1.9. This shows that the effect of the concentration on the X-ray luminosity is almost comparable to the effect of the mass, but much less important for the temperature.

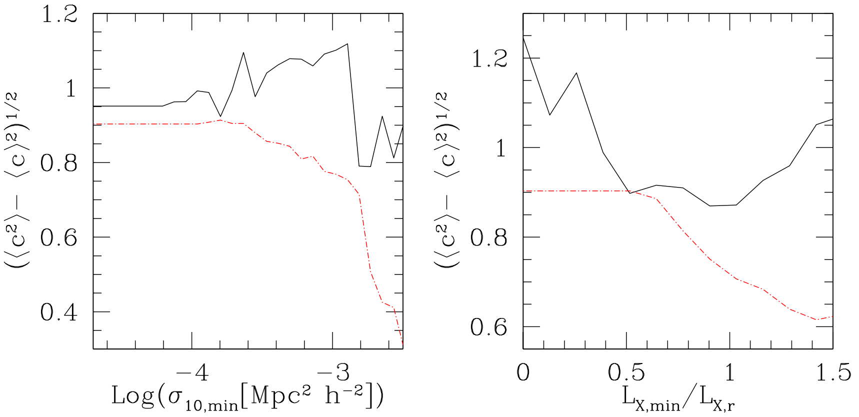

Figure 7.9: The *rms* of the concentration distribution accounting for halos in the subsample with strong-lensing cross sections (left panel) or relative X-ray luminosities (right panel) exceeding the thresholds on the abscissa. The solid black lines are obtained without mass selection, while only massive halos with mass larger than $7.5 \times 10^{14} M_{\odot} h^{-1}$ contribute to the red dashed curves.

In other words, the mass dependence of the gas temperature is overwhelmingly stronger than its concentration dependence, cancelling any kind of concentration bias that could appear in temperature-selected halos. Very hot clusters are actually less concentrated (more massive) than average. On the other hand, the stronger dependence of the luminosity on the concentration allows to invert this trend if only massive clusters are considered. Thus, very X-ray luminous clusters have higher mean and median concentrations than clusters with lower luminosity but comparable mass.

To see which concentrations we can expect in suitably selected cluster samples, we plot in Figure 7.9 the *rms* $\sqrt{\langle c^2\rangle - \langle c\rangle^2}$ of the concentration distribution as a function of the cross-section and X-ray luminosity thresholds, respectively, both with and without further mass selection. According to Figures 7.6 and 7.8, the median and the mean of the distribution are quite similar, hence the distribution itself is quite symmetric, and the *rms* is a good estimator of its width.

Without mass selection, the *rms* always remains around unity. If we introduce mass selection, it is close to unity for the entire subsample, but drops towards 0.4 when only efficient strong lenses are included, and to 0.6 when only very X-ray luminous clusters are included. This means that the concentration distribution tends to narrow in the latter cases.

7.4.5 Additional Effects

Finally, we explore the consequence for our results of two additional effects not included so far. The first is the correlation of the concentration with the triaxiality of DM halos (Jing & Suto, 2002). The second is the ellipticity distribution of projected halos due to the random orientation of the three-dimensional halos with respect to the line-of-sight (Oguri et al., 2003, 2005; Corless & King, 2007). The second effect affects only the strong lensing properties of GCs, for whose lensing potential we assumed an eccentricity of $e = 0.3$ throughout this work. The scaling laws we used for the X-ray characteristics are insensitive to the ellipticity of the DM halo. Besides, the gas distribution approximately follows equipotential surfaces and thus tends to be more spherical than the DM distribution (Gavazzi, 2005).

We assess the impact of these two effects in the following experiment. First, we considered a DM halo with mass $2 \times 10^{15} M_{\odot} h^{-1}$ and redshift $z_l = 0.3$. We computed its cross section for arcs with length-to-width ratio $d \geq 10$, assuming sources at $z_s = 1$, a lensing-potential eccentricity $e = 0.3$ and concentration derived from the algorithm of Eke et al. (2001). Then, we produced $1,000$ triaxial modifications of this original halo by drawing axis ratios from the distributions given in Jing & Suto (2002). The axis ratios allow changing the concentration of each modified halo according to the prescription of Jing & Suto (2002), predicting higher concentrations for more spherical halos. Finally, each modified halo is projected along a randomly selected line-of-sight and the ellipticity of the projected density is computed following Oguri et al. (2003). To each halo is then assigned a new lensing-potential eccentricity assuming that it is half of the eccentricity of the projected density.

As outlined in Jing & Suto (2002), the isodensity surfaces tend to be more elongated near the core of the halo than in its outer regions. Since the innermost part of a GC is most relevant for strong-lensing events, we lowered the minor-to-major and intermediate-to-major axis ratios by 0.15 prior to the projection. This is consistent with

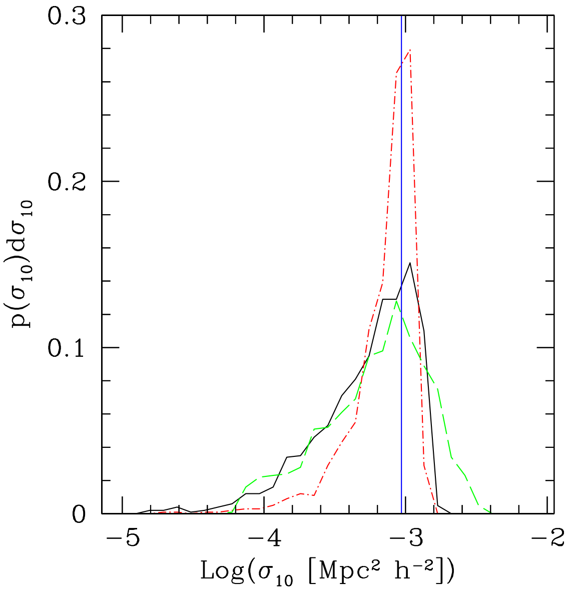

Figure 7.10: Cross section distributions. The vertical blue line shows the cross section for arcs with length-to-width ratio $d \geq 10$ computed for a DM halo of mass $2 \times 10^{15} M_{\odot} h^{-1}$ at redshift $z_{\rm l} = 0.3$ with sources at redshift $z_{\rm s} = 1$ and lensing-potential eccentricity $e = 0.3$. The red dot-dashed line is the distribution of the cross sections caused by the variation of halo concentrations with triaxiality. The green dashed line includes the ellipticity distribution of projected triaxial halos, and the black solid line contains both effects.

Figure 3 of Jing & Suto (2002).

Cross sections were computed for each modified halo, using the new values of the concentration or of the ellipticty, or both. The three resulting cross-section distributions are shown in Figure 7.10. The variation of the concentration with triaxiality introduces additional scatter in the cross section (red dot-dashed line), but significantly less than the concentration scatter introduced before. The small difference between the black solid and the green dashed curves in Figure 7.10 corroborates this conclusion.

The distribution of cross sections obtained after random projections of triaxial halos is centered on the cross section for the original halo with fixed eccentricity $e = 0.3$, indicating that this lensing-potential ellipticity is typical. This confirms the result of Meneghetti et al. (2003b), who found this value by fitting the deflection angle maps of simulated GCs (see also Meneghetti et al. 2005b). The good agreement also shows that the reduced concentration of highly triaxial halos is compensated by the higher ellipticity.

The scatter caused by the ellipticity distribution exceeds that caused by the variation of the concentration with triaxiality, but the total scatter in the cross sections due to halo triaxiality shown in Figure 7.10 is at most comparable to that caused by the intrinsic concentration distribution. Moreover, it does not systematically shift the cross sections towards higher or lower values, hence leaving unchanged the conclusions of this Chapter. It should also be noted that these results are expected to hold if more detailed gas physics (such as cooling and star formation) is included because it tends to affect the inner slope rather than the ellipticity of the cluster mass distribution (Puchwein et al., 2005).

We have applied the same test to halos of different mass and found very similar results. The effect of the variation of halo concentrations with triaxiality on the temperature and luminosity of the X-ray gas is negligibly small.

7.5 Summary and discussion

We have investigated the effect of the scatter in the relation between concentration and mass in DM halos on gravitational arc statistics and X-ray properties of GCs.

We have addressed the effect on strong-lensing cross sections of different implementations of the $c - M$ relation proposed in the literature (Navarro et al. 1997; Bullock et al. 2001; Eke et al. 2001). We found substantial differences, with the algorithms by Navarro et al. (1997) and Bullock et al. (2001) predicting the highest and the lowest cross sections, respectively. We adopt the algorithm by Eke et al. (2001) because it needs only one instead of two free parameters, has been shown to be applicable to cosmological models with dynamical DE (Dolag et al., 2004), and was found to yield strong-lensing results in good agreement with numerical simulations.

This result shows that caution must be applied when modelling GC lenses with NFW density profiles, since different implementations of the $c - M$ relation may yield largely different values for the lensing efficiency, in particular if axial symmetry is assumed.

We then used the Eke et al. (2001) algorithm to compute fiducial concentrations for a sample of $\mathcal{N} = 500$ DM halos with masses between 10^{14} and $2.5 \times 10^{15} M_{\odot} h^{-1}$ at redshift zero. Each halo is evolved backwards in time in discrete redshift steps up to a source redshift randomly drawn for each halo from a parameterisation of the observed redshift distribution of faint blue galaxies, as described in Chapetr 5. When the scatter in the concentration was taken into account, it was drawn from a log-normal distribution around the fiducial value, with a standard deviation of $\sigma_c = 0.2$. The effect of cluster mergers on the strong-lensing cross sections was also included (Torri et al., 2004; Fedeli et al., 2006), although the relative effect of the concentration scatter is insensitive to mergers.

The skewness of the log-normal distribution renders concentrations much above the fiducial value more likely than much below it, thus increasing on average the strong-lensing cross sections. Thus, the total, average optical depth, and hence also the total number of arcs expected on the sky, is increased by up to 50% by the concentration scatter. Moreover, the optical depth per unit redshift displays isolated significant peaks which are due to individual DM halos with relatively low mass that happen to reach a particularly large concentration. Such halos can thus be turned into efficient lenses and contribute strongly to the optical depth because of their high abundance.

We then used our merger trees to better understand the relationship between dark-halo concentrations and their lensing efficiency. We found that selecting halos by concentration yields average cross sections similar to those of the complete sample. This shows that the higher concentrations of lower-mass halos compensates for their lower masses in terms of their strong-lensing efficiency until their caustic curves become too small compared to the sources to produce large arcs. Massive halos, however, reveal the concentration-dependence of the strong-lensing cross sections.

Conversely, the median and mean halo concentrations do not increase if the most efficient lensing halos are selected. However, selecting massive strong lenses reveals the dependence of the cross sections on the concentration, yielding median and mean concentrations increasing with the lensing efficiency. The most massive, strong lenses turn out to be $10 - 20\%$ more concentrated than average lensing clusters.

This confirms a bias found earlier in numerically simulated clusters. Hennawi et al. (2007) found that strong cluster lenses have three dimensional concentrations $\sim 18\%$ higher than typical clusters with similar mass. We found that the median concentration is $\sim 12\%$ higher in halos with very high lensing efficiency compared to average halos with similar mass, and can grow up to 25% if very massive clusters are selected.

Apart from the qualitative agreement, the quantitative agreement is quite reassuring especially in view of our different approach of modelling the halo population and its lensing efficiency semi-analytically compared to fully numerically. The 12% increase found here is certainly consistent with their 18% increase because a broader mass selection was applied here. Caution must thus be applied when extrapolating results on the inner structure of strongly lensing clusters to the entire cluster population.

Finally, we performed a similar analysis using the temperature and the bolometric luminosity of the X-ray emitting ICM instead of the strong-lensing cross section. We assigned a temperature and an X-ray luminosity to each DM halo in our sample by extending scaling relations first derived by Eke et al. (1998). They maintain the usual scalings $T \propto M_{200}^{2/3} h(z)^{2/3}$ and $L_X \propto M_{200}^{4/3} h(z)^{7/3}$, but include a dependence on the concentration of the host DM halo.

According to this analysis, there is no concentration bias in temperature-selected clusters, while a bias similar to strong lensing occurs for objects selected by their X-ray luminosity, if clusters of similar mass are selected. In particular, the mean and median concentrations of dark halos with increasing gas temperature decrease, reflecting that the temperature is much more sensitive to the halo mass than to its concentration. This result remains true when the halos are selected by mass. Likewise, dark halos with increasing X-ray luminosity have virtually unchanged concentrations if no mass selection is applied. If only massive objects are selected, the dependence of the bolometric luminosity on the concentration appears.

It is then an interesting question whether the two concentration biases due to strong lensing and X-ray luminosity conspire to produce a stronger effect. We computed the mean and median concentrations of clusters selected for strong lensing among those already selected for their X-ray luminosity and with mass larger than $7.5 \times 10^{14} M_{\odot} h^{-1}$. The further increase in concentration is very small compared to very X-ray luminous objects only. This is because selecting massive clusters for their high bolometric X-ray luminosity, we already select objects with high concentration that are typically also the most efficient lenses.

We also checked the effect of halo triaxiality on our results, which adds scatter to the halo concentrations and projected halo ellipticities, and, even though the latter is relatively significant, it leaves the conclusions of our paper unchanged.

These results confirm the general expectation that the gas temperature is more sensitive to the depth of the overall potential well and thus to the halo mass than to the internal halo structure. This does not hold true for the luminosity, which scales with the squared gas density and is thus substantially more sensitive to structural properties of the halo other than the mass. Similarly, the lensing efficiency is very sensitive to the details of the internal structure of the lens, as demonstrated in a variety of studies (Bartelmann et al., 1995; Meneghetti et al., 2003a,b; Oguri et al., 2003; Meneghetti et al., 2007).

Chapter 8

Strong Lensing Statistics and the Power Spectrum Normalization

8.1 Introduction

As outlined in Section 1.9, the WMAP-3 data release shifted the value of the normalization of the power spectrum for linear density fluctuations from $\sigma_8 \sim 0.9$ to $\sigma_8 \sim 0.75$. This is not only in tension with the first-year data release, but also with many of the cosmological tests based on structure formation, like the GC number counts evolution and the large scale structure probed via weak gravitational lensing and big optical surveys, that tend to favor a value of $\sigma_8 \sim 0.9$ as well (See Sections 2.5 and 3.6).

In Section 3.6 it has also been explained how the order-of-magnitude inconsistency between the total number of gravitational arcs observed in complete, X-ray selected cluster samples and the corresponding theoretical predictions was first pointed out by Bartelmann et al. (1998). In that work, the authors used n-body cosmological simulations with a rather high normalization, $\sigma_8 \gtrsim 0.9$.

The introduction of finer details about the internal structure of GCs and their surroundings, as well as the redshift distribution of sources can possibly alleviate this inconsistency if the Universe has indeed high normalization. Should the case for a low normalization power spectrum come close to reality however, the abundance of high mass structures would be severely decreased, due to the exponential dependence of the mass function Eq. (2.36) on σ_8. As a consequence, a much lower number of arcs would be predicted in a standard flat model universe dominated by the cosmological constant, thus worsening the disagreement with observations. The question whether an arc statistics problem still exist and what its magnitude is in a low-normalization universe when accounting properly for the clusters dynamical activity, source redshift distribution and limited sensitivity of observations is still at dispute, and is the topic of the present Chapter.

The effect of modifing the normalization of the primordial power spectrum on the statistics of long and thin arcs was partially explored in Li et al. (2005). Moreover, Li et al. (2007) showed that while the predicted number of multiply imaged quasars with separation $> 10''$ in a standard model with $\sigma_8 \sim 0.9$ is in good agreement with the number observed in the SDSS, the prediction for a model with WMAP-3 normalization falls short of almost one order of magnitude.

In this Chapter we will investigate how the predicted amount of gravitational arcs in a standard cosmological model changes with different normalizations, and how this copes with the observed statistics. We do that accounting for realistic source redshift distribution, the details of GC interactions and the luminosity function of background sources.

We shall consider five different cosmological models. The energy density content and the Hubble constant are kept unchanging and taken from the WMAP-3 data, combined with the SDSS observations (Spergel et al., 2007). They are $\Omega_{\mathrm{m},0} = 0.265$, $\Omega_{\Lambda,0} = 0.735$ and $h = 0.71$. The values of σ_8 are chosen differently for the five models and are 0.7, 0.75, 0.8, 0.85 and 0.9 respectively. This choice allows to cover the complete range of values from the first-year WMAP data to the GC counts.

8.2 Expectations

As in Chapter 5 about early-DE models, also here we try to gain some insight into the various contributions to the arc statistics optical depths and their dependence and variation with respect to the normalization of the power

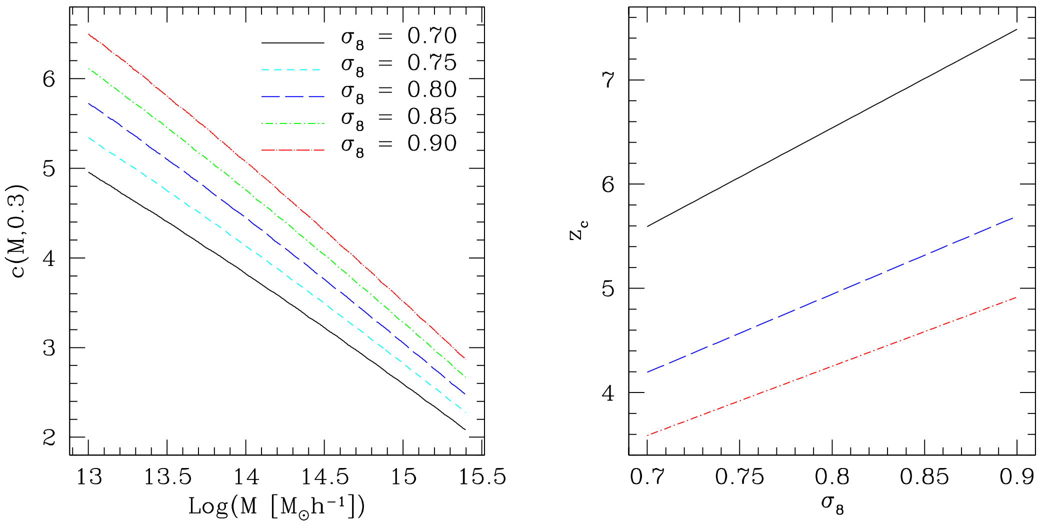

Figure 8.1: *Left panel.* Concentration of DM halos according to the prescription of Eke et al. (2001) as a function of virial mass at fized redshift $z = 0.3$. The five different values for the normalization of the power spectrum σ_8 analysed in this Chapter are considered, as labelled in the plot. *Right panel.* Collapse redshift according to Eke et al. (2001) as a function of σ_8 for DM halos at $z = 0$ with three different values of the mass: $M = 10^{14} M_\odot h^{-1}$ (black solid line), $M = 5 \times 10^{14} M_\odot h^{-1}$ (blue dashed line) and $M = 10^{15} M_\odot h^{-1}$ (red dot-dashed line).

spectrum. This will help to gain a better understanding of the subsequent results and to discriminate between various contributions to them.

We start with the internal structure of DM halos that, as described in a variety of works (Cole & Lacey, 1996; Navarro et al., 1997; Jing, 2000; Bullock et al., 2001; Eke et al., 2001) and in Section 2.3.5, depends on the complete formation history of cosmic structures. In particular, assuming that the density profile of cluster-sized DM halos can be described by an NFW fit (Eq. 2.42), we explore the dependence of the concentration of the profile on σ_8. As explained in Sections 2.3.5 and 7.2, the concentration of a DM halo is the ratio of the virial radius to the scale radius of the density profile, giving a measure of the compactness of the halo itself. The expectation is that high values for σ_8 shift the structure formation at higher redshift, meaning that clusters tend to form out of a mean background density that is larger and they have more time to relax, thus producing higher concentrations.

This expectation is verified in the left panel of Figure 8.1, where the value of the concentration of a DM halo is shown according to the prescription given by Eke et al. (2001), as a function of the mass at a fixed redshift $z = 0.3$, typical for strong lensing clusters. Apart from the very well known behaviour according to which higher mass structures have a lower concentration (Section 2.3.5), it is evident that, given mass and redshift, the concentration tends to be higher when the normalization is larger. In particular, for a cluster-sized DM halo of mass $10^{15} M_\odot h^{-1}$, the concentration is $\sim 40\%$ larger in a universe with $\sigma_8 = 0.9$ than in one with $\sigma_8 = 0.7$. This fact alone can in principle have a significant effect on arc statistics, because when the cluster core is more compact, the critical curves and caustics are pushed outwards, thus increasing their length and producing highly distorted images.

The fact that in cosmological models with high normalization clusters tend to form before can be also understood by looking at the implicit definition of collapse redshift used in Eke et al. (2001) and summarised in Eq. (7.1). As can be seen, in order to keep the right hand side of this equation constant, a higher σ_8 implies a lower growth factor at collapse redshift, hence a higher collapse redshift. The collapse redshift for DM halos of different mass at redshift zero as a function of the normalization σ_8 is reported in the right panel of Figure 8.1.

The next point that we analyse concerns the mass function and the merger rate. In Figures 8.2 and 8.3 we show the behaviour of the Press & Schechter (1974) mass function and the merger rate of Eq. (5.9) for a fixed redshift as a function of mass and for a fixed mass as a function of redshift respectively. For the mass function the behaviour is quite clear. Since in a high-normalization universe the structure formation begins earlier, there are more structures at a given redshift. This is particularly true for the high-mass tail of the mass function, due to the exponential dependence of the mass function itself on σ_8, see for instance Eq. (2.36). In particular, the difference between the mass function in universes with different normalizations of the power spectrum can be as large as several orders of magnitude on the massive GC scale.

The situation is less straightforward concerning the frequency at which structures merge together. The merger rate is larger for high normalization models compared to low normalization models if the mass of the main halo is

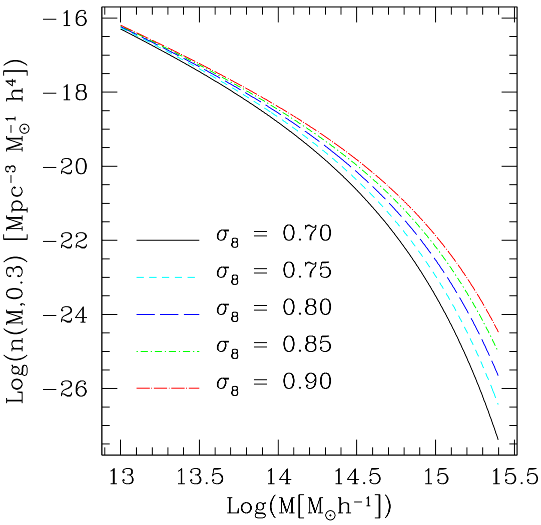

Figure 8.2: *Left panel*. Press & Schechter (1974) mass function as a function of mass at fixed redshift $z = 0.3$. *Right panel*. Merger rate between a cluster of mass $M = 10^{15}M_{\odot}h^{-1}$ and a substructure of the mass m indicated on the abscissa, at $z = 0.3$. In both panels the different values of σ_8 used in this work are labelled. Note that here and in Figure 8.3 the merger rate is the probability for a DM halo to merge with a substructure per unit logarithm of the merging mass and per unit logarithmic time.

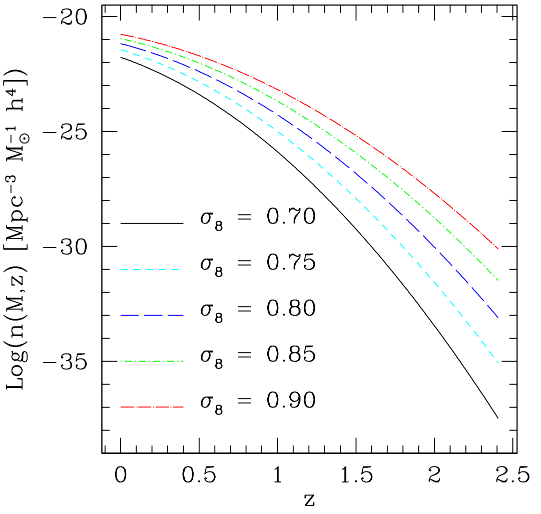

Figure 8.3: *Left panel*. Press & Schechter (1974) mass function as a function of redshift at fixed mass $M = 7.5 \times 10^{14}M_{\odot}h^{-1}$. *Right panel*. Merger rate between a cluster of mass $M = 10^{15}M_{\odot}h^{-1}$ and a substructure of mass $m = 5 \times 10^{13}M_{\odot}h^{-1}$ as a function of redshift. In both panels the different values of σ_8 used in this work are labelled

large and the substructure's mass is a considerable fraction of the main mass. This is quite a rare process because massive structures (and substructures) are rare. On the other hand, when the substructure's mass is not comparable to the main mass, the merger rate is smaller in the high-normalization model. This latter case occurs in the largest majority of circumstances, therefore we expect mergers to be on average equally likely, or even more likely in low-σ_8 models, at least in the redshift interval relevant for our pourposes. Moreover, as explained a few lines above, the concentration of cluster-sized DM halos is low in low-normalization cosmological models. Hence the strong lensing efficiency for single GCs is more sensitive to asymmetries and external perturbations, thus making the global effect of cluster mergers on the total strong lensing efficiency even more acute.

The general expectations are hence large differences in the optical depths computed in model universes with

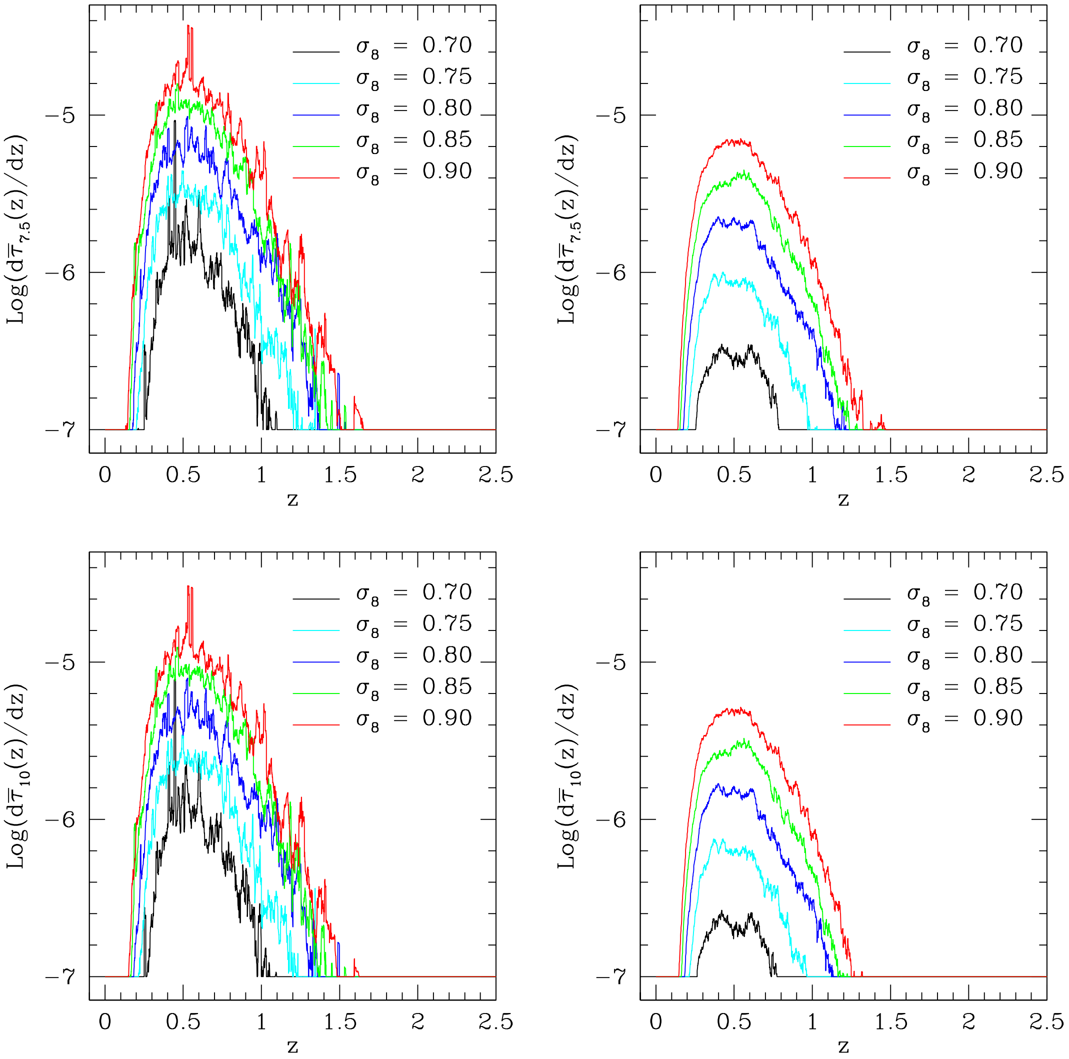

Figure 8.4: The optical depth per unit redshift for arcs with length to width ratio larger than $d = 7.5$ (top panels) and $d = 10$ (bottom panels) for the five different values of the normalization σ_8 used in this Chapter, as labelled in the plots. The left panels shows the results including the boosting effect of cluster mergers and the right ones, on the same scale, the results got ignoring it.

different values of the power spectrum normalization σ_8, and the difference between the computation performed with and that without taking into account the effect of cluster mergers to be larger for small value of σ_8. We now turn to the description of the actual results, showing how these naive expectations find actual confirmation in our numerical experiments.

8.3 Results

As in the other parts of this thesis we produce realistic models of the cluster population without time consuming numerical simulations adopting the extended Press & Schechter (1974) formalism outlined in Sections 2.3.4 and 5.2 and planting merger trees therein. Unlike previous work however, in this case we have no interest in models with a complicated time evolution of the DE component. Therefore, the computation of the relevant quantities is much faster, and we have the freedom to increase the number of clusters with simulated formation history up to $\mathcal{N} = 1,000$.

The mass coverage and the modeling of individual DM halos and of their interaction with substructures remains however identical to the the prescriptions outlined in Section 5.3. Also, for the redshift distribution of background sources we stick to Eq. (5.5).

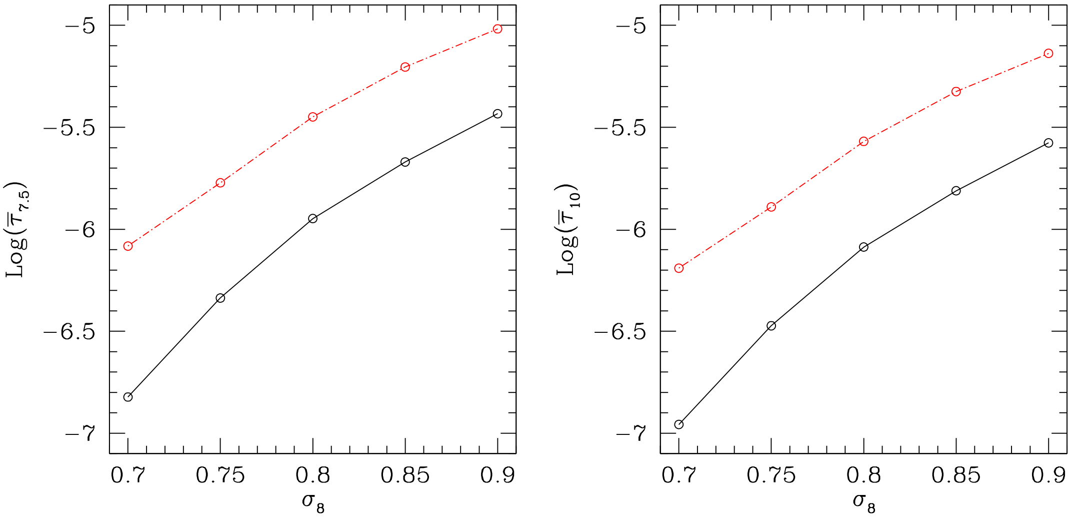

Figure 8.5: The total, average optical depth for arcs with length to width ratio larger than or equal to $d = 7.5$ (left panel) and $d = 10$ (right panel) as a function of the normalization of the power spectrum σ_8. The red, dot-dashed line shows the results including mergers, while the black, solid line shows the results ignoring them.

8.3.1 Optical Depth

In Figure 8.4 we show the results of the lensing analysis performed on our synthetic cluster population. Shown is the optical depth per unit redshift given by Eq. (5.8), computed for the five different cold DM power spectrum normalizations analysed in this Chapter. Also, the difference between the results obtained with and without taking into account the boosting effect of cluster mergers is reported. We choose two thresholds for the length-to-width ratio of gravitational arcs, namely the usual values $d = 7.5$ and $d = 10$.

As naively expected from the analysis in Section 8.2, the optical depth per unit redshift computed for a given σ_8 is systematically larger than the corresponding quantity computed with a lower power spectrum normalization. This is a combination of the larger number of potential lenses in a high normalization universe and of the different internal structures, i.e. larger concentration of individual objects. This difference is particularly striking at high redshift $z \gtrsim 1$, where the lensing efficiency is still significant for $\sigma_8 = 0.9$ while being negligible for $\sigma_8 = 0.7$. In this sense, the effect of a higher normalization of the linear power spectrum is similar to the introduction of an early-DE component (see Fedeli & Bartelmann 2007a,b and the discussion in Chapter 5). We return to this issue in further detail later. As for the difference between the two length-to-width thresholds adopted in this work, when only arcs with $d \geq 10$ are considered then the differential optical depths (and hence also the total, averaged optical depths) are obviously smaller than when $d \geq 7.5$ is adopted, but the qualitative features remain basically unchanged.

In Figure 8.5 we show the total, average optical depth Eq. (3.34), that is the integral under each of the curves shown in Figure 8.4, for the five cases considered here, both including and ignoring the effect of cluster mergers. It is striking to note that there is more than one order of magnitude difference between the case with lowest normalization $\sigma_8 = 0.7$ and that with the highest one $\sigma_8 = 0.9$, and this is true both considering or ignoring the effect of cluster mergers. As a consequence, in a high normalization universe we can expect an order of magnitude larger number of arcs than in a low normalization one, and this has important consequences for the arc statistics problem as will be discussed in detail in Section 8.3.2.

One additional piece of information that can be gathered by Figure 8.5 is that when σ_8 is smaller, the boost in the optical depth given by cluster mergers is more powerful. This fact is better appreciated in Figure 8.6, where we show the ratio between the total optical depth obtained including the boosting effect of cluster interactions and ignoring it. It is evident that dynamical activity enhance the optical depth (and hence the total number of arcs in the sky) by a factor above 5 for low normalization universes, while this factor reduces to 3 or less for high normalization models, as already verified in Fedeli & Bartelmann (2007a). This is a consequence we naively predicted in Section 8.2, based on the behaviour of the semi-analytically computed merger rate. It must be noted that the ratio between the boosted and unboosted optical depths is larger when the threshold $d = 10$ is adopted. This is a consequence of the fact that in this case the single cross sections tend to be smaller, hence they are relatively more sensitive to perturbations.

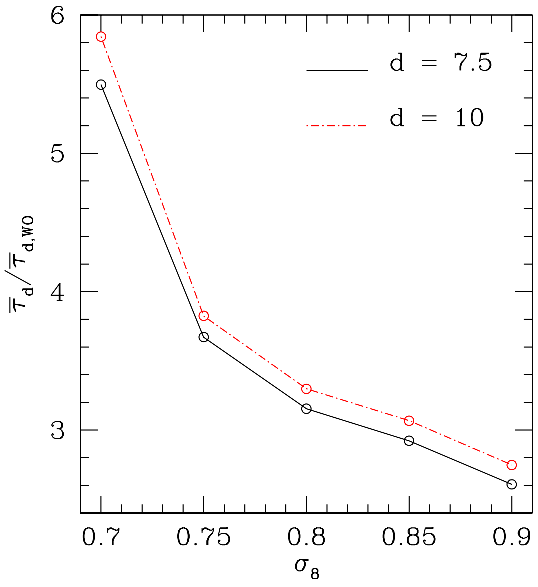

Figure 8.6: The ratio of the total, average optical depth for arcs with length to width ratio larger than or equal to $d = 7.5$ (black solid line) and $d = 10$ (red dot-dashed line) to that obtained ignoring the boosting effect of cluster mergers, as a function of σ_8.

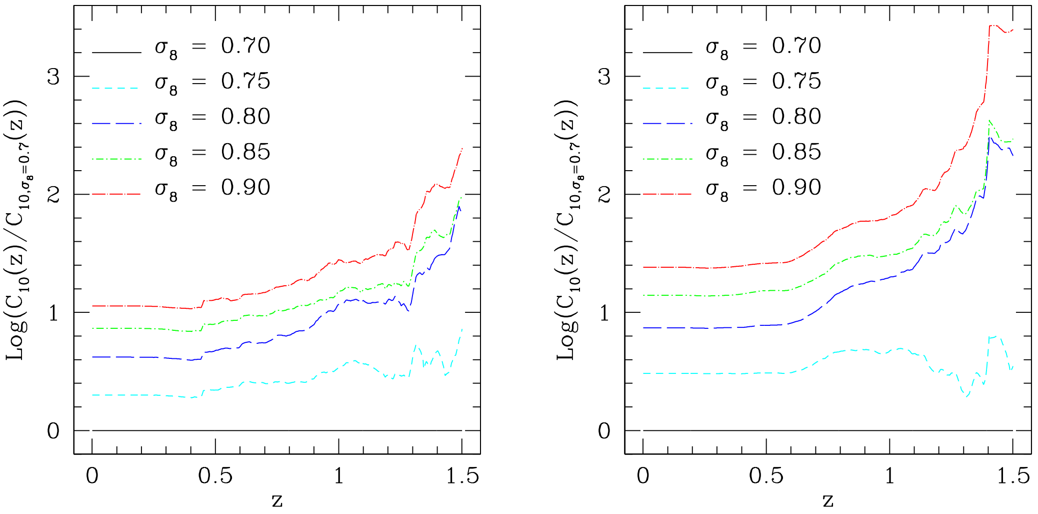

Figure 8.7: The ratio between the cumulative optical depth for the different values of the normalization used in this work and that for $\sigma_8 = 0.7$. The left panel show the result with cluster mergers taken into account, while the right panel ignores their boosting effect. Only the case with length-to-width threshold $d = 10$ is shown, since the case $d = 7.5$ is extremely similar.

It is now interesting to see what is the increase in the strong lensing efficiency at high redshift for large values of σ_8. This is particularly interesting in view of the recently observed high incidence of gravitational arcs in distant GCs (Gladders et al., 2003; Zaritsky & Gonzalez, 2003). We do that by using the cumulative optical depth defined in Eq. (5.10). In Figure 8.7 the ratio of this quantity for the five different values of the power spectrum normalization to that obtained for the $\sigma_8 = 0.7$ case is shown, both including and ignoring the effect of cluster intaractions. There is virtually no difference from the cases in which the length-to-width threshold is $d = 7.5$ and $d = 10$, therefore only the latter is shown here.

As mentioned above, we see that this ratio tends to increase at high redshift for all models with normalization larger than $\sigma_8 = 0.7$. The increase is larger when no dynamical process is included in the model (up to 3 orders

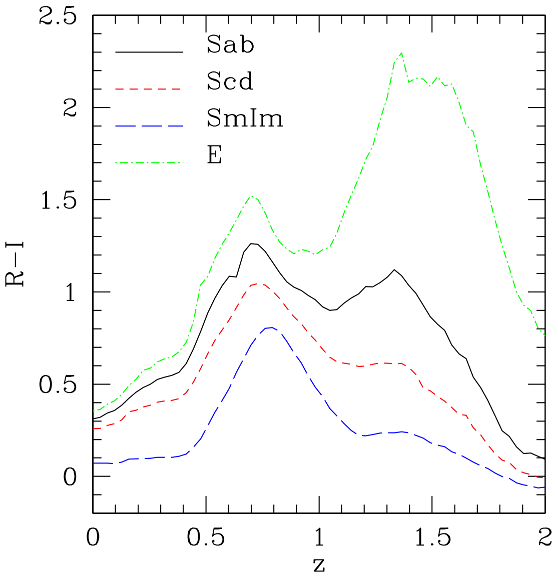

Figure 8.8: The $\mathrm{R}-\mathrm{I}$ color index as a function of redshift, computed from the spectra of three different morphological types of spirals and for elliptical galaxies, as labelled in the plot.

of magnitude) compared to when the boost due to cluster mergers is taken into account (~ 2 orders of magnitude) because the effect of structure interactions is counter-acting in this sense, as already extensively explained. However, the bottom line is that models with large σ_8 can be extremely more efficient in producing high redshift gravitational arcs than low-σ_8 models are.

8.3.2 Number of Arcs

In order to quantify the arc statistics problem when cluster mergers are properly taken into account and a realistic source redshift distribution is used, it is necessary to transform the optical depths computed in the previous section into numbers of observed arcs in the whole sky. To do this it is in principle enough to multiply the average optical depth $\bar{\tau}$ with the total number of sources in the sky (according to Eq. 3.34).

However, in order to account for the fact that arcs with an arbitrary low transmitted flux cannot be actually observed, it is necessary to include in the calculation a luminosity function for the faint blue galaxy population, and also account for the magnification effect due to gravitational lensing. The latter has a twofold impact on the observed source counts. The first is to magnify faint sources, bringing them above the flux threshold for detection, hence increasing the number of sources that are visible in the unit solid angle. The second one is that local patches of the sky are stretched, therefore diminishing the surface number density of background galaxies. It can be shown (Bartelmann & Schneider, 2001) that if the original flux distribution function of sources is a power law with logarithmic slope -1, then the two counter-acting effects of magnification cancel exactly, leaving the number of observed sources per unit solid angle unchanged.

The number counts of faint background galaxies as a function of observed magnitude were read off the work of Casertano et al. (2000) for the Hubble Deep Field. There, only the I-band magnitude is used, therefore we convert to the number counts in the R-band by using the approximate relation $\mathrm{R} \simeq \mathrm{I}+1$. This is justified by the analysis of Figure 8.8, where the color index $\mathrm{R}-\mathrm{I}$ as a function of redshift is shown for different morphological types of galaxy. It is evident that, since galaxies that are imaged as long and thin arcs are usually blue spirals (see Section 3.5), then $\mathrm{R}-\mathrm{I} \sim 1$ holds over the redshift range relevant for the present discussion.

In Figure 8.9 we show the conditional probability distribution for the magnification of background sources given the length-to-width threshold for the imaged arcs. Shown are results of ray-tracing simulations (see Section 4.2.1) in comparison with a two-Gaussian fit for both thresholds $d = 7.5$ and $d = 10$. The two-Gaussian fit can be written as

$$P(\mu_+|d) = \frac{A}{\sqrt{2\pi}\sigma_1} \exp\left[-\frac{(\mu_+ - \mu_{+,1})^2}{2\sigma_1^2}\right] + \frac{1-A}{\sqrt{2\pi}\sigma_2} \exp\left[-\frac{(\mu_+ - \mu_{+,2})^2}{2\sigma_2^2}\right], \tag{8.1}$$

where $\mu_+ \equiv |\mu|$. The value of the best fit parameters A, σ_i and $\mu_{+,i}$ both for $d = 7.5$ and $d = 10$ are summarised

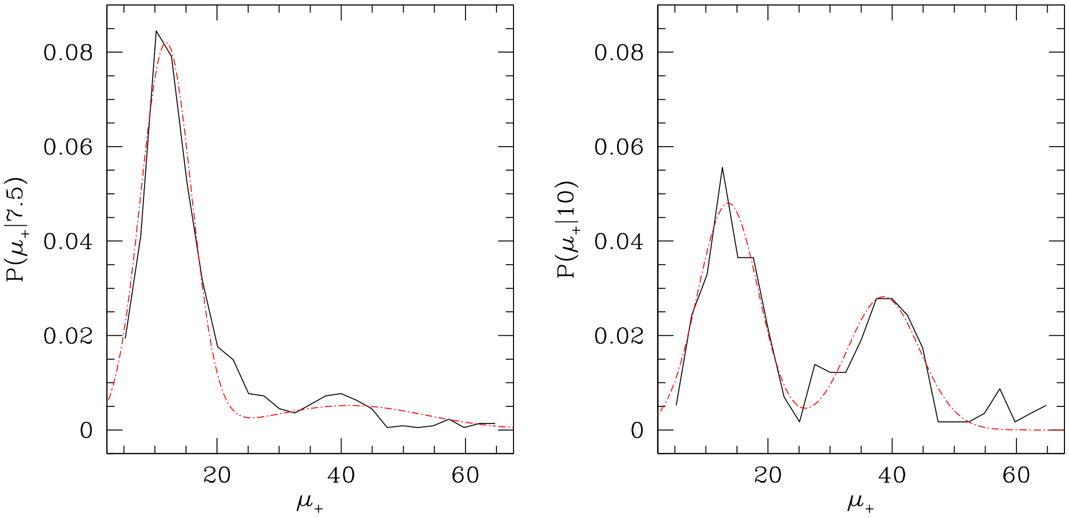

Figure 8.9: Conditional probability distribution for the magnification of images given a threshold for the length-to-width ratio of $d = 7.5$ (left panel) and $d = 10$ (right panel). The black solid lines show the result of ray-tracing simulations, while the red dot-dashed curves are the two-Gaussian best fit whose parameters are summarised in Table 8.1.

Table 8.1: Parameters for the two-gaussian fit to the conditional probability for magnification given a threshold for the length-to-width ratio of simulated gravitational arcs.

Parameter	$d = 7.5$	$d = 10$
A	0.84	0.59
σ_1	4.1	4.9
σ_2	12.3	5.8
$\mu_{+,1}$	11.8	13.6
$\mu_{+,2}$	41.3	38.6

in Table 8.1. It is important to note that the magnification is not a good proxy for the length-to width ratio of an image, expecially when high thresholds are considered.

The original number counts read off Casertano et al. (2000) are therefore convolved with the probability for arcs with thresholds $d = 7.5$ and $d = 10$, in order to get the number counts after the magnification bias. Let $n_0(F)$ be the original flux distribution function for the sources, that is the number of sources per unit solid angle that are contained in the unit flux around F. Then the magnified distribution is simply obtained as

$$n(F) = \int_0^{+\infty} n_0\left(\frac{F}{\mu_+}\right)\frac{P(\mu_+|d)}{\mu_+^2}d\mu_+. \tag{8.2}$$

Such magnified number counts are then simply multiplied with the average optical depth, to get a total number of arcs. In Figure 8.10 we show the total number of arcs with length to width ratio larger than $d = 7.5$ and $d = 10$ that are predicted to be observed on the whole sky as a function of the normalization σ_8. Shown are the results with three different limiting magnitudes, both in the I band and in the R band. Arc surveys in X-ray selected cluster samples ususally adopt a limiting magnitude $\mathrm{R_{lim}} = 21.5$, finding $\sim 10^3$ giant arcs extrapolated to the whole sky (see the discussion in Section 3.6).

The numbers given in Figure 8.10 clearly show how the prediction falls short for all values of the normalization considered here, including $\sigma_8 = 0.9$. However in the latter case the difference is just a factor of ~ 2, and can be easily ascribed to additional contributions like the effect of halo concentration distribution (Chapter 7) or a slightly different parametrization for the source redshift distribution. Much progress have been made since the first prediction given by Bartelmann et al. (1998), also reported in Figure. However, if the normalization of the power spectrum is to be close to the value measured from the WMAP-3 data, all this progress would be lost: With $\sigma_8 \sim 0.75$ the predicted number of arcs is still about one order of magnitude smaller than the observed one.

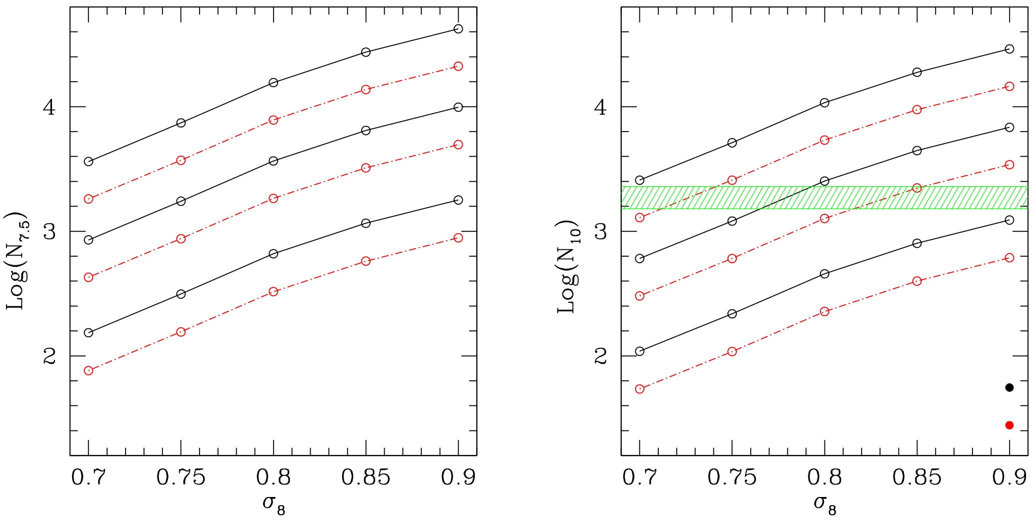

Figure 8.10: The number of arcs with length-to-width ratio threshold $d = 7.5$ (left panel) and $d = 10$ (right panel) predicted to be observed in a Λ-dominated cosmological model with normalization of the linear power spectrum as reported on the abscissa. Black solid lines refers to I-band magnitudes, while red dot-dashed lines to R-band ones. Three different limiting magnitudes are reported: 21.5 (bottom pair of curves), 24 (middle pair) and 26 (top pair). In the right panel it is also shown the observed number of giant arcs (see Section 3.6 for a definition) according to Le Fevre et al. (1994); Gioia & Luppino (1994) as a green shaded area, that should be compared with the lower red curve. Moreover, the filled black and red points represent the original result of Bartelmann et al. (1998) (in the I and R bands respectively) rescaled by using the source number counts computed in this Chapter.

8.4 Summary and Discussion

In this Chapter we computed the optical depth, differential optical depth and total number of produced gravitational arcs with length to width ratio larger than $d = 7.5$ and $d = 10$ in model universes with five different values for the normalization of the linear cold DM power spectrum σ_8. The values for the matter and DE content as well as for the expansion rate of the Universe at present are taken for the three-year data release from the WMAP satellite, while the normalization is assumed to take all the values in the set $\{0.7, 0.75, 0.8, 0.85, 0.9\}$.

The cluster population is modeled computing Monte-Carlo merger trees for a set of $\mathcal{N} = 1,000$ DM halos that at present time are extracted in the mass range $[10^{14}, 2.5 \times 10^{15}]M_\odot h^{-1}$. Each halo is represented by an NFW density profile and elliptically distorted isopotential contours, with eccentricity $e = 0.3$. The effect on the strong lensing efficiency of the interaction with substructures is also suitably taken into account according to the model of Section 5.3. Background sources are properly distributed in redshift according to the observational prescription of Eq. (5.5).

The computed average optical depth is converted into an observed number of gravitational arcs using an appropriate flux distribution function for background sources, and taking the twofold effect of lensing magnification into account. Three different limiting magnitudes both in the I and R bands are considered, including the one relevant for comparison with observational studies (Gioia & Luppino, 1994; Luppino et al., 1999)

Confirming the naively expected behaviour, we find that the total strong lensing efficiency grows for growing normalization, in a way such that the number of arcs observable in a cosmological model with $\sigma_8 = 0.7$ can be up to one order of magnitude smaller than the number related to a $\sigma_8 = 0.9$ universe.

The effect of cluster mergers depends also on the cosmology. Mergers with relatively small substructures are more likely in a low-normalization universe, and moreover single GCs are less efficient lenses in such a universe due to lower concentration, thus making the effect of interactions more significant. It turns out that cluster mergers increase the total optical depth up to a factor of ~ 5 in a model with $\sigma_8 = 0.7$ and only of a factor of ~ 3 or less in a model with $\sigma_8 = 0.9$.

Additionally, the differential optical depth for low normalization model universes can be up to several orders of magnitude smaller than in high normalization ones at $z \gtrsim 1$. This makes it highly difficult to explain the high observed incidence of long and thin arcs in high redshift clusters if the WMAP-3 value of σ_8 is assumed. Cosmological models with low σ_8 are also disfavored by the result that the number of arcs predicted to be observed in a low normalization universe, compatible with the 3-years WMAP data release is significantly lower than the number actually observed in complete, X-ray selected GCs samples. Therefore, an arc statistics problem persists in a model universe with WMAP-3 parameters, also if a suitable source redshift distribution is included and the interaction with substructures are properly accounted for.

There are two possible ways of looking at the consequence of the aforementioned results. The first one is that the normalization of the power spectrum is actually high, $\sigma_8 \sim 0.9$, and that the low value derived by the WMAP team comes from some problem encountered in the data reduction process or in Galactic foregrounds not properly accounted for (de Zotti et al., 2004; Cruz et al., 2006). The second one, and most likely, is that the actual σ_8 is in fact low, but we fail to properly account for some piece of GC physics, that affects both the cluster number counts and the relative strong lensing properties.

Finally, a possible alternative route is the presence of a dynamical DE component. As shown in Chapter 5, the presence of early-DE can play the role of an increased normalization, since it tends to shift the entire structure formation process to earlier times. As a consequence the production of gravitational arcs, and in particular the lensing efficiency for high-redshift clusters, are significantly increased. Future studies directed to the detection of a redshift evolution of the DE equation of state parameter $w_{\rm x}$ will be of fundamental importance in this sense. Also of extreme relevance for the arc statistics problem will be the application of automatic strong lensing detection algorithms to future optical surveys and combined lensing-X-ray-Sunyaev-Zel'dovich analysis of GC samples in order to gain better understanding of their physics.

Chapter 9

Asymmetric Gravitational Lenses in TeVeS and Application to the Bullet Cluster

9.1 Introduction

As is known and outlined in Chapter 1, GR cannot explain the dynamics of our Universe on large physical scales as the amount of visible mass clearly lies below what would be expected from the observed gravitational effects.

This brings to the introduction non-baryonic DM, however one can also take a different point of view and modify the law of gravity itself. In the past, there have been several suggestions for such modifications: $f(R)$ gravity (Starobinskij, 1980), conformal Weyl gravity and Aether-type theories (Zlosnik et al., 2007), to name just a few. A special realization of the latter, the so-called Tensor-Vector-Scalar gravity (TeVeS) (Bekenstein, 2004; Zlosnik et al., 2006) has recently gained interest as it provides a fully relativistic framework for the Modified Newtonian Dynamics (MOND) paradigm (Milgrom, 1983a,b,c; Bekenstein & Milgrom, 1984). Compared to other modifications, MONDian dynamics is characterized by an acceleration scale a_0, and its departure from classical Newtonian predictions depends on acceleration:

$$\tilde{\mu}\left(\frac{\|\boldsymbol{a}\|}{a_0}\right)\boldsymbol{a} = -\boldsymbol{\nabla}\Phi_{\mathrm{N}} + \boldsymbol{S}. \tag{9.1}$$

Here and in the remainder of this Chapter, Φ_{N} denotes the common Newtonian potential of the visible (baryonic) matter and $\boldsymbol{S}$ is a solenoidal vector field determined by the condition that $\boldsymbol{a}$ can be expressed as the gradient of a scalar potential. The function $\tilde{\mu}$, controlling the modification of Newton's law, has the following asymptotic behavior:

$$\begin{aligned} \tilde{\mu}(x) &\sim x \qquad x \ll 1, \\ \tilde{\mu}(x) &\sim 1 \qquad x \gg 1. \end{aligned} \tag{9.2}$$

Eq. (9.1) has been constructed to agree with the fact that the rotation curves of spiral galaxies become flat outside their central parts (Sanders & McGaugh, 2002). Analyzing observational data, Milgrom estimated $a_0 \simeq 10^{-10}$ m s^{-2}.

Within this Chapter, we shall study TeVeS and its built-in MONDian dynamics in the context of gravitational lensing, focusing on non-spherical density distributions. In particular, a numerical tool that allows the treatment of non-spherical lenses in TeVeS will be presented. In contrast to already existent MOND solvers (Brada & Milgrom, 1995, 1999; Ciotti et al., 2006) our method is based on fast Fourier techniques, achieving high-resolution solutions for the TeVeS scalar potential on time scales up to a few hours on standard PCs.

9.2 Fundamentals of TeVeS

In the following, we will give a brief review on TeVeS and the approximations used for quasi-static systems like galaxies, GCs and cosmology. As a convenient choice, in the remainder of this Chapter units with $c = 1$ shall be used.

9.2.1 Fields and Actions

TeVeS gravity is based on three dynamical fields: an Einstein metric g, analogous to the one introduced in Section 1.1, a vector field U such that

$$g^{\mu\nu}U_{\mu}U_{\nu} = -1 \tag{9.3}$$

and a scalar field ϕ. An essential feature of TeVeS is the introduction of a physical frame described by the metric $\tilde{g}$ which is needed for gravity-matter coupling only and obtained from the non-conformal relation

$$\tilde{g}_{\mu\nu} = e^{-2\phi}g_{\mu\nu} - 2U_{\mu}U_{\nu}\sinh(2\phi). \tag{9.4}$$

The geometrical part of the action, that is related to the Einstein metric, is exactly the same as in GR:

$$S_{\mathrm{g}} = \frac{1}{16\pi G}\int g^{\mu\nu}\mathcal{R}_{\mu\nu}\sqrt{-\det(g)}d^4x, \tag{9.5}$$

where $\mathcal{R}$ is the Ricci tensor of g and $\det(g)$ the determinant of g. Note that the TeVeS constant G must not be mistaken for the Newtonian gravitational constant, named G_{N} in the rest of this Chapter (cf. Section 9.2.3). The vector field's action S_{v} reads as follows:

$$S_{\mathrm{v}} = -\frac{K}{32\pi G}\int\left[\mathcal{F}^{\mu\nu}\mathcal{F}_{\mu\nu} - \lambda(g^{\mu\nu}U_{\mu}U_{\nu}+1)\right]\sqrt{-\det(g)}d^4x, \tag{9.6}$$

with $\mathcal{F}_{\mu\nu} = U_{\mu,\nu} - U_{\nu,\mu}$. Here the constant K describes the vector's coupling to gravity and λ is a Lagrangian multiplier enforcing the normalization given by Eq. (9.3). Eq. (9.6) corresponds to the classical Maxwell action, the field U now having an effective mass. The action S_{s} of the scalar field ϕ involves an additional non-dynamical scalar field σ, and takes the form

$$S_{\mathrm{s}} = -\frac{1}{2}\int\left[\sigma^2 h^{\mu\nu}\phi_{,\mu}\phi_{,\nu} + \frac{G\sigma^4}{2l^2}F(k_{\mathrm{s}}G\sigma^2)\right]\sqrt{-\det(g)}d^4x, \tag{9.7}$$

where $h^{\mu\nu} = g^{\mu\nu} - U^{\mu}U^{\nu}$ and F is a dimensionless free function. As the field σ is related to the invariant $h^{\mu\nu}\phi_{,\mu}\phi_{,\nu}$, however, it could in principle be eliminated from the action. While k_{s} is the coupling constant of ϕ to gravity, the constant l is related to Milgrom's a_0 and has the dimension of a length (see Section 9.2.2). Finally, according to the equivalence principle, the matter action is given by

$$S_{\mathrm{m}} = \int\mathcal{L}_{\mathrm{m}}\sqrt{-\det(\tilde{g})}d^4x. \tag{9.8}$$

Matter fields are coupled to gravity by the physical metric $\tilde{g}$, i.e. world lines are geodesics of the metric $\tilde{g}$ rather than g. As usual, the corresponding equations of motion can be derived by varying the total action $S = S_{\mathrm{g}} + S_{\mathrm{v}} + S_{\mathrm{s}} + S_{\mathrm{m}}$ with respect to the basic fields.

In order to obtain Newton's law in the non-relativistic high acceleration regime $(a \gg a_0)$, the coupling constants k_{s} and K have to be small compared to unity, i.e.

$$k_{\mathrm{s}} \ll 1, \quad K \ll 1. \tag{9.9}$$

Therefore, TeVeS is kept close to GR in a sense that it will recover well-known features of GR, albeit modified by the other fields.

9.2.2 The Free Function

In TeVeS, the transition from Newtonian dynamics to MOND is controlled by the free function F. Following Bekenstein (2004), the "equation of motion" for the non-dynamical field σ suggests introducing a new function $\mu(y)$ which is implicitly given by

$$-\mu F(\mu) - \frac{1}{2}\mu^2 F^{'}(\mu) = y, \tag{9.10}$$

with

$$k_{\mathrm{s}}G\sigma^2 = \mu(k_{\mathrm{s}}l^2 h^{\mu\nu}\phi_{,\mu}\phi_{,\nu}) = \mu(y). \tag{9.11}$$

For further analysis, we shall assume the function $\mu(y)$ to behave well in a physical sense, i.e to be smooth and monotonic in both cosmological $(y < 0)$ and quasi-static situations $(y > 0)$. In order to reproduce both a

MONDian and a Newtonian limit, the quasi-static branch of the inverse function $y(\mu)$ has to satisfy the following limiting conditions:

$$\begin{aligned} y(\mu) &\to \infty \quad \mu \to 1, \\ y(\mu) &\simeq b\mu^2 \quad \mu \ll 1, \end{aligned} \tag{9.12}$$

where b is a positive real constant. If this is the case, the constant l can be related to Milgrom's a_0 by

$$a_0 = \frac{\sqrt{bk_{\mathrm{s}}}}{4\pi\Xi l} \simeq \frac{\sqrt{bk_{\mathrm{s}}}}{4\pi l}, \tag{9.13}$$

where $\Xi \equiv 1 - K/2 - 2\phi_{\mathrm{c}}$ and ϕ_{c} is the cosmological value of the scalar field which is assumed to be small ($\phi_{\mathrm{c}} \ll 1$). In Section 9.4.1, we shall return to the free function and its properties in the context of gravitational lensing, concentrating on the branch relevant for quasi-static systems.

9.2.3 Quasi-static Systems

According to Bekenstein (2004), the physical metric field near a quasi-static galaxy (cluster) is identical to the metric obtained in GR if the non-relativistic gravitational potential is replaced by

$$\Phi = \Xi\Phi_{\mathrm{N}} + \phi, \tag{9.14}$$

where Φ_{N} is the Newtonian potential generated by the baryonic matter density ρ. In this approximation, it is consistent to take $U^\mu = (U^0, 0, 0, 0)$ which can be shown from the corresponding field equations. Then we have

$$k_{\mathrm{s}} l^2 h^{\mu\nu} \phi_{,\mu}\phi_{,\nu} = k_{\mathrm{s}} l^2 \|\boldsymbol{\nabla}\phi\|^2 \tag{9.15}$$

and the equation of the scalar field reduces to

$$\boldsymbol{\nabla}\left[\mu\left(k_{\mathrm{s}} l^2 \|\boldsymbol{\nabla}\phi\|^2\right)\boldsymbol{\nabla}\phi\right] = k_{\mathrm{s}} G\rho. \tag{9.16}$$

Eq. (9.16) corresponds to the non-linear elliptic boundary value problem and can be treated numerically. In Section 9.5.2, we shall give a detailed description of the method we use to determine the solution for the scalar field ϕ, including a discussion on its problems and limitations.

Since we have $K, \phi_{\mathrm{c}} \ll 1$, the quantity Ξ has a value close to unity, and the total potential Φ can essentially be written as the sum of the common Newtonian potential Φ_{N} and the additional scalar field, i.e. Eq. (9.14) may further be reduced to

$$\Phi \simeq \Phi_{\mathrm{N}} + \phi. \tag{9.17}$$

As the constant G is related to the Newtonian gravitational constant G_{N} by (Bekenstein, 2004)

$$G_{\mathrm{N}} = \left(\Xi + \frac{k}{4\pi}\right) G, \tag{9.18}$$

we will additionally assume $G \simeq G_{\mathrm{N}}$ throughout this work.

9.2.4 Cosmology

Similar to the case of GR, it is possible to derive a cosmological model in TeVeS. Assuming the basic fields to partake of the symmetries of the Robertson-Walker spacetime, the analog of the first Friedmann's equation reads

$$\frac{\dot{a}^2}{a^2} + \frac{k}{a^2} = \frac{8\pi G}{3}(\rho e^{-2\phi} + \rho_\phi), \tag{9.19}$$

where ρ_ϕ is the energy density of the scalar field given by

$$\rho_\phi \equiv \frac{\mu\dot{\phi}^2}{k_{\mathrm{s}} G} + \frac{\mu^2}{4k_{\mathrm{s}}^2 l^2 G} F(\mu) = \frac{-2\mu y(\mu) + \mu^2 F(\mu)}{4k_{\mathrm{s}}^2 l^2 G}. \tag{9.20}$$

Since we are interested in the physical metric, we have to make use of transformation Eq. (9.4) and finally obtain

$$\frac{1}{\tilde{a}}\frac{d\tilde{a}}{d\tilde{t}} = e^{-\phi}\left(\frac{\dot{a}}{a} - \dot{\phi}\right), \tag{9.21}$$

with

$$d\tilde{t} = e^{\phi} dt, \quad \tilde{a} = e^{-\phi} a. \tag{9.22}$$

In order to simplify matters, however, we shall introduce the "minimal" cosmological model proposed by Zhao et al. (2006), that is described as follows. According to Bekenstein (2004), it is consistent to assume that the cosmological scalar field evolves slowly in time throughout cosmological history. Thus, its contribution to the Hubble expansion is negligibly small, with a ratio $\mathcal{O}(k_{\mathrm{s}})$ compared to the matter contribution. Setting $\rho_{\phi} = 0$ and recalling that $\phi \ll 1$, the physical Hubble parameter can be expressed as in Eq. (1.26), depending only on matter and radiation density, curvature and a possible DE contribution.

Since there is no DM in TeVeS, we have to consider a minimal-matter cosmology that should be consistent with observational data in order to obtain a reasonable cosmological model. Zhao et al. (2006) actually find a good fit of the high-z supernovae distance moduli data set by choosing an open cosmology with cosmological constant and $\Omega_{\Lambda,0} = 0.46$, $\Omega_{\mathrm{m},0} = 0.04$ and $H_0 = 70$ km s^{-1} Mpc^{-1}. However, they also point out that when moving to very high redshifts, this open cosmology has problems, i.e. it underestimates the last scattering sound horizon, which actually seems to be an artifact of the crude approximation as recent work has shown (Zhao, 2006). Nevertheless, in the context of gravitational lensing, this simple model is sufficient for assigning the distances of lenses and sources up to a redshift of $z \sim 3$.

9.3 Gravitational Lensing in TeVeS

In general, light rays move along the null geodesics of the underlying metric field, i.e. the null geodesics of the physical metric $\tilde{g}$ considering the framework of TeVeS gravity. This means that the deflection angle map of a lens can be computed using Eq. (3.9), with the only difference that the Newtonian potential of dark and luminous matter must be replaced with the TeVeS potential Eq. (9.17) of the luminous matter only.

Therefore, in addition to the deflection angle caused by the Newtonian potential Φ_{N}, there is a contribution arising from the scalar field ϕ. Because ϕ is connected to the matter density in a highly non-linear way, it is not possible to relate the projected matter density to a two-dimensional scalar deflection potential just like in GR (see Eq. 3.17). Hence, we are obliged to solve Eq. (9.16) for calculating the TeVeS deflection angle, which is a very delicate issue (cf. Section 9.5.2). Compared to the distances between lens and source and observer and source, however, we may still assume that most of the bending occurs within a small range around the lens. This enables us to fully adopt the GR lensing formalism which was outlined in Section 3.3.

Following Zhao et al. (2006), we switch to a notation which turns out to be more suitable for analytic studies. Instead of the function μ, we shall consider a new function $\bar{\mu}$ which is defined by

$$\frac{\bar{\mu}}{1-\bar{\mu}} = \frac{4\pi}{k_{\mathrm{s}}} \frac{2}{2-K} \mu, \tag{9.23}$$

where k_{s}, K are the coupling constants of the scalar field ϕ and the vector field U, respectively. Similarly, we can relate the function y to another function δ_{ϕ} in the following way:

$$\delta_{\phi}^2 = \left[\frac{4\pi}{k_{\mathrm{s}}}\left(1 - \frac{K}{2}\right)\right]^2 \frac{y}{b} \simeq \frac{\|\boldsymbol{\nabla}\phi\|^2}{a_0^2}, \tag{9.24}$$

where b is the real-valued parameter of the function $y(\mu)$ in Eq. (9.12). Choosing the free function such that

$$\delta_{\phi}^2 = \frac{\bar{\mu}^2}{(1-\bar{\mu})^2}, \quad \bar{\mu}^2 = \frac{\delta_{\phi}^2}{(1+\delta_{\phi})^2}, \tag{9.25}$$

it is possible to obtain an analytic expression for the deflection angle of a Hernquist lens, i.e. a lens whose matter distribution follows a Hernquist profile (Hernquist, 1990) given by

$$\rho(r) = \frac{M r_{\mathrm{H}}}{2\pi r (r + r_{\mathrm{H}})^3}, \tag{9.26}$$

the Hernquist radius r_{H} being the scale length at which the logarithmic slope change from the outer -4 to the inner -1 and M the total (finite) mass. Eq. (9.26) is a spherical profile which closely approximates the de Vaucouleurs law (de Vaucouleurs, 1953) for elliptical galaxies. Using elementary calculus, we compute the *reduced deflection angle* $\hat{\boldsymbol{\alpha}}(\boldsymbol{\xi}) \equiv \overline{\boldsymbol{\alpha}}(\boldsymbol{\xi}) D_{\mathrm{l}} D_{\mathrm{s}} / D_{\mathrm{ls}}$, eventually ending up with

$$\hat{\alpha}(\xi) = \frac{r_{\mathrm{H}} A(\xi)}{\sqrt{|\xi^2 - r_{\mathrm{H}}^2|}} \left(4\xi\sqrt{GMa_0} + \frac{4GM\xi}{|\xi^2 - r_{\mathrm{H}}^2|}\right) - \frac{4GM\xi}{|\xi^2 - r_{\mathrm{H}}^2|}, \tag{9.27}$$

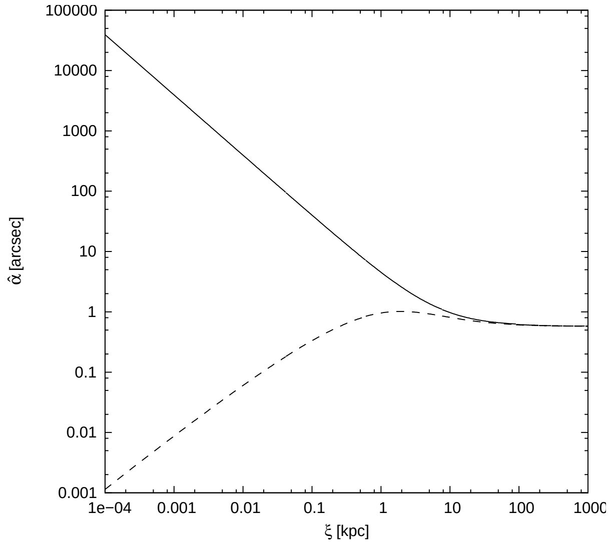

Figure 9.1: The TeVeS Hernquist lens (dashed) with $r_{\mathrm{H}} = 2$ kpc compared to its corresponding point lens (solid) with respect to the reduced deflection angle $\hat{\alpha}$ for $M = 10^{11} M_{\odot}$ and $a_0 = 10^{-10}$ m s^{-2}. For $\xi \gg 1$, both angles approach the constant $\hat{\alpha}_{\infty} \equiv 2\pi\sqrt{GMa_0} \simeq 0.58''$. The transition to the MONDian regime can be characterized by the critical radius $r_0 \equiv \sqrt{GM/a_0} \simeq 10$ kpc.

where

$$A(\xi) \quad = \quad \begin{cases} \operatorname{arcsinh}\sqrt{(r_{\mathrm{H}}/\xi)^2 - 1} & \text{if} \quad \xi < r_{\mathrm{H}} \\ \arcsin\sqrt{1 - (r_{\mathrm{H}}/\xi)^2} & \text{if} \quad \xi > r_{\mathrm{H}} \end{cases} . \tag{9.28}$$

Note that the reduced deflection angle is independent of the distances involved in the problem. In the limit $r_{\mathrm{H}} \to 0$, the Hernquist lens coincides with a point lens. In this case, we find that the reduced deflection angle is given by

$$\hat{\alpha}(\xi) = \frac{4GM}{\xi} + 2\pi\sqrt{GMa_0}. \tag{9.29}$$

Obviously, the scalar part of TeVeS gravity of a point mass seems to mimic the presence of a dark isothermal sphere. Therefore, both GR including DM and TeVeS will essentially make the same lensing predictions for ξ being much larger than the extension of the lens, but the highly non-linear coupling of the scalar field strongly suggests that there may be significant differences when moving to the strong acceleration regime near the center. Note that, although Eqs. (9.27) and (9.29) do not explicitly depend on k_{s} and K, a_0 is still given by Eq. (9.13).

Figure 9.1 shows the lensing properties of both the TeVeS Hernquist lens ($r_{\mathrm{H}} = 2$ kpc) and its corresponding point lens where we have set $M = 10^{11} M_{\odot}$ and $a_0 = 10^{-10}$ m s^{-2}. Since its deflection angle can be expressed analytically, the Hernquist lens is a perfectly suitable candidate for testing an algorithm for non-spherical problems.

9.4 Influence of the Free Function

Considering a spherically symmetric situation and applying Gauss' theorem for a spherical surface of arbitrary radius, Eq. (9.16) can be transformed into

$$\boldsymbol{\nabla}\phi = \frac{k_{\mathrm{s}}}{4\pi\mu}\boldsymbol{\nabla}\Phi_N. \tag{9.30}$$

Assuming we already know Φ_{N}, for example by solving Poisson's equation, the relation above can directly be used to calculate $\boldsymbol{\nabla}\phi$ for any given function $\mu(y)$ (Remember that $y = k_{\mathrm{s}} l^2 \|\boldsymbol{\nabla}\phi\|^2$ for quasi-static systems, with l given by Eq. 9.13). If μ or Φ_{N} cannot be obtained analytically, treatment with numerical methods, which can easily be applied in the spherically symmetric case, becomes necessary. Because of their simplicity, spherically symmetric systems are particularly suitable for investigating the effects of the free function $y(\mu)$ on the deflection angle.

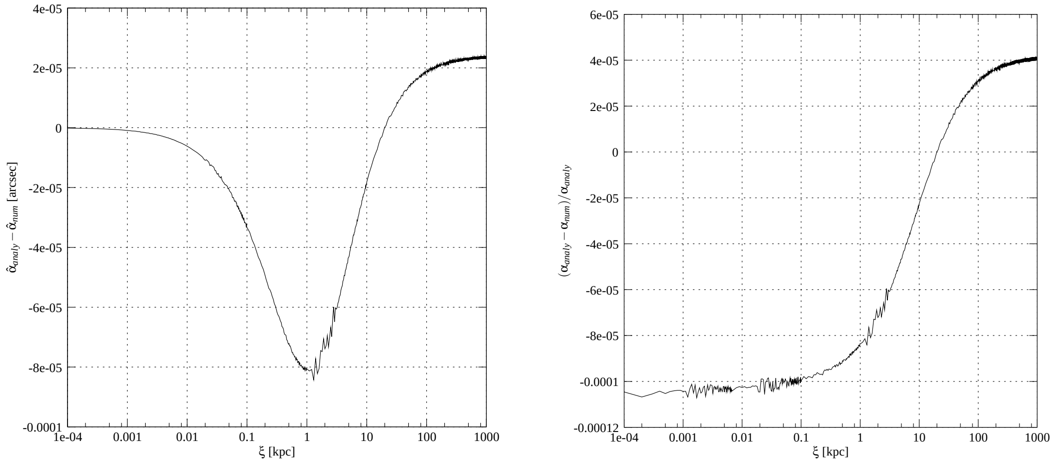

Figure 9.2: Absolute (left) and relative (right) difference between the TeVeS reduced deflection angles of the analytic and the numerical Hernquist lens choosing the parameters from Section 9.3: Clearly, the deviations are small, $\Delta\hat{\alpha} \lesssim 10^{-4}$ arcseconds and $\Delta\hat{\alpha}/\hat{\alpha}_{\text{analy}} \lesssim 10^{-4}$. For the numerical calculation, we have assumed $k_{\text{s}} = 0.01$ and $y(\mu) = \mu^2/(1-\mu)$.

9.4.1 Parameterization of the Free Function

Having set the cosmological background in Section 9.2.4, we shall focus on the free function's quasi-static branch $(y > 0)$: If $y(\mu)$ can be analytically continued into the ring domain $R = \{z \in \mathbb{C};\ 0 < |z-1| < 1\}$, it can be expanded into a Laurent series. Thus, $y(\mu)$ takes the following form for $0 < \mu < 1$:

$$y(\mu) = \sum_{n=1}^{\infty} \frac{a_n}{(1-\mu)^n} + \sum_{n=0}^{\infty} b_n \mu^n, \tag{9.31}$$

with coefficients $a_n,\ b_n \in \mathbb{R}$. Expanding the above expression for $\mu \ll 1$ to second order, we must have the following relations for the coefficients a_n, b_n to keep the second condition in Eq. (9.12):

$$\begin{aligned} b_0 + \sum_{n=1}^{\infty} a_n &= 0, \\ b_1 + \sum_{n=1}^{\infty} a_n n &= 0, \\ b_2 + \sum_{n=1}^{\infty} a_n \frac{n(n+1)}{2} &\neq 0. \end{aligned} \tag{9.32}$$

As a simple example, we take the function

$$y(\mu) = \frac{\mu^2}{1-\mu} \tag{9.33}$$

and find that the non-zero coefficients are given by

$$a_1 = 1, \quad b_0 = -1, \quad b_1 = -1. \tag{9.34}$$

Setting the coefficients a_n and b_n, we are able to directly control the specific transition behavior from MONDian to Newtonian dynamics. Using the expansion Eq. (9.31), we shall study the effects of varying the free function $y(\mu)$ on the deflection angle within numerical analysis.

9.4.2 Comparison to the Analytic Model

Taking the simple choice Eq. (9.33), we compare the numerical result of the TeVeS Hernquist lens to the analytic solution derived in Section 9.3. Figure 9.2 shows the absolute and relative difference between the reduced deflection angles of the analytic and the numerical lens models using the same parameters as in Section 9.3, where we have set $k_{\rm s} = 0.01$ for the numerical calculation. Although we have considered two different free functions $y(\mu)$, the actual differences are fairly small, $\Delta\hat{\alpha} \lesssim 10^{-4}$ arcseconds and $\Delta\hat{\alpha}/\hat{\alpha}_{\rm analy} \lesssim 10^{-4}$, and thus negligible with respect to today's observational resolution limit.

Considering the above, it appears that we could be able to determine classes of free functions $y(\mu)$ that nearly produce the same deflection angle. Although we do expect an infinite number of such classes, a closer look will be of advantage (cf. Section 9.5.1). For a systematic approach, we shall make use of the parameterization introduced in Section 9.4.1 to analyze the effects of a varying free function.

9.4.3 Varying Parameters

Still considering deflection by the Hernquist lens, we now focus on a varying form of the free function $y(\mu)$ and the value of the coupling constant $k_{\rm s}$. For our investigation, all remaining parameters are chosen as in Section 9.3 unless specified in any other way.

Starting from an arbitrary set (a_n, b_n), e.g. the set Eq. (9.34), we begin with a variation of the constants a_n where we have to adjust b_0, b_1 and b_2 according to Eq. (9.32), setting $k_{\rm s}$ to a fixed value, e.g. $k_{\rm s} = 0.01$. Interestingly, numerical analysis has shown that there are no significant changes to the reduced deflection angle for a wide range of parameters, i.e. the relative changes are comparable to those we found in the last section, $\Delta\hat{\alpha}_{\rm rel} \equiv \Delta\hat{\alpha}/\hat{\alpha}_{\rm analy} \lesssim 10^{-5} - 10^{-4}$. For instance, if we choose

$$a_{18} = 1, \quad a_{19} = -2, \quad a_{20} = 1, \tag{9.35}$$

which is the expansion of

$$y(\mu) = \frac{\mu^2}{(1-\mu)^{20}}, \tag{9.36}$$

the relative deviation is of order 10^{-5}. As we have seen, the singularity at $\mu = 1$ recovers the Newtonian limit in quasi-static situations, but remarkably, the transition behavior seems almost insensitive to the particular realization of this singularity.

Similarly, we have also examined the effect of a changing coupling constant $k_{\rm s}$ taking the coefficients a_n, b_n as constants. Again, the relative differences turned out to be very small, $\Delta\hat{\alpha}_{\rm rel} \lesssim 10^{-5} - 10^{-4}$, varying $k_{\rm s}$ within the range of $10^{-4} - 10^{-2}$ for different sets (a_n, b_n). Obviously, as long as it is small, i.e. $k_{\rm s} \lesssim 0.01$, the calculation of the deflection angle does not really depend on the exact value of $k_{\rm s}$.

As for the coefficients b_n with $n > 2$, however, there is a strong influence on the deflection angle, basically allowing to create arbitrary transitions from MOND to Newtonian dynamics. In accordance with the above analysis, it seems that the b_n alone can be used to characterize the free function. In general, the exact form of $y(\mu)$ has to by constrained by observational data being independent of the particular law of gravity, which is subject to other work, e.g. Zhao & Famaey (2006).

9.5 Non-spherical Lens Models

Within this section, we will examine the properties of more general lens systems using numerical methods. Introducing our algorithm for the treatment of non-spherical lenses in TeVeS, we will investigate a set of different matter distributions including a toy model of the cluster merger 1E0657 $-$ 558.

9.5.1 Choice of the Free Function

Setting $k_{\rm s} = 0.01$, we shall restrict all further analysis to the following form of $y(\mu)$:

$$y(\mu) = \frac{\mu^2}{(1-\mu)^2}. \tag{9.37}$$

We will make use of this specific $y(\mu)$ for two reasons: First of all, the choice of Eq. (9.37) is easily inverted, i.e.

$$\mu(y) = \frac{\sqrt{y}}{1+\sqrt{y}}, \tag{9.38}$$

and therefore it is possible to express the derivative with respect to y analytically:

$$\frac{\partial\mu}{\partial y} = \frac{1}{2\sqrt{y}(1+\sqrt{y})^2}. \tag{9.39}$$

As will become clear in Section 9.5.2, both $\mu(y)$ and $\partial\mu/\partial y$ are part of Eq. (9.16). Since $\partial\mu/\partial y \to \infty$ for $y \to 0$, a possible solver of Eq. (9.16) might be extremely sensitive to the corresponding run of $\partial\mu/\partial y$ in that regime. By choosing the analytic expressions of Eqs. (9.38) and (9.39), respectively, we are able to avoid numerical inversion and differentiation of the free function, which may prevent a destabilizing influence on the algorithm.

Secondly, our choice allows us to use the analytic Hernquist lens for comparison in order to test the accuracy of a non-spherical solver for this specific density profile. According to Section 9.4, Eq. (9.37) is close to the choice of Eq. (9.25) and produces nearly the same deflection angle, thus justifying such a comparison.

9.5.2 Calculating the Scalar Potential

Since $\mu = \mu(y)$ and $y = k_{\mathrm{s}}l^2\|\boldsymbol{\nabla}\phi\|^2$ for quasi-static systems, an expansion of the left hand side of Eq. (9.16) yields

$$2\frac{\partial\mu}{\partial y}k_{\mathrm{s}}l^2\left((\partial_i\phi)(\partial_j\phi)(\partial_i\partial_j\phi)\right) + \mu\Delta\phi = k_{\mathrm{s}}G\rho. \tag{9.40}$$

Defining an effective matter density $\bar{\rho}$ such that

$$\Delta\phi = \bar{\rho}, \tag{9.41}$$

where

$$\bar{\rho} = \frac{k_{\mathrm{s}}G}{\mu}\rho - 2\frac{k_{\mathrm{s}}l^2}{\mu}\frac{\partial\mu}{\partial y}\left((\partial_i\phi)(\partial_j\phi)(\partial_i\partial_j\phi)\right), \tag{9.42}$$

we may choose an appropriate first guess of ϕ and calculate an initial density $\bar{\rho}^{(0)}$ by using Eq. (9.42). Solving Poisson's equation by means of Fourier methods, i.e. Eq. (9.41) with the right hand side being fixed ($\bar{\rho} = \bar{\rho}^{(0)}$), we find a new field $\phi^{(1)}$, which can be used to obtain $\bar{\rho}^{(1)}$ and so forth.

Without any further modification, this approach fails to converge in most cases, with the $\phi^{(n)}$ oscillating rapidly. Including a relaxation into the iteration, however, it is possible to enforce convergence for a variety of problems, and thus our final iterative scheme reads as ($\bar{\rho}^{(0)}$ is calculated from an initial guess $\phi^{(0)}$)

$$\begin{aligned}\Delta\tilde{\phi}^{(n)} &= \bar{\rho}^{(n)},\\ \phi^{(n+1)} &= \omega\tilde{\phi}^{(n)} + (1-\omega)\phi^{(n)},\end{aligned} \tag{9.43}$$

where we have introduced the relaxation parameter $\omega \in \mathbb{R}$, an additional iteration field $\tilde{\phi}^{(n)}$ and

$$\begin{aligned}\bar{\rho}^{(n)} &= \frac{k_{\mathrm{s}}G}{\mu^{(n)}}\rho - 2\left(\frac{\partial\mu}{\partial y}\right)^{(n)}\frac{k_{\mathrm{s}}l^2}{\mu^{(n)}}\left[(\partial_i\phi^{(n)})(\partial_j\phi^{(n)})(\partial_i\partial_j\phi^{(n)})\right],\\ \mu^{(n)} &= \mu(y^{(n)}),\quad \left(\frac{\partial\mu}{\partial y}\right)^{(n)} = \frac{\partial\mu}{\partial y}(y^{(n)}),\quad y^{(n)} = k_{\mathrm{s}}l^2\|\boldsymbol{\nabla}\phi^{(n)}\|.\end{aligned} \tag{9.44}$$

For suitable values of ω, our method turns out to work very well for a wide range of density profiles (cf. Section 9.5.2). However, our investigation has shown that the relaxation's success is very sensitive to the particular choice of ω, i.e. ω has to be chosen from a very narrow range, $\omega = 0.75 \pm 1$. Although convergence is achieved within a wider range of ω, its behaviour quickly deteriorates. Fortunately, this value seems to be almost independent of the particular density profile, and therefore it will not be necessary to adjust ω once it has been determined for a certain density.

Point Lens Approximation

As the scalar field's gradient decreases much more slowly compared to the Newtonian one far away from the lens, one would actually be obliged to move to very large volumes in order to neglect contributions from outside the box and obtain correct results for the deflection angle. Thus, assuming a fixed grid size, this would excessively degrade the resolution of the corresponding two-dimensional lensing maps. In the following, we shall discuss an approximation allowing us to avoid this problem.

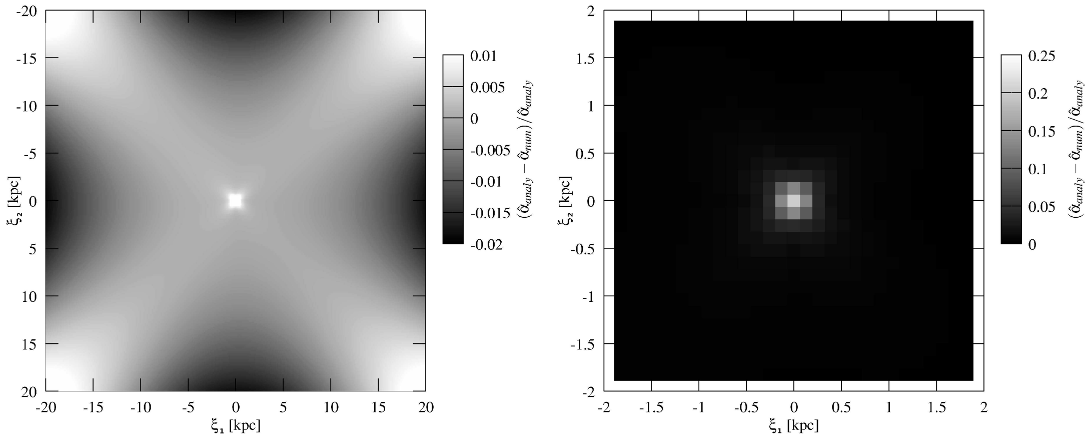

Figure 9.3: Accuracy test of our numerical method: Assuming a Hernquist lens with the parameters from Section 9.3, we compare the numerical result for the reduced deflection angle $\hat{\alpha}$ to the analytic one. The left panel shows the relative difference $\Delta\hat{\alpha}_{\rm rel} = (\hat{\alpha}_{\rm analy} - \hat{\alpha}_{\rm num})/\hat{\alpha}_{\rm analy}$. Please note that the quantity $\Delta\hat{\alpha}_{\rm rel}$ is limited by $-0.02 \leq \Delta\hat{\alpha}_{\rm rel} \leq 0.01$ for reasons of presentation, values outside this range are truncated. The right panel illustrates the relative deviation for the central part where $\Delta\hat{\alpha}_{\rm rel}$ reaches a maximum of approximately 20%.

Considering a finite grid with $N + 1$ points per dimension (N is chosen as an even number), we may rewrite the scalar part of the reduced deflection angle as the sum of contributions coming from both inside and outside the grid's volume:

$$\hat{\boldsymbol{\alpha}}_{\rm s} = 2\int_{-\frac{N}{2}\Delta\xi}^{\frac{N}{2}\Delta\xi} \boldsymbol{\nabla}\phi^{(\rm in)} d\zeta + 4\int_{\frac{N}{2}\Delta\xi}^{\infty} \boldsymbol{\nabla}\phi^{(\rm out)} d\zeta, \tag{9.45}$$

with the quantity $\Delta\xi$ denoting the distance between neighboring grid points. Assuming that the scalar field at the boundaries is approximately given by that of a point lens, i.e.

$$\phi^{(\rm out)} \simeq \sqrt{GMa_0}\log(r), \tag{9.46}$$

we obtain the following expression (M denotes the total mass inside the volume):

$$\hat{\boldsymbol{\alpha}}_{\rm s} = 2\int_{-\frac{N}{2}\Delta\xi}^{\frac{N}{2}\Delta\xi} \boldsymbol{\nabla}\phi^{(\rm in)} d\zeta + 4\boldsymbol{A}, \tag{9.47}$$

where

$$\boldsymbol{A} = \frac{\sqrt{GMa_0}}{\xi}\left[\frac{\pi}{2} - \arctan\left(\frac{N\Delta\xi}{2\xi}\right)\right]\begin{pmatrix}\xi_1\\ \xi_2\end{pmatrix}. \tag{9.48}$$

If applicable, we need to perform the integration only over our finite grid since all contributions from outside the box can be expressed analytically. Concerning our iterative solver, we may additionally assume the boundary conditions of the fields $\phi^{(n)}$ to be of spherical symmetry, and it turns out to be sufficient to use Eq. (9.46) as an initial guess for ϕ. To achieve a reasonable resolution compatible with the limitations of our computer hardware, we set $N = 384$ for all numerical calculations. Before turning to non-spherical lens systems, however, we shall examine our method's accuracy.

Accuracy

Comparing the numerically obtained reduced deflection angle of a Hernquist lens to the analytic result Eq. (9.27), we will determine the accuracy of our tool assuming the parameters from Section 9.3, which correspond to a galaxy-sized mass distribution. As previously mentioned, such a comparison is justified according to our analysis in Section 9.4.1. Concerning the numerical setup, we choose a grid volume of $V = (50 \text{ kpc})^3$ (the lens is placed in the grid's center) and in order to obtain a sufficiently large value of $D \equiv D_{\rm ls}D_{\rm l}/D_{\rm s}$, we set the redshifts of source and lens to $z_{\rm s} = 3$ and $z_{\rm l} = 0.63$, respectively. If not explicitly noted, we shall keep this choice of redshifts throughout the following sections. At $\xi \simeq 25$ kpc, the relative deviation between the analytic Hernquist and its corresponding point lens is approximately 6%. Although this difference is quite large, we assume the validity of

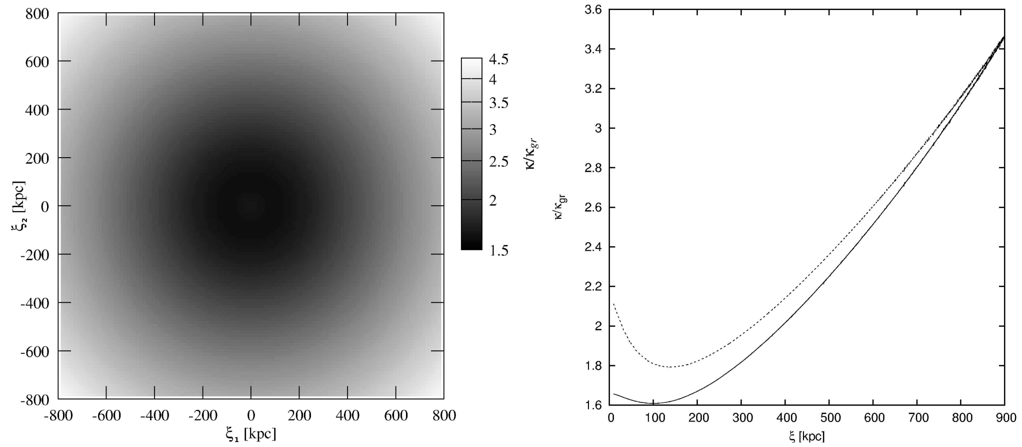

Figure 9.4: *Left panel.* Numerically calculated TeVeS convergence map for the King-like profile Eq. (9.49) expressed in terms of the GR convergence κ_{gr} assuming $\zeta_0 = 50$ kpc. *Right panel.* Since Eq. (2.49) corresponds to an axisymmetric configuration, the effective TeVeS convergence κ and the ratio $\kappa/\kappa_{\mathrm{gr}}$ depend on the radial coordinate ξ only. As the calculated convergence maps relatively deviate from circular symmetry by $\mathcal{O}(10^{-3})$, which is due to our Fourier method, the presented results are averaged over all directions. Choosing $\zeta_0 = 50$ kpc (solid) and $\zeta_0 = 400$ kpc (dashed), we see that κ is significantly amplified in the central region when moving to higher values of ζ_0.

Eq. (9.46) in order to balance accuracy and resolution ($N = 384$). Thus, we are able to resolve structures up to a minimum extent of $\Delta\xi \simeq 130$ pc.

The left panel of Figure 9.3 shows the relative difference $\Delta\hat{\alpha}_{\mathrm{rel}} = (\hat{\alpha}_{\mathrm{analy}} - \hat{\alpha}_{\mathrm{num}})/\hat{\alpha}_{\mathrm{analy}}$ between the numerical and the analytic reduced deflection angle of the Hernquist lens. For reasons of presentation, we have limited the range of $\Delta\hat{\alpha}_{\mathrm{rel}}$ to $-0.02 \leq \Delta\hat{\alpha}_{\mathrm{rel}} \leq 0.01$. Ignoring the very center of the map (right panel), we find the relative deviations in the interior are of order 10^{-3}. Moving outwards, i.e. to larger ξ, these deviations increase and reach values up to $5-6\%$ at the grid's boundaries ($\xi \gtrsim 25$ kpc). However, as long as $\xi \lesssim 15$ kpc, we still have $\Delta\hat{\alpha}_{\mathrm{rel}} \lesssim 1\%$, again neglecting the central part. The large differences close to the boundaries are likely to be a mixture of artifacts caused by the Fourier transform of actual non-periodic fields and contributions due to Eq. (9.48) which become more significant with increasing ξ. Having a look at the right panel of Figure 9.3, we see that $\Delta\hat{\alpha}_{\mathrm{rel}}$ strongly increases in the central region reaching a maximum value of roughly 20%. The reasons for these large deviations are probably related to both the limited resolution of our grid and the small values of $\hat{\alpha}$ in the center. According to Section 9.3, the TeVeS deflection angle of the analytic Hernquist lens decreases to zero for $\xi \rightarrow 0$. Since this transition happens on a rather small scale, our numerical model cannot fully recover the deflection angle in the central region. Moreover, we have to consider that the matter density in Eq. (9.26) becomes infinite at $\xi = 0$, which, of course, cannot be accomplished in a numerical calculation. Due to the grid, this singularity is smoothed out, causing an effective loss of mass in our numerical model. This loss has an overall influence on the deflection angle and may significantly contribute to the errors we have discussed above. Investigating non-spherical systems, however, we shall only consider lenses which follow smooth density distributions.

For numerical simulations that similarly allow using the point lens approximation, we may assume an accuracy equal to that of the Hernquist lens. As we are mainly interested in the strong lensing regime, we shall restrict ourselves to the grid's interior where the relative deviations are of order 10^{-3}. Due to finite resolution, however, we expect the accuracy to degrade to some extent in regions where the deflection angle $\hat{\alpha}$ approaches values close to zero when moving to more generic lens systems. Although smooth density profiles will probably not produce deviations as large as we have found around $\xi = 0$ for the Hernquist lens, we cannot make any specific statements on the quality of our simulations in such areas. Still, this should affect but a fraction of the overall result, thus being acceptable for the following analysis.

Problems

As for the solver of the scalar field, we have encountered some problems that we briefly want to mention here: Considering more complicated density distributions, we have found the relaxed iteration to be less efficient, i.e. the iteration generally takes more time to converge. As it turns out, this cannot be compensated by changing the

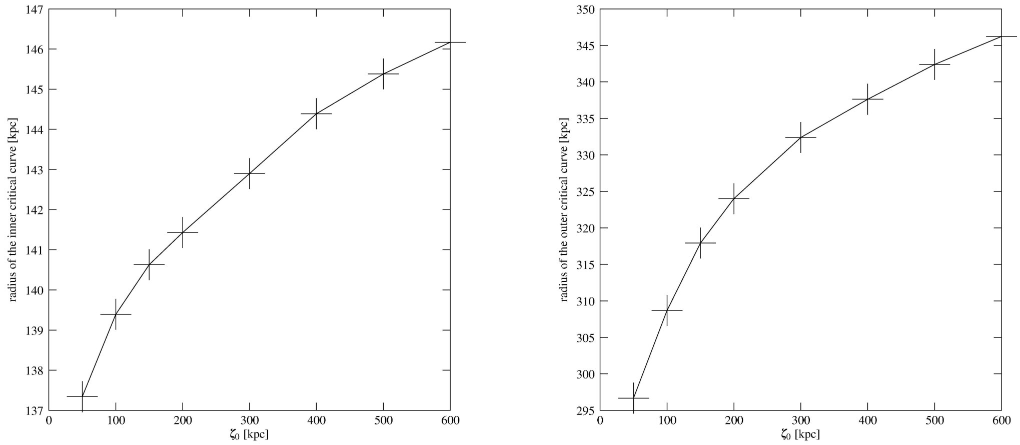

Figure 9.5: Radii of the inner (left) and outer (right) critical curve for different choices of ζ_0: Increasing the lens' extent along the line of sight, the radius of the inner (outer) critical curve is driven outwards showing relative changes of up to roughly 6% (16%). The critical lines are calculated by interpolation between the grid points.

relaxation parameter ω, which would actually lead to even worse convergence properties or a complete failure of the method. Still, the additional amount of time that has to be employed is acceptable in most cases.

Furthermore, independently of the corresponding value of ω, we encounter the relaxation to generally fail for certain choices of ρ. Since it can mostly be resolved by slightly modifying the original density profile, this second problem is probably of purely numerical origin. Although it seems very unlikely, however, we point out that it might also hint on an exceptional behavior of the scalar field ϕ that is not accessible to our solver. Considering the Hernquist profile, for instance, the difficulties found in the central part may reflect its intrinsic instability with respect to TeVeS/MOND, rather than a negative feature of our code (Ciotti & Binney, 2004).

9.5.3 Thin Lens Approximation

As our first task, we want to investigate the validity of the thin lens approximation in TeVeS. According to former work considering lensing in classical MOND (Mortlock & Turner, 2001), we expect a break-down of the approximation due to the non-linear coupling of the scalar field to the 3-dimensional matter density. In the following, however, we are rather interested in quantifying this break-down by exploring the lensing properties of a mass distribution being contracted or stretched along the line of sight, i.e. the ζ-direction, making use of our new numerical tool. For this purpose, let us consider a three-dimensional density distribution ρ following a King profile (King, 1972) which is given by Eq. (2.49). This is an empirical law that fairly describes the distribution of both galaxies and gas inside a GC. However, in order to analyze TeVeS effects which are only due to the lens's extent along the line of sight, we have to parameterize its thickness and additionally ensure a constant projected mass density. Thus, we introduce a slightly modified profile:

$$\rho(\xi,\zeta) = \rho_0 \mathcal{Q}(\xi)\mathcal{Z}(\zeta), \tag{9.49}$$

where

$$\mathcal{Q}(\xi) = \left[1 + \left(\frac{\xi}{\xi_0}\right)^2\right]^{-1} \tag{9.50}$$

and

$$\mathcal{Z}(z) = \left[1 + \left(\frac{\zeta}{\zeta_0}\right)^2\right]^{-\frac{1}{2}}, \tag{9.51}$$

with ξ_0, $\zeta_0 > 0$ being the corresponding core lengths. Since the expressions in Eqs. (9.50) and (9.51) are obtained by integrating Eq. (2.49) over one and two dimensions, respectively, our new choice Eq. (9.49) is actually kept close to the original King profile. Varying the parameter ζ_0, we are now able to directly control the lens's extent in the ζ-direction.

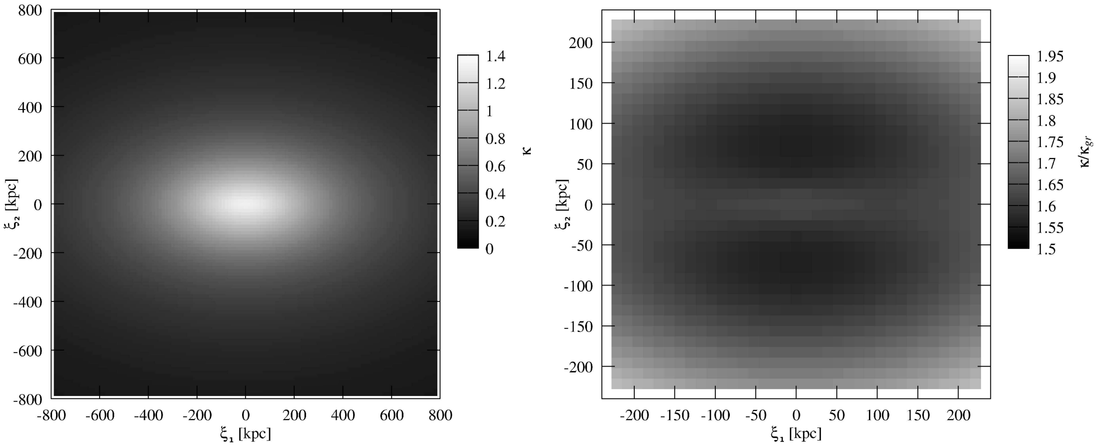

Figure 9.6: Numerically calculated TeVeS convergence κ (left panel) and the corresponding ratio $\kappa/\kappa_{\mathrm{gr}}$ (right) for an elliptical profile of type Eq. (9.52) with $\xi_{1,0} = 350$ kpc and $\xi_{2,0} = \zeta_0 = 200$ kpc: In the central part, the TeVeS convergence κ is unevenly amplified, thus breaking the elliptical symmetry. Compared to the dominant GR contributions, however, this effect is almost negligible.

Concerning the numerical setup, we take the point of origin, i.e. $\xi_1 = \xi_2 = \zeta = 0$, to coincide with the grid's center and assume the density profile (9.49) to be smoothly cut at a radius of 1.5 Mpc, which is necessary as, otherwise, our King-like profile would contain an infinite amount of mass. In accordance with the point lens approximation, we set the grid's volume to $V = (5 \text{ Mpc})^3$, thus having a spatial resolution of $\Delta\xi \simeq 13$ kpc $(N = 384)$. Furthermore, we take $\xi_0 = 200$ kpc and choose ρ_0 such that the lens's total mass is given by $M = 10^{15} M_{\odot}$, which now corresponds to a cluster-sized mass distribution. Regarding the remaining parameters, we keep the settings introduced in Section 9.3, the redshifts of source and lens being fixed to $z_{\mathrm{s}} = 3$ and $z_{\mathrm{l}} = 0.63$, respectively. Henceforth, if not explicitly noted, all presented numerical results are based upon these settings, including the spherical cut-off of the particular density profile at 1.5 Mpc. As we have to meet condition in Eq. (9.46) in order to apply the point lens approximation, we are obliged to satisfy $\zeta_0 \lesssim 600$ kpc in our numerical simulations.

The right panel of Figure 9.4 shows the effective TeVeS convergence of our King-like profile expressed in terms of the corresponding GR convergence κ_{gr} for $\zeta_0 = 50$ kpc and $\zeta_0 = 400$ kpc, respectively. Note that the GR maps are independent of the particular choice of ζ_0. Increasing the value of ζ_0, we observe a significant amplification of the TeVeS convergence around the center while there is basically no change in the outer region. As expected, the variation of ζ_0 has no effect on the symmetry properties of the convergence map. Concerning the TeVeS shear map, we find a similar behavior: While there is a strong increase of γ in the very center, we find only small changes in the outer parts. Interestingly, the TeVeS shear is not exactly circularly symmetric in that region any longer, with the actual form depending on the particular extent of the lens. Rather than being intrinsic to TeVeS, however, this is probably due to Fourier artifacts caused by the scalar field solver or the point lens approximation, an influence of the latter being actually expected as the choice of ζ_0 has an impact on Eq. (9.46).

Let us continue our analysis considering the effects on the critical lines due to the changes of κ and γ: Since Eq. (9.49) is axially symmetric, the corresponding lines turn into circles. In Figure 9.5, the radii of both the inner and outer critical curve are presented for different values of the parameter ζ_0. Obviously, these radii are increased when stretching the lens along the line of sight, showing relative deviations of up to roughly 6% and 16% for the radial and tangential critical radius, respectively. Note that the critical lines are calculated by interpolation between the grid points, thus allowing to determine positions which are below the grid's resolution. Although our investigation is limited to a small range of ζ_0, we find appreciable differences between the lensing maps which are assumed to considerably grow when stretching the lens further.

Summarizing the above, we may conclude that the lens's extent along the line of sight significantly affects the strong lensing properties. Therefore, the mass distribution along the ζ-axis can be regarded as an additional degree of freedom in TeVeS.

9.5.4 Elliptical Lenses

In this section, we shall consider lens systems whose projected mass density follows an elliptic profile. Therefore, introducing the scale lengths $\xi_{1,0}, \xi_{2,0}, \zeta_0 > 0$, let us consider a matter density distribution of the form

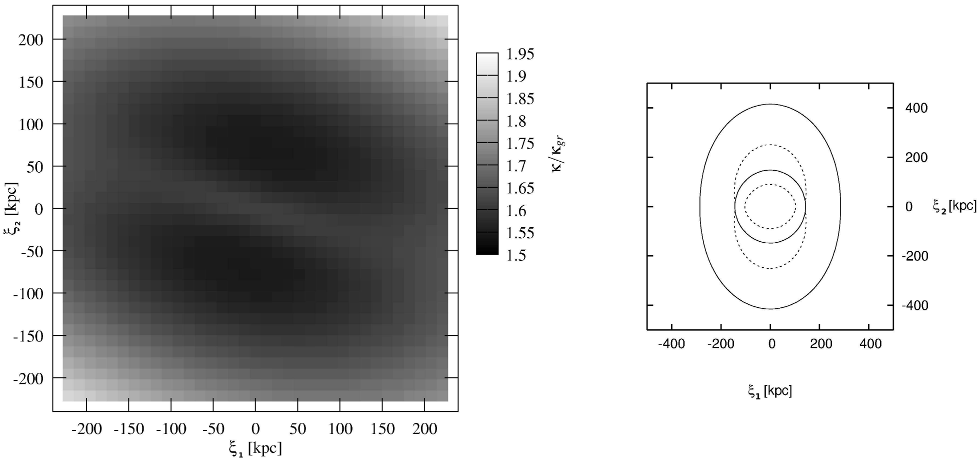

Figure 9.7: *Left panel.* Numerically calculated TeVeS convergence ratio $\kappa/\kappa_{\mathrm{gr}}$ for the rotated profile Eq. (9.52) with $\xi_{1,0} = 350$ kpc: In the central part, the TeVeS convergence κ is unevenly amplified, similar to the unrotated case shown in the bottom panel of Figure 9.6. Thus, it seems unlikely that the observed effect is a numerical artifact caused by our method. *Right panel.* Critical curves for both TeVeS (solid) and GR (dashed) assuming an elliptical profile of type Eq. (9.52) with $\xi_{1,0} = 150$ kpc and $\xi_{2,0} = \zeta_0 = 200$ kpc.

$$\rho(r) = \rho_0 \left[1 + \left(\frac{\xi_1}{\xi_{1,0}} \right)^2 + \left(\frac{\xi_2}{\xi_{2,0}} \right)^2 + \left(\frac{\zeta}{\zeta_0} \right)^2 \right]^{-\frac{3}{2}} . \tag{9.52}$$

Keeping $\xi_{2,0}$ and ζ_0 fixed, $\xi_{2,0} = \zeta_0 = 200$ kpc, we investigate the lensing properties for different choices of the parameter $\xi_{1,0}$, again setting the total mass to $M = 10^{15} M_\odot$. Figure 9.6 illustrates both the TeVeS convergence κ and the corresponding ratio $\kappa/\kappa_{\mathrm{gr}}$, with $\xi_{1,0}$ set to a value of 350 kpc. Although the symmetry properties of the GR convergence map are virtually sustained in TeVeS, we can observe an interesting feature located in the central part: Compared to its neighborhood, there is a slightly increased amplification close to the semi-major axis, breaking the elliptical symmetry. If this effect was larger, it could actually account for loosing track of the baryonic matter distribution, thus yielding a qualitatively different looking TeVeS convergence κ. For $\xi_{1,0} = 350$ kpc, we additionally present a simulation where the density profile Eq. (9.52) has been rotated around the ζ-, ξ_2- and ξ_1-axis by $10°$, $20°$ and $30°$, respectively. Clearly, the ratio $\kappa/\kappa_{\mathrm{gr}}$ illustrated in Figure 9.7 (left panel) shows essentially the same inner structure as in Figure 9.6. Therefore, it seems unlikely that the observed effect is a numerical artifact caused by our method.

In the right panel of Figure 9.7, we compare the critical lines in TeVeS to those obtained in GR assuming $\xi_{1,0} = 150$ kpc. The found symmetry-breaking effect does not appear to have any significant influence on the critical curves which therefore do not show any unfamiliar shapes compared to elliptical GR lenses. As the TeVeS convergence κ is calculated by a weighted amplification of κ_{gr}, however, the critical curves appear at a larger distance from the origin and their forms are varied to some extent compared to GR. Varying the value of $\xi_{1,0}$ from 100 kpc to 400 kpc, we substantially obtain the same findings.

9.5.5 Lenses with Multiple Components

Next, we want to explore gravitational lensing by multiple objects. For this purpose, let us consider a rather simple case and start with two density distributions, ρ_1 and ρ_2, following the King profile. Choosing $r_0 = 200$ kpc and $M_1 + M_2 = M = 10^{15} M_\odot$ (M_i denotes the total mass of the object located at $\boldsymbol{r}_i$ inside our volume), we shall place our densities at the following positions inside the grid volume ($r = \|\boldsymbol{r}\| = 0$ corresponds to the grid's origin):

$$\boldsymbol{r}_1 = \begin{pmatrix} \xi_1^{(2)} \\ 0 \\ \zeta_2 \end{pmatrix} , \quad \boldsymbol{r}_2 = - \begin{pmatrix} \xi_1^{(2)} \\ 0 \\ \zeta_2 \end{pmatrix} . \tag{9.53}$$

Thus, varying the parameters $\xi_1^{(2)}$ and ζ_2, we are able to control the relative alignment of our objects along the line of sight, i.e. the ζ-direction, as well as perpendicular to it.

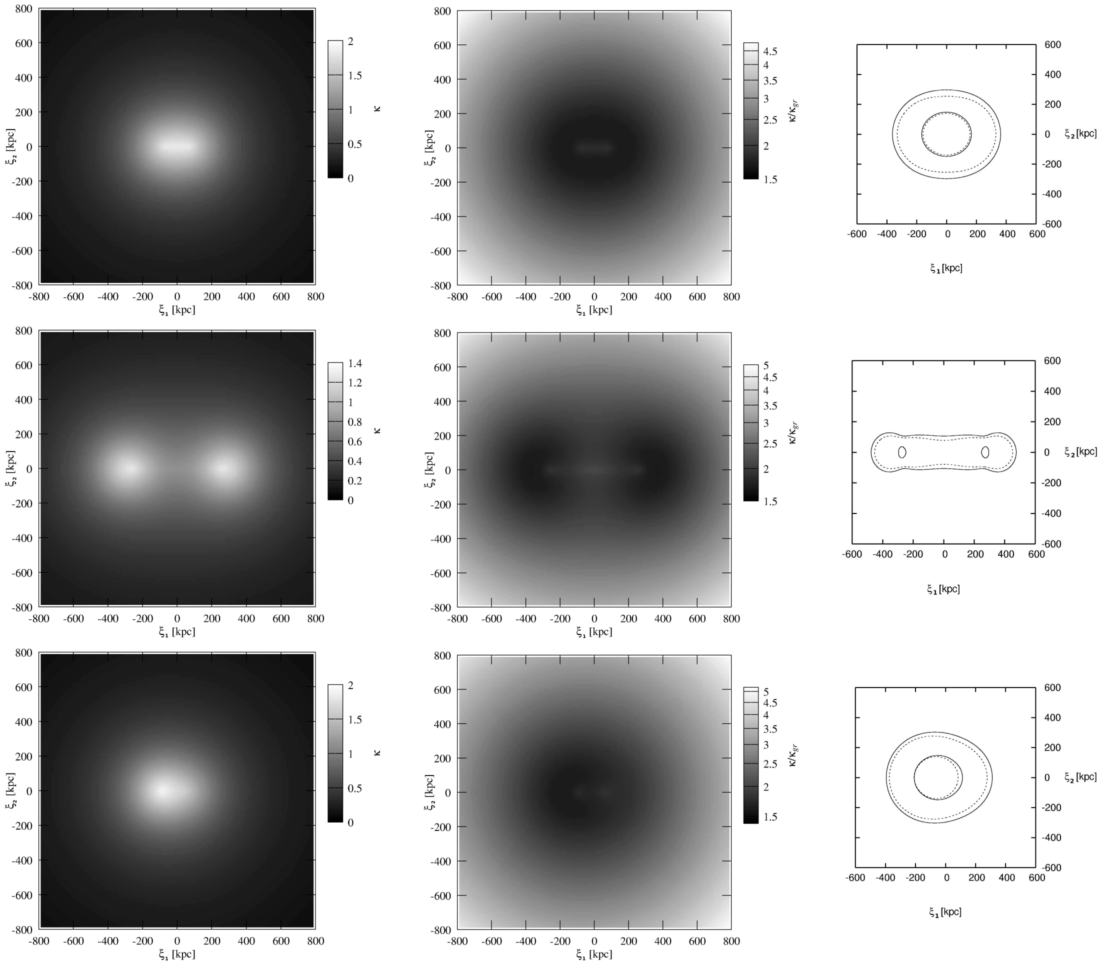

Figure 9.8: Lensing properties of our two-bullet system assuming $\xi_1^{(2)} = 100$ kpc and $M_1 = M_2$ (top panel), $\xi_1^{(2)} = 300$ kpc and $M_1 = M_2$ (middle panel), and $\xi_1^{(2)} = 100$ kpc and $3M_1 = M_2$ (bottom panel), respectively: We present the numerical results for both the TeVeS convergence κ (left) and the corresponding ratio $\kappa/\kappa_{\mathrm{gr}}$ (middle) setting $\zeta_2 = 400$ kpc. On the right, the TeVeS critical lines are plotted for $\zeta_2 = 0$ (dashed) and $\zeta_2 = 400$ kpc (solid). Note that the radial critical curve for $\xi_1^{(2)} = 300$ kpc and $\zeta_2 = 0$ does not appear due to the grid's finite resolution.

Equal Masses

As a first approach, we shall assume the total mass M to be evenly distributed on our two bullet-like objects, i.e. $M_1 = M_2$. Varying $\xi_1^{(2)}$ from 100 kpc to 300 kpc, we calculate the convergence maps and critical lines for different alignments along the line of sight, with the results for $\zeta_2 = 400$ kpc (and $\zeta_2 = 0$ for the critical curves) presented in Figure 9.8 (top and middle panel). Again, we notice that κ is amplified such that the symmetry properties of the surface density κ_{gr}, are virtually conserved, similar to the result found in the last section. Having a look at the central region, we additionally observe that κ is increased between the object's positions, which is actually expected since the Newtonian gradient $\boldsymbol{\nabla}\Phi_{\mathrm{N}}$ becomes small there. Altogether, as the TeVeS convergence map closely tracks the baryonic matter distribution, and we do not encounter any new surprising TeVeS effects considering our two-bullet system.

Increasing the quantity ζ_2, we discover a significant growth of κ around the central part, which is in accordance with our previous result from Section 9.5.3. Consequently, the corresponding critical lines, shown on the right hand side of Figure 9.8 (top and middle panel), are spatially driven outwards. Please also note that, due to the non-spherical symmetry of our problem, the shape of those curves is slightly changed when varying ζ_2.

Different Masses

In analogy to Section 9.5.5, we can perform a similar simulation choosing $3M_1 = M_2$.

Table 9.1: Component masses and positions for our toy model of the cluster merger 1E0657 $-$ 558: Concerning the masses of our toy model components, we use those derived by Clowe et al. (2006). The plasma mass is reconstructed from a multicomponent 3-dimensional cluster model fit to the Chandra X-ray image. Assuming a mass-to-light ratio of $M/L_{\mathrm{I}} = 2$, stellar masses are calculated from the I-band luminosity of all galaxies equal in brightness or fainter than the component's brightest cluster galaxies. Please note that all masses are averaged within an aperture of 100 kpc radius around the given position. For each component, the position perpendicular to the line of sight is approximately determined from the corresponding Magellan and Chandra images.

Component	(ξ_1, ξ_2, ζ) [kpc]	M_X [$10^{12} M_\odot$]	M_* [$10^{12} M_\odot$]	M_{total} [$10^{12} M_\odot$]
Main cluster	$(-350, -50, \zeta_1)$	5.5	0.5	6.0
Main cluster plasma	$(-140, 50, \zeta_2)$	6.6	0.2	6.8
Subcluster	$(350, -50, \zeta_3)$	2.7	0.6	3.3
Subcluster plasma	$(200, -10, \zeta_4)$	5.8	0.1	5.9

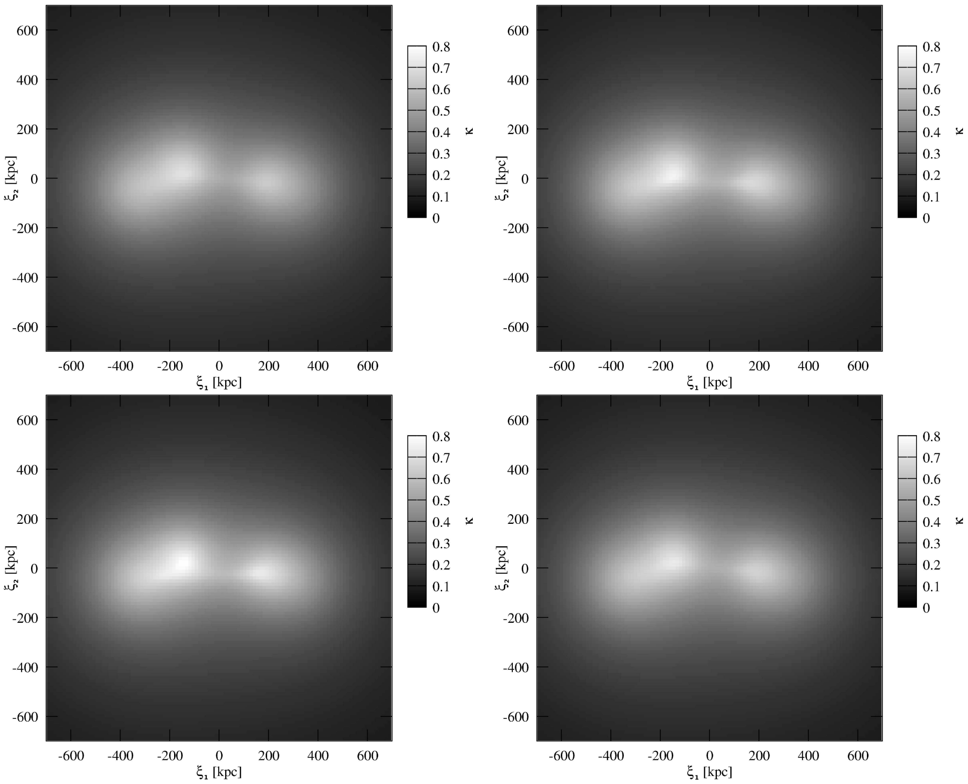

Figure 9.9: TeVeS convergence maps for our toy model of the bullet cluster: Assuming the framework of TeVeS, we present the numerically obtained convergence κ for the parameter sets A (upper left), B (upper right), C (lower left) and D (lower right).

Assuming $\xi_1^{(2)} = 100$ kpc, both the calculated convergence map and the critical lines are presented in the bottom panel of Figure 9.8 for $\zeta_2 = 400$ kpc (and $\zeta_2 = 0$ for the critical curves). As can be seen from the ratio $\kappa/\kappa_{\mathrm{gr}}$, the convergence is more strongly amplified in the $\xi_1 > 0$ regime, i.e. the region of lower mass density. Accordingly, the corresponding critical lines are drawn further outwards in that region. As the MONDian influence increases for smaller values of the Newtonian gradient's norm $\|\boldsymbol{\nabla}\Phi_{\mathrm{N}}\|$, however, this is exactly what one would expect. Choosing other bullet alignments or mass weightings, we basically obtain the same results.

9.5.6 Modeling the Bullet Cluster

Only recently, the cluster merger 1E0657 $-$ 558, has been announced as a direct empirical proof of the existence of DM (Clowe et al., 2006; Bradac et al., 2006) as the weak lensing reconstruction of κ shows peaks that are clearly detached from the dominant baryonic components, i.e. the plasma clouds.

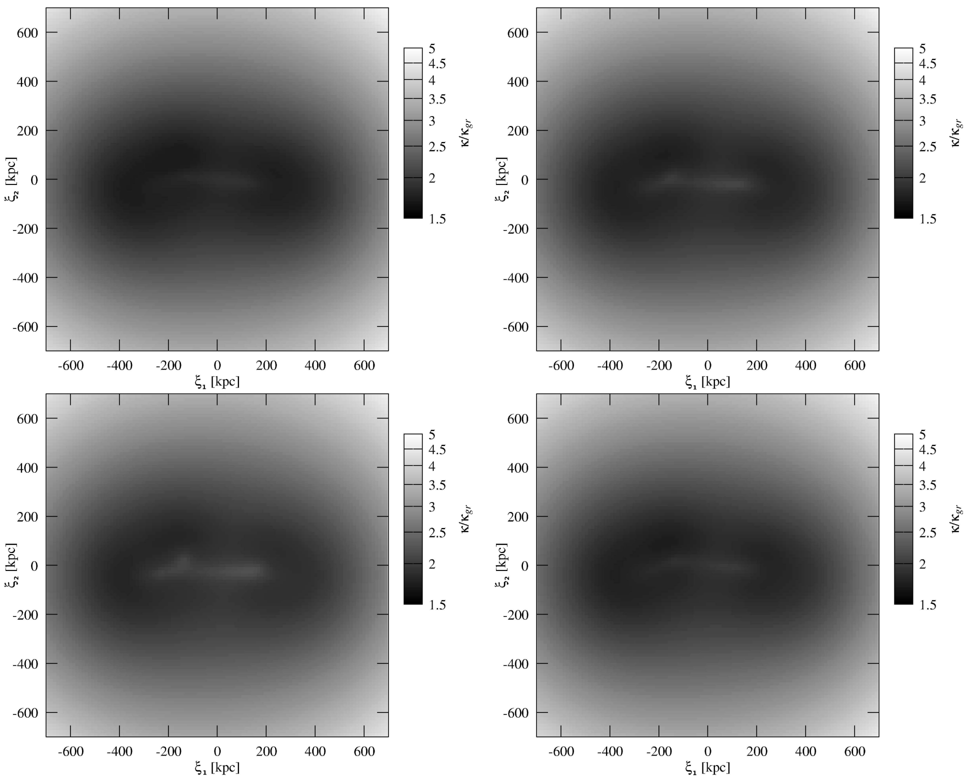

Figure 9.10: TeVeS convergence ratio $\kappa/\kappa_{\rm gr}$ for our toy model of the bullet cluster: Assuming the framework of TeVeS, we present the numerically obtained convergence ratio $\kappa/\kappa_{\rm gr}$ for the parameter sets A (upper left), B (upper right), C (lower left) and D (lower right).

Using an analytic model, Angus et al. (2007) have fit this map and derived the corresponding baryonic matter density in MOND-like gravity, concluding that it is not possible to model the merger without assuming an additional invisible mass component located in the central parts of the two clusters. As they have used the weak lensing reconstruction of Clowe et al. (2006), however, their convergence map does not account for the observed strong lensing features within this system.

In addition, the same convergence map appears to be incompatible with the values of plasma masses independently estimated from Chandra observations, which, as remarked by the authors, may be due to the smoothing scale of the weak lensing reconstruction. To avoid such discrepancies, we shall create a simple toy model of the bullet cluster's baryonic matter density that allows to be treated with our numerical method.

The bullet cluster basically consists of four objects: The main cluster, a slightly smaller subcluster and two plasma clouds appearing in between. For the 3-dimensional matter density, we shall model these components using the analytic King profile Eq. (2.49), choosing core radii r_0 of 200 kpc and 150 kpc for the clusters and the plasma clouds, respectively. Concerning the particular masses, we use the values of Clowe et al. (2006) which are derived independently of gravitational lensing. According to the authors, the plasma mass is reconstructed from a multicomponent 3-dimensional cluster model fit to the Chandra X-ray image while, assuming a mass-to-light ratio of $M/L_{\rm I} = 2$, the stellar mass is calculated from the I-band luminosity of all galaxies equal in brightness or fainter than the component's brightest cluster galaxies. Together with the approximate positions of the components, the corresponding mass values are presented in Table 9.1. Please note that all masses are averaged within an aperture of 100 kpc radius around the given position.

For the calculation of the lensing maps, we set the redshift of the bullet cluster, i.e. the lens, to $z_{\rm l} = 0.296$ (Clowe et al., 2006) and assume a source redshift of $z_{\rm s} = 1$.

Since the position of the particular constituents can only be constrained perpendicular to the line of sight, we actually have substantial freedom in selecting their alignment along the ζ-direction. For our analysis, we choose four different sets of ζ_i which are shown in Table 9.2. Let us briefly discuss the meaning of these choices: Clearly, the parameter set A implies that all components are located in the same plane perpendicular to the line of sight. The choices B and C account for the plasma clouds to be displaced in opposite directions along the ζ-axis, which is a reasonable assumption considering today's view of the bullet cluster to be a post-merger snapshot. Finally, the parameter set D fairly describes the situation of the axis connecting the cluster centers being inclined with respect

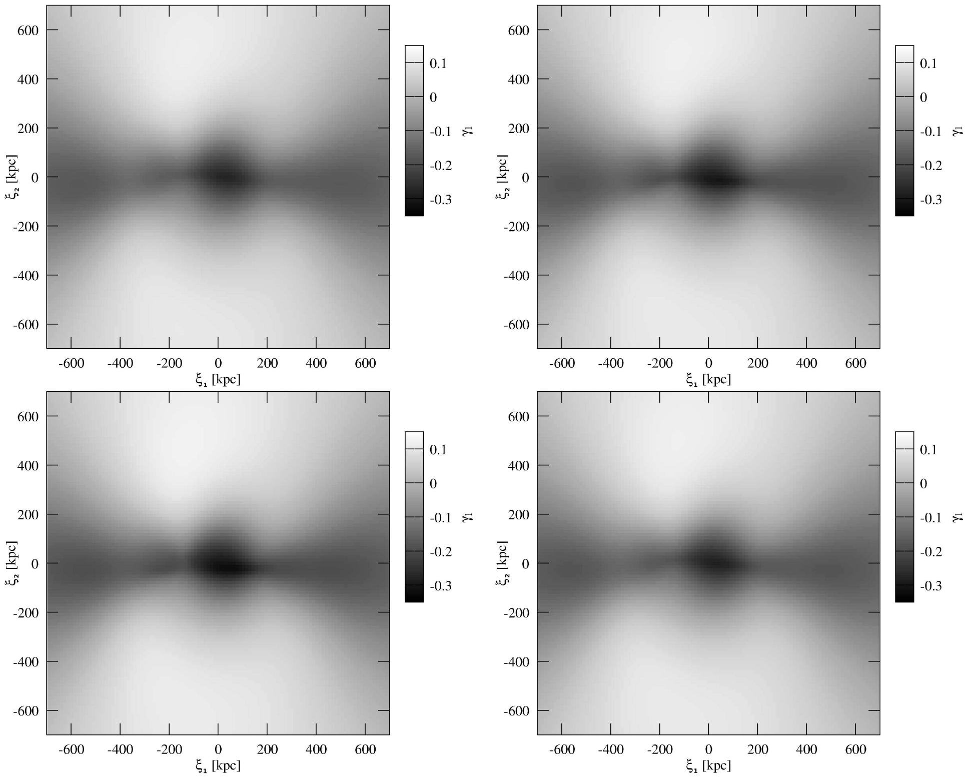

Figure 9.11: TeVeS maps of the shear component γ_1 for our toy model of the bullet cluster: Assuming the framework of TeVeS, we present the numerically obtained shear component γ_1 for the parameter sets A (upper left), B (upper right), C (lower left) and D (lower right).

Table 9.2: Parameter sets used within the toy model of the cluster merger $1E0657-558$: In our simulations, the above sets are used to specify the component's alignment along the line of sight, i.e. the ζ- direction.

Parameter set	ζ_1	ζ_2	ζ_3	ζ_4
A	0	0	0	0
B	0	300	0	-300
C	0	500	0	-500
D	300	100	-300	-100

to the ζ-direction.

Figures 9.9 and 9.10 illustrate both the resulting TeVeS convergence map κ and the corresponding ratio $\kappa/\kappa_{\mathrm{gr}}$ for the parameter sets listed in Table 9.2. From Figure 9.10, we again find that there are TeVeS effects causing additional structure within the central part, and increasing the constituent's relative displacement along the ζ-axis, we observe these structures growing stronger to some extent. Similar to our previously considered lens models, however, the TeVeS effects are not large enough to account for displacements from the dominant baryonic components. Additionally, we present maps of the TeVeS shear components γ_1 and γ_2 which are shown in Figures 9.11 and 9.12, respectively.

Clearly, our result confirms the findings of Angus et al. (2007). To provide an acceptable explanation of the observations, TeVeS needs an additional mass component centered at the cluster positions. As has been suggested by others, e.g. Sanders (2007), primordial neutrinos with mass on the order of 2 eV might be able to resolve the problem. Checking the y-values, i.e. the arguments of the free function, near the cluster centers in our simulation, we found that the nonlinearity of Eq. (9.16) still has a relevant impact on the resulting scalar field. Therefore, it is not possible to isolate neutrino effects as a pure additive contribution to the overall convergence map and to give constraints on the amount and distribution of such neutrinos for a given mass. Current work is trying to find an approximate way of dealing with this issue using our previous numerical results.

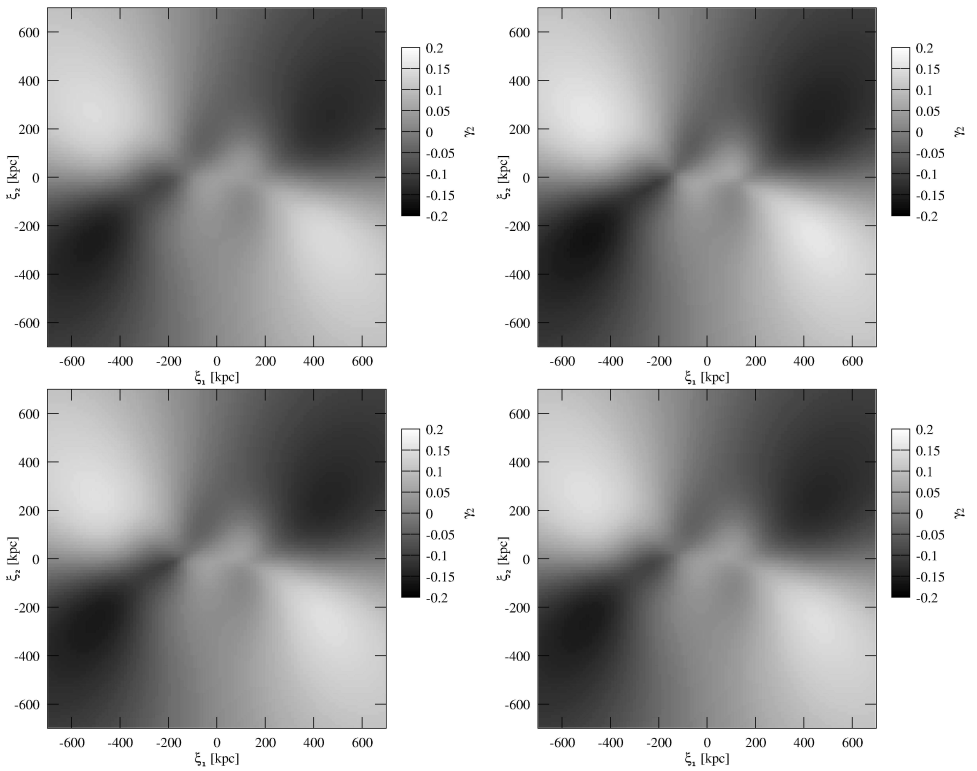

Figure 9.12: TeVeS maps of the shear component γ_2 for our toy model of the bullet cluster: Assuming the framework of TeVeS, we present the numerically obtained shear component γ_2 for the parameter sets A (upper left), B (upper right), C (lower left) and D (lower right).

9.6 Conclusions

In this Chapter, we have analyzed the effects of gravitational lensing within the framework of TeVeS, focusing on asymmetric systems.

Considering spherically symmetric lenses, we introduced a parameterization of the free function $y(\mu)$ showing that the particular realization of the singularity at $\mu = 1$ has a trifling influence on the deflection angle. Furthermore, we concluded that variations of the coupling constant k_s lead to negligibly small effects as long as $k_\mathrm{s} \lesssim 10^{-2}$. Thus, we were able to determine classes of $y(\mu)$ that nearly produce the same deflection angle.

Choosing a single form of the free function, we succeeded in building a fast Fourier-based solver for scalar potential ϕ which could be applied to a set of different non-spherical lens types. Concerning variations on rather small scales, we noticed a strong dependence of the lensing properties on the lens's extent along the line of sight, with a significant impact on the critical curves. Additionally, every simulated TeVeS convergence map showed a strong resemblance with the dominant baryonic mass components, other effects, being capable of counteracting this trend, turned out to be very small. To study a more complex lens system, we finally created a toy model of the bullet cluster's baryonic matter density. The outcome of our simulation clearly confirms the results of Angus et al. (2007) as it is not possible to explain the observed weak lensing map without assuming an additional dark mass component in both cluster centers.

Future work will address even more complex lens systems like, for example, the GC Abell 2390 with its straight arc (Kassiola et al., 1992). Increasing the lens' level of substructure, effects that account for loosing track of the projected matter density could become more important, thus influencing the ability of TeVeS to model such a lens. In addition, one can use these models to check if TeVeS is consistent with the assumption of massive neutrinos in GCs.

Conclusions

In this thesis we have used a semi-analytic approach to the study of the statistics of long and thin gravitational arcs. Attention was also directed to the interplay between strong lensing efficiency and X-ray emission in galaxy clusters, as well as to the effect of the internal structure of dark matter halos on X-ray observables. A minor part of the investigation was also dedicated to the study of gravitational lensing in theories of gravity alternative to general relativity.

Particular emphasis was paid to the so-called arc statistics problem, namely the fact that the observed number of arcs in statistically complete cluster samples is in strong disagreement with the predicitions based on a standard ΛCDM cosmology. This problem was first point out by Bartelmann et al. (1998), who found a discrepancy of about one order of magnitude. In this work we aimed at finding possible explanations for this disagreement, quantify it in light of more accurate theoretical estimates and help evaluating the relative importance of the different contributions to arc statistics.

The main results of the investigation are briefly summarised below. Additional discussions can be found in the main body of this thesis and in the reference quoted.

- ▷ We presented a novel semi-analytic method for the computation of strong lensing cross sections, along with its validity and limitations. The algorithm performs more than one order of magnitude faster than standard fully numerical ray-tracing simulations, producing results that are in eccellent agreement with them. These characteristics make our method ideally suited for parameter studies involving the statistics of long and thin arcs. We have applied the method to the evaluation of the global strong lensing efficiency of a synthetic cluster population, with realistic merger histories extracted from a high-resolution numerical simulation. The boosting effect of cluster mergers on the efficiency for the production of strong lensing features was analysed through simple modelling. The result is that the interaction between structures can boost the total number of arcs produced in the sky by at least a factor of ~ 2, expecially at intermediate and high redshift, where the merger activity is most significant. We also performed a brief study regarding the effect of source properties on the arc statistics, and comparing to previous work. All the results are presented in Fedeli et al. (2006).

- ▷ We used the semi-analytic method mentioned above to study the effect of different models of dark energy on the gravitational arc statistics. The cluster population was modelled using Monte-Carlo simulations of merger trees, following the lines of the extended Press & Schechter (1974) formalism. Moreover, a background source redshift distribution fitting observational data was used. The dark energy models studied include a standard ΛCDM cosmology, a universe where the equation of state parameter for dark energy is constant and equals $w_\mathrm{x} = -0.8$, and two models with early-dark energy, characterised by a small but still significant amount of quintessence at high redshift. The latter two models have slightly different spectral indices and normalizations of the power spectrum in order to comply with present observational constraints. The generic consequence of primordial dark energy is that structure formation is shifted to higher redshift, thus producing more massive structures at low redshift. As a consequence it is found that the efficiency for the production of long and thin arcs increases by a factor of ~ 3 in early-dark energy models, when compared to models with constant w_x. Also, it was confirmed that cluster mergers enhance the lensing efficiency by factors between 2 and 3, with little change due to cosmology. An important point is that the lensing efficiency in early-dark energy models is still important at high redshift, where it is negligible for a ΛCDM model. This can have important consequences from an observational point of view. This work is described in Fedeli & Bartelmann (2007a).

- ▷ As a subsequent step, we asked how arc statistics could be modified by selection effects. Given the fact that strong lensing features are usually searched for in X-ray selected galaxy clusters, we assigned an X-ray flux to each cluster in the populations previously evolved in different dark energy cosmologies. To that end we used the virial mass-temperature relation, whose normalization was calibrated against numerical simulations, and an observationally fitted mass-luminosity relation. The boosting effect of cluster mergers on temperature and luminosity of the intracluster medium was suitably taken into account using a simplified model based on fits to numerical hydrodynamical simulations. It was shown that the scatter in the relation between bulk properties is consistent with the observed one, hence confirming the goodness of the model. Instrumental effects like background subtraction and PSF convolution were taken into account with reference to the ROSAT satellite, and flux-limited X-ray cluster catalogues were constructed using the same procedure as for the construction of the observed *Reflex* cluster sample. We computed the total optical depth for long and thin arcs obtained from cluster samples with different limiting fluxes, finding that, quite independent of cosmology, X-ray bright clusters above a flux limit of $\sim 3 \times 10^{-14}$ erg s^{-1} cm^{-2} produce about 60% of the total strong lensing optical depth, and only $\sim 1\%$ above $\sim 3 \times 10^{-12}$ erg s^{-1} cm^{-2}. The boosting effect of cluster mergers on arc statistics is quite insensitive to the limiting flux. Moreover, it was shown that the observed redshift distribution of clusters in the *Reflex* sample can be reproduced only if cluster interaction is considered. These results are published in Fedeli & Bartelmann (2007b).

▷ We investigated the effect on the arc statistics of the distribution in the concentration of dark matter halos around the nominal value. Only results in a ΛCDM cosmological model are studied in this case. As a preliminary analysis we checked the difference in terms of cross sections arising when the concentration of a halo of fixed mass is computed according to the three different prescriptions available in the literature. We find that the best motivated of these prescriptions, namely the one from Eke et al. (2001), gives results that lie in between the Bullock et al. (2001) and the Navarro et al. (1997) algorithms. Next, we assumed a log-normal distribution for the concentration around its nominal value and introduced it into the calculation of the strong lensing properties of our synthetic cluster population. Since a log-normal distribution is skewed toward high values, the result is a modest increase in the lensing optical depth, of the order of $\sim 50\%$. Finally, we analysed the relation between halo concentration and cross section for long and thin arcs and X-ray luminosity and temperature of single clusters. It is found that, when structures of similar mass are considered, strong lensing and X-ray luminous clusters are also on average more concentrated. On the other hand, the opposite is true for the gas temperature, because of the very mild dependence on the internal structure of the host dark matter halo. The results of this work are also found in (Fedeli et al., 2007).

▷ The effect on the statistics of long and thin arcs of the normalization for the primordial power spectrum was studied. An increase in the normalization σ_8 has the effect of shifting the structure formation process at higher redshift, hence producing more massive clusters at low redshift. We showed that the total number of arcs produced in the sky can increase by up to one order of magnitude when moving from a WMAP-3 normalization to a value $\sigma_8 \sim 0.9$. Qualitatively the effect is somewhat similar to the introduction of a dynamical quintessence model, since in this case as well the high redshift lensing efficiency displays the largest difference. As for the effect of cluster mergers, this is partially reduced in high normalization models because there clusters have a higher concentration, that implies a lower sensitivity of the strong lensing cross section to external perturbations. Moreover, high values of σ_8 shift the merger activity at high redshifts, where part of its effect is lost due to the constant source redshift distribution. We also convolved the optical depth computed in the different models with a realistic source luminosity function, in order to predict the total number of arcs that could be observed up to a given limiting magnitude. The result is that the contrast with observational data is much alleviated when compared to the original results of Bartelmann et al. (1998), but only when $\sigma_8 \sim 0.9$. If a low normalization is used instead, as seems to be indicated by the latest WMAP results, then there still is an order of magnitude discrepancy.

▷ For a final investigation, we developed and tested a numerical algorithm for the computation of lensing properties in the fremwork of the TeVeS gravity theory. This theory received much attention recently since it represents the fully covariant generalization of the older MOND paradigm. As such, it turns out that, even in the non-relativistic limit, the gravity field is coupled in a highly non-linear way to the matter fields. As is showed in this work this implies that, opposite to the general relativity case, the lensing properties depend on the extension of the deflector along the line of sight. Therefore it is not possible to develop a formalism that deals only with projected quantities, and in particular it is not possible to relate the projected matter density with derivatives of the projected Newtonian potential. Moreover, it was proven that the free function of the theory has often little influence on the deflection angle, so that large classes of free functions can be identified that virtually produce the same lensing properties for a given lensing configuration. Finally, we applied the numerical algorithm to the solution of non-spherically symmetric systems, and in particular systems with multiple components, including a naive model for the cluster merger $1\mathrm{E}0657-558$. It was found that the highly non-linear coupling between the gravity fields and matter can produce the TeVeS convergence to lose track of the real matter distribution, buth such an effect is very mild, and cannot account alone for the observed data on the bullet cluster. The work is published in Feix et al. (2007).

The statistics of gravitational arcs is in principle a powerful tool to probe the underlying cosmology, because such events are extremely rare and their probability depends in a highly non-linear fashion on the structure formation process and the geometry of the Universe. However, it was shown in this work that the arc statistics problem still hold when sources are suitably distributed in redshift and the effect of cluster mergers is properly taken into account. In particular, the discrepancy becomes worst when the low normalization suggested by the WMAP-3 data release is used. Here we gave a contribution into understanding which pieces of the cluster physics have relevance and how to the arc statistics, and also explored some alternative possibilities, like more general models for dark energy. The issues that we inspected can help to figure out what is missing from the present picture and also to explain peculiar observations, like the high incidence of gravitational arcs in high redshift clusters, recently pointed out by Gladders et al. (2003); Zaritsky & Gonzalez (2003).

Much work remains to be done in this direction. For instance, more thorough analyses of the effect of the source redshift distribution, as well as irregularities in the background galaxies would be welcome. Study of the strong lensing properties of model galaxy clusters extracted by large cosmological simulations with high space and time resolution and their relation to the structural and dynamical parameters of the clusters themselves would also be extremely useful. This would be particularly true if gas physics is included in the simulations, so as to account for possible selection effects. Additional work in simulating real observational conditions is also required.

In addition to this, the observational situation is going to improve in the near future thanks to dedicated surveys like the DUNE project (Réfrégier et al., 2006) and to the application therein of automatic algorithms for the detection of long and thin features. Up to hundreds of new systems of gravitational arcs are expected to become availble in the forthcoming years, greatly ameliorating the test ground for theoretical models.

Bibliography

Adler, R. J. 1981, The Geometry of Random Fields (The Geometry of Random Fields, Chichester: Wiley, 1981)

Albrecht, A., Bernstein, G., Cahn, R., et al. 2006, ArXiv Astrophysics e-prints, astro-ph/0609591

Albrecht, A. & Steinhardt, P. J. 1982, Physical Review Letters, 48, 1220

Aldering, G., Akerlof, C. W., Amanullah, R., et al. 2002, in Presented at the Society of Photo-Optical Instrumentation Engineers (SPIE) Conference, Vol. 4835, Future Research Direction and Visions for Astronomy. Edited by Dressler, Alan M. Proceedings of the SPIE, Volume 4835, pp. 146-157 (2002)., ed. A. M. Dressler, 146–157

Allen, S. W. & Fabian, A. C. 1998, MNRAS, 297, L57

Angus, G. W., Shan, H. Y., Zhao, H. S., & Famaey, B. 2007, ApJ, 654, L13

Arnaud, K. A. 1996, in Astronomical Society of the Pacific Conference Series, Vol. 101, Astronomical Data Analysis Software and Systems V, ed. G. H. Jacoby & J. Barnes, 17–+

Arnold, V. I. 1978, Mathematical methods of classical mechanics (Graduate texts in mathematics, New York: Springer, 1978)

Astier, P., Guy, J., Regnault, N., et al. 2006, A&A, 447, 31

Babul, A., Balogh, M. L., Lewis, G. F., & Poole, G. B. 2002, MNRAS, 330, 329

Baccigalupi, C., Balbi, A., Matarrese, S., Perrotta, F., & Vittorio, N. 2002, Phys. Rev. D, 65, 063520

Baccigalupi, C., Matarrese, S., & Perrotta, F. 2000, Phys. Rev. D, 62, 123510

Bardeen, J. M., Bond, J. R., Kaiser, N., & Szalay, A. S. 1986, ApJ, 304, 15

Bartelmann, M. 1996, A&A, 313, 697

Bartelmann, M., Doran, M., & Wetterich, C. 2006, A&A, 454, 27

Bartelmann, M., Huss, A., Colberg, J. M., Jenkins, A., & Pearce, F. R. 1998, A&A, 330, 1

Bartelmann, M. & Schneider, P. 2001, Phys. Rep., 340, 291

Bartelmann, M. & Steinmetz, M. 1996, MNRAS, 283, 431

Bartelmann, M., Steinmetz, M., & Weiss, A. 1995, A&A, 297, 1

Bartelmann, M. & Weiss, A. 1994, A&A, 287, 1

Bartelmann, M. & White, S. D. M. 2003, A&A, 407, 845

Bekenstein, J. & Milgrom, M. 1984, ApJ, 286, 7

Bekenstein, J. D. 2004, Phys. Rev. D, 70, 083509

Benson, A. J., Kamionkowski, M., & Hassani, S. H. 2005, MNRAS, 357, 847

Binney, J. & Tremaine, S. 1987, Galactic dynamics (Princeton, NJ, Princeton University Press, 1987, 747 p.)

Blandford, R. D. & Kochanek, C. S. 1987, ApJ, 321, 658

Böhringer, H., Schuecker, P., Guzzo, L., et al. 2001, A&A, 369, 826

Bond, J. R., Cole, S., Efstathiou, G., & Kaiser, N. 1991, ApJ, 379, 440

Brada, R. & Milgrom, M. 1995, MNRAS, 276, 453

Brada, R. & Milgrom, M. 1999, ApJ, 519, 590

Bradac, M., Clowe, D., Gonzalez, A., et al. 2006, in Bulletin of the American Astronomical Society, Vol. 38, Bulletin of the American Astronomical Society, 955–+

Bradač, M., Clowe, D., Gonzalez, A. H., et al. 2006, ApJ, 652, 937

Bradač, M., Erben, T., Schneider, P., et al. 2005, A&A, 437, 49

Brans, C. & Dicke, R. H. 1961, Physical Review, 124, 925

Brax, P. & Martin, J. 2000, Phys. Rev. D, 61, 103502

Brown, R. L., Wild, W., & Cunningham, C. 2004, Advances in Space Research, 34, 555

Bryan, G. L. & Norman, M. L. 1998, ApJ, 495, 80

Bullock, J. S., Kolatt, T. S., Sigad, Y., et al. 2001, MNRAS, 321, 559

Buote, D. A., Gastaldello, F., Humphrey, P. J., et al. 2007, ApJ, 664, 123

Cabanac, R. A., Alard, C., Dantel-Fort, M., et al. 2007, A&A, 461, 813

Cacciato, M., Bartelmann, M., Meneghetti, M., & Moscardini, L. 2006, A&A, 458, 349

Casertano, S., de Mello, D., Dickinson, M., et al. 2000, AJ, 120, 2747

Cassano, R. & Brunetti, G. 2005, MNRAS, 357, 1313

Cavaliere, A. & Fusco-Femiano, R. 1976, A&A, 49, 137

Cavaliere, A. & Fusco-Femiano, R. 1978, A&A, 70, 677

Chandrasekhar, S. 1943, Reviews of Modern Physics, 15, 1

Ciotti, L. 2000, Lecture notes on stellar dynamics (Pisa, Scuola Normale Superiore, 2000, 160 p.)

Ciotti, L. & Binney, J. 2004, MNRAS, 351, 285

Ciotti, L., Londrillo, P., & Nipoti, C. 2006, ApJ, 640, 741

Clowe, D., Bradač, M., Gonzalez, A. H., et al. 2006, ApJ, 648, L109

Cole, S. & Lacey, C. 1996, MNRAS, 281, 716

Cole, S., Percival, W. J., Peacock, J. A., et al. 2005, MNRAS, 362, 505

Coles, P. & Jones, B. 1991, MNRAS, 248, 1

Coles, P. & Lucchin, F. 2002, Cosmology: The Origin and Evolution of Cosmic Structure, Second Edition (Cosmology: The Origin and Evolution of Cosmic Structure, Second Edition, by Peter Coles, Francesco Lucchin, pp. 512. ISBN 0-471-48909-3. Wiley-VCH , July 2002.)

Collins, C. A., Guzzo, L., Böhringer, H., et al. 2000, MNRAS, 319, 939

Comerford, J. M. & Natarajan, P. 2007, MNRAS, 379, 190

Cooray, A. R. 1999, A&A, 341, 653

Corless, V. L. & King, L. J. 2007, MNRAS, 380, 149

Cruz, M., Tucci, M., Martínez-González, E., & Vielva, P. 2006, MNRAS, 369, 57

Dalal, N., Holder, G., & Hennawi, J. F. 2004, ApJ, 609, 50

de Vaucouleurs, G. 1953, MNRAS, 113, 134 de Zotti, G., Burigana, C., Baccigalupi, C., & Ricci, R. 2004, in Observing, Thinking and Mining the Universe, ed. G. Miele & G. Longo, 95–+

Diaferio, A. 1999, MNRAS, 309, 610

Dickey, J. M. & Lockman, F. J. 1990, ARA&A, 28, 215

Dolag, K., Bartelmann, M., Perrotta, F., et al. 2004, A&A, 416, 853

Doran, M. & Robbers, G. 2006, Journal of Cosmology and Astro-Particle Physics, 6, 26

Doran, M., Schwindt, J.-M., & Wetterich, C. 2001, Phys. Rev. D, 64, 123520

Dubinski, J. & Carlberg, R. G. 1991, ApJ, 378, 496

Dvali, G., Gabadadze, G., & Porrati, M. 2000, Physics Letters B, 485, 208

Eddington, A. S. 1919, The Observatory, 42, 119

Einstein, A. 1915a, Sitzungsberichte der Königlich Preußischen Akademie der Wissenschaften (Berlin), Seite 778-786., 778

Einstein, A. 1915b, Sitzungsberichte der Königlich Preußischen Akademie der Wissenschaften (Berlin), Seite 799-801., 799

Einstein, A. 1916, Annalen der Physik, 354, 769

Einstein, A. 1919, Naturwissenschaften, 7, 776

Einstein, A. & de Sitter, W. 1932, Proceedings of the National Academy of Science, 18, 213

Eisenstein, D. J. & Hu, W. 1998, ApJ, 496, 605

Eisenstein, D. J., Zehavi, I., Hogg, D. W., et al. 2005, ApJ, 633, 560

Eke, V. R., Cole, S., & Frenk, C. S. 1996, MNRAS, 282, 263

Eke, V. R., Navarro, J. F., & Frenk, C. S. 1998, ApJ, 503, 569

Eke, V. R., Navarro, J. F., & Steinmetz, M. 2001, ApJ, 554, 114

Ellis, R. S. 1997, ARA&A, 35, 389

Etherington, I. M. H. 1933, Phil. Mag., 15, 761

Evrard, A. E., Bialek, J., Busha, M., et al. 2007, ArXiv Astrophysics e-prints, astro-ph/0702241

Faltenbacher, A., Gottloeber, S., & Mathews, W. G. 2006, ArXiv Astrophysics e-prints, astro-ph/0609615

Fedeli, C. & Bartelmann, M. 2007a, A&A, 461, 49

Fedeli, C. & Bartelmann, M. 2007b, A&A, 474, 355

Fedeli, C., Bartelmann, M., Meneghetti, M., & Moscardini, L. 2007, A&A, 473, 715

Fedeli, C., Meneghetti, M., Bartelmann, M., Dolag, K., & Moscardini, L. 2006, A&A, 447, 419

Feix, M., Fedeli, C., & Bartelmann, M. 2007, ArXiv Astrophysics e-prints, 0707.0790

Ferreira, P. G. & Joyce, M. 1998, Phys. Rev. D, 58, 023503

Flores, R. A., Maller, A. H., & Primack, J. R. 2000, ApJ, 535, 555

Freedman, W. L., Madore, B. F., Gibson, B. K., et al. 2001, ApJ, 553, 47

Friedmann, A. 1922, Z. Phys., 10, 377

Fukazawa, Y., Makishima, K., Tamura, T., et al. 1998, PASJ, 50, 187

Fukushige, T. & Makino, J. 1997, ApJ, 477, L9+

Gavazzi, R. 2005, A&A, 443, 793

Geller, M. J., Diaferio, A., & Kurtz, M. J. 1999, ApJ, 517, L23

Gioia, I. M., Luppino, G., Annis, J., Hammer, F., & Le Fèvre, O. 1996, in IAU Symposium, Vol. 168, Examining the Big Bang and Diffuse Background Radiations, ed. M. C. Kafatos & Y. Kondo, 549–+

Gioia, I. M. & Luppino, G. A. 1994, ApJS, 94, 583

Gladders, M. D., Hoekstra, H., Yee, H. K. C., Hall, P. B., & Barrientos, L. F. 2003, ApJ, 593, 48

Goldstein, J. H., Ade, P. A. R., Bock, J. J., et al. 2003, ApJ, 599, 773

Golse, G. & Kneib, J.-P. 2002, A&A, 390, 821

Grossi, M., Dolag, K., Branchini, E., Matarrese, S., & Moscardini, L. 2007, ArXiv Astrophysics e-prints, 0707.2516

Guth, A. H. 1981, Phys. Rev. D, 23, 347

Hammer, F. & Rigaut, F. 1989, A&A, 226, 45

Harrison, E. R. 1970, Phys. Rev. D, 1, 2726

Hashimoto, Y., Hasinger, G., Arnaud, M., Rosati, P., & Miyaji, T. 2002, A&A, 381, 841

Hasinger, G., Boese, G., & Predehl, P. e. a. 1995, MPE/OGIP Calibration Memo CAL/ROS/93-015

Hawkins, E., Maddox, S., Cole, S., et al. 2003, MNRAS, 346, 78

Hebecker, A. & Wetterich, C. 2001, Physics Letters B, 497, 281

Hennawi, J. F., Dalal, N., Bode, P., & Ostriker, J. P. 2007, ApJ, 654, 714

Henriksen, R. N. 2006, ApJ, 653, 894

Henriksen, R. N. 2007, ArXiv Astrophysics e-prints, 0709.0434

Henry, J. P. 2004, ApJ, 609, 603

Hernquist, L. 1990, ApJ, 356, 359

Hinshaw, G., Nolta, M. R., Bennett, C. L., et al. 2007, ApJS, 170, 288

Hoekstra, H. 2007, MNRAS, 379, 317

Hoekstra, H., Mellier, Y., van Waerbeke, L., et al. 2006, ApJ, 647, 116

Hopkins, P. F., Bahcall, N. A., & Bode, P. 2005, ApJ, 618, 1

Horesh, A., Ofek, E. O., Maoz, D., et al. 2005, ApJ, 633, 768

Hu, W. 1999, ApJ, 522, L21

Hubble, E. 1929, Proceedings of the National Academy of Science, 15, 168

Hubble, E. P. 1930, ApJ, 71, 231

Ikebe, Y., Reiprich, T. H., Böhringer, H., Tanaka, Y., & Kitayama, T. 2002, A&A, 383, 773

Jansen, F., Lumb, D., Altieri, B., et al. 2001, A&A, 365, L1

Jarosik, N., Barnes, C., Greason, M. R., et al. 2007, ApJS, 170, 263

Jaynes, E. T. 1957a, Physical Review, 106, 620

Jaynes, E. T. 1957b, Physical Review, 108, 171

Jenkins, A., Frenk, C. S., White, S. D. M., et al. 2001, MNRAS, 321, 372

Jing, Y. P. 2000, ApJ, 535, 30

Jing, Y. P. & Suto, Y. 2002, ApJ, 574, 538

Jones, L. R., Scharf, C., Ebeling, H., et al. 1998, ApJ, 495, 100

Kaiser, N. 1986, MNRAS, 222, 323

Kaiser, N., Squires, G., & Broadhurst, T. 1995, ApJ, 449, 460

Kassiola, A. & Kovner, I. 1993, ApJ, 417, 450

Kassiola, A., Kovner, I., & Blandford, R. D. 1992, ApJ, 396, 10

Kay, S. T., Pearce, F. R., Frenk, C. S., & Jenkins, A. 2002, MNRAS, 330, 113

Keeton, C. R. 2001a, ArXiv Astrophysics e-prints, astro-ph/0102341

Keeton, C. R. 2001b, ApJ, 562, 160

Keeton, C. R., Kochanek, C. S., & Seljak, U. 1997, ApJ, 482, 604

Keeton, C. R. & Madau, P. 2001, ApJ, 549, L25

King, I. R. 1966, AJ, 71, 64

King, I. R. 1972, ApJ, 174, L123+

King, I. R. 1981, QJRAS, 22, 227

Kneller, J. P. & Steigman, G. 2004, New Journal of Physics, 6, 117

Kochanek, C. S. & Blandford, R. D. 1987, ApJ, 321, 676

Kovac, J. M., Leitch, E. M., Pryke, C., et al. 2002, Nature, 420, 772

Kuhlen, M., Keeton, C. R., & Madau, P. 2004, ApJ, 601, 104

Lacey, C. & Cole, S. 1993, MNRAS, 262, 627

Landau, L. D. & Lifshitz, E. M. 1975, The classical theory of fields (Course of theoretical physics - Pergamon International Library of Science, Technology, Engineering and Social Studies, Oxford: Pergamon Press, 1975, 4th rev.engl.ed.)

Le Fevre, O., Hammer, F., Angonin, M. C., Gioia, I. M., & Luppino, G. A. 1994, ApJ, 422, L5

Lee, J., Kang, X., & Jing, Y. P. 2005, ApJ, 629, L5

Lenzen, F., Schindler, S., & Scherzer, O. 2004, A&A, 416, 391

Li, G.-L., Mao, S., Jing, Y. P., et al. 2005, ApJ, 635, 795

Li, G. L., Mao, S., Jing, Y. P., Lin, W. P., & Oguri, M. 2007, MNRAS, 378, 469

Linde, A. D. 1982a, Physics Letters B, 108, 389

Linde, A. D. 1982b, Physics Letters B, 116, 335

Linde, A. D. 1983, Physics Letters B, 129, 177

Luppino, G. A., Gioia, I. M., Hammer, F., Le Fèvre, O., & Annis, J. A. 1999, A&AS, 136, 117

Lynden-Bell, D. 1967, MNRAS, 136, 101

Lynds, R. & Petrosian, V. 1986, in Bulletin of the American Astronomical Society, Vol. 18, Bulletin of the American Astronomical Society, 1014–+

Manera, M. & Mota, D. F. 2006, MNRAS, 371, 1373

Maor, I. & Lahav, O. 2005, Journal of Cosmology and Astro-Particle Physics, 7, 3

Mathiesen, B. F. & Evrard, A. E. 2001, ApJ, 546, 100

Mellier, Y. 1999, ARA&A, 37, 127

Meneghetti, M., Argazzi, R., Pace, F., et al. 2007, A&A, 461, 25

Meneghetti, M., Bartelmann, M., Dolag, K., et al. 2005a, A&A, 442, 413

Meneghetti, M., Bartelmann, M., Jenkins, A., & Frenk, C. 2005b, ArXiv Astrophysics e-prints, astro-ph/0509323

Meneghetti, M., Bartelmann, M., & Moscardini, L. 2003a, MNRAS, 346, 67

Meneghetti, M., Bartelmann, M., & Moscardini, L. 2003b, MNRAS, 340, 105

Meneghetti, M., Bolzonella, M., Bartelmann, M., Moscardini, L., & Tormen, G. 2000, MNRAS, 314, 338

Meszaros, P. 1974, A&A, 37, 225

Michie, R. W. 1963, MNRAS, 125, 127

Michie, R. W. & Bodenheimer, P. H. 1963, MNRAS, 126, 269

Milgrom, M. 1983a, ApJ, 270, 371

Milgrom, M. 1983b, ApJ, 270, 384

Milgrom, M. 1983c, ApJ, 270, 365

Miralda-Escude, J. 1993, ApJ, 403, 497

Moffat, J. W. 2006, Journal of Cosmology and Astro-Particle Physics, 3, 4

Mohr, J. J., Mathiesen, B., & Evrard, A. E. 1999, ApJ, 517, 627

Moore, B., Governato, F., Quinn, T., Stadel, J., & Lake, G. 1998, ApJ, 499, L5+

Moore, B., Quinn, T., Governato, F., Stadel, J., & Lake, G. 1999, MNRAS, 310, 1147

Mortlock, D. J. & Turner, E. L. 2001, MNRAS, 327, 557

Moscardini, L., Matarrese, S., Lucchin, F., & Messina, A. 1991, MNRAS, 248, 424

Mota, D. F. & van de Bruck, C. 2004, A&A, 421, 71

Mushotzky, R. F. & Scharf, C. A. 1997, ApJ, 482, L13+

Narayan, R. & Bartelmann, M. 1996, ArXiv Astrophysics e-prints, astro-ph/9606001

Navarro, J. F., Frenk, C. S., & White, S. D. M. 1995, MNRAS, 275, 56

Navarro, J. F., Frenk, C. S., & White, S. D. M. 1996, ApJ, 462, 563

Navarro, J. F., Frenk, C. S., & White, S. D. M. 1997, ApJ, 490, 493

Navarro, J. F., Hayashi, E., Power, C., et al. 2004, MNRAS, 349, 1039

Oguri, M., Lee, J., & Suto, Y. 2003, ApJ, 599, 7

Oguri, M., Takada, M., Umetsu, K., & Broadhurst, T. 2005, ApJ, 632, 841

Oguri, M., Taruya, A., & Suto, Y. 2001, ApJ, 559, 572

O'Hara, T. B., Mohr, J. J., Bialek, J. J., & Evrard, A. E. 2006, ApJ, 639, 64

Padmanabhan, T. 1990, Phys. Rep., 188, 285

Padmanabhan, T. 1993, Structure Formation in the Universe (Structure Formation in the Universe, by T. Padmanabhan, pp. 499. ISBN 0521424860. Cambridge, UK: Cambridge University Press, June 1993.)

Page, L., Hinshaw, G., Komatsu, E., et al. 2007, ApJS, 170, 335

Peacock, J. A. & Dodds, S. J. 1996, MNRAS, 280, L19

Peebles, P. J. & Ratra, B. 2003, Reviews of Modern Physics, 75, 559

Perlick, V. 1990a, Classical and Quantum Gravity, 7, 1319

Perlick, V. 1990b, Classical and Quantum Gravity, 7, 1849

Perlick, V. 2000a, in Lecture Notes in Physics, Berlin Springer Verlag, Vol. 540, Einstein's Field Equations and Their Physical Implications, ed. B. G. Schmidt, 373–+

Perlick, V. 2000b, Ray Optics, Fermat's Principle, and Applications to General Relativity (Ray Optics, Fermat's Principle, and Applications to General Relativity, by Volker Perlick. Lecture Notes in Physics, Monographs Series, v.61. Published by Springer-Verlag (Berlin Heidelberg New York), 2000.)

Perlick, V. 2004, Living Reviews in Relativity, 7, 9

Poole, G. B., Babul, A., McCarthy, I. G., et al. 2007, MNRAS, 380, 437

Poole, G. B., Fardal, M. A., Babul, A., et al. 2006, MNRAS, 373, 881

Power, C., Navarro, J. F., Jenkins, A., et al. 2003, MNRAS, 338, 14

Pratt, G. W., Arnaud, M., & Pointecouteau, E. 2006, A&A, 446, 429

Press, W. H. & Schechter, P. 1974, ApJ, 187, 425

Puchwein, E. & Bartelmann, M. 2007, A&A, 474, 745

Puchwein, E., Bartelmann, M., Dolag, K., & Meneghetti, M. 2005, A&A, 442, 405

Randall, S. W., Sarazin, C. L., & Ricker, P. M. 2002, ApJ, 577, 579

Ratra, B. & Peebles, P. J. E. 1988, Phys. Rev. D, 37, 3406

Raymond, J. C. & Smith, B. W. 1977, ApJS, 35, 419

Readhead, A. C. S., Mason, B. S., Contaldi, C. R., et al. 2004, ApJ, 609, 498

Rebolo, R., Battye, R. A., Carreira, P., et al. 2004, MNRAS, 353, 747

Réfrégier, A., Boulade, O., Mellier, Y., et al. 2006, in Presented at the Society of Photo-Optical Instrumentation Engineers (SPIE) Conference, Vol. 6265, Space Telescopes and Instrumentation I: Optical, Infrared, and Millimeter. Edited by Mather, John C.; MacEwen, Howard A.; de Graauw, Mattheus W. M.. Proceedings of the SPIE, Volume 6265, pp. 62651Y (2006).

Reichart, D. E., Castander, F. J., & Nichol, R. C. 1999, ApJ, 516, 1

Reiprich, T. H. & Böhringer, H. 2002, ApJ, 567, 716

Reynolds, J. H. 1913, MNRAS, 74, 132

Ricker, P. M., Dodelson, S., & Lamb, D. Q. 2000, ApJ, 536, 122

Ricker, P. M. & Sarazin, C. L. 2001, ApJ, 561, 621

Riess, A. G., Strolger, L.-G., Tonry, J., et al. 2004, ApJ, 607, 665

Rines, K. & Diaferio, A. 2006, AJ, 132, 1275

Rines, K., Diaferio, A., & Natarajan, P. 2007, ApJ, 657, 183

Robertson, H. P. 1933, Reviews of Modern Physics, 5, 62

Robertson, H. P. 1935, ApJ, 82, 284

Rood, H. J., Page, T. L., Kintner, E. C., & King, I. R. 1972, ApJ, 175, 627

Rubin, V. C., Ford, Jr., W. K., Thonnard, N., & Burstein, D. 1982, ApJ, 261, 439

Rubin, V. C., Thonnard, N., & Ford, Jr., W. K. 1978, ApJ, 225, L107

Rubin, V. C., Thonnard, N., & Ford, Jr., W. K. 1980, ApJ, 238, 471

Salvador-Solé, E., Manrique, A., González-Casado, G., & Hansen, S. H. 2007a, ApJ, 666, 181

Salvador-Solé, E., Serra, S., Domínguez-Tenreiro, R., & Manrique, A. 2007b, ArXiv Astrophysics e-prints, 0704.2228

Sanders, R. H. 2007, MNRAS, 380, 331

Sanders, R. H. & McGaugh, S. S. 2002, ARA&A, 40, 263

Schäfer, B. & Bartelmann, M. 2007, MNRAS, 377, 253

Schindler, S. 1999, A&A, 349, 435

Schmidt, R. W. & Allen, S. W. 2007, MNRAS, 379, 209

Schneider, P., Ehlers, J., & Falco, E. E. 1992, Gravitational Lenses (Gravitational Lenses, XIV, 560 pp. 112 figs.. Springer-Verlag Berlin Heidelberg New York. Also Astronomy and Astrophysics Library)

Schramm, T. 1990, A&A, 231, 19

Schramm, T. 1994, A&A, 284, 44

Schuecker, P., Böhringer, H., Guzzo, L., et al. 2001, A&A, 368, 86

Seidel, G. & Bartelmann, M. 2007, A&A, 472, 341

Semboloni, E., Mellier, Y., van Waerbeke, L., et al. 2006, A&A, 452, 51

Shannon, C. E. 1948, The Bell System Technical Journal, 27, 279

Sheth, R. K., Mo, H. J., & Tormen, G. 2001, MNRAS, 323, 1

Sheth, R. K. & Tormen, G. 2002, MNRAS, 329, 61

Smail, I., Hogg, D. W., Yan, L., & Cohen, J. G. 1995, ApJ, 449, L105+

Smith, K. M., Zahn, O., & Doré, O. 2007, Phys. Rev. D, 76, 043510

Smith, R. E., Peacock, J. A., Jenkins, A., et al. 2003, MNRAS, 341, 1311

Smoot, G. F., Bennett, C. L., Kogut, A., et al. 1992, ApJ, 396, L1

Snowden, S. L. & Schmitt, J. H. M. M. 1990, Ap&SS, 171, 207

Soldner, J. 1804, Berliner Astron. Jahrb., 161

Somerville, R. S. & Kolatt, T. S. 1999, MNRAS, 305, 1

Soucail, G., Fort, B., Mellier, Y., & Picat, J. P. 1987, A&A, 172, L14

Spergel, D. N., Bean, R., Doré, O., et al. 2007, ApJS, 170, 377

Spergel, D. N., Verde, L., Peiris, H. V., et al. 2003, ApJS, 148, 175

Springel, V. 2005, MNRAS, 364, 1105

Springel, V., White, S. D. M., Jenkins, A., et al. 2005, Nature, 435, 629

Springel, V., Yoshida, N., & White, S. D. M. 2001, New Astronomy, 6, 79

Stanek, R., Evrard, A. E., Böhringer, H., Schuecker, P., & Nord, B. 2006, ApJ, 648, 956

Starobinskij, A. A. 1980, Physics Letters B, 91, 99

Starobinsky, A. A. 1979, Soviet Journal of Experimental and Theoretical Physics Letters, 30, 682

Steinhardt, P. J., Wang, L., & Zlatev, I. 1999, Phys. Rev. D, 59, 123504

Straumann, N. 2004, General relativity with applications to astrophysics (General relativity with applications to astrophysics, by Norbert Straumann. Springer Texts and monographs in physics. Berlin: Springer, 2004)

Sunyaev, R. A. & Zeldovich, I. B. 1980, MNRAS, 190, 413

Sunyaev, R. A. & Zeldovich, Y. B. 1972, Comments on Astrophysics and Space Physics, 4, 173

Syer, D. & White, S. D. M. 1998, MNRAS, 293, 337

Tegmark, M., Strauss, M. A., Blanton, M. R., et al. 2004, Phys. Rev. D, 69, 103501

Tormen, G., Moscardini, L., & Yoshida, N. 2004, MNRAS, 350, 1397

Torri, E., Meneghetti, M., Bartelmann, M., et al. 2004, MNRAS, 349, 476

Treu, T. & Koopmans, L. V. E. 2002, ApJ, 575, 87

Tsallis, C. 1999, Brazilian Journal of Physics, 29, 1

Tyson, J. A. 1988, AJ, 96, 1

Valluri, M., Vass, I. M., Kazantzidis, S., Kravtsov, A. V., & Bohn, C. L. 2007, ApJ, 658, 731

Vanzella, E., Cristiani, S., Dickinson, M., et al. 2005, A&A, 434, 53

Vanzella, E., Cristiani, S., Dickinson, M., et al. 2006, A&A, 454, 423

Vikhlinin, A., VanSpeybroeck, L., Markevitch, M., Forman, W. R., & Grego, L. 2002, ApJ, 578, L107

Voges, W. 1993, Advances in Space Research, 13, 391

Walker, A. G. 1933, MNRAS, 94, 159

Walsh, D., Carswell, R. F., & Weymann, R. J. 1979, Nature, 279, 381

Wambsganss, J., Bode, P., & Ostriker, J. P. 2004, ApJ, 606, L93

Wang, L. & Steinhardt, P. J. 1998, ApJ, 508, 483

Wang, P. 2006, ApJ, 640, 18

Warren, M. S., Abazajian, K., Holz, D. E., & Teodoro, L. 2006, ApJ, 646, 881

Weinberg, S. 1972, Gravitation and Cosmology: Principles and Applications of the General Theory of Relativity (Gravitation and Cosmology: Principles and Applications of the General Theory of Relativity, by Steven Weinberg, pp. 688. ISBN 0-471-92567-5. Wiley-VCH , July 1972.)

Weisskopf, M. C., Brinkman, B., Canizares, C., et al. 2002, PASP, 114, 1

Wetterich, C. 1988a, Nuclear Physics B, 302, 645

Wetterich, C. 1988b, Nuclear Physics B, 302, 668

Wetterich, C. 1995, A&A, 301, 321

Wetterich, C. 2004, Physics Letters B, 594, 17

White, S. D. M. 1982, in Saas-Fee Advanced Course 12: Morphology and Dynamics of Galaxies, ed. L. Martinet & M. Mayor, 289–420

White, S. D. M., Efstathiou, G., & Frenk, C. S. 1993, MNRAS, 262, 1023

White, S. D. M. & Rees, M. J. 1978, MNRAS, 183, 341

Wu, X.-P. & Hammer, F. 1993, MNRAS, 262, 187

Wu, X.-P. & Mao, S. 1996, ApJ, 463, 404

Wu, X.-P. & Xue, Y.-J. 2000, ApJ, 529, L5

Wyithe, J. S. B., Turner, E. L., & Spergel, D. N. 2001, ApJ, 555, 504

Yepes, G., Sevilla, R., Gottlöber, S., & Silk, J. 2007, ApJ, 666, L61

Zaritsky, D. & Gonzalez, A. H. 2003, ApJ, 584, 691

Zavala, J., Núñez, D., Sussman, R. A., Cabral-Rosetti, L. G., & Matos, T. 2006, Journal of Cosmology and Astro-Particle Physics, 6, 8

Zel'dovich, Y. B. 1970, A&A, 5, 84

Zeng, D.-f. & Gao, Y.-h. 2005a, ArXiv Astrophysics e-prints, astro-ph/0505163

Zeng, D.-f. & Gao, Y.-h. 2005b, ArXiv Astrophysics e-prints, astro-ph/0505164

Zhao, H. 2006, ArXiv Astrophysics e-prints, astro-ph/0610056

Zhao, H., Bacon, D. J., Taylor, A. N., & Horne, K. 2006, MNRAS, 368, 171

Zhao, H. S. & Famaey, B. 2006, ApJ, 638, L9

Zlosnik, T. G., Ferreira, P. G., & Starkman, G. D. 2006, Phys. Rev. D, 74, 044037

Zlosnik, T. G., Ferreira, P. G., & Starkman, G. D. 2007, Phys. Rev. D, 75, 044017

Zwicky, F. 1933, Helvetica Physica Acta, 6, 110

Zwicky, F. 1937, ApJ, 86, 217

Acknowledgements

First of all it is my pleasure to thank Matthias for supervising my Ph.D. project and for being a constant source of scientific knowledge and wisdom over the past three years. I am profundly indebted to him for sparing much of his (scarce) free time into many discussions about my project, career and life in general. Much of what I have learned over the past years is certainly due to him.

I furthermore acknowledge support by the German Science Foundation.

I am also grateful to Massimo for his support and encouragement especially at the beginning of the project, when things were not extremely smooth. I am indebted to him for teaching me many of the things I know about lensing and not only.

Then I wish to acknowledge Lauro, for helping me in finding a Ph.D. position and keeping listening to my problems (scientific and not) long after the end of my diploma thesis. I am also grateful to him for giving me the possibility to spend few months in Italy and for accepting to be my second corrector and part of my Ph.D. committee. For the latter reason I also acknowledge Prof. Dr. Ralf Klessen and Prof. Dr. Hans-Walter Rix.

I acknowledge all my friends, both in Italy and in Germany. The former for being sad when I left and keeping in touch afterwards, and the latter because they will do the same when I will leave Heidelberg. Most of my friends are also my colleagues, therefore I am grateful to all of them as well, former and present. If I embark in the attempt of listing them all I am sure I would forget someone, so I do not even try. I just thank them all, for everything they did for me in the past three years. An exception is however in order for my officemates, Christian and Claudia, for tolerating me all this time, especially when I was utterly annoying.

A separate acknowledgement goes to my parents and my sister, that never stopped helping and encouraging me. For sure, without their support I would never have entered the wonderful world of astrophysics, and this work would not exist.

Last, but first in order of importance, I am immensely grateful to Irene, for countless reasons. For all the patience she had with me despite the distance, for watching me leave so many times, for never giving up, even when things did not look very good. She is the deepest reason for each one of my actions, and to her goes my infinite and enduring gratitude.